TECHNISCHE CHEMIE

Rheinland-Pfälzische Technische Universität Kaiserslautern Landau

Vom Fachbereich Chemie der Rheinland-Pfälzischen Technischen Universität Kaiserslautern-Landau (RPTU) zur Verleihung des akademischen Grades

„Doktor der Naturwissenschaften“

genehmigte Dissertation

DE - 386

Generation of heterogenous Fe- and Fe/Co-based catalysts from metal-organic framework precursors for the Fischer-Tropsch synthesis from carbon dioxide and hydrogen

vorgelegt von

M. Sc. Tim Herrendorf

geboren in Moers

Betreuer der Arbeit: Prof. Dr. Wolfgang Kleist

Tag der wissenschaftlichen Aussprache:

30. August. 2024

The practical work for this thesis was conducted between 15.10.2019 and 15.07.2023 at the Ruhr University Bochum (RUB, Faculty of Chemistry and Biochemistry) and the RPTU Kaiserslautern-Landau, (Department of Chemistry) under the supervision of Prof. Dr. Wolfgang Kleist.

Abstract

In this work, novel catalyst systems generated *via* the MOF-mediated synthesis (MOFMS) approach were investigated regarding their activity for the CO_2-based Fischer-Tropsch synthesis (FTS). MOFMS catalysts feature unique properties due to the presence of metal particles within a carbon matrix. A carbon shell, which prevents oxidation of the metal particles, high metal loadings in combination with comparatively small particle size and an enhanced carbide formation due to the close proximity of metal and carbon source should be particularly interesting for the CO_2-FTS process. Hence, the topic of this thesis was the synthesis and catalytic testing of different Fe- and Fe/Co-containing MOFMS catalysts for CO_2-FTS applications.

In the first part of this work, Fe-based MOF precursors were synthesized and characterized using PXRD, ICP-OES, ATR-IR spectroscopy, nitrogen physisorption and TGA measurements. The MIL-53(Fe) precursors were thermally decomposed at 400 °C, 600 °C and 800 °C, respectively, to generate MOFMS catalysts. The catalysts contained reduced iron, iron carbide and oxidized iron phases in different oxidation states embedded in a porous carbon matrix, depending on the used decomposition temperature. The generated phases were analyzed *via* PXRD, XAS and Mössbauer spectroscopy and the carbon matrix was investigated by ICP-OES and nitrogen physisorption measurements. Afterwards, their CO_2-FTS activity was tested in a time-on-stream experiment over 12 h and a temperature variation experiment between 200 °C and 400 °C. The best catalyst was the one that has been decomposed at 800 °C (Fe@C_800°C) and showed a C_{2+} selectivity of 53.9 % and C_{5+} selectivity of 14.2 % at a CO_2 conversion of 29.1 % at 350 °C. The catalysts were characterized again after the catalytic testing, which revealed a potential damage of the carbon matrix. This was concluded due to the observed phase transition towards oxidized iron for all catalysts.

In the second part, bimetallic Fe/Co-containing MOFMS catalysts were investigated. The first step was the synthesis and characterization of the MIL-53(Fe_xCo_{1-x}) precursor materials with different Fe/Co ratios. The same characterization techniques as for the Fe-based MOF precursors were used. The MOFMS process was carried out at 800 °C, which resulted in reduced Fe and FeCo metal nanoparticles with a bcc

structure embedded in a carbon matrix for all catalysts. This was revealed by PXRD and XAS measurements. Furthermore, the carbon matrix was analyzed *via* ICP-OES and nitrogen physisorption measurements. Additionally, the oxidation preventing effect of MOFMS catalysts was investigated *via* TPR measurements and it was assumed that a thin layer of Fe_3C carbide was formed around the metal nanoparticles, which prevents further oxidation while also allowing catalytic activity for the CO_2-FTS process. The same catalytic testing experiments as for the Fe-based catalyst series were performed. The best Fe/Co catalysts were the Fe-rich variants, thus, $Fe_{0.75}Co_{0.25}$@C displayed a maximum C_{2+} selectivity of 46.3 % and C_{5+} selectivity of 8.0 % at a CO_2 conversion of 33.0 % at 400 °C. $Fe_{0.80}Co_{0.20}$@C showed a maximum C_{2+} selectivity of 68.2 % and C_{5+} selectivity of 11.6 % at a CO_2 conversion of 38.2 % at 400 °C. After the catalytic testing, all Fe/Co-containing catalysts exhibited no structural changes of the reduced metal phases with the exception of $Fe_{0.80}Co_{0.20}$@C_spent, which generated a χ-Fe_5C_2 carbide phase during the time-on-stream experiment.

In the third part, the best unpromoted catalysts (Fe@C_800°C, $Fe_{0.80}Co_{0.20}$@C and $Fe_{0.75}Co_{0.25}$@C) were modified *via* the addition of either potassium, manganese or copper as promoter. The MIL-53(Fe_xCo_{1-x})-$Y_{0.20}$ precursor materials were again characterized using the same techniques as for the unpromoted variants. After the MOFMS process, the catalysts showed reduced metal phases alongside Fe_3C phases for the catalysts without cobalt. This was concluded from PXRD and XAS measurements. Furthermore, ICP-OES, nitrogen physisorption and TPR measurements were performed. The TPR results matched the results of the unpromoted Fe/Co-containing catalysts, where a thin protective layer of Fe_3C around the reduced metal nanoparticles was assumed. The catalytic tests showed the highest selectivity towards FTS products for the K-containing catalysts with a maximum C_{2+} selectivity of 65.7 % and C_{5+} selectivity of 23.7 % at a CO_2 conversion of 28.1 % at 350 °C for Fe@C-$K_{0.20}$ and a maximum C_{2+} selectivity of 61.1 % and C_{5+} selectivity of 13.8 % at a CO_2 conversion of 27.4 % at 300 °C for $Fe_{0.80}Co_{0.20}$@C-$K_{0.20}$. The Mn-containing catalysts displayed an inferior performance compared to the unpromoted variants, both regarding selectivity and CO_2 conversion. The Cu-containing catalysts exhibited the overall highest CO_2 conversions but showed higher methane selectivities than the K-containing variants. After the catalytic

testing, the Fe- and Co-containing catalysts displayed reduced metal phases and χ-Fe_5C_2, while the catalysts without cobalt contained oxidic species. This further indicated a stabilizing effect of cobalt on the MOFMS CO_2-FTS catalysts.

In summary, the goal of the thesis was achieved with the catalysts Fe@C_800 °C and $Fe_{0.80}Co_{0.20}$@C being the most promising from the monometallic Fe-containing and bimetallic Fe/Co-containing systems, respectively. Furthermore, potassium showed the most beneficial effects from the tested promoters for all catalysts.

Kurzfassung

Im Rahmen dieser Arbeit wurden neuartige Katalysatorsysteme mittels des MOF-mediierten Syntheseansatzes hergestellt und hinsichtlich ihrer Aktivität in der CO_2-basierten Fischer-Tropsch-Synthese (FTS) untersucht. MOFMS-Katalysatoren zeichnen sich durch einzigartige Eigenschaften aus, die auf Metallpartikel zurückzuführen sind, welche von einer Kohlenstoffmatrix umschlossen sind. Für den CO_2-FTS-Prozess sind insbesondere die Oxidationsprävention, die hohen erreichbaren Metallbeladungen bei vergleichsweise kleiner Kristallitgröße und die verstärkte Carbidbildung aufgrund der räumlichen Nähe von Metall und Kohlenstoffquelle von Interesse. Folglich wurden die Synthese und die katalytischen Untersuchungen verschiedener Fe- und Fe/Co-haltigen MOFMS-Katalysatoren für CO_2-FTS Anwendungen als Ziel der Arbeit definiert.

Zunächst wurden Fe-basierte MOF-Vorstufen synthetisiert und mittels PXRD, ICP-OES, ATR-IR-Spektroskopie, Stickstoff-Physisorptionsmessungen und thermogravimetrischer Analyse charakterisiert. Die MIL-53(Fe)-Vorstufen wurden bei 400 °C, 600 °C und 800 °C thermisch zersetzt um MOFMS-Katalysatoren herzustellen. Die Katalysatoren entwickelten je nach Zersetzungstemperatur reduzierte Eisen- und Eisencarbidphasen sowie oxidierte Eisenphasen in unterschiedlichen Oxidationsstufen, die jeweils in eine Kohlenstoffmatrix eingebettet waren. Die gebildeten Phasen wurden mittels PXRD, XAS und Mössbauer-Spektroskopie identifiziert und die Kohlenstoffmatrix wurde mittels ICP-OES und Stickstoff-Physisorptionsmessungen bestimmt. Anschließend wurden die Katalysatoren im CO_2-FTS-Prozess mit einem Time-on-Stream-Experiment über 12 Stunden und einem Temperaturvariationsexperiment zwischen 200 °C und 400 °C getestet. Der aktivste Katalysator Fe@C_800°C zeigte eine C_{2+}-Selektivität von 53,9 % und eine C_{5+}-Selektivität von 14,2 % bei einem CO2-Umsatz von 29,1 % bei 350 °C. Alle Materialien wurden nach den katalytischen Tests erneut charakterisiert, wobei oxidierte Eisenphasen in allen Katalysatoren gefunden wurden. Dies lässt auf eine Beschädigung der Kohlenstoffmatrix unter Reaktionsbedingungen schließen.

Im zweiten Teil wurden bimetallische Fe/Co-basierte MOFMS-Katalysatoren untersucht. Den ersten Schritt stellte die Synthese und Charakterisierung der

MIL-53(Fe_xCo_{1-X})-Vorstufenmaterialien mit unterschiedlichen Fe/Co-Verhältnissen dar. Es wurden die gleiche Charakterisierungstechniken wie bei den Fe-basierten MOF-Vorläufern eingesetzt. Der MOFMS-Prozess wurde bei 800 °C durchgeführt, wobei reduzierte Fe- und FeCo-Metall-Nanopartikel mit einer bcc-Struktur entstanden, welche von einer Kohlenstoffmatrix umschlossen waren. Dies wurde durch PXRD- und XAS-Messungen nachgewiesen. Außerdem wurde die Kohlenstoffmatrix mittels ICP-OES und Stickstoffphysisorptionsmessungen analysiert. Zusätzlich wurde die oxidationsinhibierende Wirkung der MOFMS-Katalysatoren mit Hilfe von TPR-Messungen untersucht. Aus diesen Messungen konnte abgeleitet werden, dass sich um die Metallnanopartikel eine dünne Schicht aus Fe_3C-Carbid bildet, welche eine weitere Oxidation verhindert und gleichzeitig die katalytische Aktivität für den CO_2-FTS-Prozess ermöglicht. Es wurden dieselben Katalysetests wie für die Fe-basierte Katalysatorserie durchgeführt. Die leistungsstärksten Fe/Co-Katalysatoren waren die Fe-reichen Varianten. $Fe_{0.75}Co_{0.25}$@C zeigte eine maximale C_{2+}-Selektivität von 46,3 % und eine C_{5+}-Selektivität von 8,0 % bei einem CO_2-Umsatz von 33,0 % bei 400 °C. $Fe_{0.80}Co_{0.20}$@C zeigte eine maximale C_{2+}-Selektivität von 68,2 % und eine C_{5+}-Selektivität von 11,6 % bei einem CO_2-Umsatz von 38,2 % bei 400 °C. Nach den katalytischen Tests wiesen die Fe/Co-Katalysatoren keine strukturellen Veränderungen der reduzierten Metallphasen auf, mit Ausnahme des Katalysators $Fe_{0.80}Co_{0.20}$@C_spent, welcher während den katalytischen Tests eine χ-Fe_5C_2-Carbidphase ausbildete.

Im dritten und letzten Teil wurden die vielversprechendsten unpromotierten Katalysatoren (Fe@C_800°C, $Fe_{0.80}Co_{0.20}$@C und $Fe_{0.75}Co_{0.25}$@C) mit den Promotoren Kalium, Mangan und Kupfer modifiziert. Die MIL-53(Fe_xCo_{1-x})-$Y_{0.20}$-Vorstufenmaterialien wurden mit denselben Techniken charakterisiert wie die unpromotierten Varianten zuvor. Nach dem MOFMS-Prozess wiesen alle Katalysatoren reduzierte Metallphasen auf und die Katalysatoren ohne Cobalt zeigten zusätzlich Fe_3C-Phasen, was mittels PXRD- und XAS-Messungen festgestellt wurde. Weiterhin wurden ICP-OES-, Stickstoffphysisorptions- und TPR-Messungen durchgeführt. Die TPR-Ergebnisse stimmten mit den Ergebnissen der unpromotierten Fe/Co Katalysatoren überein, bei denen eine dünne Schutzschicht aus Fe_3C um die reduzierten Metallnanopartikel angenommen wurde. Die kaliumhaltigen Katalysatoren zeigten in den Katalysetests die höchste Selektivität für

FTS-Produkte mit einer maximalen C_{2+}-Selektivität von 65,7 % und einer C_{5+}-Selektivität von 23,7 % bei einem CO_2-Umsatz von 28,1 % bei 350 °C für Fe@C-$K_{0.20}$ und einer maximalen C_{2+} Selektivität von 61,1 % und einer C_{5+} Selektivität von 13,8 % bei einem CO_2-Umsatz von 27,4 % bei 300 °C für $Fe_{0.80}Co_{0.20}$@C-$K_{0.20}$. Die manganhaltigen Katalysatoren hingegen zeigten im Vergleich zu den unpromotierten Varianten eine niedrigere Aktivität, sowohl hinsichtlich der Selektivität als auch des CO_2-Umsatzes. Die kupferhaltigen Katalysatoren wiesen insgesamt die höchsten CO_2-Umsätze auf, jedoch auch höhere Methanselektivitäten als die kaliumhaltigen Varianten. Im Anschluss an die katalytischen Tests zeigten die Fe- und Co-haltigen Katalysatoren reduzierte Metallphasen und χ-Fe_5C_2, während die Katalysatoren ohne Cobalt oxidierte Phasen enthielten. Dieser Umstand ist ein weiteres Indiz für die stabilisierende Wirkung von Cobalt auf die MOFMS CO_2-FTS-Katalysatoren.

Zusammenfassend lässt sich sagen, dass das Ziel der Arbeit erreicht wurde, wobei die Katalysatoren Fe@C_800 °C und $Fe_{0.80}Co_{0.20}$@C die vielversprechendsten der monometallischen Fe- bzw. bimetallischen Fe/Co-haltigen Systeme waren. Darüber hinaus zeigte Kalium bei allen Katalysatoren die vorteilhaftesten Auswirkungen der getesteten Promotoren.

List of abbreviations

Abbreviation	Meaning
^{1}H-NMR	Proton nuclear magnetic resonance (spectroscopy)
ATR-IR	Attenuated total reflection infrared (spectroscopy)
BET method	Brunauer-Emmett-Teller method
BJH plot	Barrett-Joyner-Halenda plot
Cf.	Confer
CNT	Carbon nano tubes
DESY	Deutsches Elektronen Synchrotron
DFT	Discrete Fourier transform
DMF	*N*,*N*-Dimethylformamide
DTG	Derivative of TGA graph
DUT	Dresden University of Technology
EDX	Energy dispersive X-ray (analysis)
EXAFS	Extended X-ray absorption fine structure
FID	Flame ionization detector
FT	Fischer-Tropsch
FTS	Fischer-Tropsch synthesis
GC	Gas chromatography
GHSV	Gas hourly space velocity
H_2BDC	Terephthalic acid
H_2BPDC	4,4‘-biphenyldicarboxylic acid
HK plot	Horvath-Kawazoe plot
HKUST	Hong Kong University of Science and Technology
ht-form	High-temperature form
HTFT	High-temperature Fischer-Tropsch
ICP-OES	Inductively coupled plasma optical emission spectroscopy
IUPAC	International union of pure and applied chemistry

KWI	Kaiser Wilhelm institute for Coal Research
lt-form	Low-temperature form
LTFT	Low-temperature Fischer-Tropsch
MIL	Material Institute Lavoisier
MOF	Metal-organic framework
MOFMS	Metal-organic framework mediated synthesis
NPs	Nano particles
PXRD	Powder X-ray diffraction
QMS	Quadrupole mass spectrometer
RT	Room temperature
rWGS	Reverse water-gas shift
SBU	Secondary building units
SMSI	Strong metal-support interaction
STY	Space time yield
TCD	Thermal conductivity detector
TGA	Thermogravimetric analysis
TOF	Turn over frequency
TOS	Time-on-stream
TPR	Temperature-programmed reduction
WGS	Water-gas shift
XANES	X-ray absorption near edge spectroscopy
XAS	X-ray absorption spectroscopy
XPS	X-ray photoelectron spectroscopy
ZIF	Zeolitic imidazolate framework

Table of contents

1 Scientific background

1.1 History of the Fischer-Tropsch synthesis

The Fischer-Tropsch synthesis (FTS) was discovered in the 1920s by the German scientists Franz Fischer and Hans Tropsch at the Kaiser Wilhelm institute for Coal Research (KWI), during the investigation of a process to convert coal into synthetic liquid hydrocarbons. The first step of the process was the generation of syngas (CO + H_2) by hydrocracking of the coal with steam. The gas was then converted over a cobalt catalyst at pressures in the range of 1 atm to 10 atm and at temperatures between 453 K and 473 K into a petroleum-like liquid.[1] The industrial application of the FTS process started in Germany with nine operating plants in 1938 (capacity of $660 \cdot 10^3$ t per year), due to the constantly rising crude oil prices.[2] The newly found technological success was exported from Germany to the United States, Britain, Japan, France and South Africa since the early 1930s. Despite the pioneering work of Germany, serious development of the practical applications of the FTS began after World War II in the United States, due to a rapid increase in fuel consumption and concerns from the government of the limitations of crude oil sources.[3] During the same time period a coal-based FTS plant was constructed by Sasol in South Africa. Until the 1970s the economic viability of the FTS process varied considerably, due to it being closely linked to the crude oil prices. However, during the oil crises of the 1970s, Sasol constructed two additional FTS plants with a combined capacity of $6000 \cdot 10^3$ t per year.[4] In modern days, the FTS process can be used to produce petrochemical products out of green hydrogen and captured carbon dioxide or biomass, which will be discussed in detail in the following chapters.

1.2 CO-based Fischer-Tropsch synthesis

Since the discovery of the Fischer-Tropsch synthesis, the reaction was intensively investigated regarding reaction parameters, possible catalysts, products and reaction mechanisms. The reaction is classified as a surface polymerization reaction of hydrogen and carbon monoxide, which takes place at the surface of the catalyst.[5,6] The FT reaction involves the formation and subsequent polymerization of -CH_2- building blocks, which results in the general reaction equation shown below (Eq. 1).

FTS $$CO + 2\,H_2 \rightarrow -(CH_2) - + H_2O\ (\Delta H = -166\,kJ \cdot mol^{-1})$$ Eq. 1

However, the FTS yields a wide spectrum of products ranging from C_1 to C_{40} hydrocarbons in form of alkanes, olefins and alcohols. This phenomenon results from the occurrence of several different reactions at the catalyst surface and the respective yields depend on the thermodynamics and kinetics of these reactions. Mechanistic studies of the FTS attracted a lot of researchers in the past.[7,8] The complex reaction network of the carbon-carbon bond formation, the hydrogenation of carbon monoxide and the subsequently proceeding FT reaction are all based on the ability of the metallic catalysts to dissociatively chemisorb carbon monoxide. As of today, three mechanisms have been proposed, which all describe the three major reaction steps of initiation, propagation and chain termination. However, the mechanisms differ in the description of the formation of the monomer units and the paths of the surface reaction which determine the generated hydrocarbons.[3] The carbide mechanism represents the most important proposed mechanism with the initial step of chemisorption of carbon monoxide in a bridging position at two surface sites. Afterwards the C-O bonds subsequently dissociates into adsorbed C and O atoms. Simultaneously, hydrogen is also chemisorbed and dissociated at the metal surface (Scheme 1 a). This leads to the subsequential formation of monomer units (M-CH_2-) *via* the hydrogenation of the surface C atoms (Scheme 1 b). The surface oxygen is removed *via* the reaction with the surface hydrogen to water (Scheme 1 a). The chain growth occurs *via* the reaction of two monomer units or the insertion of a monomer unit into a growing alkyl species (Scheme 1 c). The termination takes place by the addition of either -CH_3 or hydrogen to generate alkanes or by cleavage of a C-H bond of the adsorbed species to form an alkene.[3,9–11]

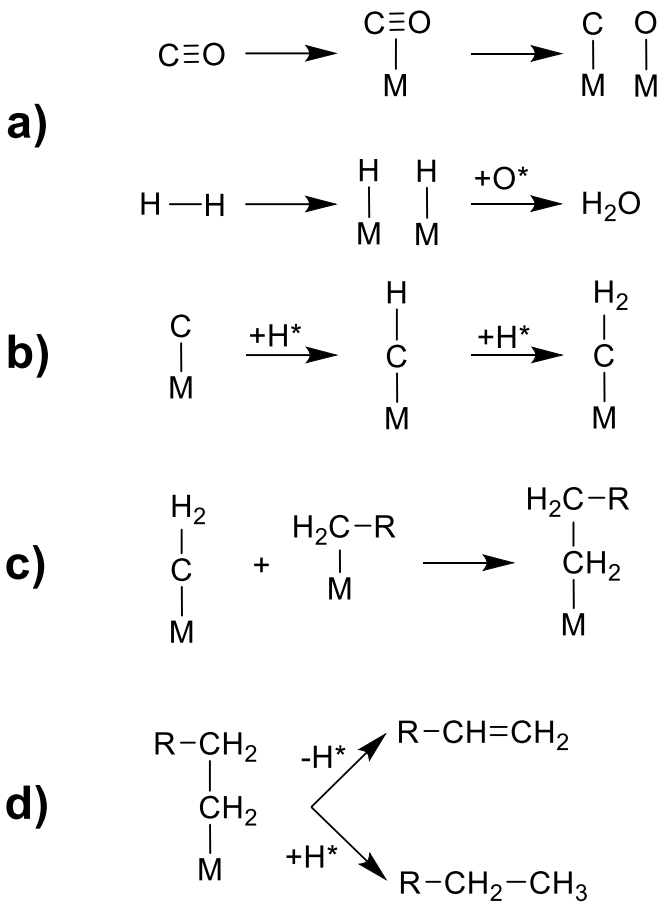

Scheme 1: Four steps of the carbide mechanism.

The second proposed mechanism is called the CO insertion mechanism, which is shown in Scheme 2. Here, a CO insertion into the M-H bond initiates the polymerization reaction, followed by the insertion of another carbon monoxide into the metal-alkyl bonds, which acts as a chain growth mechanism. The acyl groups are reduced afterwards and the hydrogenation of such groups leads to the termination of the reaction.[3,10,12]

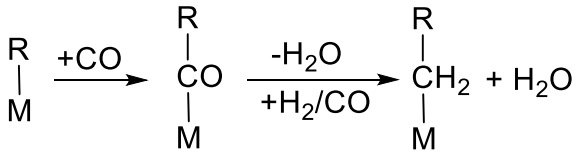

Scheme 2: Chain growth step of the FTS according to the CO insertion mechanism.

The third reported mechanism is called the hydroxycarbene mechanism, which is based on the formation of CHOH surface species as intermediates. Hydroxymethylene groups are formed by the hydrogenation of chemisorbed carbon

monoxides with chemisorbed atomic hydrogen. The C-C bonds are generated by water elimination *via* condensation of two hydroxycarbene species. The chain growth occurs afterwards at the remaining oxygenated C atom (Scheme 3).[3,12]

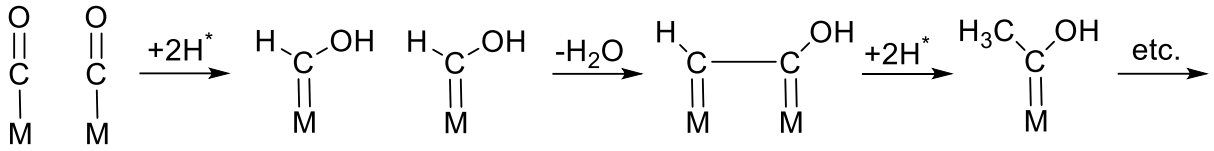

Scheme 3: Chain growth step of the FTS according to the hydroxycarbene mechanism.

Additional to the many different surface reactions occurring during the FTS, the water-gas shift (WGS) and reverse water-gas shift reaction (rWGS) were also observed during the FT process. The reaction shown in Eq. 2 converts CO and water into the unwanted by-product CO_2 and additional H_2. The reaction plays a significant role particularly for iron-based catalysts, due to the catalytic activity of iron for both the FTS and the WGS reaction.[13] The chemical equilibrium of the WGS reaction depends on the H_2/CO ratio, whereby the formation of H_2O is favored for high H_2/CO ratios and the formation of CO_2 is favored for lower H_2/CO ratios.[3]

WGS $$CO + H_2O \leftrightarrows CO_2 + H_2 \ (\Delta H = -41\ kJ \cdot mol^{-1})$$ Eq. 2

The resulting product distribution of the FTS is strongly dependent on the reaction conditions. Due to the polymerization mechanism of the FTS, the product spectrum shows generally an Anderson-Schulz-Flory (ASF) distribution. The distribution function describes the weight fraction (W_n) of the hydrocarbons with the carbon number n dependent on the chain growth probability (α) (Eq. 3). To calculate the chain growth probability, the propagation rate (r_p) and the termination rate (r_t)) are used (Eq. 4).[14]

$$\frac{W_n}{n} = (1-\alpha)^2 \cdot \alpha^{n-1}$$ Eq. 3

$$\alpha = \frac{r_p}{r_p + r_t}$$ Eq. 4

The most important hydrocarbon fraction is in general the light olefins fraction (C_2-C_4), with an optimal α value in the range of 0.4 to 0.5 for the highest selectivity towards this fraction. However, due to the limitations of the ASF distribution a high

C_2-C_4 selectivity is coupled with an increase of the selectivity towards the mostly unwanted methane. According to the ASF model, the highest attainable selectivity towards the C_2-C_4 fraction is about 57 %.[9,14] Depending on the desired product fractions, the process parameters can be varied during the FTS. The most influential parameters are reaction temperature, pressure, H_2/CO ratio and space velocity of the feed gases. The reaction temperature for the exothermic FTS is particularly relevant, which has led to two main process variations of the FTS. The variations are called high temperature Fischer-Tropsch synthesis (HTFT) and low temperature Fischer-Tropsch synthesis (LTFT).[15] The HTFT process (300–350 °C) uses iron-based catalysts due to the rWGS utilization and the lower methane selectivity of Fe catalysts in this temperature range. The main product fractions contain mostly gasoline products, 1-olefins and oxygenates.[16] LTFT is generally used to produce longer chain hydrocarbons like diesel and jet fuel, but also waxes and base oils, which are later converted *via* hydrocracking. This process variation utilizes cobalt-based catalysts at temperatures in the range 180–250 °C. Co-based catalyst materials show a better FTS activity and higher stability against deactivation compared to Fe-based systems, but the selectivity shifts heavily towards methane at higher reaction temperatures.[10,17] Generally, an increased reaction temperature during the FTS process leads to more chain branching, a lower alcohol selectivity and shorter chain lengths. Additionally, the deposition of carbonaceous species is increased and the methane selectivity is enhanced and, therefore, the reaction temperature is usually kept below 400 °C even under HTFT process conditions.[18] The operating pressure is kept in the range of 10-40 bar. High pressure conditions enhance the chain length of the product fraction and the selectivity towards alcohols.[9,18] High H_2/CO ratios shift the selectivity towards lighter products and decrease the olefin selectivity.[19] A low H_2/CO ratio is particularly problematic for Co-based catalysts due to their inability to catalyze the rWGS reaction and to adjust the ratio *in situ*.[9] A high space velocity is beneficial to shift the selectivity towards alcohols and olefins.[20,21]

1.3 CO_2-based Fischer-Tropsch synthesis as renewable energy source

One of the greatest challenges of today is climate change and the resulting global warming. CO_2 is one of the most potent greenhouse gases and, consequently, one of the major contributor to the global warming.[22] Over the past century, the CO_2 emissions increased constantly up to an atmospheric concentration, which far exceeds the earths uptake in the natural carbon cycle. The high concentration of atmospheric CO_2 leads to a heat-trapping effect, whereby the absorption of longer wavelengths of sunlight is increased. This effect has a serious impact on the ecosystem, particularly the marine ecosystem due to the rise of water temperatures in the oceans. Another effect is the increase of the water acidity due to the increased atmospheric concentration of CO_2. Therefore, a significant reduction of atmospheric CO_2 and particularly a reduction of the CO_2 emissions (in 2020 the annual CO_2 emission stood at over 34.8 billion tons) is necessary in the next years.[23–25] The most effective way to reduce these greenhouse gas emissions is the transition to greener and less carbon-based energy sources. However, at the moment the modern world is highly dependent on energy derived from fossil fuels and a full transition to non-carbon-based energy sources is not realistic in just a couple of years.[22–24] An interim solution is given by capturing CO_2 from the atmosphere or industrial processes and convert the unwanted greenhouse gas into highly valuable chemical products, thus, creating a cycle for CO_2.[24,26,27] An important aspect in the CO_2 cycle is the conversion of CO_2 into C_1 products like methane and methanol. Particularly methane can by utilized for an efficient energy storage due to its high energy density.[25] However, the conversion of CO_2 into C_{2+} products can offer even higher value both as a chemical feedstock and as an energy source. The commercially most interesting C_{2+} fraction are light olefines (C_2-C_4). These alkenes can function as chemical building blocks for various syntheses resulting in polymers, alcohols, solvents, etc..[28] As of today, these building blocks are mainly generated through steam cracking of hydrocarbons. However, the CO_2-based Fischer-Tropsch synthesis (CO_2-FTS) offers an elegant way to produce these valuable base chemicals within a closed CO_2 cycle.[29] The CO_2-FTS reaction utilizes CO_2 instead of CO and the mechanism is widely agreed to function similarly to the conventional CO-FTS. For CO_2-FTS the rWGS plays a major role as the first step of the process. *Via* the rWGS

reaction (Eq. 5) CO_2 is reduced to CO and subsequently the Fischer-Tropsch reaction (Eq. 1) between CO and H_2 can take place.[30,31]

rWGS $$CO_2 + H_2 \leftrightarrows CO + H_2O \ (\Delta H = 44\ kJ\ \cdot mol^{-1})$$ Eq. 5

The most common mechanisms that have been proposed for the propagation of the -CH_2- monomer units are the previously mentioned carbide mechanism and the CO insertion route.[23] In a recent study, Zhou *et al.* provided experimental evidence that supports both types of insertion mechanisms over Fe-based catalysts. The product distribution also follows the ASF distribution similar to the conventional CO-FTS.[32] However, CO_2-FTS provides a lot of new challenges compared to the conventional CO-FTS. The first crucial issue is the chemical inertness of CO_2, which leads to high energy requirements for the initial endothermic rWGS. In contrast, the C-C bond formation, which is required for the chain growth is based on the exothermic FTS. This leads to challenging reaction kinetics for the CO_2-FTS considering the rate imbalance between CO generation and the slow hydrogenation that is necessary for the C-C bond formation.[23] Another important reaction parameter is the H_2/CO_2 ratio used for the process. A balance of the H_2/CO_2 ratio is required to ensure the activation of both species and to enhance the chain growth while simultaneously to oppose the overhydrogenation to methane and the desorption of CO. A feed with a low H_2/CO_2 ratio hinders the chain growth probability whereas a too high ratio shifts the selectivity towards methane and lighter fractions.[33–35] An increase in the reaction temperature leads to an enhanced conversion and a high CO dissociation rate, while also increasing the hydrogenation rate leading to an increased selectivity for methane. Similarly, high pressure conditions improve both the CO_2 and CO conversion, while promoting secondary hydrogenation of light olefins, which can lead to irreversibly adsorbed carbon species blocking the active surface sites.[36] Despite these challenges, CO_2-FTS is the favorable route from an environmental point of view compared to conventional CO-FTS.[24] The commonly used industrial reaction conditions are relatively mild with 250-400 °C, 20-50 bar and a H_2/CO_2 ratio of 3.[23,31]

1.4 Catalysts for CO_2-FTS

The Fischer-Tropsch reaction is catalyzed by the transition metals from the groups 8-10. Hence, the metals with high catalytic activity are Fe, Co, Ni and Ru. Ruthenium exhibits the highest overall catalytic FTS activity. Unfortunately, Ru is very rare and because of that very expensive, which limits its utilization as catalyst in commercial applications. Nickel on the other hand is limited due to the poor selectivity towards the Fischer-Tropsch reaction. Ni shows much greater potential as catalyst for the Sabatier reaction, which is the rivaling CO hydrogenation reaction leading to the formation of methane.[34] Therefore, the following chapter will only discuss iron and cobalt as monometallic and bimetallic catalysts for the CO_2-based FTS.

1.4.1 Iron and iron carbide as CO_2-FTS catalysts

For the conventional CO-FTS iron-based catalysts are utilized at high reaction temperatures leading to a high fraction of lighter hydrocarbons (gasoline production).[37] The combination of inherent catalytic activity for the FTS and rWGS reactions makes iron also the most studied metal for CO_2-FTS processes.[26] The mechanism for the CO_2-FTS over Fe-based catalysts is complex and involves many different phases of iron, iron oxides and iron carbides. The exact roles of the various Fe phases is still heavily discussed. However, it is generally agreed that the reduction of CO_2 to CO occurs at Fe_3O_4 sites and the following FTS with hydrogenation and dissociation of CO whereas the C-C coupling is catalyzed mainly by the Hägg carbide χ-Fe_5C_2.[23] Riedel *et al.* proposed five episodes for the *in situ* phase evolution of the active Fe species during the CO_2-FTS process:

I - Reactant adsorption and carbidization

II - Initialization of the rWGS reaction

III - Dominance of rWGS reaction with higher CO production than consumption

IV - Initialization of FTS

V - Stabilization of FTS

During the first three episodes, high amounts of Fe_3O_4 and α-Fe and only insignificant amounts of χ-Fe_5C_2 are present. During the fourth episode, the α-Fe content decreased while the χ-Fe_5C_2 content increased. Similarly, during the fifth episode, Fe_3O_4 also decreased leading to a higher χ-Fe_5C_2 content. These observations led to the conclusion that iron oxide is mainly used for the rWGS reaction. α-Fe does not possess initial FTS activity, but it allows for an *in situ* generation of the highly FTS active iron carbide χ-Fe_5C_2 (Figure 1).[38]

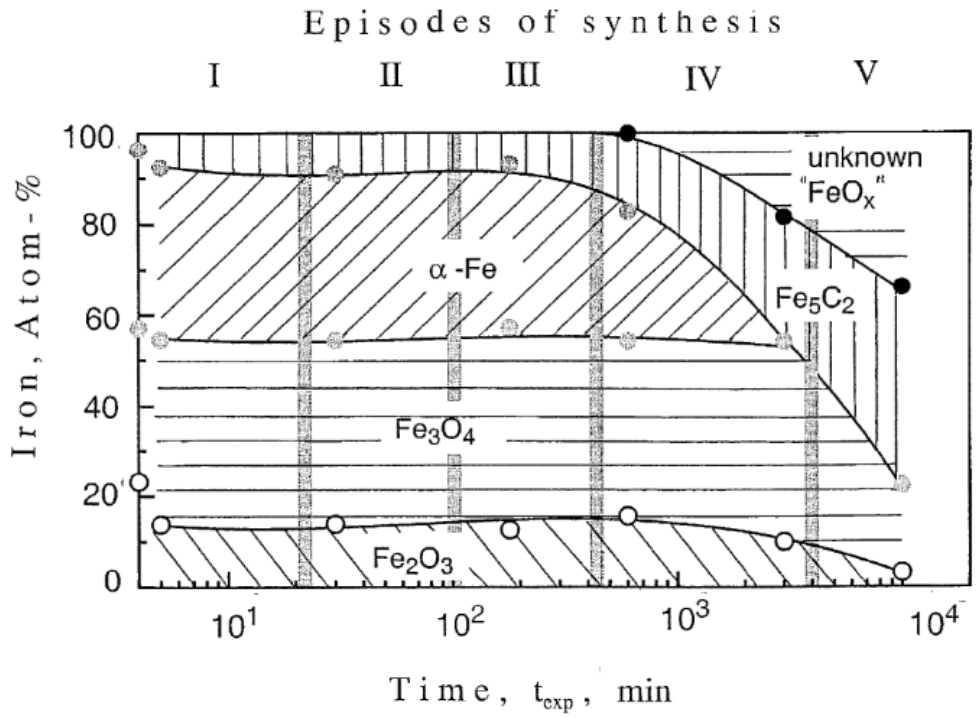

Figure 1: Five episodes of Fe phase transitions during the FTS process.[38]

The conclusions from the studies by Riedel *et al.* are supported by recent density function theory (DFT) calculations by the groups of Guo and Yu. The study of Guo compared the CO_2 adsorption and activation over different surface sites for Fe-based CO_2-FTS catalysts, including Fe_3O_4(111), Fe_5C_2(510) and Fe(100). The adsorption of CO_2 is dependent on the surface geometry with Fe_3O_4(111) as the favored surface site. On the iron oxide surface, CO_3^- species with high symmetry are formed, which indicated a H-assisted dissociation pathway.[39] The study of Yu focused on the chain growth mechanism during the FTS. Similar to the observation of Riedel *et al*., the iron carbide site Fe_5C_2(510) displayed the highest activity for olefin production from syngas according to their calculation.[40] Additionally to the three discussed iron phases (α-Fe, Fe_3O_4 and χ-Fe_5C_2) many other oxide (α-Fe_2O_3, γ-Fe_2O_3 and FeO)

and carbide (ε-Fe_2C, Fe_7C_3 and Fe_3C) species can be formed and coexist during the CO_2-FTS process.[23,41] Zhang *et al.* identified differences in the reduction pathway between α-Fe_2O_3 and γ-Fe_2O_3 and claimed α-Fe_2O_3 as a precursor favors the formation of χ-Fe_5C_2 whereas γ-Fe_2O_3 favors the generation of Fe_3C. During the following FTS process, it was observed that χ-Fe_5C_2 enhanced the formation of lighter olefins due to a weaker hydrogenation ability and a high energy barrier for the first C-C coupling. On the other hand, Fe_3C promoted the formation of C_{5+} products due to the greater CO_2 adsorption.[42] However, other studies describe the FTS activity of Fe_3C (Cementite) as low due its tendency towards the deposition of inactive carbonaceous species.[43,44] The group of Li compared the FTS activities of the three different iron carbide phases. While the Fe_7C_3-enriched catalyst showed the highest FTS activity and the ε-Fe_2C-enriched catalysts displayed the lowest methane selectivity, the study concluded that χ-Fe_5C_2 is the most valuable carbide phase for the CO_2-FTS process. This conclusion was based on the superior stability χ-Fe_5C_2 under FTS conditions.[45] Despite the exceptional properties of χ-Fe_5C_2 (Hägg-carbide), the phase is very prone to oxidation and carbon deposition, particularly in the case of unsupported systems.[44,46,47] In addition to carbon deposition and sintering, the main deactivation pathway for χ-Fe_5C_2 is related to the *in situ* oxidation of the carbide phase. The oxidation process occurs stepwise from χ-Fe_5C_2 to the less FTS active Fe_3C and further to FeO. The FeO phase shows no disadvantages effect regarding the initial transformation of α-Fe to χ-Fe_5C_2 however, the further oxidation to Fe_3O_4 results in major loss of FTS activity. For the oxidative deactivation process, both CO_2 and H_2O can serve as oxidant, particularly if an oxygen-rich CO_2/H_2 feed gas is used.[48,49]

1.4.2 Cobalt-based CO_2-FTS catalysts

Cobalt was the first catalyst found by Fischer and Tropsch that showed FTS activity.[3] Since then, Co was widely investigated and showed exceptional properties as a CO-FTS catalyst.[50,51] Compared to iron, its FTS activity is higher and, therefore, the formed hydrocarbon chains are longer even at lower reaction temperatures. Cobalt as FTS catalyst displays also a higher stability than iron as well as a high resistance against coking. Despite these favorable traits, Co is often not considered as a catalyst for the CO_2-FTS.[23,52] A major disadvantage compared to Fe-based catalysts is the inability to catalyze the rWGS reaction and, therefore, to regulate the

CO_2/CO ratio during the FTS process. The supposedly greatest limitation of Co-based CO_2-FTS catalysts is closely linked to this disadvantage and was investigated by Riedel *et al*. during a comparative study with Co- and Fe-catalysts for CO- and CO_2-FTS. The tested Co/MnO catalyst displayed a selectivity shift towards methane with increasing CO_2 concentration in the feed gas. The authors showed further that the use of CO_2 as feed gas acts as a diluent lowering the CO concentration. The lower CO partial pressure hinders the FTS at the active sites and, therefore, results in a selectivity shift towards methane.[34] Similar results were shown by the group of Davis who used a Co/SiO_2 catalysts and a H_2/CO_2 feed. The group reported a selectivity towards methane of over 70 %. It was speculated that methanol was formed as an intermediate which was afterwards hydrogenated to methane. The authors concluded this subsequent reaction path due to similar rates for the formation of the first O-H and C-H bonds from CO_2.[53] Visconti *et al.* explained the high selectivity towards the methanation reaction with the low stability of adsorbed CO_2 over Co, the resulting low C/H ratio favored the formation of lighter products. The low amount of C_{2+} products was explained by the poor activation of CO_2 over Co catalysts and, therefore, a lack of CO at the catalyst surface, that would be necessary for further polymerization.[54] However, some groups still investigated the properties of Co-based catalysts for CO_2-FTS. The introduction of alkali metals as promoters offered a way to enable the rWGS and thereby to suppress an excessive methane formation. The promoter also enhances the chemisorption of CO_2 and increases the selectivity towards C_{5+} products. A downside of this method is the additional decrease of the H_2 adsorption, which leads to a lower overall CO_2 conversion. Among the tested alkali metals, Na showed the smallest decrease in CO_2 conversion and the highest increase in C_{5+} formation.[55] Similarly to Fe-based CO_2-FTS catalysts, Co-based catalysts also displayed different co-existing phases under FTS conditions. Metallic cobalt is assumed to be a FTS active phase and occurs generally as a mix of two stable crystal phases (α-Co (hcp) and β-Co (fcc)).[56,57] The low temperature hcp phase can be transformed into fcc at around 400 °C in bulk Co.[56] It is assumed that hcp Co nano particles (NPs) inherit higher FTS activity due to the more favorable direct dissociation of CO. However, fcc Co-NPs are more resistant against a water induced re-oxidation and the formation of cobalt carbide.[57] In contrast to Fe-based CO_2-FTS catalysts, Co-based catalysts display major differences regarding their FTS activity and selectivity depending on the particle size.

Hence, cobalt NPs below 6 nm showed an excessive methane formation, while Co NPs larger than 10 nm displayed a significantly lower turnover frequency (TOF).[58] Besides metallic Co, cobalt oxide particles often co-exist under FTS conditions. While CoO exhibits a lower FTS activity than metallic Co, the group of Guo presented a potential bifunctional Co/CoO approach for CO_2-FTS in a recent study. They compared metallic Co and CoO catalysts in the CO_2 hydrogenation and observed excessive methane formation in the presents of Co^0 due to the strongly adsorbed CO and the more active H surface species. In contrast, the cobalt oxide catalysts generated mainly CO with a rWGS rate 1.6 times higher compared to Co^0.[59] They concluded that a bifunctional catalyst with rWGS active CoO sites and FT-active Co^0 could potentially possess superior properties for the CO_2-FTS process. However, further research is needed to clarify the exact role of CoO and Co/CoO during CO_2-FTS. Another influential parameter for Co-based CO_2-FTS catalysts is the support material. The group of Jones investigated the effect of mixed TiO_2/SiO_2 supports on Co-based CO_2-FTS catalysts. Co and TiO_2 are known for strong metal support interactions (SMSI), which allows only a partial reduction of the surface Co-NPs and suppresses agglomeration. In contrast, Co and SiO_2 show weak interactions, which allow a full reduction of the surface Co-NPs.[60] During the catalytic testing, an increased TiO_2 content led to a decreased CO_2 conversion, while an increasing SiO_2 content shifted the selectivity heavily towards methane. The lowest methane selectivity was measured at 23.1 % for the pure TiO_2 support with a C_{5+} selectivity of 24.2 %, but with a CO_2 conversion of only 13.5 %.[61]

1.4.3 Bimetallic Fe/Co catalysts for CO_2-FTS

Catalysts containing a combination of the previously discussed FTS active metals iron and cobalt should, in theory, display a beneficial performance due to synergy effects. The missing rWGS activity of Co could be complemented by the addition of iron while Co-based catalysts are superior in terms of FTS activity and stability at a CO concentration similar to conventional CO-FTS. For the conventional CO-FTS process, advantageous effects for the CO hydrogenation were observed in several studies. The bimetallic catalysts showed improvements in both selectivity and activity, which was associated with the formation of Fe/Co alloy phases.[62–64] However, bimetallic Fe/Co catalysts for CO_2-FTS have been rarely investigated as of today.[60] Major obstacles for such catalyst systems are the dramatically different catalytic

properties of Fe and Co for the hydrogenation of CO_2. Similar to monometallic Co catalysts, Riedel *et al*. observed the same limitations for bimetallic Co-containing CO_2-FTS catalysts. The strong adsorption and the low concentration of CO at the Co sites caused a selective inhibition of crucial reaction steps. The inhibition mainly affected the chain growth and therefore shifted the selectivity heavily towards methane. In this study the inhibition effect was explained with the decreased or diluted CO concentration within the syngas. According to Riedel *et al*., even hydride catalysts with additional rWGS activity were not feasible for CO_2-FTS due to the fast conversion of CO and the same inhibiting effect of decreased CO concentration was observed.[34] However, more recent studies further investigated bimetallic Fe/Co catalysts regarding the optimal metal ratio as well as the ideal type and amount of promoters. Satthawong *et al*. tested different Fe/Co ratios as well as K-promoted and non-promoted catalysts supported on Al_2O_3. The group observed a strong promoting effect of the bimetallic catalysts, towards the formation of C_{2+} hydrocarbons. The tested bimetallic Fe/Co and Fe/Co-K catalysts both displayed a maximum space time yield (STY) of C_2-C_7 at 20 % Co content. The STY of C_2-C_7 products decreased heavily at higher Co contents and at around 50 % Co the measured STY was near zero for the unpromoted catalyst. The STY of methane on the other hand increased steadily up to around 50 % of Co (Figure 2).[65]

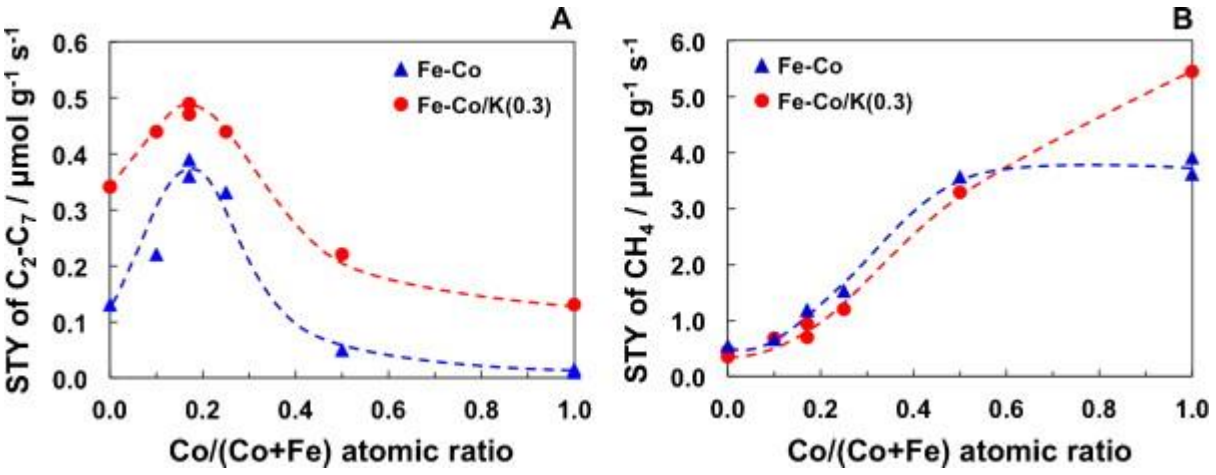

Figure 2: Space time yield of C_2-C_7 (a) and CH_4 (b) during CO_2-FTS for catalysts with different Co/Fe ratio.[65]

The group of Liu further observed that the product spectrum strongly depended on the intimacy of the active Fe and Co sites. A close contact between the rWGS active Fe and Co site led to a high concentration of CO at the active Co site, which resulted

in a high selectivity towards C_{2+} products. In contrast, spatially separated Fe and Co sites favored the formation of methane due to high concentrations of CO_2 at the active Co sites.[66] Both studies showed that the addition of Co could improve the CO_2-FTS activity of Fe-based catalysts. However, the metal ratio and a close proximity of both metals proved to be crucial to suppress an excessive methane formation and to favor the generation of longer chain hydrocarbons.

1.4.4 Support materials for CO_2-FTS catalysts

Another important component for an efficient catalyst design is the utilized support material. The most commonly used support materials for CO_2-FTS catalysts are metal oxides such as Al_2O_3, TiO_2, SiO_2 and CeO_2. The metal oxide supports are employed due to their abundance of metal-oxide heterojunctions and defect sites, both features improve the CO_2 adsorption as well as activation and enhance the dispersion of the active metal. An improved dispersion enhances the CO_2 dissociation and promotes the chain growth due to an increased C/H ratio.[67] The metal oxide support that has most been used for Fe-based FTS catalysts is Al_2O_3. The large pore sizes of this material are particularly advantages due to the beneficial effect on the reduction of iron oxide to α-Fe and the enhanced CO hydrogenation capability. It was shown that larger pores in Al_2O_3 generated up to 2 % more olefin yield compared to smaller pore sizes.[68] TiO_2 is another commonly used support for FTS catalysts. This material provides additional sites for CO_2 adsorption where bridged carbonate species are formed. These species can be easily decomposed into intermediates, which are beneficial for the C-C coupling reaction.[69,70] SiO_2 greatly enhances the dispersion of active species and also suppresses aggregation of the active phase, which leads to overall higher CO_2 conversions. However, the material also enhances the selectivity towards methane and can generate Fe-O-Si bonds that prevent the reduction of iron oxide, therefore, suppressing the formation of carbide phases.[71] The high reducibility of CeO_2 nanorods with exposed (110) surface planes displays favorable properties as FTS catalysts support. The high oxygen concentration at the surface of these planes can lead to an increased ratio of olefins/paraffins.[72]

Besides metal oxides, also carbon-based supports display greatly beneficial characteristics for the CO_2-FTS. Carbon supports offer a high thermal conductivity, a

decreased interaction with the active metal sites compared to metal oxides and a tunable porous texture. Several studies reported a high selectivity to hydrocarbons of around 60 % for different carbon supported CO_2-FTS catalysts.[73,74] The most utilized carbon-based materials are activated carbon, carbon nanotubes (CNTs) and N-doped carbon. CNTs are favored for lower olefin conversion due to their inherent porosity, mechanical strength and thermal conductivity. Another beneficial characteristic of CNTs is the increasing degree of graphitization at high temperatures, which leads to a decreased oxygen adsorption. These oxygen deficient surfaces proved to increase the overall FTS activity.[75,76] The nitrogen-containing groups of N-doped carbon supports generally favor the generation of lighter olefin compared to the heavier C_{5+} fraction.[77] The group of Kondratenko presented an unpromoted CO_2-FTS catalyst, synthesized *via* a cellulose-templated method, that gave a CO_2 conversion of 40 % and a selectivity towards hydrocarbon fractions of 85 %.[78] Despite the commercial availability of activated carbon, this material possess the lowest stability of the carbon supports and also showed the lowest conversions in several studies.[52,79] Unsupported catalysts for CO_2-FTS were also investigated during several studies.[80–82] However, the reported CO_2 conversions were comparably low in every study with under 21 %.[52] Exceptions were only observed if the reaction was operated at very high gas hourly space velocities (GHSV). The low conversion in the presence of unsupported catalysts results from the poor adsorption of CO_2 and H_2 and therefore a limited formation of -CH_2- monomer units.[83]

1.4.5 Promoters for CO_2-FTS catalysts

To further improve the overall CO_2-FTS activity additional promoter species are commonly used to improve the CO_2 adsorption/dissociation or the formation and stabilization of the Hägg carbide phase. The most investigated and utilized promoter materials for CO_2-FTS catalyst are alkali metals, manganese and copper.[23,84] Alkali metal promoters are electron donors, which can be beneficial for the FTS in three particular areas. This promoter class is assumed to enhance the basicity, which increases the adsorption of acidic CO and CO_2 species. Another favorable property is the decrease of surface H species, because lower hydrogen concentrations on the catalyst surface promote the olefin formation and suppress the methane formation. The third beneficial characteristic of alkali metal promoters is the improved formation of the highly FTS-active Hägg carbide phase.[65,85,86] The most commonly used alkali

promoter for Fe-based catalysts is potassium. Already in the 1980s, the loading of Fe-based catalysts with K was reported to improve the chain growth mechanism during conventional CO-FTS.[2] Most of the recent studies concluded that a low K loading is most beneficial for Fe-based CO_2-FTS catalyst promotion due to an increased chain growth probability α with high loadings and, therefore a diminished olefine formation.[23,87] However, Satthawong *et al*. investigated the influence of the K/Fe ratio on the product distribution. The relation of the K/Fe ratio (Figure 3) displayed a decrease of the selectivity for methane and C_2-C_4 fractions and a simultaneous increase of the C_{5+} selectivity. However, the selectivity to light olefines also increased with higher amounts of K promoter. The group concluded that the decreased amount of surface H species for high K loaded catalysts can be used to shift the selectivity towards light olefins while at the same time suppressing the formation of methane and the secondary hydrogenation of the olefines.[88]

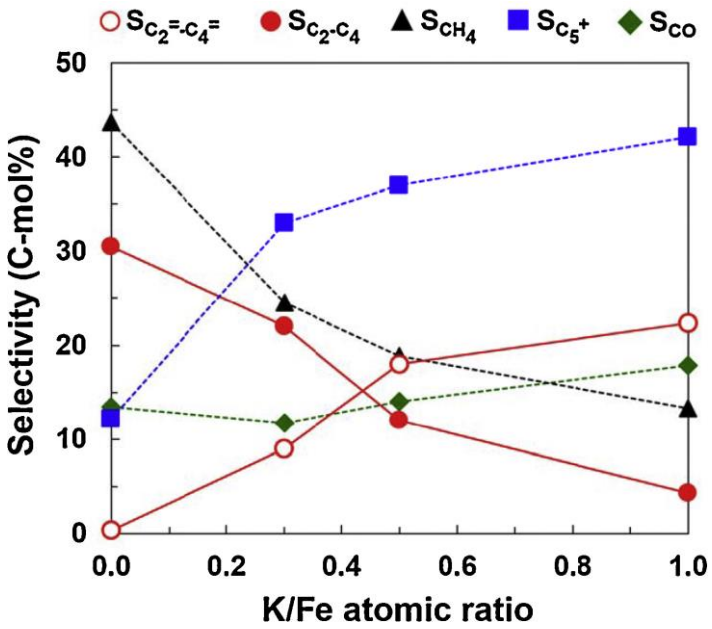

Figure 3: Selectivity of different C_n-fractions depending on the K/Fe ratio of the tested catalyst.[88]

Barrios *et al*. further investigated the influence of the K/Fe ratio on the product formation during the CO_2-FTS process. In contrast to the previous study, higher promoter loadings in the tested Fe/ZrO_2 catalyst exhibited a different trend. The selectivity of light olefins and the CO_2 conversion decreased in favor of the production of longer hydrocarbon chains. It was suggested that the active sites of Fe were blocked in the presence of excessive amounts of K promoter. Therefore, the H consumption was obstructed, and the initial reduction of iron oxide hindered.[89] For

monometallic Co-based FTS catalysts, K addition has been widely described as unfavorable due to a heavy decrease in FTS activity above K/Co ratios of 0.04. The activity loss was attributed to blocking of active Co sites by potassium.[90] However, recent studies have shown that K can be a promising promoter for bimetallic Fe/Co containing catalysts. The group of Hwang reported a stable K-promoted Fe/Co alloy catalyst with an outstanding CO_2 conversion and C_{5+} selectivity of up to 42 %. Unfortunately, the CH_4 selectivity was also very high with around 21 %. Based on DFT calculations the group suggested that Fe-Co mixed carbides could suppress the excess methane formation.[91] The group of Gascon investigated the influence of different Co and K ratios on the CO_2-FTS performance of Fe-based CO_2-FTS catalysts. Co enhanced the catalyst activity by facilitating H_2 dissociation and potassium increased the formation of carbide phases, which are crucial for the chain growth mechanism. Despite the increased FTS activity, the improved hydrogenation activity of Co also shifts the product selectivity substantially towards methane. However, potassium also strongly regulates the hydrogenation activity of Co by decreasing the amount of surface hydrogen, which leads to a suppression of the methane formation. Therefore, a fine tuning of both components is necessary to maximize the FTS selectivity and activity of the catalysts.[92] The influence of different alkali metal promoters on the formation of χ-Fe_5C_2 was recently investigated by the group of Kondratenko. They tested Fe-based catalysts with different loadings of Li, Na, K, Rb and Cs as promoters (Figure 4). The CO_2 adsorption and dissociation were improved while the adsorption strength of olefins was decreased with increasing electronegativity of the promoter species. The highest fraction of Hägg carbide in the catalyst was found for the Fe catalysts promoted with 5 % K.[93]

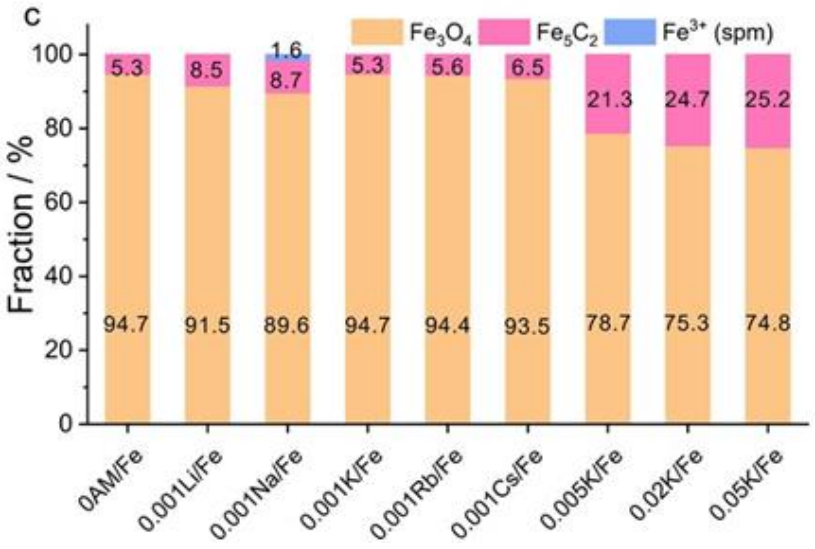

Figure 4: Fe phase formation depending on the promoter ratio in different Fe catalysts.[93]

CO_2-FTS catalysts with alkali promoters featured exceptional improvements in terms of CO_2 adsorption, as well as generation and stabilization of χ-Fe_5C_2 and selectivity of light olefins. However, balancing of the promoter loading is important for an optimized performance due to the equilibrium between an increasing number of activated surface C species and the decreasing amount of surface H species.[23]

The addition of a secondary metal or metal oxide is another effective way to promote CO_2-FTS catalysts. The electronic and chemical behavior of bimetallic catalysts can be significantly different to the monomeric variants.[84,94] This phenomenon allows to tailor particular characteristics of the catalyst for certain applications, a concept, which is widely used for many different types of catalysts. Particularly, the synergistic effects of Fe/Cu catalysts have been investigated and applied in many different research fields.[95,96] For CO_2-FTS, Cu is known to promote the reduction of iron oxide and to suppress metal sintering. Besides an increased dispersion of the active Fe particles, the strong interaction between Fe and Cu facilitates also the reduction of Fe, which results in increased CO_2 adsorption.[97,98] However, the group of van Steen found only an enhancing effect of Cu on the reduction of Magnetite to α-Fe in hydrogen atmosphere. The further formation of Hägg carbide under FTS condition was not promoted by Cu.[99,100] Beside the increase of the CO_2 conversion of Cu promoted CO_2-FTS catalysts, the product selectivity can also be influenced by the additional transition metal. The selectivity was shifted towards longer hydrocarbons (C_{5+}) and the selectivity towards olefins is simultaneously decreased. It is assumed

that formed olefines can be again hydrogenated due to the strong adsorption at the Cu site, which leads to an increase in C_{5+} selectivity. The group of Guo showed a possible way to tune this strong metal interaction and, thus, to influence the selectivity of the catalyst by variation of the Fe/Cu ratio and the spatial distribution of the two active metals *via* sequential impregnation and co-impregnation, respectively.[101] Interestingly, Choi *et al*. found a correlation between the precursor material and the promoting effect of Cu on Fe catalysts. The group tested spinel $CuFe_2O_4$ (Cu^{2+}) and delafossite $CuFeO_2$ (Cu^{+}) precursors for CO_2-FTS. While $CuFe_2O_4$ showed only minor effects on the iron carbide formation, the chain growth and the olefin selectivity, the $CuFeO_2$ precursor exhibited an enhanced formation of χ-Fe_5C_2 and a higher overall FTS activity.[102] Other studies showed that Cu-modified Fe catalysts displayed an increased rWGS activity.[94] It is assumed that the interfacial regions between metallic Cu and Fe oxide form active surface oxygen species, which enhance the CO_2 activation rate. Furthermore, Cu^0 functions as a center for H_2 dissociation, which increases the reduction of surface oxygen species *via* hydrogen spillover.[84]

The transition metal manganese can also act as a structural and an electronic promoter. Particularly for Fe-based catalysts, Mn has been used to increase the dispersion of the active metal, which led to an increase of the overall FTS activity. Additionally, Mn oxides can catalyze the rWGS reaction. Therefore the reduction of Fe oxides to α-Fe is improved and the generated oxygen vacancies are beneficial for the adsorption and dissociation of CO_2.[103] Besides these advantages, Mn species decrease the adsorption of CO and therefore reduce the ability for C-C coupling, which leads to a lower C_{5+} selectivity. The C_{5+} selectivity is further decreased by the strong interaction between Fe and Mn that weakens the chain growth mechanism. However, the reduced C_{5+} formation of Mn-promoted CO_2-FTS catalysts can also be beneficial if light olefines are the target products.[104]

1.5 Metal-organic frameworks (MOFs)

Metal-organic frameworks (MOFs) are a class of porous materials constructed by inorganic nodes, consisting of metal ions or metal-oxo clusters, and organic linkers with at least two functional groups. The cationic metal centers are connected to electron donors of the linkers, most commonly in form of carboxylate groups. The

resulting metal containing nodes are called secondary building units (SBUs) and form the center pieces of the network structure. MOFs are typically synthesized in a solvothermal one-pot procedure, where the framework is formed *in situ*. The topology of MOFs which can be one-, two- or three-dimensional framework structure with generally stable pores and very high specific surface areas of up to 10000 m^2 g^{-1} (measured *via* the BET method) is determined by geometry of the ligand and the SBU.[105,106] MOF materials can be obtained in a wide variety of possible metal center and linker combinations with over 20000 MOF structures known today.[107] The stability of MOF materials is closely linked to the type of metal-linker combination and, therefore, if a flexible linker is used, a flexible or stimuli-responsive MOF can be obtained.[106] The near endless combinations allow the synthesis of specifically tailored porous materials with different pore architectures and metal centers. Additionally, MOFs feature up to three anchoring positions for further functionalization at the metal center, at the organic linker and in the pore structure. This tunable nature of MOFs makes the material class very interesting for varies fields of research, which is illustrated by the annually increasing number of publications on the topic each year.[108,109] The first researched application of metal-organic frameworks was gas adsorption and gas separation to utilize the large inner surface areas.[110,111] Since then, the possible applications that have been proposed for MOFs include many different fields such as energy conversion,[112] food packaging,[113] removal of organic pollutants,[114] chemical sensing,[115] drug delivery,[109] proton conductivity[116] and various catalytic applications with photo catalytic processes as the most prominent.[117] The currently most utilized basic MOF structures are MIL-53, HKUST-1 and ZIF-8.[107] In earlier publications the terms porous coordination polymer, coordination network or hybrid organic-inorganic materials have also been used to describe MOFs. In 2012, a classification of MOF structures was introduced by IUPAC, which defined metal-organic frameworks as coordination networks with cavities connected by organic ligands. Thus, MOFs are a subclass of coordination networks which, in turn, are a subclass of coordination polymers.[118,119] The general nomenclature of MOFs consists of an abbreviation of the discovering institute, a number which is characteristic for the resulting framework structure and the used metal ions of the SBUs. For example, DUT-5(Al) describes a material first synthesized by Senkovska *et al*. at Dresden University of Technology (DUT), which

consists of aluminum hydroxide chains connected *via* 4,4‘-biphenyldicarboxylic acid (H_2BPDC).[120]

1.5.1 Multicomponent MOFs

Additionally to the wide variety of known MOF materials today, it is also possible to combine different metal and or linker variants into a single framework structure. The resulting materials, which feature multiple metal centers or different linkers, are called mixed-metal or mixed-linker MOFs or simply multicomponent MOFs.[121,122] Mixed-metal MOFs are particularly interesting for applications in heterogeneous catalysis, because mixing of different metals is a common concept for conventional supported catalysts.[123] The combination of two or more metals in one framework is possible if the different metals occupy chemically identical lattice positions and, hence, only certain metal combinations are possible with this approach. Until now the successful synthesis of up to ten different metals in one structure has been claimed with this approach.[124] Other approaches to generate mixed-metal MOFs are the immobilization of additional metal species at the linker or the SBU *via* post-synthetic modifications or the incorporation of metal nanoparticles into the pore structure of the framework (Figure 5).[125–127]

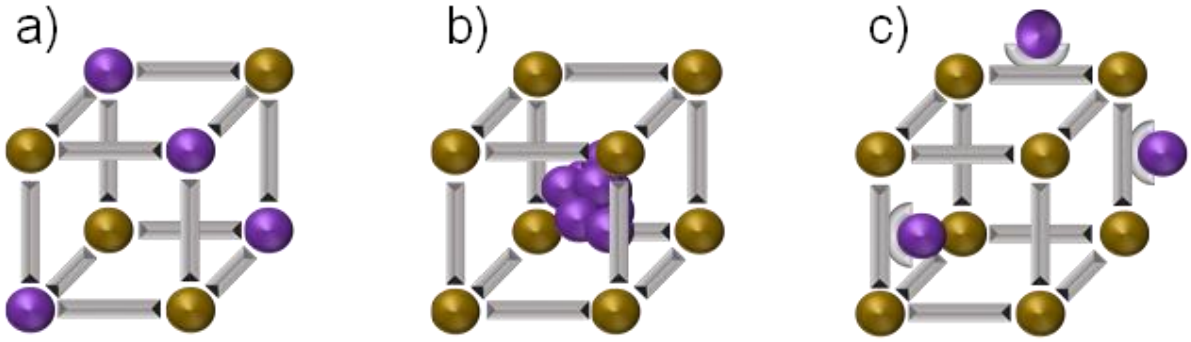

Figure 5: Schematic representation of mixed-metal MOFs with statistical distribution of two metals (a), incorporated nanoparticles in the pores (b) and immobilized metal species at the linker (c).[121]

The second form of multicomponent MOFs are mixed-linker materials, which include two or more different types of organic linker molecules. The used linkers can be either isostructural and therefore incorporated at chemically equal lattice positions or the linkers are different in for example their length or coordination geometry. In the second case a heterostructural framework is formed with specific linkers in defined

positions, which result, e.g. in MOFs with pillar-layered, rod-spacer or cluster-space structures (Figure 6).[128,129]

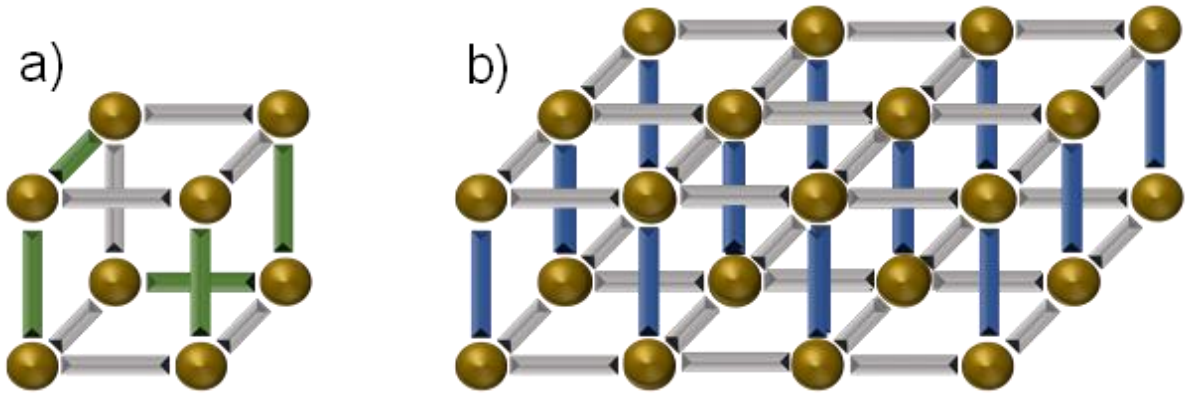

Figure 6: Schematic representation of mixed-linker MOFs with statistical distributed linkers (a) and with two linkers forming a heterostructural framework (b).[121]

Multicomponent MOFs with homogenous frameworks, such as mixed-metal materials with similar sized metals or mixed-linker MOFs with linkers of similar length, are often synthesized *via* a direct synthesis which is comparable to their conventional MOF counterparts. For heterostructural MOFs, the synthesis route can be more complicated with the inclusion of post-synthetic modifications to ensure that the additional metals or linkers are located at the desired lattice positions.[121] Another challenging part concerning multicomponent MOFs is the characterization of such materials. The ratio of the incorporated materials can often be determined by elemental analysis or nuclear magnetic resonance spectroscopy (^{1}H-NMR) for mixed-linker materials.[130] Unfortunately, these techniques give no information about the actual framework position of the metals or linkers. To identify these properties of the materials combinations of energy dispersive X-ray spectroscopy (EDX),[131] X-ray photoelectron spectroscopy (XPS)[132] and X-ray absorption spectroscopy (XAS)[133] are often necessary.

1.5.2 MIL-53 family

The metal-organic framework structure of MIL-53 (Matériaux de l'Institut Lavoisier, MIL) was first introduced by the group of Férey. The structure consists of benzene-1,4-dicarboxylic acid (terephthalic acid) as organic linker and metal ions in the oxidation state +III, which form octahedral (MO_6) units with four oxygen atoms from

four different linkers and two oxygen atoms form bridging μ^2-OH ions of neighboring metal centers. The resulting framework features a characteristic one-dimensional diamond-shaped pore structure.[134,135] A special property of the MIL-53 family is called the breathing effect that describes a flexible framework structure, which can open or contract its pores in respond to external stimuli.[136] The structures of open and contracted MIL-53 materials are shown in Figure 7. The first synthesized MIL-53 materials were based on Cr as metal center in 2002, but since then many different metals have been used successfully to generate crystalline MOF structures, most commonly with Al, Fe, Ga, Cr, Sc and In.[134] The most interesting variation of MIL-53 for this work is the Fe-based material. The first MIL-53(Fe) material was synthesized by the group of Férey in 2008. MIL-53(Fe) showed a different breathing behavior than the Cr and Al variant with a reversible dehydration which leads to a distorted metastable anhydrous phase under 423 K.[137] More recent research displayed great potential of MIL-53(Fe) as electrochemical sensor[115] and for the removal of organic pollutants *via* the Fenton reaction.[114] Another application of MIL-53(Fe) is the use as a sacrificial template for the MOF mediated synthesis approach, which will be discussed in detail in the following chapter.

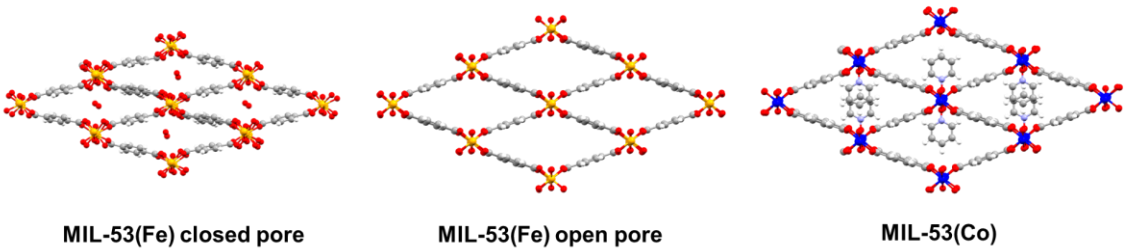

Figure 7: Structure of MIL-53(Fe) with closed and open pore geometry and MIL-53(Co) with pyridine-*N*-oxide as co-ligand.

Munn *et al*. further increased the amount of possible metals for MIL-53 by the introduction of pyridine-*N*-oxide (PNO) as co-ligand. If the bridging μ^2-OH ions are replaced by the neutral co-ligand PNO, the generation of a framework with metal ions of the oxidation state +II becomes feasible. The authors synthesized and characterized MIL-53 variants with Mn, Co and Ni as metal centers using this approach. Despite the successful generation of the framework, the characteristic flexibility and large specific surface area of the materials were lost due to the PNO

co-ligand blocking the pores.[138] The mixed-metal concept was also investigated for MIL-53 and the successful synthesis and characterization of various combinations of the metals listed above has been reported. Additionally, functionalized linkers have also been used to synthesize the framework. The linker variation that has been used most often is amino-functionalized MIL-53-NH_2(Al) with alumina as metal center due to its exceptionally high thermal stability. The functionalized MOF materials were mostly utilized in gas separation or gas adsorption applications.[139,140] Additionally, the material showed potential in the field of environmental remediation.[141] The group of Kleist combined the mixed-metal and mixed-linker concept for MIL-53 and investigated the impact of multicomponent MIL-53 on the breathing behavior. Different metal and linker combinations and ratios have been tested and a characteristic step in the adsorption isotherm was observed, which changed in height and position for different linker and metal combinations. Thereby, the MIL-53 even allowed tailoring of the breathing effect with the right selection of metal combinations and linker ratios.[136]

1.6 MOF-mediated synthesis (MOFMS)

In principle, metal-organic frameworks should be well suited for applications in heterogenous catalysis due to the toolbox with various anchor points for additional functionalization and the characteristically large specific surface area of the highly porous materials. The post-synthetic modification concept allows for customized functionalization at either the metal centers, the linkers or within the pore structure.[121,122] However, the generally poor thermal and chemical stability of MOFs hinders their application in heterogenous catalysis due to the high temperatures of such processes.[142] The MOF-mediated synthesis (MOFMS) concept evades these limitations while creating catalysts with additional unique properties. The MOFMS approach envisions not the MOFs as solid catalysts themselves, but as sacrificial precursor materials. Hence, the organic linker molecules are partially burned or carbonized into a carbon matrix under a controlled temperature and in a specific atmosphere. For instance, the high decomposition temperature in inert atmosphere leads to the collapse of the MOF framework, which creates catalyst systems with metal nanoparticles embedded into a protective carbon matrix.[143] The MOFMS approach is not only simple but also very versatile and allows the generation of various types of materials through the variation of temperature, atmosphere and the

parenting MOF material. The parenting MOF is mainly selected according to the metal centers, however the linker is also crucial for the successful synthesis of the MOF and also to control the thickness and porosity of the resulting carbon matrix. The decomposition atmosphere can be oxidizing, inert or slightly reducing.[142] Oxidizing atmospheres are used for the preparation of MOF derived metal oxides similar to classical calcination, but fine tuning of the MOFMS parameters allows control of shape, composition and porosity of the resulting metal oxide particles. The carbon shell for oxidizing MOFMS is thinner compared to the inert approach or in some cases fully removed during the treatment.[144,145] MOFMS in inert atmosphere puts more emphasis on the formation of a protective carbon shell around the metal particles. With this approach the resulting materials are highly dispersed metal nanoparticles embedded into a carbon matrix. The carbon matrix offers some unique features compared to conventional supported catalysts. Further sintering of the metal nanoparticles is minimized despite the very high metal loadings of often over 50 % due to the encapsulated nature of the metal particles. The arrangement of metals from multi-metal parenting MOFs is also often preserved during MOFMS, which allows for a close contact between different metal species leading to synergistic effects. Additionally, the close contact between carbon and metal enhances the generation of carbide phases during the decomposition procedure, which proved to be beneficial for FTS catalysts (cf. Chapter 1.4). Another interesting feature of MOFMS catalysts is the oxidation state of the resulting metal particles.[146,147] Das *et al*. found that thermal decompositions in N_2 atmosphere and up to 900 °C generated reduced metal particles for metal ions with a standard reduction potential of -0.27 V or higher (Co, Ni, Cu) and metal oxide particles for metal ions with a lower standard reduction potential of -0.27 V (Mg, Al, Mn, Zn or Cr). The partial oxidation of the organic MOF structure during the thermal decomposition acts as reducing agent and allows, therefore, the generation of reduced metals. For the metal ions with a standard reduction potential of -0.27 V or lower, the oxygen from the linker molecules still leads to oxidic particles.[148] However, the generated reduced metal particles are protected by the carbon matrix and remain stable even after storage in air. The last important parameter for the MOFMS approach is the decomposition temperature. The decomposition temperature is closely linked to the Tammann temperature of the containing metal species. This temperature is approximately half of the melting point of the respective metal species and is defined as the sufficient energy that solids

need to acquire for bulk diffusion. For the MOFMS process, the Tammann temperature is in general above the necessary temperature to decompose the framework structure. Therefore, after the collapse of the framework, the atoms start to migrate and form nanoparticles. Exceeding such temperatures lead to the formation of larger particles like in the classical sintering process. The relevant melting points of the metals used in this work are: Co : 1495 °C, Cu : 1085 °C, Fe : 1538 °C and Mn : 1246 °C.[142] The most studied applications of MOFMS catalysts to this day are linked to electro-catalysis. However, there are also some catalyst systems tested for heterogeneous catalyzed processes like the Fischer-Tropsch synthesis.[149,150] For Co-containing MOFMS catalysts mostly ZIF-67 and ZIF-8 have been the primary chosen parent MOFs due to the convenient synthesis from aqueous solutions at fairly low reaction temperatures.[151] Hence, Li *et al.* showed a highly active Co-based MOFMS catalyst for CO-FTS. The catalysts system was generated from Co-MOF-71 with impregnated Si species. The resulting Si-doped Co@C catalyst featured a high Co content of dispersed Co_{fcc} nanoparticles.[152] The group of Spivey also generated a Co-based MOFMS catalyst for CO-FTS. The parenting MOF was ZIF-67 with added potassium, which was calcined at 500 °C for 2 h in air. The resulting MOFMS catalyst consisted of cobalt oxide nodes that showed an improved selectivity towards higher oxygenates during the tested CO hydrogenation reaction.[153] Another example for a Co-based MOFMS catalyst was presented by Luo *et al*. with a series of ZIF-67 derived materials, which were decomposed at different temperatures and for various times. The varied parameters led to particle sizes between 8.4 ± 1.9 nm and 74.8 ± 11.6 nm. The differently sized cobalt nanoparticles were afterwards tested in the CO-FTS with a methane selectivity decrease and a C_{5+} selectivity increase for particles above 47.8 ± 2.3 nm.[154] For Fe-based MOFMS catalysts, MIL-53(Fe) and MIL-88(Fe) seem to be the most frequently used parenting MOF materials.[142] Interestingly, during the thermal decomposition in nitrogen atmosphere reduced metal particles are formed similarly to Co and, additionally, the generation Fe_3C carbide phase was observed by the group of Gascon.[147,155] The group of Lin designed a Fe-based MOF-derived catalyst system with highly dispersed nanoparticles despite of very high metal contents of over 40 wt%. An *et al*. tested MIL-88B(Fe) as parenting MOF with and without an additional amine-group at the linker for CO-FTS at 300 °C and 2 MPa. MIL-88B(Fe)-NH_2 showed an increased C_{5+} selectivity of 63 % compared to 51 % of MIL-88B(Fe), but a slightly decreased

selectivity towards olefins with 18 % compared to 21 %.[156] Gascon *et al*. also tested different parenting MOFs for generation *via* MOFMS of Fe-based FTS catalysts. All tested MOFMS catalysts displayed very high activity in the HTFT process variation, while the lowest methane selectivity was obtained with the MIL-88 derived catalysts and the highest overall activity with the Basolite F300 derived catalysts.[146]

2 Motivation

Considering current challenges related to the progressing climate change, which is largely caused by excessive emissions of the greenhouse gas CO_2 into the atmosphere, the CO_2-FTS process represents a possibility to reduce greenhouse gas emissions while also producing valuable hydrocarbon products like light olefines and synthetic fuel. Particularly carbon-supported catalysts displayed many beneficial traits for CO_2-FTS applications such as their inherent porosity, mechanical strength and thermal conductivity. Another property of carbon supported CO_2-FTS catalysts is the decreased oxygen adsorption, which proved to increase the overall FTS activity. However, up to now mostly Fe-based catalysts containing carbon nanotubes (CNT) or N-doped carbon supports have been studied in the CO_2-FTS process. Another interesting carbon-supported material class are catalysts, which are prepared *via* MOF-mediated synthesis. Those materials are generated by the thermal decomposition of metal-organic frameworks, which leads to some unique properties, such as the presence of an oxidation preventing carbon matrix around the metal nanoparticles. Furthermore, MOFMS catalysts feature exceptionally high metal loadings despite comparatively small particle sizes due to the encapsulated nature of the metal particles within the carbon matrix. The goal of this work was to combine the MOFMS approach with the CO_2-FTS and therefore, to synthesize metal nanoparticles embedded within an oxidation-preventing carbon matrix for CO_2-FTS applications. The potential beneficial effects of these novel catalysts as well as the effects of bimetallic Fe/Co systems on the CO_2-FTS process are the focus of this work.

To achieve this goal, the results part of the thesis will be structured into three main chapters. The first chapter will focus on the effect of different MOF-mediated synthesis conditions on the resulting catalysts and their respective CO_2-FTS behavior. To study this effect, monometallic Fe-based MOFMS catalysts will be used. In the first step, Fe-based MOF precursor materials will be synthesized and characterized. PXRD, ATR-IR spectroscopy, ICP-OES and nitrogen physisorption measurements will be used as characterization methods to determine the successful synthesis of purified MOF precursor materials. Additionally, TGA measurements under nitrogen atmosphere will be used to analyze the behavior of the precursor

material under MOFMS conditions. Based on the TGA results, different decomposition temperatures will be chosen for the following MOFMS procedure. The generated catalysts will also be analyzed by a combination of different characterization techniques. To identify the newly formed metal phases within the MOFMS materials, a combination of PXRD, Mössbauer spectroscopy and XAS measurements will be utilized. The protective carbon matrix generated *via* the thermal decomposition will be analyzed by ICP-OES, nitrogen physisorption and TGA measurements of the fresh catalysts. Afterwards, catalytic testing experiments will be done in a CO_2-FTS model plant, which will include a time-on-stream experiment over 12 h to analyze the stability of the catalysts and a temperature-variation experiment to understand the behavior of the catalysts under LTFT and HTFT conditions. Additionally, the selectivity towards light olefines at each temperature step will be analyzed. After the catalytic testing, the MOFMS catalysts will be analyzed again using PXRD and ICP-OES to interpret the effects of the CO_2-FTS conditions on the catalysts and to better understand the catalytic testing results.

The second chapter will focus on the generation of bimetallic Fe/Co-containing MOFMS catalysts and their potentially beneficial effects on the FTS activity. The first step will be to find a suitable synthesis method to incorporate both metals within a MOF structure and to generate bimetallic MOF precursors with different metal ratios of Fe and Co. The precursor materials will be analyzed using PXRD, ATR-IR spectroscopy and nitrogen physisorption measurements to ensure a successful synthesis of the bimetallic frameworks. Furthermore, ICP-OES measurements will be utilized to confirm the successful incorporation of the desired amount of each metal within the structure. The MOFMS conditions will be chosen based on the most promising results of the first chapter and the TGA measurements. The MOFMS catalysts will again be analyzed by PXRD and XAS measurements to identify the newly generated metal phases. Structure and properties of the carbon matrix will be investigated by a combination of nitrogen physisorption, ICP-OES and TGA measurements. Furthermore, TPR measurements will be utilized to understand the oxidation-preventing effect of the protective carbon matrix around the metal nanoparticles. The catalysts will be tested regarding their CO_2-FTS behavior under the same conditions as the monometallic Fe-based MOFMS catalysts series. Hence, a time-on-stream experiment for 12 h, followed by a temperature variation experiment

in the temperature range of 200 - 400 °C will be conducted. Afterwards, the spent catalysts will be analyzed again *via* PXRD, ICP-OES and TRP measurements to investigate possible changes during the time-on-stream tests and to further understand the catalytic testing results.

The third chapter will focus on the optimization of the MOFMS catalysts for the CO_2-FTS process. Therefore, the effects of the addition of different promoters will be investigated for the best catalysts from the first two chapters. Potassium, manganese and copper will be used as promoters in different concentrations, because these metals are known as promising systems from literature. The MOF precursors will be analyzed regarding the generated framework structure and phase purity using a combination of PXRD, ATR-IR spectroscopy, ICP-OES and nitrogen physisorption measurements. Furthermore, TGA measurements will be performed and based on these results as well as the findings from the previous studies, the MOFMS conditions will be determined. The fresh MOFMS catalysts will be investigated *via* PXRD, XAS, ICP-OES, TPR and nitrogen physisorption measurements to analyze the generated metal phases and the nature of the carbon matrix. Afterwards, the catalyst series will be tested for their respective CO_2-FTS activity under the same conditions as the unpromoted catalysts. Therefore, a time-on-stream experiment of 12 h and a temperature variation experiment will be performed. The spent catalysts will be analyzed again *via* PXRD, XAS, TPR and ICP-OES to understand possible changes to the catalysts during the time-on-stream tests.

3 Results and discussion

3.1 Fe-based CO_2-FTS catalysts obtained *via* MOFMS

In addition to the contribution of the main author, Marco Tummeley from the group of Prof. Dr. Schünemann has contributed the measurements of the Mössbauer spectra and the evaluation of the results.

3.1.1 Synthesis and characterization of Fe-based MOF precursor

The goal of this work is the investigation of the catalytic properties of MOF-derived bimetallic MOFMS catalysts for the CO_2-FTS process. The first step for the generation of MOFMS materials is the synthesis of the respective MOF precursor. For a better understanding of the influence of different parameters during the synthesis and MOFMS process, in the first step monometallic systems were investigated to reduce the complexity of the materials. Fe-based MOFs were chosen due to the better suited properties of such materials for the CO_2-FTS process, based on the previously discussed literature (cf. Chapter 1). The MIL-53(Fe) structure was chosen as the MOF precursor from the wide variety of available MOF materials. The first reason for this decision was the simple solvothermal one-pot synthesis approach coupled with the comparable low priced terephthalic acid linker (Scheme 4). Furthermore, the MIL-53 MOF-family has been well investigated and allows for an increase in complexity with many known successful synthesis approaches of different metal centers besides iron. Furthermore, another anchor point for further functionalization is given by the comparably large pore volume of the open pore geometry of the MIL-53 material class. Scheme 4 shows the synthesis approach used to generate the MIL-53(Fe) precursor materials.

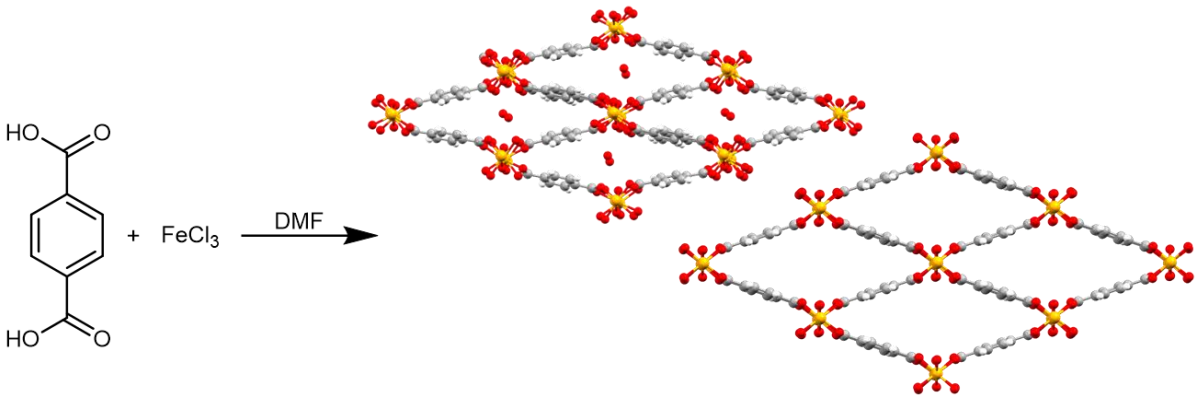

Scheme 4: Reaction scheme of the MIL-53(Fe) precursor synthesis.

As mentioned in Chapter 1.5.2, MIL-53 materials feature a unique breathing behavior with an open or contracted pore structure according to external circumstances. Under room temperature (RT) conditions the low temperature form, with contracted pores *via* hydrogen bonds of H_2O within the pores, is present. To shift the pore geometry towards the high temperature form with open pore geometry, elevated temperatures are usually needed to remove contraction-enhancing guest molecules. To confirm the successful synthesis of the MIL-53(Fe) precursors a combination of different characterization techniques was used. Powder X-ray diffraction (PXRD) was the first method utilized to confirm the successful generation of the material. Figure 8 shows the calculated patterns of the high temperature (ht) and low temperature (lt) form of the flexible MOF structure. The resulting MOF precursor matches the low temperature form with water molecules incorporated into the pores. This result was expected due to the PXRD measurement conditions in air and at RT. The characteristic reflections at 2θ = 9.17 °, 12.69 °, 17.55 °, 18.47 ° and 25.46 ° are all visible in the measured pattern. Furthermore, no reflections from metallic or oxidic iron phases are present in the diffractogram. However, despite the relatively sharp reflections, the pattern displays a noisy background which indicates a relatively low crystallinity.

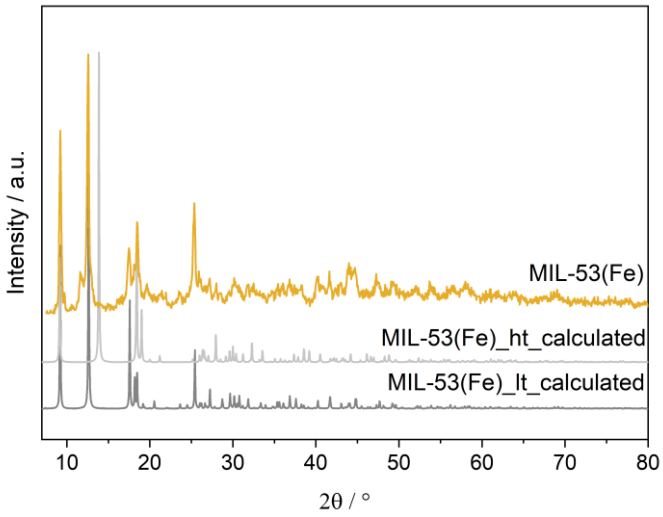

Figure 8: PXRD pattern of the MIL-53(Fe) precursor and calculated reference patterns of the lt and ht forms of MIL-53(Fe).

To investigate the purity of the precursor materials, ATR-IR measurements were performed. This method was used to analyze the characteristic absorption band of the MOF material and also to confirm the absence of characteristic absorption bands of free linkers and the solvent *N,N*-dimethylformamide (DMF). Figure 9 shows the ATR-IR spectrum of the precursor material MIL-53(Fe). The successfully formed MOF structure is indicated by the absorbance band at 885 cm^{-1} generated by the δ (OH) modes of the bridging hydroxyl group (Fe−O(H)−Fe). Another indication for the successful synthesis of the framework structure are the bands of the symmetric and asymmetric stretching vibrations of C-O at 1597 cm^{-1} and 1382 cm^{-1}. The assigned bands confirm the presence of linked carboxylate groups within the structure. The C-H bending vibrations of the benzene rings exhibit a peak at 739 cm^{-1}. The absorption band peak at 1665 cm^{-1} can be assigned to stretching vibrations of C=O bounds found in either free terephthalic acid linkers or DMF. Due to the comparatively high intensity of the absorption band it can be assumed that the MOF precursor material is not fully purified, which matches the noisy baseline found in the PXRD pattern. Additionally, the broad absorption band at 3450 cm^{-1} arising from the stretching vibrations of the O-H bonds indicates the hydrated lt form of the MOF.[157] This also matches the PXRD pattern, which showed a close pore (cp) form with water incorporated within the pores.

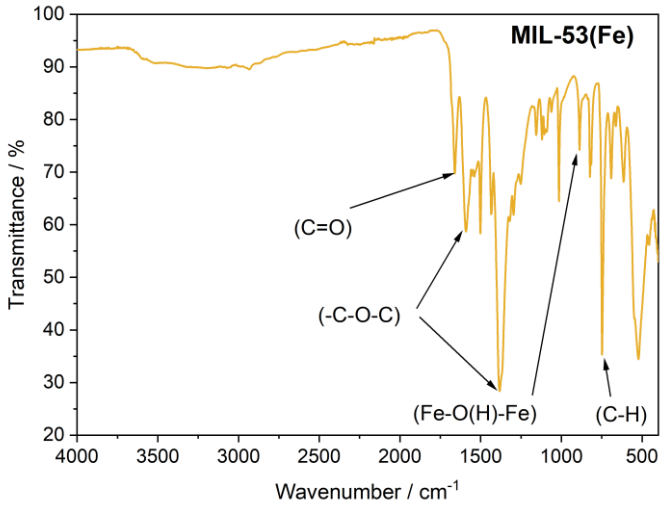

Figure 9: ATR-IR spectrum of the MIL-53(Fe) precursor.

Furthermore, the specific surface area and the pore volume were analyzed with nitrogen physisorption measurements. Both parameters are crucial for a further functionalization, which will be discussed in the later chapters. The specific surface area was calculated using the BET method from the nitrogen physisorption isotherm and the pore volume was derived from the BJH plot (Table 1). The surface area is with 5 $m^2 g^{-1}$ relatively small for a metal-organic framework, which is caused by the contraction of the pores due to the incorporated water and the resulting hydrogen bonds. Another important parameter is the metal content of the MOF precursors. It was determined *via* ICP-OES measurements and matches the reported iron content for MIL-53(Fe), which also indicates the absence of additional reduced or oxidic phases (Table 1).[137]

Table 1: Specific surface area form nitrogen physisorption measurements and ICP-OES results of the MIL-53(Fe) precursor.

Sample	**Specific surface area / $m^2 g^{-1}$**	**Pore Volume / $cm^3 g^{-1}$**	**Fe content / %**
MIL-53(Fe)	5	0.034	17.1

The most important characteristic of the MOF precursor for the further MOFMS procedure is its decomposition behavior. To mimic the conditions of the thermal decomposition during the MOFMS synthesis, thermogravimetric measurements were

performed under inert nitrogen atmosphere. Unfortunately, the TGA setup was not connected to a quadrupole mass spectrometer (QMS) and, therefore, only estimated assignments of the observed weight loss fractions were possible. The TG and DTG profile of the MOF precursor are shown in Figure 10. The thermal decomposition of the framework structure under N_2 atmosphere seems to occur in three major steps. During the first step, additional crystal water was evaporated at about 100 °C. Between 220 °C and 460 °C, the MOF structure starts to decompose and the oxygen in the framework begins to oxidize the organic linkers. This is followed by a plateau between 500 °C and 650 °C, where no weight loss is observed. At temperatures above 650 °C the formation of iron carbides occurs, which matches the weight loss step between 650 °C and 740 °C. However, further investigations are needed to understand the origin of the weight loss during the carbide formation.

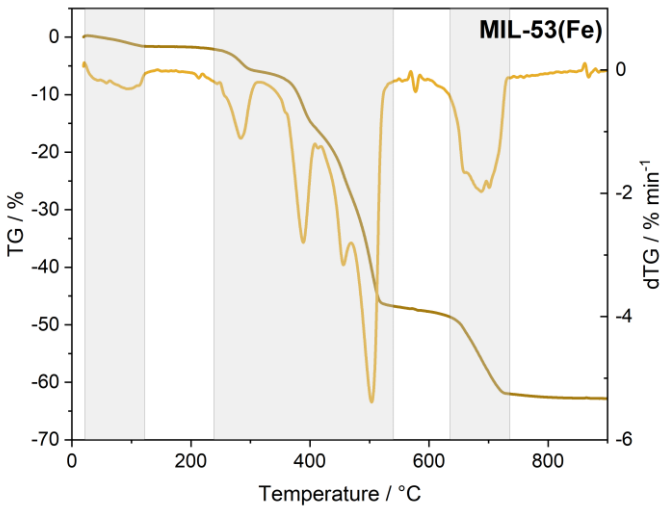

Figure 10: TG and DTG curves of the MIL-53(Fe) precursor measured in N_2 atmosphere.

The TGA measurement showed three potentially interesting decomposition temperatures, which were subsequently tested using the MOFMS procedure (cf. Chapter 3.1.2). At 400 °C, the MOF decomposition is not fully completed and therefore a thicker carbon shell around the metal nanoparticles is expected. At 600 °C, the MOF decomposition is finished with a weight loss of about 50 %, but no carbide formation has occurred yet. At 800 °C, the MOF decomposition and the carbide formation are completed with a final weight loss of about 60 %. Hence, the following MOFMS approach will be tested at the three decomposition temperatures of 400 °C, 600 °C and 800 °C.

3.1.2 Synthesis and characterization of Fe-based MOFMS catalysts

To increase the inherently low stability of the previously synthesized MOF precursors, the materials were thermally decomposed at a defined temperature and atmosphere. This procedure is called MOF-mediated synthesis (MOFMS) and allows the generation of catalysts with exceptional high metal loadings, excellent oxidation resistance and close contact between the metal nanoparticles and the carbon species. These unique properties are enabled *via* a protective carbon matrix, which forms around the metal nanoparticles during the thermal decomposition process. As mentioned in Chapter 3.1.1, the three decomposition temperatures 400, 600 and 800 °C were chosen for the MOFMS synthesis of the MIL-53(Fe) precursors based on the TGA measurement results. The time for the thermal decomposition was 2 h for all three temperatures and the atmosphere was inert (N_2) to retain as much protective carbon shell as possible. To analyze the newly synthesized catalyst systems and the effect of the catalytic testing under CO_2-FTS conditions, the material series was analyzed with a combination of different characterization techniques before and after the catalytic testing within the FTS setup in our lab. To investigate the newly formed catalyst structures during the MOFMS procedure and also the impact of the CO_2-FTS conditions, PXRD measurements were performed (Figure 11). Directly after the MOFMS, the catalysts decomposed at three different temperatures display completely different diffraction patterns. The pattern of Fe@C_400 °C illustrates an uncomplete degradation of the MOF structure and, therefore, a refection at 2θ = 8.5 ° from the MIL-53(Fe) phase is found. Furthermore, the formed iron phase shows very broad reflections, which leads to the assumption of a small crystallite size of the active metal component in the catalyst and a thick carbon shell around it. The incomplete decomposition of the organic part was expected due to the TGA result (Figure 10). The pattern of Fe@C_600°C shows intense reflections of different iron containing phases whereas the reflections at 2θ = 44.5 ° and 64.9 ° can be assigned to reduced α-Fe (bcc), the other reflections can be assigned to magnetite (Fe_3O_4) and wuestite (FeO), respectively. The appearance of three oxidation states of iron (Fe^0, Fe^{2+} and Fe^{3+}) and the previously mentioned effect of oxidation prevention though the formed carbon shell[155] leads to the assumption of a poorly formed carbon shell around the metal particles. At the highest decomposition temperature no oxidic

iron phase was found in the catalyst Fe@C_800°C. At the 2θ positions of 44.5 ° and 64.9 ° the reduced α-Fe phase is still present, additionally a newly formed iron carbide phase was found for the catalyst material. The carbide phase could be assigned to mainly Fe_3C, but the reflections are of low intensity and overlap with reflections generated by the Fe phase. The reduction of the iron during the MOFMS process occurs due to the reaction of the carbon within the MOF structure with the oxygen from the MOF lattice. In redox processes, the iron centers are reduced to metallic Fe. The calculation of crystallite sizes of the active metal components *via* the Scherrer equation was difficult due to the strong overlap of the reflections of the mixed-phase materials and the broad and low intensity reflections displayed by Fe@C_400°C.

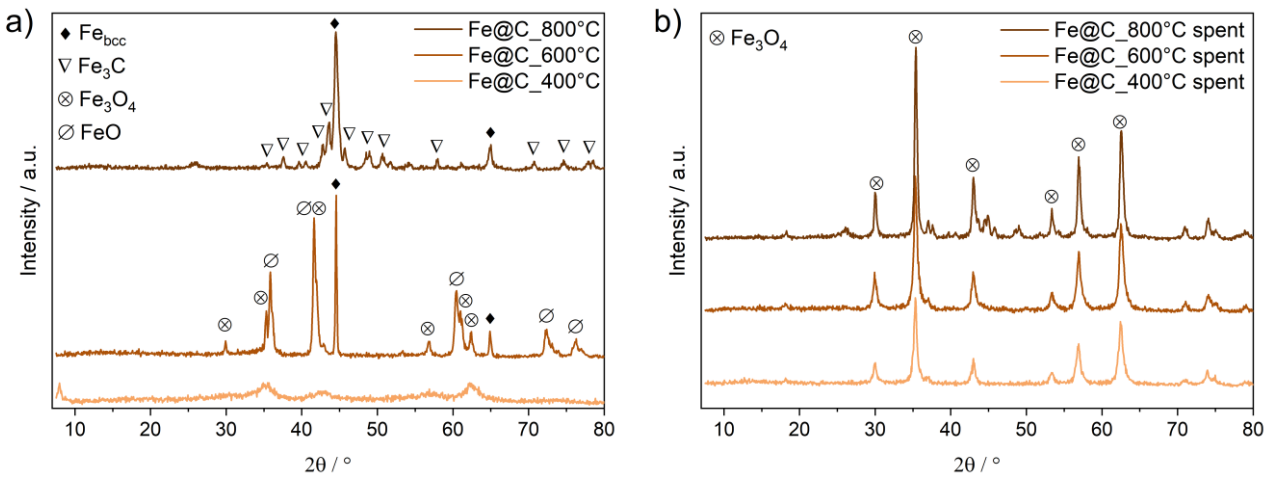

Figure 11: PXRD patterns of the Fe@C catalyst series generated *via* MOFMS before (a) and after (b) the catalytic testing.

During the catalytic testing under the harsh CO_2-FTS conditions (cf. Chapter 3.1.3), all Fe-based catalysts underwent another phase transition. Despite the different metal, metal oxide and carbide phases observed directly after the MOFMS process, all three catalysts display the same metal oxide phase (Fe_3O_4) with comparable intensities (Figure 11 b) after the time-on-stream experiments. The formation of the Fe_3O_4 phases, which contains ions in relatively high oxidation states, indicates a degradation of the carbon shells of all three catalysts. Despite the phase transition during the catalytic testing, no phase transition was observed for all three materials (without catalytic testing) after storage in air for six months. These observations further indicate the formation of a partial carbon shell around the metal particles of Fe@C_600°C and the formation of a complete oxidation preventing shell around the

metal particles of Fe@C_800°C due to stabilized metallic iron phases in both catalysts. However, the occurrence of oxidized iron after the catalytic testing implies a relatively low stability of the carbon shell and, therefore, its degradation under CO_2-FTS conditions.

Mössbauer spectroscopy was used to confirm the generated phases for each catalyst during the MOFMS process. Figure 12 and Table 2 display the Mössbauer spectra and the respective fitting parameters used for the three iron-based catalysts. The spectrum of Fe@C_400°C shows a doublet with an isomer shift δ = 0.39 mms^{-1} and a quadrupole splitting ΔE_Q = 0.88 mms^{-1}. These parameters are typical for ferric high spin iron present in superparamagnetic iron oxide particles. This matches the observations of the PXRD measurements and confirms the generation of fully oxidized iron particles. The Mössbauer spectrum of Fe@C_600°C shows a mixture of three components. Component 1 with a relative contribution of 35 % has an isomer shift of δ = 1.11 mms^{-1} and negligible quadrupole splitting and can be attributed to a high spin ferrous FeO phase. Component 2 shows a magnetic sextet with both zero values of δ and ΔE_Q and a magnetic hyperfine field B_{hf} = 33.3 T which is characteristic for metallic α-Fe and contributes with 39 % to the total spectral area. Component 3 exhibits an isomer shift of δ = 0.6 mms^{-1}, ΔE_Q = 0 and a magnetic hyperfine field B_{hf} = 46.7 T with a relative contribution of 26 %. These parameters are typical for an iron oxide phase. Similarly, the PXRD pattern displays a mixture of reduced α-Fe, wuestite (FeO) and magnetite (Fe_3O_4). Furthermore, the Mössbauer spectrum of Fe@C_800°C shows mainly a mixture of two main components with a third minor component. The minor component (1) contributes 15 % and is assigned to oxidized iron (Fe^{3+}) with δ = -0.1 mms^{-1} and a quadrupole splitting of zero.[158] Component 2 with a relative contribution of 45 % has both zero values of δ and ΔE_Q and a magnetic hyperfine field B_{hf} = 33.3 T, which can again be assigned to α-Fe. Component 3 shows a magnetic sextet with δ = 1.11 mms^{-1} and a magnetic hyperfine field B_{hf} = 20 T which matches the iron carbide phase Fe_3C. The relative contribution of component 3 is 40 %. Hence, the results match the PXRD pattern, which displayed a mixture of α-Fe and the carbide Fe_3C as the main phases for Fe@C_800°C.

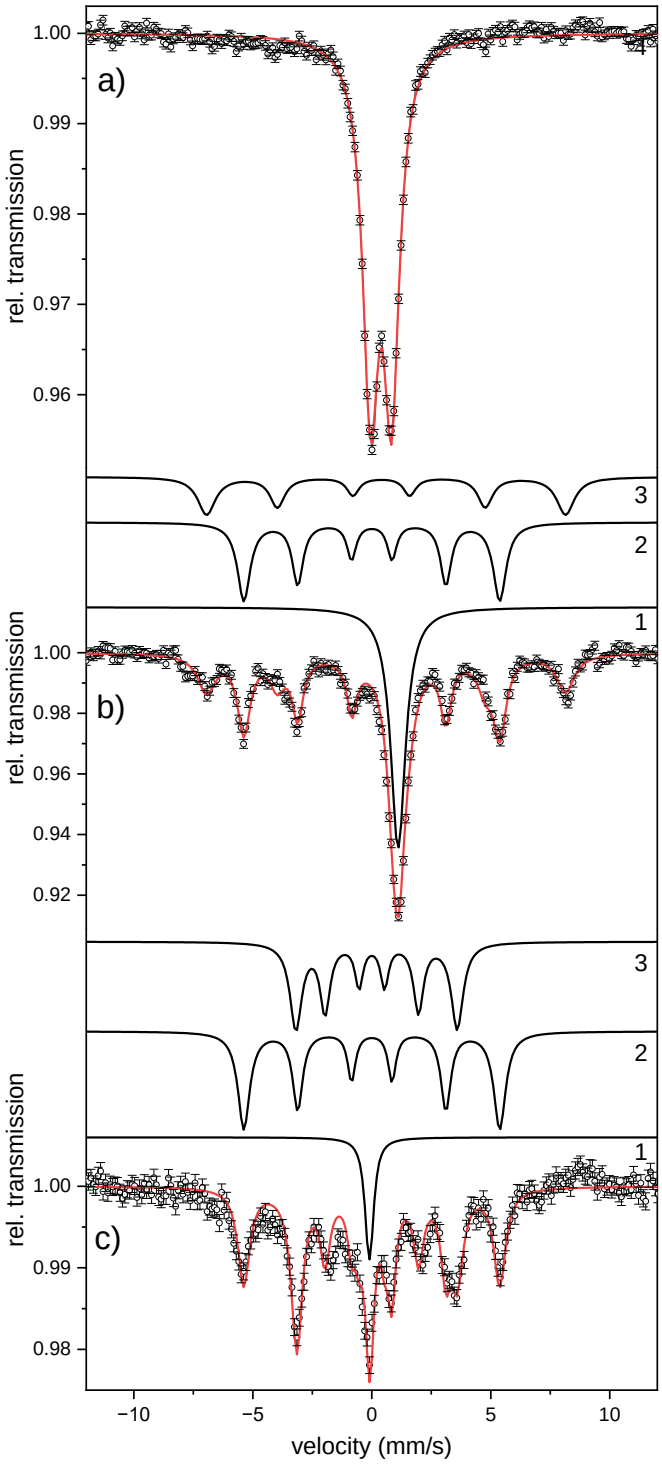

Figure 12: Mössbauer spectra of Fe@C_400°C (a), Fe@C_600°C (b) and Fe@C_800°C (c) obtained at room temperature. The solid lines are the result of a fit using Lorentzian line shapes and the fitting parameters given in Table 2.

Table 2: Fitting parameter of the Mössbauer spectra of Fe@C_400°C, Fe@C_600°C and Fe@C_800°C.

Sample	Comp	δ / mms^{-1}	ΔE_Q / mms^{-1}	B_{Hf} / T	$G_{3,4}$ / mms^{-1}	$G_{2,5}$ / mms^{-1}	$G_{1,6}$ / mms^{-1}	Area / %
Fe@C_400 °C	1	0.39	0.88		0.79			100
Fe@C_600 °C	1	1.11	0		0.75			35
	2	0	0	33.3	0.47	0.55	0.65	39
	3	0,6	0	46.7	0.62	0.75	0.9	26
Fe@C_800 °C	1	-0.1	0		0.5			15
	2	0	0	33.3	0.4	0.5	0.6	45
	3	1.11	0	20	0.4	0.5	0.6	40

The carbon matrix, formed around the metal nanoparticles is the most prominent attribute for the unique properties of MOFMS catalysts. This unique feature was investigated before and after the catalytic testing *via* ICP-OES, TGA and nitrogen physisorption measurements. ICP-OES measurements of the samples were performed to analyze the metal content of the catalysts and, therefore, to draw conclusions about thickness of the newly formed carbon shell. Table 3 shows an increase of the relative metal content with increasing thermal decomposition temperature. This result is expected due to the increasing amount of carbon decomposed at higher temperatures and the previously discussed TGA measurements of the MOF precursor (cf. Figure 10). Fe@C_800°C displays the highest metal content with 55.2 wt% and Fe@C_400°C, where an incomplete decomposition was indicated by the PXRD pattern, shows the lowest relative metal content with 26.9 wt%. Despite the lower relative metal content of Fe@C_600°C (42.3 wt%) compared to Fe@C_800°C the carbon shell should be of similar thickness due to additional oxygen within the metal oxide phases of Fe@C_600°C.

Table 3: ICP-OES measurement results for the Fe@C catalyst series before and after the catalystic testing.

Sample	Initial metal content / wt%	Metal content after catalytic testing / wt%
Fe@C_800°C	55.2	46.5
Fe@C_600°C	42.3	43.8
Fe@C_400°C	26.9	37.9

After the catalytic testing, the ICP-OES measurements were repeated. Interestingly, the metal content of the three catalysts converge to a certain degree. Therefore, the spent Fe@C_800°C catalyst shows a lower relative metal content compared to Fe@C_800°C due to the newly added oxygen within the new metal oxide phase. The metal content of the spent Fe@C_600°C catalyst displays no significant changes with 43.8 % compared to 42.3 %. This indicates that the carbon shell was further decomposed under the CO_2-FTS conditions due to the additional weight of the oxygen introduced *via* the oxidation of the iron phases. The spent Fe@C_400°C catalyst shows an increased relative metal content of 37.9 % due to additional thermal decomposition of the remaining organic MOF parts under the harsh CO_2-FTS conditions.

According to the literature, one main advantage of MOFMS catalysts compared to conventional MOFs should be their increased thermal stability. This hypothesis was analyzed using TGA measurements in air atmosphere. The thermogravimetric measurements of the three samples show a total weight loss of 54.3 % at 670 °C for Fe@C_400°C, 33.7 % at 640 °C for Fe@C_600°C and 23.5 % at 610 °C for Fe@C_800°C (Figure 13 a + b). The increased weight loss with decreasing decomposition temperature during MOFMS is expected due to the oxidation of the thicker carbon shell, which was already indicated by the PXRD and ICE-OES measurements. Fe@C_400°C is the only catalyst that shows a straight weight loss, the other two samples exhibit a weight gain at around 230 °C and 175 °C respectively. The increase in mass can be explained by the oxidation state of the

catalysts prior to the TGA measurements. Hence, Fe@C_600°C contained partially reduced iron oxides and Fe@C_800°C contained only metallic and carbidic iron, which got oxidized during the TGA and therefore results in a mass increase due to the uptake of oxygen. The mass increase is more pronounced for Fe@C_800°C, because no oxidic iron was observed prior to the measurement.

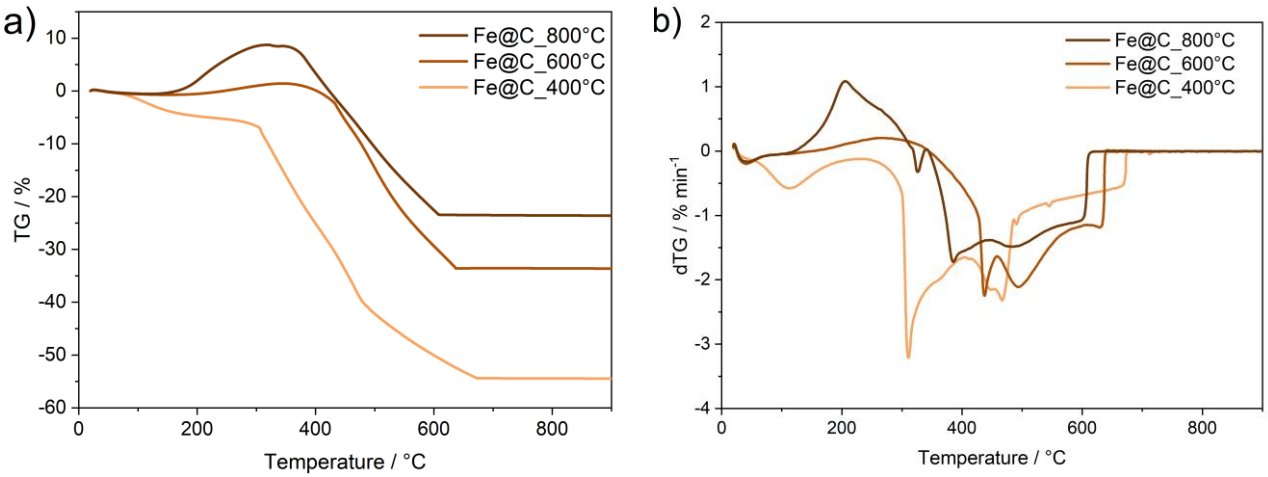

Figure 13: TG (a) and the DTG (b) curves of the Fe@C catalyst series in air.

Furthermore, nitrogen physisorption isotherms were measured to investigate the porosity of the newly generated catalyst materials. The isotherms of the catalyst materials decomposed at higher temperatures show type IV isotherms with a hysteresis between the adsorption and desorption branches. This is typical for mesoporous materials (Figure 14). The effect is generated through capillary condensation in the mesopores. Fe@C_400°C shows a type II isotherm similarly to activated carbon due to the large amount of carbon around the active metals. Therefore, mainly micropores are present in the sample that was decomposed at 400 °C.

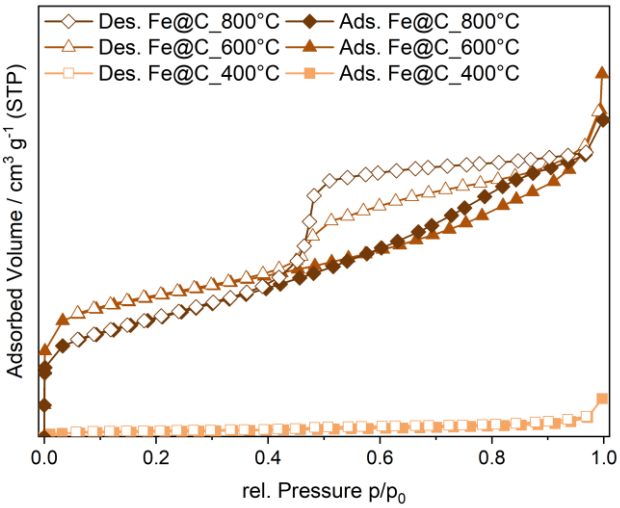

Figure 14: Physisorption isotherms of the Fe@C catalyst series.

Based on the isotherms, the specific surface areas and the average pore diameters of the materials were calculated using the BET method, BJH plot and HK plot, respectively. Compared to the precursor material the specific surface areas of the MOFMS catalysts increase drastically, particularly for the catalyst systems with high decomposition temperatures (Table 4). The catalysts Fe@C_600°C and Fe@C_800°C display specific surface areas of 270-330 m^2 g^{-1}. This is expected due to the mesoporous nature of the carbon matrix compared to the MOF precursor, which featured a closed pore geometry.

Table 4: Specific surface areas, pore diameters and pore volumes of for the Fe@C catalyst series derived from BET method, BJH plot and HK plot.

Sample	**Specific surface area / m^2 g^{-1}**	**Average pore diameter / nm**	**Pore Volume / cm^3 g^{-1}**
Fe@C_800°C	270	4	0.266
Fe@C_600°C	330	5	0.301
Fe@C_400°C	15	1.8*	0.032

*determined *via* HK-plot.

The average pore diameters were determined from HK plot and BJH plot, respectively. Unfortunately the pore size distribution for the materials is quite broad due to the meso- and microporous nature of the carbon shell. However, the resulting

average pore diameters match relatively small mesopores for Fe@C_600°C and Fe@C_800°C and micropores for Fe@C_400°C (Table 4). The pore volumes which were derived from the BJH plot display also an increase with increasing decomposition temperature. This was expected due to the higher porosity of Fe@C_600°C and Fe@C_800°C compared to Fe@C_400°C shown by the physisorption isotherms (Figure 14).

Fe@C_800°C is the only material from the Fe-based MOFMS catalyst series that shows both of the desired features of oxidation prevention *via* a carbon shell and the formation of cabidic iron. To further analyze the structure of the catalyst Fe@C_800°C and its MOF precursor XAS measurements were performed. Figure 15 a) shows the E-space of Fe@C_800 °C compared to a reference Fe foil and the MIL-53(Fe) precursor material. The white line of the precursor material is greatly enhanced compared to the other two spectra due to the oxidized nature of the Fe centers in the framework structure of MIL-53. The spectrum of Fe@C_800°C shows only a slight increase of the white line compared to the reduced metal foil. Therefore, it can be assumed that the sample was in a fairly reduced state, which matches the PXRD results with no metal oxide phase present and reduced Fe_{bcc} as the main phase. The slight increase in the white line indicates the presence of the carbide phase, which leads to an oxidized state of the iron. Furthermore, the first coordination shell of the R-space of the three materials is shown in Figure 15 b). The first feature of Fe@C_800°C matches the peak of the Fe foil reference with a decreased intensity. The difference between these two spectra is the shoulder peak of Fe@C_800°C found between 1.2 Å and 1.6 Å. The shoulder is most likely generated by the Fe_3C phase and this is also indicated by the first coordination shell of the MOF precursor. The peak of MIL-53(Fe) is shifted to a lower radial distance compared to the reduced metal particles due to the neighboring atoms from the organic linkers in the MOF structure.

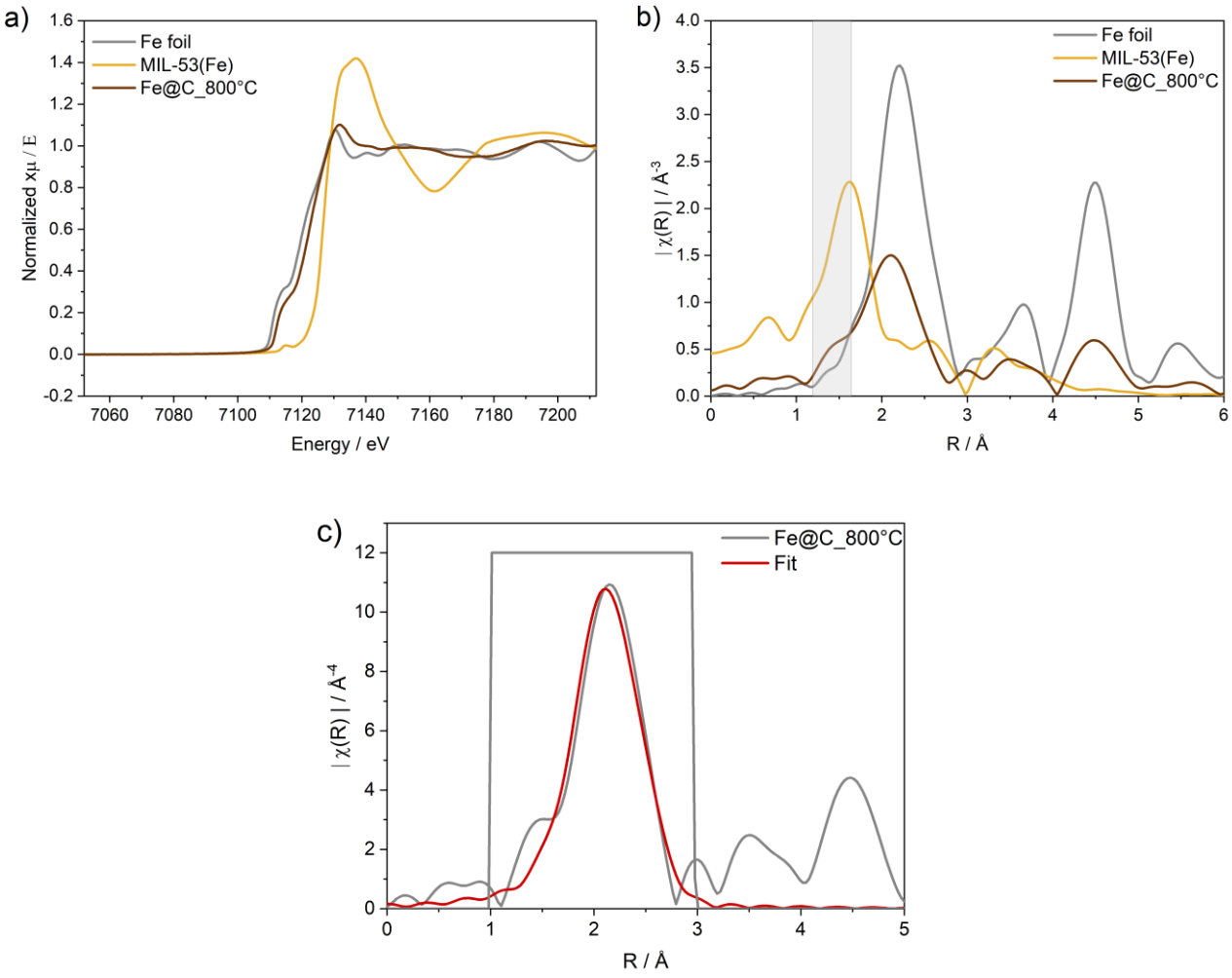

Figure 15: E-space of Fe@C_800°C, MIL-53(Fe) and Fe foil (a), R-space of Fe@C_800°C, MIL-53(Fe) and Fe foil (b) and first coordination shell fit in R-space of Fe@C_800°C (c).

The measured spectra of Fe@C_800°C was fitted with Fe_{bcc} as reference to further investigate the coordination environment of the sample (Figure 15 c). The simulation of the extended X-ray absorption fine structure (EXAFS) results in only negligible deviations for the Fe-Fe distances of the first two coordination spheres around the central Fe atom (Table 5). The fit confirms the previous assumptions of reduced F_{bcc} as the main phase. However, the contribution of Fe_3C could neither be confirmed nor excluded. The main part of the first coordination shell peak matches the fit and the shoulder peak that is potentially generated by the carbide phase is not included. Unfortunately, no combination fit of the two phases was possible due to the unknown ratio of the phases.

Table 5: Fitting parameter for the first coordination shell fit of Fe@C_800°C with Fe (bcc) as fitting model.

Scattering Path	N_{eff}	R_{eff}	ΔR	σ^2
Fe1 – Fe_{bcc}	8	2.45	0.0001 ± 0.0162	0.0134 ± 0.0015
Fe2– Fe_{bcc}	12	2.84	-0.0362 ± 0.0124	0.0134 ± 0.0015

3.1.3 Catalytic testing of Fe-based MOFMS catalysts

Prior to each catalytic testing process, 500 mg of the undiluted catalyst was activated *in-situ* under reducing conditions for 30 minutes at 400 °C. The chosen activation time was relatively short compared to the literature due to the already comparatively reduced states of the catalysts. To analyze the stability of the catalyst systems under Fischer-Tropsch synthesis conditions, the first catalytic testing was a time-on-stream measurement for 12 h at a temperature of 350 °C and a pressure of 20 bar. The CO_2 conversion of the three catalyst systems is visualized in Figure 16. All catalysts show a steady-state like condition after 5 h on stream, where the CO_2 conversion stabilizes and only minor fluctuations are visible. The catalysts Fe@C_400°C and Fe@C_800°C show a slightly higher conversion in the first hours of the measurement, in contrast to the catalyst synthesized at 600 °C, which shows a slightly lower conversion at the start of the testing. The CO_2 conversion of Fe@C_800°C is overall the highest with around 23 % compared to around 13 % of the other two materials. According to the literature, Hägg carbide χ-Fe_5C_2 is the most active phase for CO_2-FTS. This phase can be generated *in situ* under FTS reaction conditions from reduced α-Fe and Fe_3C (cf. Chapter 1.4.1). During the PXRD measurements Fe@C_800 °C showed a reduced α-iron phase and a Fe_3C carbide phase, while the other catalysts displayed oxidic iron phases. Hence, it can be assumed that the reduction period of only 30 minute was too short to fully reduce Fe@C_400°C and Fe@C_600 °C and that the superior FTS activity of Fe@C_800°C is linked to an *in situ* formation of χ-Fe_5C_2. However, Fe@C_400 °C and Fe@C_600 °C displayed very similar CO_2 conversions during the time-on-stream experiment despite the vastly different metal loading of 26.9 wt% and 42.3 wt%

(cf. Table 3). This indicates that the formed metal phases during the MOFMS process and the thickness of carbon shell are more important than the overall metal loading.

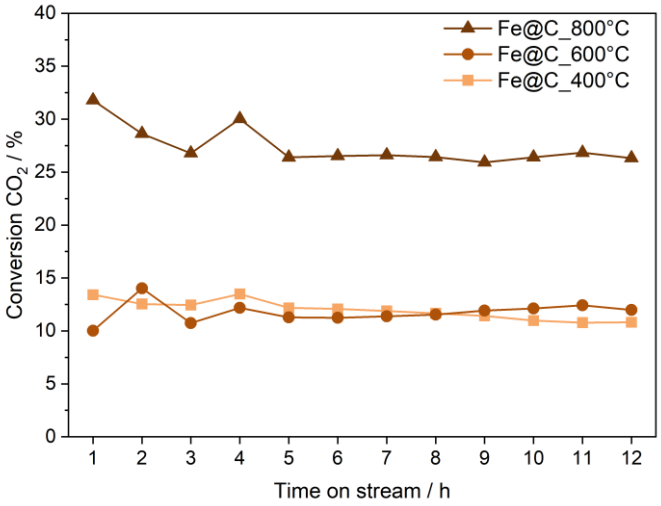

Figure 16: CO_2 conversion measurements of the Fe@C catalysts (500 mg) for a TOS of 12 h at 350 °C and 20 bar with a total flow of 25 mL/min (H_2/CO_2 = 3:1).

After the TOS experiment, the catalyst materials were tested in the temperature range between 200 °C and 400 °C, which covers the LTFT and HTFT conditions of conventional CO-FTS. The pressure was again kept at 20 bar for all measurements due to the thermodynamic equilibrium for the FTS reaction (cf. Chapter 1.3). The CO_2 conversions of the MOFMS material catalysts are shown in Figure 17 a). Fe@C_400°C with the largest carbon shell starts only to be active at higher reaction temperatures, above 300 °C, however, the main product generated was CO. The other two catalyst systems start to show FTS activity at a reaction temperature of 250 °C. Similar to the time on stream measurements, the CO_2 conversion is significantly higher for the Fe@C_800°C catalyst at every tested temperature. The conversion increases with increasing reaction temperature due to exothermic nature of the FT reaction. The highest measured CO_2 conversion is 36.4 % for Fe@C_800°C at 400 °C.

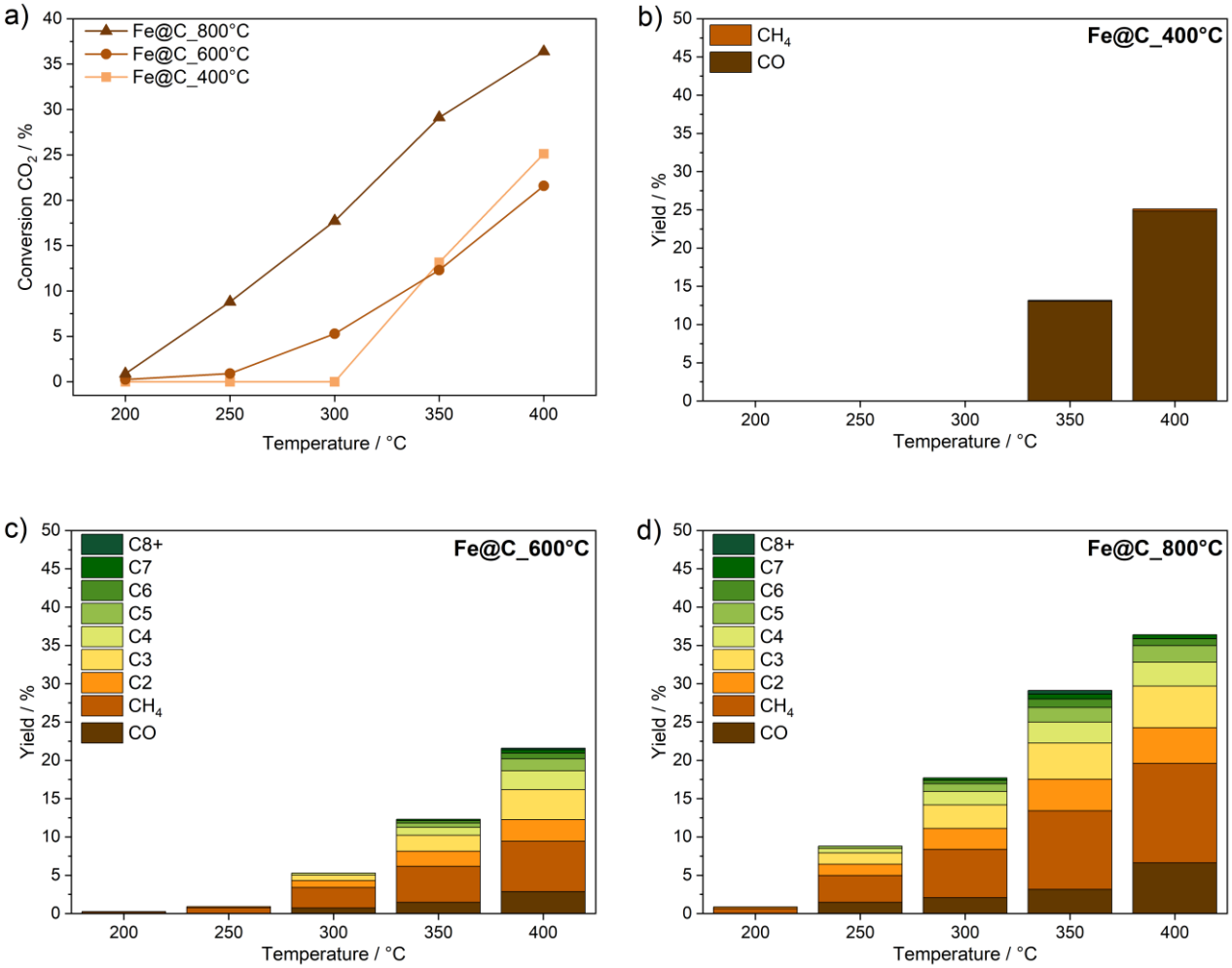

Figure 17: Temperature-dependent CO_2 conversion for the Fe@C catalyst series (a), temperature-dependent C-fraction yield distribution for the catalysts Fe@C_400°C (b), Fe@C_600°C (c) and Fe@C_800°C (d). All catalytic investigations were conducted at 20 bar with a total flow of 25 mL/min (H_2/CO_2 = 3:1).

Additionally, the CO_2 conversion at different temperatures and the product yields were also screened for all reaction temperatures, respectively. The product fractions of the three tested catalysts were classified after the resulting hydrocarbon chain length (Figure 17 b – d). The selectivities toward CO, CH_4, C_{2+} fractions and C_{5+} fractions of the three FTS catalyst systems were calculated from the measured temperature-dependent yields and are shown in Table 6.

Fe@C_400°C shows no significant FTS activity at any temperature during the testing. At higher temperatures of 350 °C and 400 °C the catalyst generates a high CO yield of 13 % and 24 %, respectively. However, even at the high reaction temperatures no selectivity towards methane or other hydrocarbons was observed.

This indicates an activity for the rWGS reaction but no further chain growth. The carbon shell of the material seems to be too thick. The physisorption isotherm of this material also indicates a microporous environment, which could hinder the chain growth mechanism necessary for higher C-chain fractions. Hence, no significant FTS activity and comparatively low CO_2 conversion were observed for the catalysts Fe@C_400°C and the poor properties make this material uninteresting for CO_2-FTS applications but also for other CO_2 hydrogenation reactions like methanation.

Fe@C_600°C produces only small amounts of CO at low reaction temperatures of 200 °C and 250 °C, however, at temperatures above 300 °C the material starts to show FTS activity with a small hydrocarbon yield up to a chain length of C_4. At HTFT conditions, the system produces hydrocarbon fractions with C-chain lengths of up to C_8. The selectivity toward longer hydrocarbon products (C_{5+}) starts at 350 °C with 8.5 %. At 400 °C the selectivity towards C_{2+} products as well as towards C_{5+} products increases again for Fe@C_600°C, with 56.3 % and 13.6 %, respectively. In contrast, the selectivity towards methane decreases with increasing reaction temperature from 50.3 % at 300 °C to 30.5 % at 400 °C. Despite the favorable selectivity shift towards the formation of hydrocarbon chains, the selectivity towards methane is still relatively high and the overall CO_2 conversion is comparatively low with a maximum of 21.6 % at 400 °C. Due to the incomplete carbon shell of the material and the resulting three Fe phases in the fresh catalyst, the formation of highly FTS active carbide phases could be hindered at lower reaction temperatures. This would explain the comparably low FTS activity under 350 °C and also the lower overall CO_2 conversion (compared to Fe@C_800°C).

The third tested catalyst system, Fe@C_800°C, features the thinnest carbon shell around the active metal and displayed metallic and carbidic iron phases prior to the catalytic testing. The catalyst displays the overall highest CO_2 conversions at all tested temperatures as well as the highest FTS activity with the longest generated hydrocarbon chains of C_8. In contrast to Fe@C_600°C, the material starts to display FTS activity already at 250 °C with selectivity towards C_{2+} of 43.5 % and towards C_{5+} of 3.3 %. Despite the constant increase of CO_2 conversion with increasing temperature, the selectivity towards FTS products peaks at 350 °C with 14.2 % selectivity towards C_{5+} products compared to only 9.8 % at 400 °C. The selectivity towards the competing methane formation displays also a different trend compared to

Fe@C_600°C. Hence, only minor selectivity changes concerning the methane formation are observed between 250 °C and 400 °C. However, even at 350 °C the selectivity towards methane is still relatively high with 35.7 %. Fe@C_800°C is the only catalyst from the Fe-based MOFMS catalyst series that showed both the desired effects of oxidation prevention *via* the carbon shell and the presence of a carbide phase. It can be assumed that both properties of the catalyst system have a beneficial influence on the CO_2-FTS activity because the highest hydrocarbon yields as well as the highest selectivity towards C_{2+} and C_{5+} products are obtained with this catalyst.

Table 6: Temperature-dependent selectivity towards CO, CH_4, C_{2+} fractions and C_{5+} fractions for Fe@C_400°C, Fe@C_600°C and Fe@C_800°C.

Sample	Temperature	X_{CO_2}	S_{CO}	S_{CH_4}	$S_{C_{2+}}$	$S_{C_{5+}}$
Fe@C 800°C	200 °C	0.9	0.0	75.9	24.1	0.0
	250 °C	8.8	16.7	39.8	43.5	3.3
	300 °C	17.7	11.7	35.7	52.6	10.1
	350 °C	29.1	10.8	35.2	53.9	14.2
	400 °C	36.4	18.2	35.7	46.1	9.8
Fe@C 600°C	200 °C	0.2	0.0	78.6	21.3	0.0
	250 °C	0.9	0.0	84.9	15.1	0.0
	300 °C	5.3	13.7	50.3	35.9	0.0
	350 °C	12.3	11.8	38.5	49.9	8.5
	400 °C	21.6	13.2	30.5	56.3	13.6
Fe@C 400°C	200 °C	0.0	0.0	0.0	0.0	0.0
	250 °C	0.0	0.0	0.0	0.0	0.0
	300 °C	0.0	0.0	0.0	0.0	0.0
	350 °C	13.2	99.3	0.7	0.0	0.0
	400 °C	25.1	98.9	1.1	0.0	0.0

The temperature-dependent distribution of alkane and olefin fractions generated by the two catalytic active systems (Fe@C_600°C and Fe@C_800°C) is visualized in Figure 18. Due to the increase in possible isomers within higher C-fractions and the resulting difficulties to assign them only the yields of the C_2 and C_3 fraction are shown, respectively. Fe@C_600°C has a strong selectivity towards alkane fractions

with only minor amounts of olefin products at the higher reaction temperature ranges. However, the yield of ethylene and propylene is below 0.5 %. In comparison the yield of ethane ranges between 1 % and 2.8 % and the yield of propane ranged between 0.7 % and 3.6 % in the FTS active region of 300 – 400 °C. On the other hand, Fe@C_800°C shows a higher selectivity towards olefins. The ethene yield starts at a reaction temperature of 300 °C and ranged between 0.5 % and 0.9 % compared to the ethane yield of 2.3 % and 3.7 %. However, the catalyst produces propylene at even lower reaction temperatures and the ratios between alkane and olefin fraction are comparable. Therefore, the observed yields are 1.5 % at 300 °C and 2.4 % and 2.2 % at 350 °C, respectively. A reaction temperature of 400 °C seems to lower the selectivity towards propylene with a yield of only 1.9 %. The comparatively low selectivity towards olefins was expected for the Fe-based MOFMS catalysts without additional promoters. Based on the current literature a selectivity shift towards the formation of light olefines as main product is only possible by the addition of alkali metal promoter due to the increased CO_2 adsorption and an enhanced Hägg carbide formation.[23]

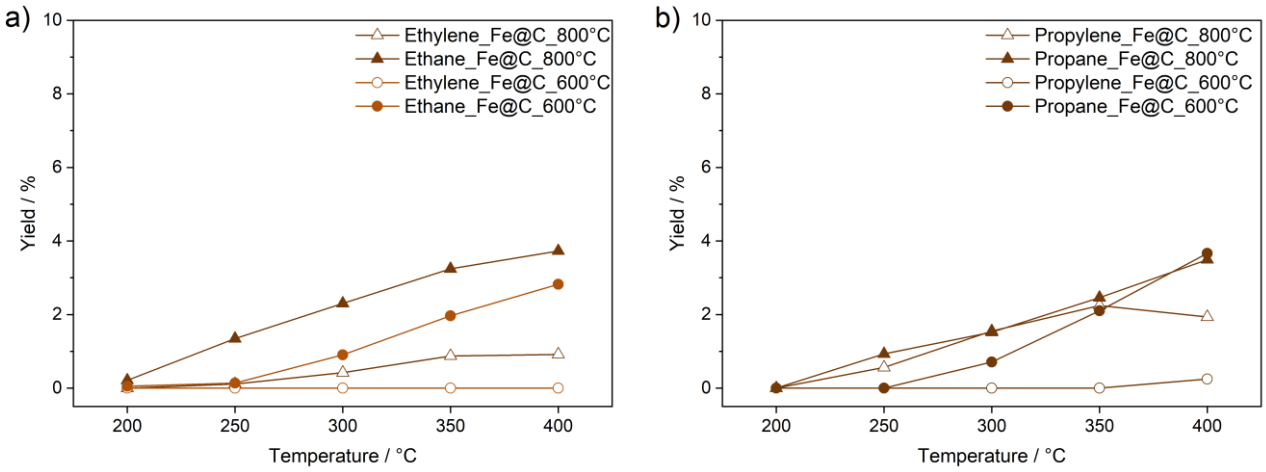

Figure 18: Temperature-dependent product distribution of the C_2 fractions (a) and C_3 fractions (b) for Fe@C_600°C and Fe@C_800°C, measured at 20 bar with a total flow of 25 mL/min (H_2/CO_2 = 3:1).

3.2 Bimetallic Fe/Co-containing MOFMS CO_2-FTS catalysts

3.2.1 Synthesis and characterization of bimetallic Fe/Co MOF precursor

The previously discussed monometallic Fe-based MOFMS catalysts showed promising features for CO_2-FTS applications. Fe@C_800°C achieved a selectivity of 53.9 % towards C_{2+} products and a CO_2 conversion of 29.1 % at a reaction temperature of 350 °C. The catalyst also displayed FTS activity even at lower reaction temperatures of 250 °C. Additionally, Fe@C_800°C exhibits the desired MOFMS features of an oxidation preventing carbon shell around the metal nanoparticles and enhanced formation of iron carbide phases. However, the selectivity towards methane was still comparatively high with around 35 % at all measured temperatures and all catalysts of the Fe-based series displayed a low stability under the harsh CO_2-FTS conditions. Hence, the materials got oxidized after the catalytic testing, which indicates a damaged carbon shell of the catalysts.

Based on the previously shown results, the topic of the following chapters will be the synthesis, characterization and catalytic testing of bimetallic Fe/Co-containing MOFMS catalysts. Despite the unfavorable properties of monometallic Co for the CO_2-FTS process (cf. Chapter 1.4.2), recent literature suggests a potential synergy for bimetallic CO_2-FTS catalysts (cf. Chapter 1.4.3). To further investigate these beneficial attributes and the influence of the unique properties of MOFMS materials, a series of bimetallic Fe/Co-containing MOF precursors with different metal ratios was synthesized. The chosen MOF structure was again MIL-53, because both monometallic variations of this framework are known to literature.[135,138] Another MOF-family that features both a Fe- and Co-containing variant is ZIF-67. However, the decomposition temperature of these MOF types is exceptionally high with over 800 °C, which excludes the materials for the further MOFMS process.[159] To analyze the potential effects of additional cobalt the bimetallic MOF precursors were synthesized with six different Fe/Co ratios (1:3, 1:2, 1:1, 2:1, 3:1 and 4:1). The resulting MOF precursors were named according to their specific metal ratio MIL-53($Fe_{0.25}Co_{0.75}$), MIL-53($Fe_{0.33}Co_{0.67}$), MIL-53($Fe_{0.50}Co_{0.50}$), MIL-53($Fe_{0.67}Co_{0.33}$),

MIL-53($Fe_{0.75}Co_{0.25}$) and MIL-53($Fe_{0.80}Co_{0.20}$), respectively. However, despite the known synthesis approaches for both monometallic MOF variants, MIL-53(Fe) and MIL-53(Co) feature some key differences, which resulted in two separate synthesis approaches for the MOF precursors with Co contents >50 % and <50 %, respectively. The cobalt and iron metal centers within the framework structure feature different oxidation states (Fe^{3+} and Co^{2+}). To stabilize the framework structure of MIL-53(Co), pyridine-*N*-oxide is needed for charge compensation (cf. Chapter 1.5.2). This results not only in different pore geometries, but also in different synthesis conditions for the MIL-53(Fe) without the stabilizer and MIL-53(Co) with the addition of pyridine-*N*-oxide. The bimetallic materials with a cobalt content >50 % could be synthesized with a solvothermal direct synthesis similar to the monometallic variants (Scheme 5).

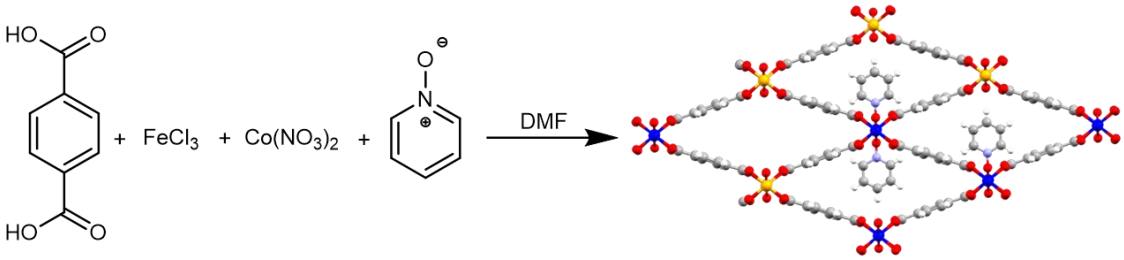

Scheme 5: Reaction scheme of the direct synthesis approach used for the generation MIL-53(Fe_xCo_{1-x}) precursor materials with a Fe content under 50 %.

However, the greatest difference between the two monometallic synthesis approaches is the reaction temperature (150 °C for MIL-53(Fe) and 120 °C for MIL-53(Co)). This parameter needs to be adjusted according to the desired metal ratio to generate a crystalline framework structure. Contrary to the reported monometallic synthesis approaches, higher reaction temperatures are favored for MOF materials with high Co content and lower reaction temperatures are favored for the synthesis of MOF materials with lower Co content (Figure 19). Hence, MIL-53($Fe_{0.50}Co_{0.50}$) was synthesized at 120 °C, MIL-53($Fe_{0.33}Co_{0.67}$) was synthesized at 130 °C and MIL-53($Fe_{0.25}Co_{0.75}$) was synthesized at 150 °C.

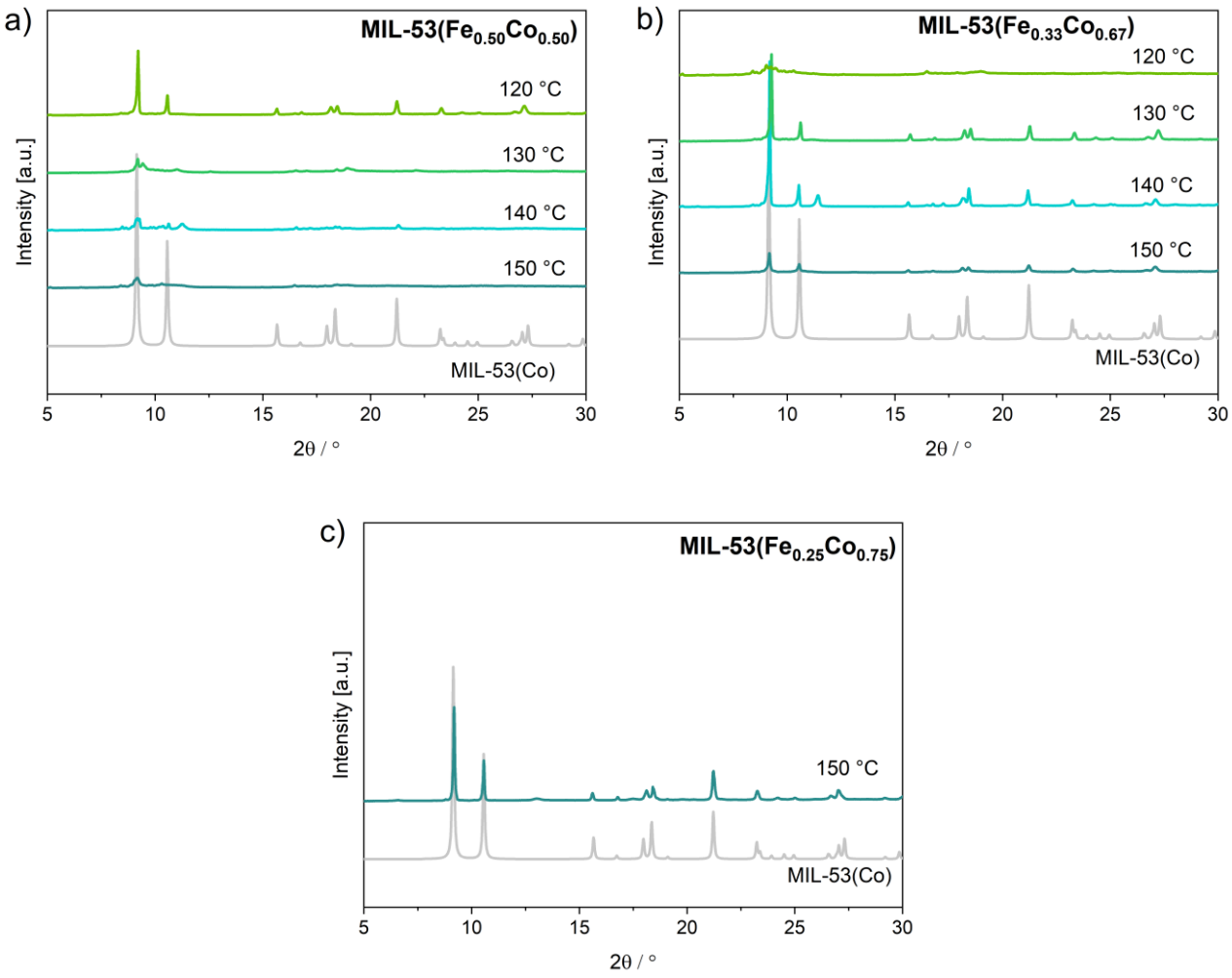

Figure 19: PXRD patterns of MIL-53($Fe_{0.50}Co_{0.50}$) (a), MIL-53($Fe_{0.33}Co_{0.67}$) (b) and MIL-53($Fe_{0.25}Co_{0.75}$) (c) synthesized at different temperatures.

Despite the testing of different synthesis approaches for bimetallic MIL-53(Fe_xCo_{1-x}) materials with a Fe/Co ratio >1 no successful direct synthesis route was found during this work. Above an iron content of 50 %, the formation of MIL-53(Fe) dominated the synthesis process, which resulted in the generation of mostly iron-containing MOF materials (between 95 and 99 % Fe according to ICP-OES measurements). Hence, a different approached was used to synthesize the MOF precursor with the Fe/Co ratios of 2:1, 3:1 and 4:1. The used two-step synthesis approach is shown in Scheme 6 and involves the synthesis of MIL-53(Fe) according to the previously presented synthesis approach in Chapter 3.1.1 as first step and the subsequent addition of Co *via* an additional incipient wetness impregnation.

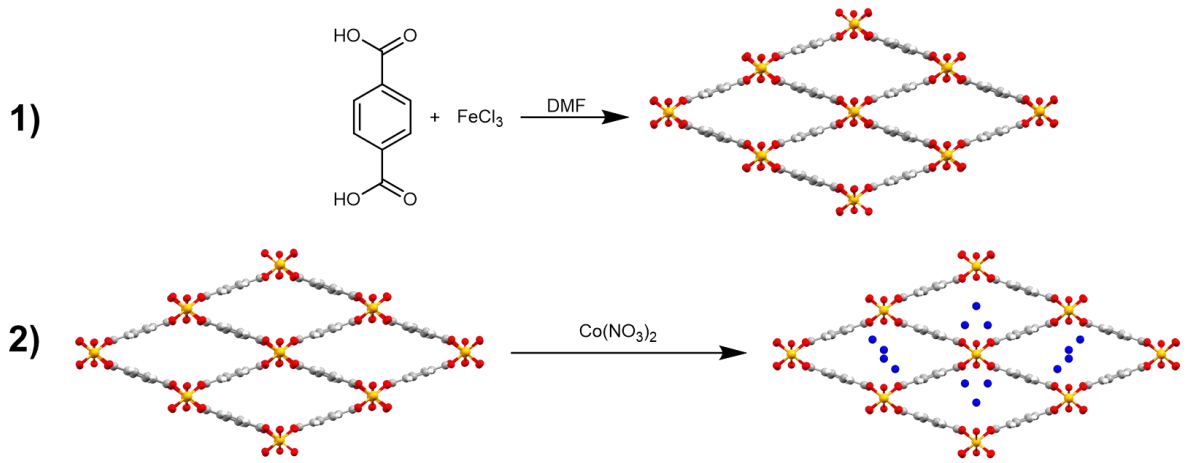

Scheme 6: Reaction scheme of the two-step synthesis approach used for the generation of MIL-53(Fe_xCo_{1-x}) precursor materials with a Fe content >50 %, consisting of the synthesis of MIL-53(Fe) (1) followed by an incipient wetness impregnation with Co (2).

The successfully synthesized bimetallic Fe/Co-containing MOF precursor series was characterized with the same combination of techniques as shown for the monometallic MOF precursor series in Chapter 3.1.1. Hence, to confirm the generation of a crystalline MIL-53 framework structure PXRD data were collected (Figure 20). All precursor materials show the characteristic reflections of the open pore geometry of MIL-53(Co), with pyridine-*N*-oxide in the pores. The reflections at 2θ = 9.1 ° and 10.5 ° indicate the open pore geometry even for the materials with high Fe content.[138] This result is expected due to the incorporated pyridine-*N*-oxide for the materials with high Co content and the Co embedded into the pores for the materials with high Fe content, which were synthesized *via* the two-step approach. Hence, the MOF pores are prevented from developing a close pore form. The reflection at 2θ = 21.9 is particularly pronounced for the materials with Fe contents above 50 %. This reflection is generated from (hkl) = (220) planes stacked diagonal through the pore, which suggest a distortion of the pore geometry due to the impregnation of Co. The higher intensity of the reflection therefore indicates a successful impregnation with the metal embedded into the pore structure of the MOF materials.

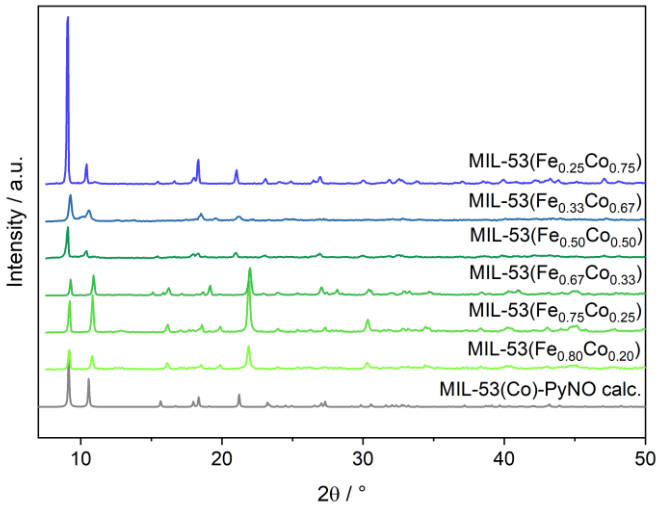

Figure 20: PXRD patterns of the MIL-53(Fe_xCo_{1-x}) MOF precursors with different Fe/Co ratios.

To confirm the theoretical metal ratios within the bimetallic precursor materials ICP-OES measurements were performed (Table 7). The samples of the series show only minor deviations to the target metal ratios with discrepancies of 1-3 %. The largest deviation is displayed by the bimetallic precursor with a target Fe/Co ratio of 1:1 with 53:47 %. The overall metal contents of the MOF precursors are relatively small for MIL-53($Fe_{0.25}Co_{0.75}$) and MIL-53($Fe_{0.33}Co_{0.67}$) due to the additional pyridine-*N*-oxide used to equalize the charge of the introduced Co^{2+} centers. The MOF materials with Fe amounts >50 % display higher metal contents. This is also a result from the chosen synthesis route, since Co is not linked in the framework structure but was added additionally *via* incipient wetness impregnation, which increases the overall metal loading of the precursor materials.

Table 7: ICP-OES measurement results for the MIL-53(Fe_xCo_{1-x}) MOF precursor series.

Sample	Experimental Fe/Co ratio / %	Metal content in MOF precursor / wt%
MIL-53($Fe_{0.25}Co_{0.75}$)	24 : 76	13.3
MIL-53($Fe_{0.33}Co_{0.67}$)	35 : 65	11.2
MIL-53($Fe_{0.50}Co_{0.50}$)	53 : 47	22.4
MIL-53($Fe_{0.67}Co_{0.33}$)	67 : 33	27.3
MIL-53($Fe_{0.75}Co_{0.25}$)	74 : 26	22.7
MIL-53($Fe_{0.80}Co_{0.20}$)	82 : 18	26.3

To confirm the purity of the synthesized MOF precursors, ATR-IR spectroscopy was used. The spectra reveal that only small amounts of incorporated solvent DMF (*N,N*-dimethylformamide) or free linker molecules, which both show a characteristic IR-band at 1665 cm^{-1} and no significant amounts of pyridine-*N*-oxide (broad IR-band at 3400 cm^{-1} and sharp band at 1460 cm^{-1}) are present in the pores of the Fe_xCo_{1-x}@C MOF precursors (Figure 21).[160] Hence, the linker molecules are incorporated into the framework structure, which is further supported by the intensity of the symmetric and asymmetric stretching vibrations of C-O at 1385 cm^{-1} and 1240 cm^{-1}. The absorption band at 855 cm^{-1} is generated by the δ (OH) modes of the bridging hydroxyl group (Fe−O(H)−Fe) and the C-H bending vibration of the benzene ring of the terephthalic acid is displayed at 750 cm^{-1}.[157] Similar to the PXRD results, no significant differences are observed between the MOF precursors, despite the two synthesis approaches.

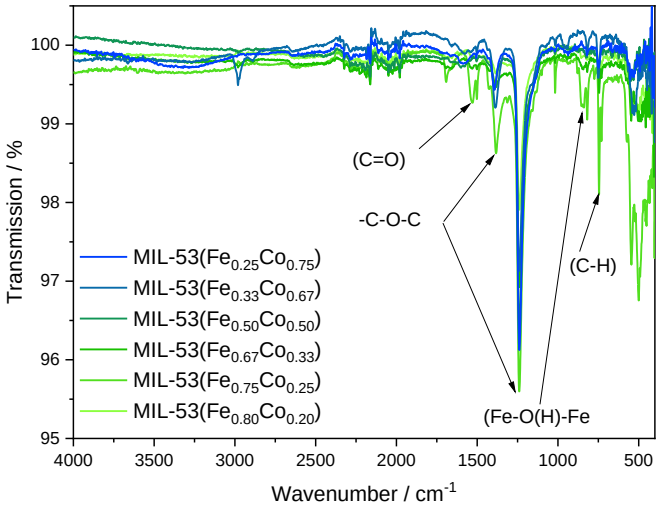

Figure 21: ATR-IR measurements of the MIL-53(Fe_xCo_{1-x}) MOF precursor series.

Additionally, nitrogen physisorption was measured for the bimetallic MOF precursor series. The specific surface areas of the materials were determined from the observed isotherms *via* the BET method (cf. Appendix Figure A 2). The specific surface areas of the Fe/Co-containing materials are relatively small for MOFs and more comparable to the monometallic MIL-53(Fe) with a closed pore geometry (Table 8). Unlike conventional MOFs, the pores of the precursor materials are blocked with either pyridine-*N*-oxide for the Co-rich materials or the impregnated Co for the Fe-rich materials, thus, the small specific surface areas match the expectation for the MOF precursor systems.

Table 8: Specific surface areas of the MIL-53(Fe_xCo_{1-x}) MOF precursor series determined from nitrogen physisorption isotherms using the BET method.

Sample	Specific surface area / $m^2\ g^{-1}$
MIL-53($Fe_{0.25}Co_{0.75}$)	138
MIL-53($Fe_{0.33}Co_{0.67}$)	55
MIL-53($Fe_{0.50}Co_{0.50}$)	98
MIL-53($Fe_{0.67}Co_{0.33}$)	39
MIL-53($Fe_{0.75}Co_{0.25}$)	57
MIL-53($Fe_{0.80}Co_{0.20}$)	24

In order to determine the decomposition behavior of the precursor materials for the following MOFMS procedure, TGA measurements in inert N_2 atmosphere were performed (Figure 22). The DTG curve reveals a two-step decomposition for the materials with high Co content and a four-step decomposition for the materials with higher Fe content. The additional weight loss step for the Fe-rich materials results most likely from the incipient wetness impregnation synthesis method. Hence, the additional weight loss at 200 °C can be assigned to the decomposition of nitrate residues within the pores. Furthermore, the first weight loss step of physisorbed water (around 100 °C) is more pronounced for the Fe-rich precursor materials also due to the impregnation synthesis approach. Between 250 °C and 600 °C, all six MOF materials display a similar behavior, which also matches the TGA behavior of the Fe-based MOF precursor (cf. Figure 10). Therefore, these weight losses can be assigned to the decomposition of the organic MOF parts into the desired carbon matrix. The Fe-rich MOF precursors display an additional weight loss step above 600 °C. This step was previously found during the TGA measurements of the monometallic Fe-based precursor (cf. Chapter 3.1.1) and a relation to the generation of a carbide phase was assumed. This indicates the necessity of larger quantities of Fe within the catalysts to generate the iron carbide phase during the decomposition process.

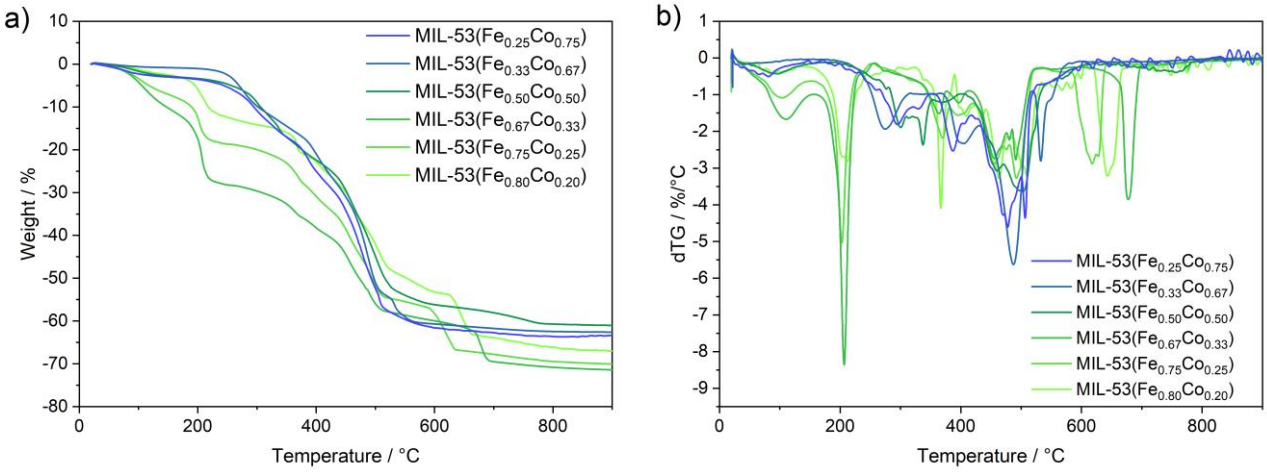

Figure 22: Thermogravimetric analysis of the MIL-53(Fe_xCo_{1-x}) precursor series in N_2 atmosphere with TGA (a) and DTG (b) curves.

3.2.2 Synthesis and characterization of bimetallic Fe/Co MOFMS catalysts

The series of bimetallic MOF precursors was thermally decomposed at 800 °C for 2 h in an inert nitrogen atmosphere, which resulted in a series of bimetallic MOFMS catalysts. The MOFMS conditions were chosen based on the previous results of the monometallic Fe-based MOFMS catalyst series (cf. Chapter 3.1) and the TGA results of the precursor materials (cf. Chapter 3.2.1). The high decomposition temperature of 800 °C proved to be most beneficial to generate catalysts with the desired MOFMS features. Additionally, Fe@C_800°C was the best performing catalyst during the CO_2-FTS testing regarding CO_2 conversion and FTS product selectivity. The newly synthesized bimetallic MOFMS catalysts were named in accordance with their specific Fe/Co ratio (Fe_xCo_{1-x}@C). The catalyst series was fully characterized by a combination of techniques to analyze the newly gained properties and to understand the potential effects of these properties on the catalytic behavior during the following test in the CO_2-FTS process. To understand the formed metal phases and possible oxidation state changes during the MOFMS procedure and the following catalytic testing, PXRD patterns were measured directly after the thermal decomposition at 800 °C (Figure 23 a) and after the catalytic testing (Figure 23 b). All six fresh catalysts show only reduced metal phases and no further oxidic phases or residue of the MOF structure. The main reflections for the catalysts systems are at 2θ = 44.5 ° and 64.9 ° and can both be assigned to either Fe_{bcc} or an alloyed FeCo phase

(wairauite). Unfortunately, both phases contain only overlapping reflections, which hinders further assignment. Particularly, the second reflection at 2θ = 64.9 ° gets broader and less intense with increasing Co content in the catalysts, which indicates less sintering and a smaller overall crystallite size. This observation matches the TGA measurements of the MOF precursors, where an increased amount of Co led to a higher thermal stability and therefore a slower formation and growth of the metal nanoparticles (cf. Chapter 3.2.1). $Fe_{0.25}Co_{0.75}$@C and $Fe_{0.33}Co_{0.67}$@C show an additional Co_{fcc} phase at the 2θ = 43.9 °, 51.4 ° and 75.5 ° positions. Hence, it can be assumed that the excessive Co of these two materials generates a separate Co_{fcc} phase additional to the bimetallic FeCo phase, which features a bcc crystal structure. The observed metal phases are stable under ambient conditions, which was revealed by remeasuring the materials after six months of storage in air without significant changes to the diffraction pattern.

After the catalytic testing there were no significant differences observable regarding the phases in the diffraction patterns for the catalysts from $Fe_{0.25}Co_{0.75}$@C to $Fe_{0.75}Co_{0.25}$@C. However, the pattern of $Fe_{0.80}Co_{0.20}$@C featured a new χ-Fe_5C_2 phase after the time-on-stream tests under FTS conditions. The newly generated Hägg carbide phase is known to be highly active for FTS but unstable against oxidation in contrast to the Fe_3C phase generated during the MOFMS process of Fe@C_800°C. Surprisingly, also the χ-Fe_5C_2 phase remained stable after several months of storage under air, despite being prone to oxidation. This indicates a formation of the carbide phase within a protective carbon matrix and further confirms the increased stability of the carbon shell formed around the bimetallic metal nanoparticles against the CO_2-FTS conditions.

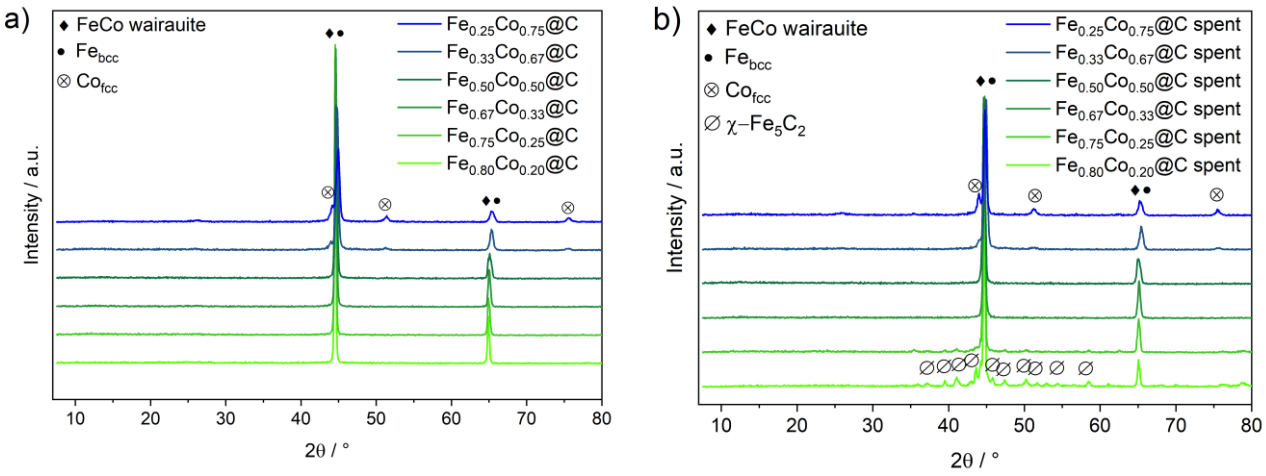

Figure 23: PXRD patterns of the Fe_xCo_{1-x}@C catalyst series with different Fe/Co ratios measured directly after the synthesis (a) and after the catalytic testing (b).

Additionally, the crystallite size of the bimetallic catalysts was determined using the Scherrer equation. The reflection at 2θ = 44.5 ° was chosen for all samples. Table 9 visualizes the increase of the crystallite size with the increase of Fe content. Hence, $Fe_{0.25}Co_{0.75}$@C shows the smallest crystallite size with 15 nm and the crystallite size increases with increasing Fe content up to 38 nm for $Fe_{0.80}Co_{0.20}$@C. The crystallite size was likewise determined for the spent catalysts after the catalytic testing. Surprisingly, after the catalytic testing the crystallite sizes converge to a similar range of around 24 nm. Therefore, the smaller particles of the catalysts with high Co content increase in crystallite size and the larger particles of the Fe-rich materials decrease from over 30 nm to 27 nm and 22 nm, respectively. This indicates *in situ* phase transitions during the FTS process, similarly to conventional FTS catalysts, although the protective carbon shell around the metal nanoparticles stays intact due to the remaining oxidation-preventing effect observed even after the catalytic testing.

Table 9: Crystallite sizes of the Fe_xCo_{1-x}@C catalyst series before and after catalytic testing determined using the Scherrer equation for the reflection at 2θ = 44.47 °.

Sample	Crystallite size (fresh) / nm	Crystallite size (spent) / nm
$Fe_{0.25}Co_{0.75}$@C	15	21
$Fe_{0.33}Co_{0.67}$@C	23	21
$Fe_{0.50}Co_{0.50}$@C	23	22
$Fe_{0.67}Co_{0.33}$@C	32	28
$Fe_{0.75}Co_{0.25}$@C	35	23
$Fe_{0.80}Co_{0.20}$@C	38	27

The Fe/Co ratio as well as the metal loading of the catalyst materials were determined *via* ICP-OES measurements before and after the catalytic testing. The measured metal ratios and the overall metal contents of the catalyst series are displayed in Table 10. The metal contents are similar for the catalysts before their catalytic application with 53-61 wt%. The metal content also matches the metal content of 55.2 % measured for Fe@C_800°C in Chapter 3.1.1. The Fe/Co ratios match the measured ratio of the parenting MOF with the exception of $Fe_{0.25}Co_{0.75}$@C, which displays a slightly higher Fe content than targeted. Both are expected results due to the same MOFMS conditions, a similar TGA decomposition behavior of the catalyst series compared to Fe@C_800°C and the fact that no changes to the metal ratio occurred during the thermal decomposition process. The metal amount after the catalytic testing deviates only slightly from the fresh catalysts. Hence, the carbon matrix of the systems remained stable during the CO_2-FTS with slight amounts of coking, which explains the slightly lower metal contents.

Table 10: ICP-OES results for the Fe_xCo_{1-x}@C catalyst series.

Sample	Experimental Fe/Co ratio / %	Metal content in catalysts (fresh) / wt%	Metal content in catalysts (spent) / wt%
$Fe_{0.25}Co_{0.75}$@C	32 : 62	55.1	52.6
$Fe_{0.33}Co_{0.67}$@C	38 : 62	53.3	52.3
$Fe_{0.50}Co_{0.50}$@C	57 : 43	59.6	55.6
$Fe_{0.67}Co_{0.33}$@C	69 : 31	56.2	56.9
$Fe_{0.75}Co_{0.25}$@C	76 : 24	58.4	56.4
$Fe_{0.80}Co_{0.20}$@C	80 : 20	61.3	58.5

The unusual presence of reduced iron and cobalt found within the MOFMS catalysts was further investigated by XAS measurements at the K-edges of Fe and Co, respectively. The XAS measurements were used to analyze the coordination environment of each bimetallic catalyst of the series. The normalized E-space, k-space and R-space measured at both edges are shown in Figure 24. The E-space spectra of the bimetallic catalyst series measured at the Fe K-edge (Figure 24 a) are very similar to the Fe foil reference (black) with a very small white line, which indicates the reduced nature of the metal particles. The E-space spectra measured at the Co K-edge shows a white line with similar low intensity. However, contrary to the Fe K-edge measurements the curve progression differs from the Co foil reference. This is in accordance with the measured PXRD patterns due to the presence of Co_{fcc} in the foil and the predominant bcc phase of Co within the bimetallic MOFMS catalysts. Similar to the E-space, the k-space spectra display only minor differences between the measured catalysts with clear oscillation up to a wavenumber of 11 Å at both edges. This result is also expected due to the comparatively large particle size (for XAS measurements) of over 15 nm and the high metal loading of all MOFMS catalysts. The R-space contains information about the direct coordination environment of the measured metals. The measured spectra at the Fe K-edge are in

line with the reference foil (Figure 24 e). Hence, the metal particles contain only reduced Fe_{bcc} and no traces of oxidized Fe could be found. Furthermore, the first coordination spheres below a radial distance of 5 Å are filled due to the appearance of all characteristic peaks for Fe_{bcc} at 2.2 Å, 3.6 Å and 4.5 Å. This led to the assumption of fully reduced Fe_{bcc} particles with a crystallite size above 5 nm. These findings are in accordance with the previously mentioned PXRD results for the crystallite sizes of the materials. The measured spectra at the Co K-edge (Figure 24 f) show similar peaks to the absorption at the Fe K-edge. All catalysts of the series display the same peaks at 2.2 Å, 3.6 Å and 4.5 Å, which leads to the assumption of the same crystal structure formation regardless of the metal ratio. An exception is $Fe_{0.25}Co_{0.75}$@C, where the second and third features are shifted slightly to shorter radial distances. This is in accordance with the measured PXRD pattern of the material, which is the only catalyst that features an additional Co_{fcc} phase. The Co foil reference (black) contains reduced Co_{fcc} and matches the shift of the second and third feature to shorter radial distances. Hence, it is assumed that most of the Co in the catalyst materials forms a FeCo wairauite phase with bcc crystal structure and only excessive Co centers form the additional Co_{fcc} phase.

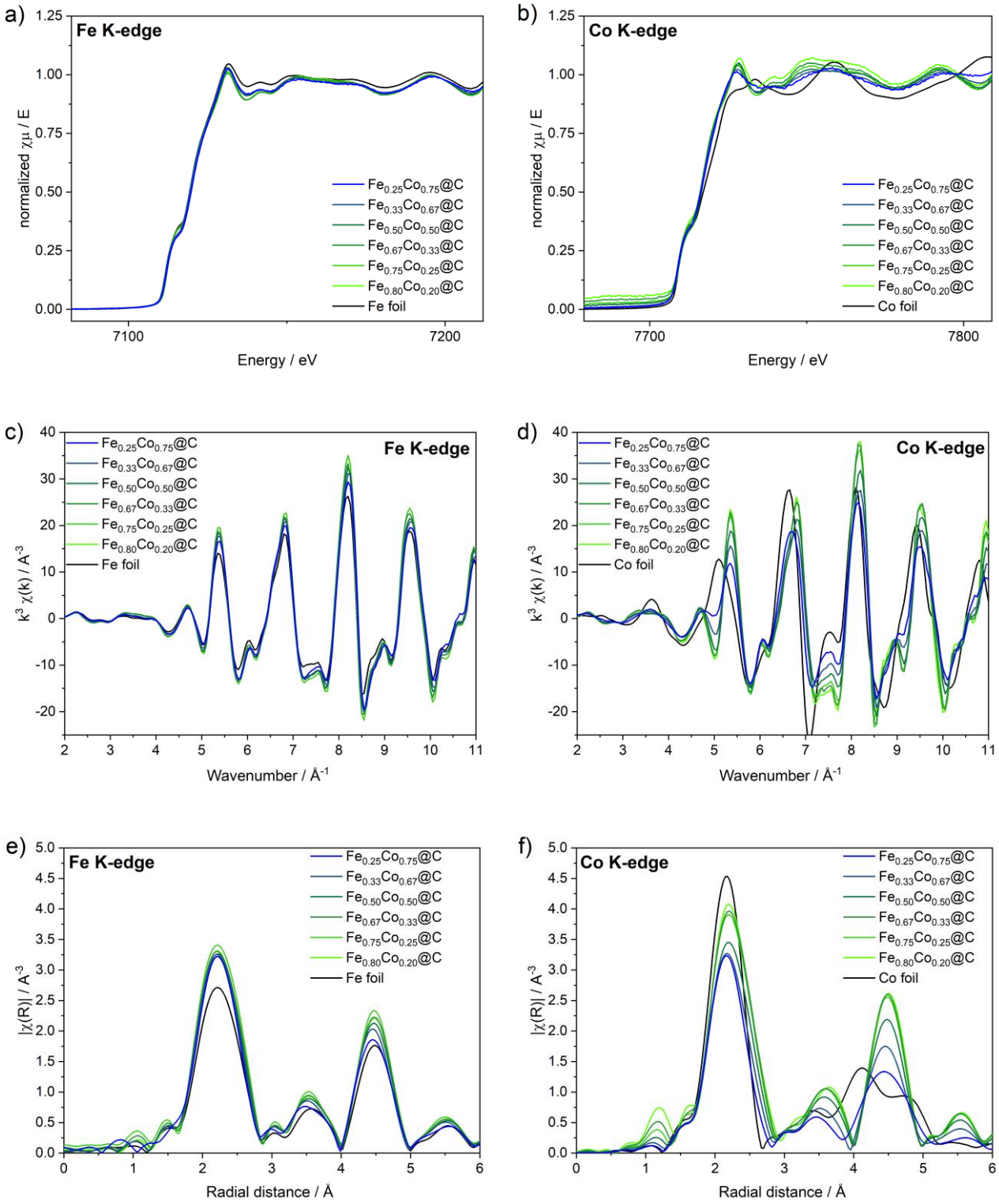

Figure 24: XAS measurements of the Fe_xCo_{1-x}@C catalyst series in E-, k- and R-space measured at the Fe K-edge (a, c and e) and the Co K-edge (b, d and f).

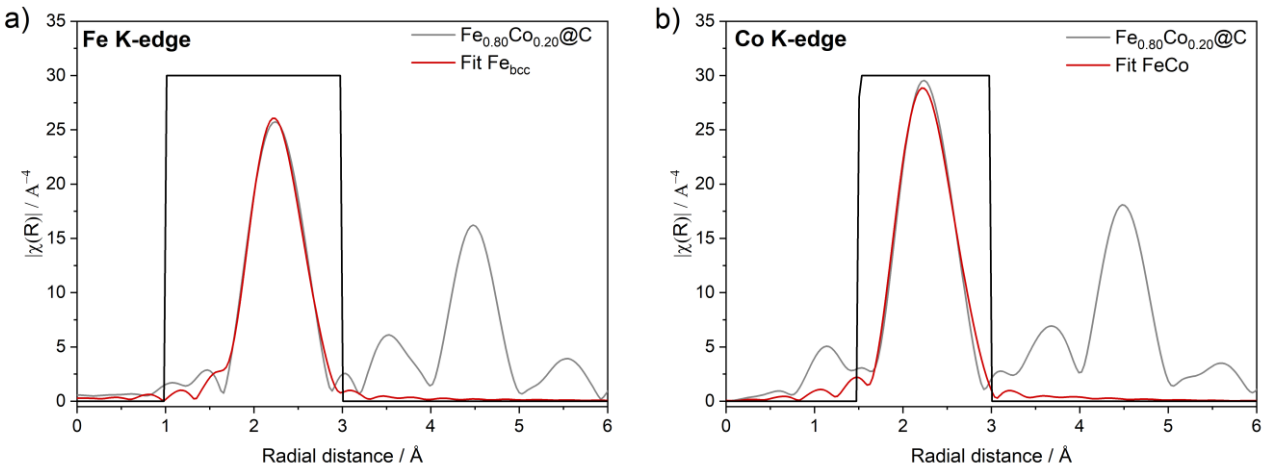

Figure 25: First coordination shell fit of $Fe_{0.80}Co_{0.20}$@C at the Fe K-edge (a) and Co K-edge (b).

Furthermore, the first coordination shell of the Fe K- and Co K-edge of each catalyst of the series was fitted using different metal phases. Exemplary fitting results for both edges are shown in Figure 25 and Table 11 of $Fe_{0.80}Co_{0.20}$@C. Due to the minor differences between the catalysts, the fits of all other catalysts of the series are found in the Appendix. In accordance with the PXRD results, the best fit was obtained with Fe_{bcc} for the Fe K-edge spectra and with the bimetallic FeCo wairauite phase as fitting model for the Co K-edge spectra. The fitted bond lengths show only minor deviations from the calculated models with $\Delta R = 0.0182 \pm 0.0106$ Å and $\Delta R = 0.0003 \pm 0.0108$ Å for Fe_{bcc} and the measured Fe K-edge XAS spectra of $Fe_{0.80}Co_{0.20}$@C. A similar trend was observed for the fitted spectra measured at the Co K-edge of $Fe_{0.80}Co_{0.20}$@C with a deviation of $\Delta R = 0.0005 \pm 0.0201$ Å for the first Fe coordination sphere and $\Delta R = 0.0114 \pm 0.0208$ Å for the first Co coordination sphere.

Table 11: Fitting parameters of the first coordination shell fit at the Fe K-edge and Co K-edge of $Fe_{0.80}Co_{0.20}$@C

Sample	Scattering path	N	R_{eff}	ΔR	R	σ^2
$Fe_{0.80}Co_{0.20}$@C	Fe1- Fe_{bcc}	8	2.460	0.0182±0.0106	2.478	0.0076± 0.0004
Fe K-edge	Fe2- Fe_{bcc}	6	2.840	0.0003±0.0108	2.840	0.0076± 0.0004
$Fe_{0.80}Co_{0.20}$@C	Fe - $FeCo_{bcc}$	8	2.458	0.0005±0.0201	2.458	0.0057± 0.0010
Co K-edge	Co - $FeCo_{bcc}$	6	2.839	0.0114±0.0208	2.850	0.0052± 0.0020

The unique properties of the carbon shell, which was generated during the MOFMS procedure, were further investigated by TGA, nitrogen physisorption and temperature-programmed reduction (TPR) measurements. The newly acquired thermal stability of the MOFMS catalyst series was analyzed *via* TGA measurements in synthetic air (Figure 26). The mostly reduced metal containing catalysts all display a weight gain at ≈260 °C for the Co-rich samples and at ≈410 °C for the Fe-rich samples due to the oxidation of the metal nanoparticles. Surprisingly, larger Fe-contents seem to increase thermal stability and the protection against oxidation. The weight gain is more pronounced for the Fe-rich systems than for their Co-rich counterparts. It can be assumed that this is caused by the larger observed crystallite sizes (Table 10) and the formation of oxides like Fe_2O_3 and Fe_3O_4, which contain larger amounts of oxygen than CoO.

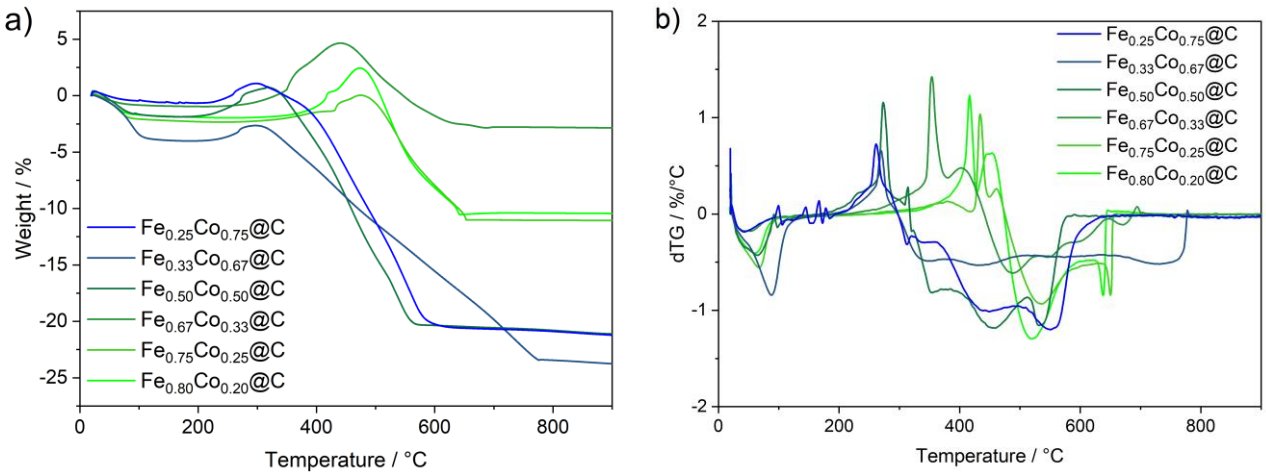

Figure 26: TGA (a) and DTG (b) measurements of the Fe_xCo_{1-x}@C catalyst series measured in synthetic air.

After the thermal decomposition of the MOF precursors, the catalyst materials feature metal nanoparticles encapsulated into a carbon matrix. According to this, the nitrogen physisorption isotherms show type IV isotherms with a characteristic hysteresis in the desorption curve, which are typical for mesoporous materials (the measured nitrogen physisorption isotherms of the series are displayed in the Appendix Figure A 3). The specific surface areas derived from the BET method show a slight increase compared to the MOF precursor with blocked pores. The specific surface areas are between 170 $m^2\ g^{-1}$ for $Fe_{0.25}Co_{0.75}$@C and 315 $m^2\ g^{-1}$ for $Fe_{0.50}Co_{0.50}$@C. This result is similar to Fe@C_800°C, which was synthesized under the same conditions. The pore diameters of the catalyst series were determined using the with BJH plot, which revealed a diverse pore size distribution of meso- and micropores within the carbon matrix. Contrary to the comparable small average pore diameter of Fe@C_800°C (cf. Table 4) the average pore diameter calculated seems to increase slightly with increasing Fe content. The calculated pore volume displays also an increase with increasing Fe content within the catalysts from 0.32 $cm^3\ g^{-1}$ for $Fe_{0.25}Co_{0.75}$@C up to 0.67 $cm^3\ g^{-1}$ for $Fe_{0.80}Co_{0.20}$@C. However, $Fe_{0.50}Co_{0.50}$@C does not follow the trend and shows a relatively large pore volume of 0.62 $cm^3\ g^{-1}$ (Table 12).

Table 12: Specific surface areas and average pore diameters of the Fe_xCo_{1-x}@C catalyst series, derived from the measured nitrogen physisorption isotherms using the BET method and the BJH plot, respectively.

Sample	Specific surface area / $m^2 g^{-1}$	Average pore diameter / nm	Pore volume / $cm^3 g^{-1}$
$Fe_{0.25}Co_{0.75}$@C	170	10	0.324
$Fe_{0.33}Co_{0.67}$@C	255	14	0.392
$Fe_{0.50}Co_{0.50}$@C	315	13	0.625
$Fe_{0.67}Co_{0.33}$@C	190	12	0.410
$Fe_{0.75}Co_{0.25}$@C	260	14	0.531
$Fe_{0.80}Co_{0.20}$@C	260	17	0.674

One of the most important properties of MOFMS materials is the oxidation preventing effect of the carbon shell, which was discussed several times up to this point. Despite the oxidation prevention the CO_2-FTS process is still catalyzed by the encapsulated metal nanoparticles (cf. Chapter 3.1.3 and 3.2.3). To understand this unique property, temperature-programmed reduction measurements were performed with both the fresh synthesized catalysts and the spent catalysts after the catalytic testing (Figure 27). Although the PXRD measurements display only reduced metal phases, all Fe_xCo_{1-x}@C catalysts exhibit a small peak of H_2 consumption between 250 °C and 425 °C. This peak which is observed for all fresh and spent catalysts of the series seems to be the key to the protective properties of the MOFMS catalysts. To further investigate its origin, χ-Fe_5C_2@C and Fe_3O_4 reference samples were measured under the same TPR conditions (grey and black). The iron oxide exhibits a two peak pattern above 400 °C, which matches the literature.[161] The iron carbide reference on the other hand displays a characteristic peak at 200 °C and a broader peak between 250 °C and 400 °C. These peaks can be assigned to the reduction from χ-Fe_5C_2 to Fe_3C, followed by the further reduction of Fe_3C to reduced Fe.

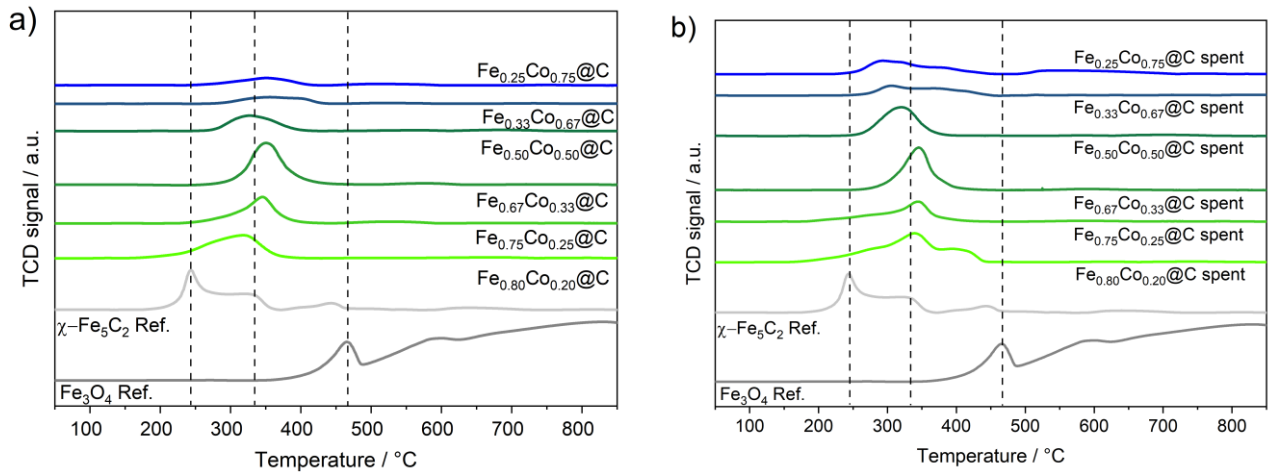

Figure 27: TPR measurements of the Fe_xCo_{1-x}@C catalyst series before (a) and after (b) the catalytic testing.

Hence, a formation of a thin Fe_3C carbide layer around the active metal particles during the MOFMS procedure is assumed. The generation of the thin layer is encouraged by the close proximity of metal and carbon. The carbidic layer should form only at high temperatures above 600 °C. This would explain the high resistance of Fe@C_800°C and the Fe/Co-containing catalysts (generated at 800 °C) against oxidation and the poor protection against oxidation displayed by Fe@C_400°C and Fe@C_600°C. This assumption is further supported by the peak position in the TPR measurements, which show mainly H_2 consumption at temperatures between 270 °C and 400 °C. The measured references (Figure 27) display a reduction of iron oxide above 400 °C which is significantly higher than for the MOFMS catalysts. However, χ-Fe_5C_2 exhibits a two-step reduction in this temperature range with the first peak at under 250 °C and a second broader peak between 250 °C and 350 °C. In the first reduction step χ-Fe_5C_2 is reduced to Fe_3C and in the second step, which matches the peak position found in the MOFMS catalyst series, the Fe_3C carbide is further reduced to Fe. Hence, the H_2 consumptions peak observed by the Fe/Co-containing catalysts can be explained by the presence of a thin protective layer of Fe_3C.

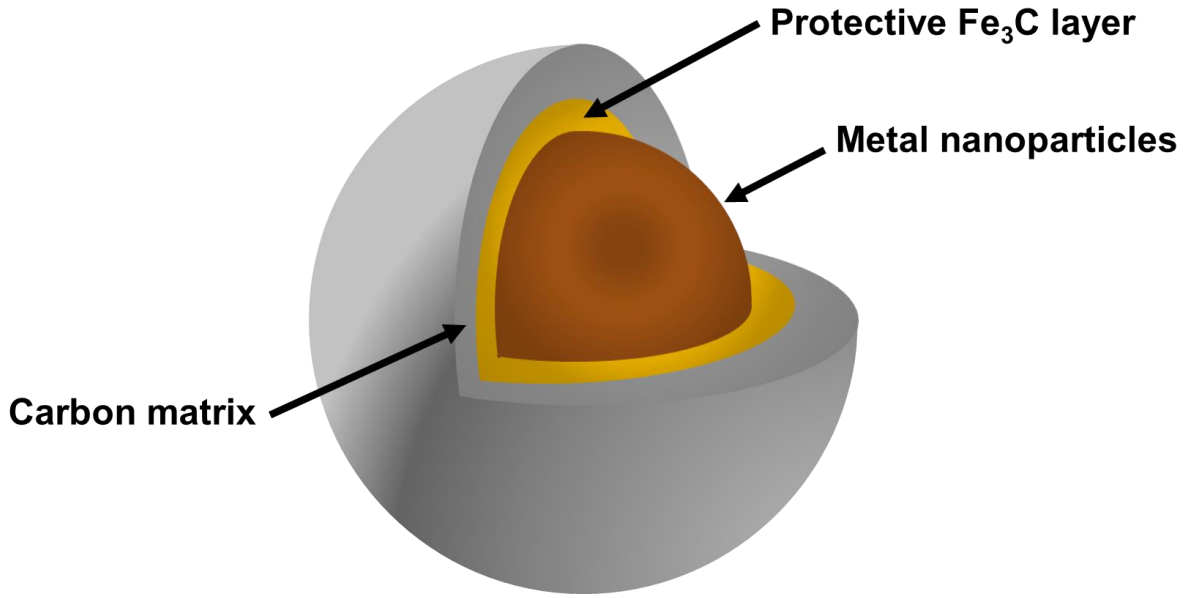

Figure 28: Model of the MOFMS catalysts with reduced metal nanoparticles embedded into a carbon matrix and protected by a thin iron carbide layer.

Figure 28 displays a schematic representation of the MOFMS-derived catalysts. The formation of a carbide layer would not only explain the oxidation preventing properties of the material, but also match to the previously shown results of the catalyst characterization. Due to the small thickness of the carbide layer compared to the metal particles the phase is hard to detect for other methods than TPR. Furthermore, the thin layer would explain the catalytic activity despite the oxidation protection. As shown by the PXRD and crystallite size measurements of the spent catalysts, the metal nanoparticles experience an *in situ* phase transition during the CO_2-FTS process without a destruction of the carbon matrix. Nevertheless, it is still unclear how the regeneration of the carbidic monolayer occurs after the CO_2-FTS process.

3.2.3 Catalytic testing of bimetallic Fe/Co MOFMS catalysts

The fully characterized Fe/Co containing bimetallic MOFMS catalysts were granulated to a particle size of 250 – 355 µm and tested for their respective CO_2-FTS activity in different experiments. Analogous to the catalytic testing of the monometallic Fe-based MOFMS catalyst series, the first step of the catalytic testing for the bimetallic series was a CO_2 conversion measurement during a time-on-stream period of 12 h (Figure 29 a). $Fe_{0.25}Co_{0.75}$@C displays the highest CO_2 conversion with around 27 % for each measured point. Contrary, $Fe_{0.33}Co_{0.67}$@C shows a

relatively low CO_2 conversion of only 8-12 %. Surprisingly, the conversion constantly increases during the tested time period. A further decrease of the Co content leads to a significant decrease of CO_2 conversion with $Fe_{0.50}Co_{0.50}$@C showing the lowest measured CO_2-conversions with around 1 %. However, the MOF precursor for this catalyst displayed the lowest measured crystallinity (cf. Figure 20), which could be linked to an inhomogeneous distribution of Fe and Co centers within the MOF. The resulting separation of Fe and Co sites within the catalysts would explain this observation and match the observations found in the literature, whereby a close contact between both metals is necessary to achieve FTS activity.[66] The measured CO_2 conversion increases again for catalysts with higher Fe content, hence $Fe_{0.67}Co_{0.33}$@C and $Fe_{0.75}Co_{0.25}$@C show a constant CO_2 conversion of 11 % and 23 %, respectively. $Fe_{0.80}Co_{0.20}$@C with the largest amount of Fe exhibits a stepwise conversion increase after 5 h time-on-stream with an initial rate of 13 %, which increases to about 25 %. It is to assume that the unconventional conversion curve is linked to structural changes to the catalyst during the testing due to the *in situ* formation of the χ-Fe_5C_2 phase (Figure 23 b). The high amount of Fe and the close proximity of metal and carbon may lead to an excessive carbide formation after 5 h time-on-stream, which would explain the steep increase in CO_2 conversion due to the high FTS activity of χ-Fe_5C_2.[45,97,162]

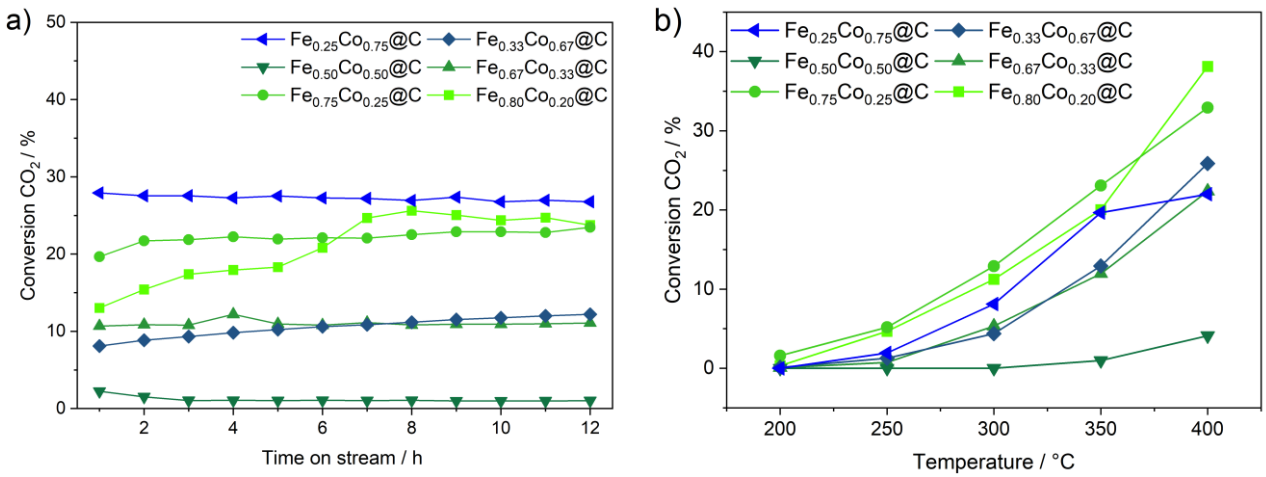

Figure 29: CO_2 conversion measurements of the Fe_xCo_{1-x}@C catalysts (500 mg) for a TOS of 12 h at 350 °C and 20 bar with a total flow of 25 mL/min (3:1 H_2:CO_2) (a) and temperature-dependent CO_2 conversion measurements of the Fe_xCo_{1-x}@C catalysts (500 mg) at 350 °C and 20 bar with a total flow of 25 mL/min (H_2/CO_2 = 3:1) (b).

Afterwards, the catalyst series was screened regarding the temperature-dependent CO_2 conversion in the range between 200 °C and 400 °C to include LTFT as well as HTFT conditions (Figure 29 b). Trends for the temperature-dependent CO_2 conversions are similar for all catalysts of the series with nearly no conversion at 200 °C and an increase in CO_2 conversion at higher reaction temperatures as expected. Independent of the reaction temperature, the catalyst series displays the same trend observed during the time-on-stream experiment: Hence, the two catalysts with the highest Fe content and the two catalysts with the highest Co content exhibit comparatively high CO_2 conversions at each temperature, while the two catalysts with a more balanced Fe/Co ratio show relatively low CO_2 conversions. The highest CO_2 conversion at 350 °C is obtained for $Fe_{0.75}Co_{0.25}$@C with 23.1 % and at 400 °C with 38.2 % for $Fe_{0.80}Co_{0.20}$@C. Those two reaction temperatures exhibited also the best FTS activity for the monometallic Fe@C_800°C. Compared to the Fe-rich bimetallic catalysts, Fe@C_800°C displayed a higher CO_2 conversion at 350 °C (29.1 %) and a slightly lower conversion at 400 °C (36.4 %). During the temperature dependent measurements, the yields of the respective C-fractions were also measured and the resulting temperature-dependent product distribution for each bimetallic catalyst is illustrated in Figure 30. Using the yields of the C-fractions, the temperature-dependent selectivities towards CO, CH_4, C_{2+} and C_{5+} formation were calculated analog to the monometallic catalyst series (Table 13).

The measured product yield fractions of the two most Co-rich catalysts, $Fe_{0.25}Co_{0.75}$@C and $Fe_{0.33}Co_{0.67}$@C (Figure 30 a and b), display a large methane fraction and only minor fractions of higher hydrocarbons up to a chain length of C_4. Except for the highest tested reaction temperature, $Fe_{0.33}Co_{0.67}$@C shows at all temperature steps a lower conversion than $Fe_{0.25}Co_{0.75}$@C. Surprisingly, the C_{2+} selectivity at higher reaction temperatures is also lower for $Fe_{0.33}Co_{0.67}$@C (Table 13). $Fe_{0.33}Co_{0.67}$@C also shows the highest CO production of all tested bimetallic catalysts, regarding both yield and selectivity. The comparatively high selectivity towards the C_1 fraction was expected for the Co-rich catalysts and matches the literature. Despite the addition of some rWGS active Fe, the CO concentration seems still too low at the active Co site. Combined with the strong CO adsorption at the Co sites, the chain growth is inhibited and the methane formation enhanced.[54,163]

Similarly to the time-on-stream results, the bimetallic catalyst with the 1:1 ratio shows the lowest CO_2 conversion at any reaction temperature and also the lowest FTS activity, with only minor CO and methane amount at high reaction temperatures (Figure 30 c). Despite the increased Fe content, methane is still the main product generated by $Fe_{0.67}Co_{0.33}$@C, even at the higher reaction temperatures of 350 °C and 400 °C the catalyst generates only minor C_{2+} fractions at relatively low CO_2 conversion rates (Figure 30 d). The high methane yields at the higher reaction temperature indicate that the Co content is still too high, thus, lowering the selectivity towards longer hydrocarbon chains.

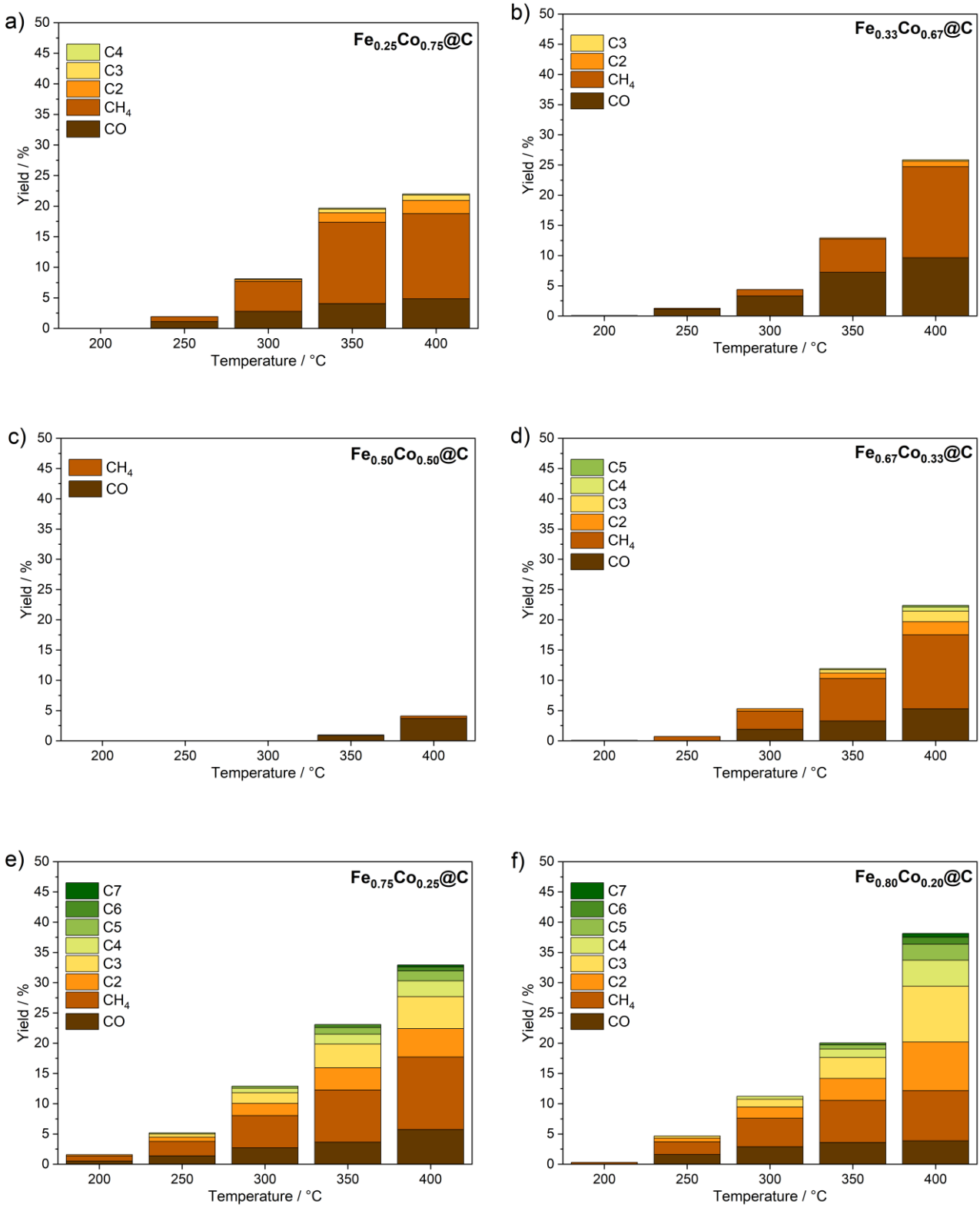

Figure 30: Temperature-dependent yield distribution for the catalysts $Fe_{0.25}Co_{0.75}$@C (a), $Fe_{0.33}Co_{0.67}$@C (b), $Fe_{0.50}Co_{0.50}$@C (c), $Fe_{0.67}Co_{0.33}$@C (d), $Fe_{0.75}Co_{0.25}$@C (e) and $Fe_{0.80}Co_{0.20}$@C (f) measured at 20 bar with a total flow of 25 mL/min (H_2/CO_2 = 3:1).

The highest conversion at all measured reaction temperatures is displayed by the Fe-rich MOFMS catalysts $Fe_{0.75}Co_{0.25}$@C and $Fe_{0.80}Co_{0.20}$@C. Additionally, both catalysts generate the longest hydrocarbon chains within the tested series, with a chain length up to C_7 (Figure 30 e and f). Both catalysts start to show FTS activity at reaction temperatures above 250 °C. The systems start to generate longer hydrocarbon chains above 350 °C and at the highest tested reaction temperature of 400 °C the CO_2 conversion with $Fe_{0.80}Co_{0.20}$@C is significantly higher than with $Fe_{0.75}Co_{0.25}$@C. Both catalysts exhibit an overall increased selectivity towards higher hydrocarbon fractions and simultaneously a decreased selectivity towards methane. The highest C_{2+} selectivity is shown by $Fe_{0.80}Co_{0.20}$@C with 68.2 % at 400 °C and a methane selectivity of 21.8 %. Similarly, the highest C_{5+} selectivity is also shown by the χ-Fe_5C_2-containing catalyst $Fe_{0.80}Co_{0.20}$@C with 11.6 % at 400 °C (Table 13). The selectivity toward methane is particularly lower for these two catalysts compared to the other tested systems of the series. The observed results match the study of Satthawong *et al*., who tested different Fe/Co ratios of conventional supported bimetallic CO_2-FTS catalysts. The group observed a maximum for the C_2-C_7 generation at 20 % Co. At this metal ratio, the yield and selectivity towards FTS products exceeded even monometallic Fe-based reference catalysts.[65] However, compared to the previously shown catalytic testing results of the most FTS-active catalyst (Fe@C_800°C), $Fe_{0.80}Co_{0.20}$@C only shows a higher CO_2 conversion and higher selectivities towards C_{2+} and C_{5+} generation at the highest reaction temperature of 400 °C.

Table 13: Temperature-dependent selectivity towards CO, CH_4, C_{2+} fractions and C_{5+} fractions for $Fe_{0.67}Co_{0.33}$@C, $Fe_{0.75}Co_{0.25}$@C and $Fe_{0.80}Co_{0.20}$@C calculated from the yields of the temperature-dependent experiments.

Sample	Temperature	X_{CO_2}	S_{CO}	S_{CH_4}	$S_{C_{2+}}$	$S_{C_{5+}}$
$Fe_{0.25}Co_{0.75}$@C	200 °C	0.0	0.0	0.0	0.0	0.0
	250 °C	1.9	58.0	42.0	0.0	0.0
	300 °C	8.1	34.3	60.4	5.3	0.0
	350 °C	19.7	20.6	67.6	11.8	0.0

	400 °C	22.0	22.1	63.3	14.7	0.0
$Fe_{0.33}Co_{0.67}$@C	200 °C	0.1	91.9	8.1	0.0	0.0
	250 °C	1.3	85.9	14.1	0.0	0.0
	300 °C	4.4	75.5	24.5	0.0	0.0
	350 °C	12.9	56.0	42.5	1.5	0.0
	400 °C	25.9	37.2	58.3	4.5	0.0
$Fe_{0.50}Co_{0.50}$@C	200 °C	0.0	0.0	0.0	0.0	0.0
	250 °C	0.0	0.0	0.0	0.0	0.0
	300 °C	0.0	0.0	0.0	0.0	0.0
	350 °C	1.0	91.6	8.4	0.0	0.0
	400 °C	4.1	90.1	9.9	0.0	0.0
$Fe_{0.67}Co_{0.33}$@C	200 °C	0.1	0.0	100.0	0.0	0.0
	250 °C	0.7	0.0	100.0	0.0	0.0
	300 °C	5.3	35.7	57.0	7.3	0.0
	350 °C	12.0	27.3	58.9	13.8	0.0
	400 °C	22.4	23.6	54.6	21.8	1.3
$Fe_{0.75}Co_{0.25}$@C	200 °C	1.6	32.6	52.4	15.0	0.0
	250 °C	5.2	26.8	46.1	27.2	0.0
	300 °C	12.9	21.0	41.3	37.7	2.7
	350 °C	23.1	15.7	37.3	47.0	6.9
	400 °C	33.0	17.3	36.3	46.3	8.0

	200 °C	0.3	0.0	100.0	0.0	0.0
	250 °C	4.7	34.5	44.6	21.0	0.0
$Fe_{0.80}Co_{0.20}$@C	300 °C	11.7	24.5	40.0	31.2	0.0
	350 °C	20.1	17.9	34.6	47.4	5.0
	400 °C	38.2	10.1	21.8	68.2	11.6

Additionally to the yields of the C-fraction, the yield of ethane/ethylene and propane/propylene were measured to investigate the selectivity towards alkanes or olefins during the CO_2-FTS process. The temperature-dependent yields are displayed in Figure 31 for the three most FTS active catalysts ($Fe_{0.67}Co_{0.33}$@C, $Fe_{0.75}Co_{0.25}$@C and $Fe_{0.80}Co_{0.20}$@C). The Co-richest catalyst $Fe_{0.67}Co_{0.33}$@C displays only a minor olefin formation at all tested reaction temperatures. At the highest tested temperature, the generated yields of ethylene and propylene are only 0.1 % and 0.3 %, respectively. For the two catalysts with higher Fe contents ($Fe_{0.75}Co_{0.25}$@C and $Fe_{0.80}Co_{0.20}$@C) the main C_2 and C_3 product fractions are still alkanes. However, at reaction temperatures over 300 °C both catalysts start to generate significant amounts of olefins. For both catalysts propylene is produced with higher yields with a propylene yield of 3.0 % and an ethylene yield of 0.2 % for $Fe_{0.80}Co_{0.20}$@C at 400 °C and a propylene yield of 1.5 % and an ethylene yield of 0.5 % for $Fe_{0.75}Co_{0.25}$@C at 400 °C. The selectivity towards propylene is higher than for ethylene for both catalysts, similar to the observations for the Fe-based MOFMS catalysts (cf. Chapter 3.1.3). The poor selectivity towards olefins was expected due to the unpromoted nature of the tested bimetallic MOFMS catalysts. To shift the selectivity towards light olefine fractions, usually alkali promoters like K or Na are added to the catalysts.[88] Therefore, the next chapter will focus on the optimization of the MOFMS catalysts *via* the addition of promoter materials.

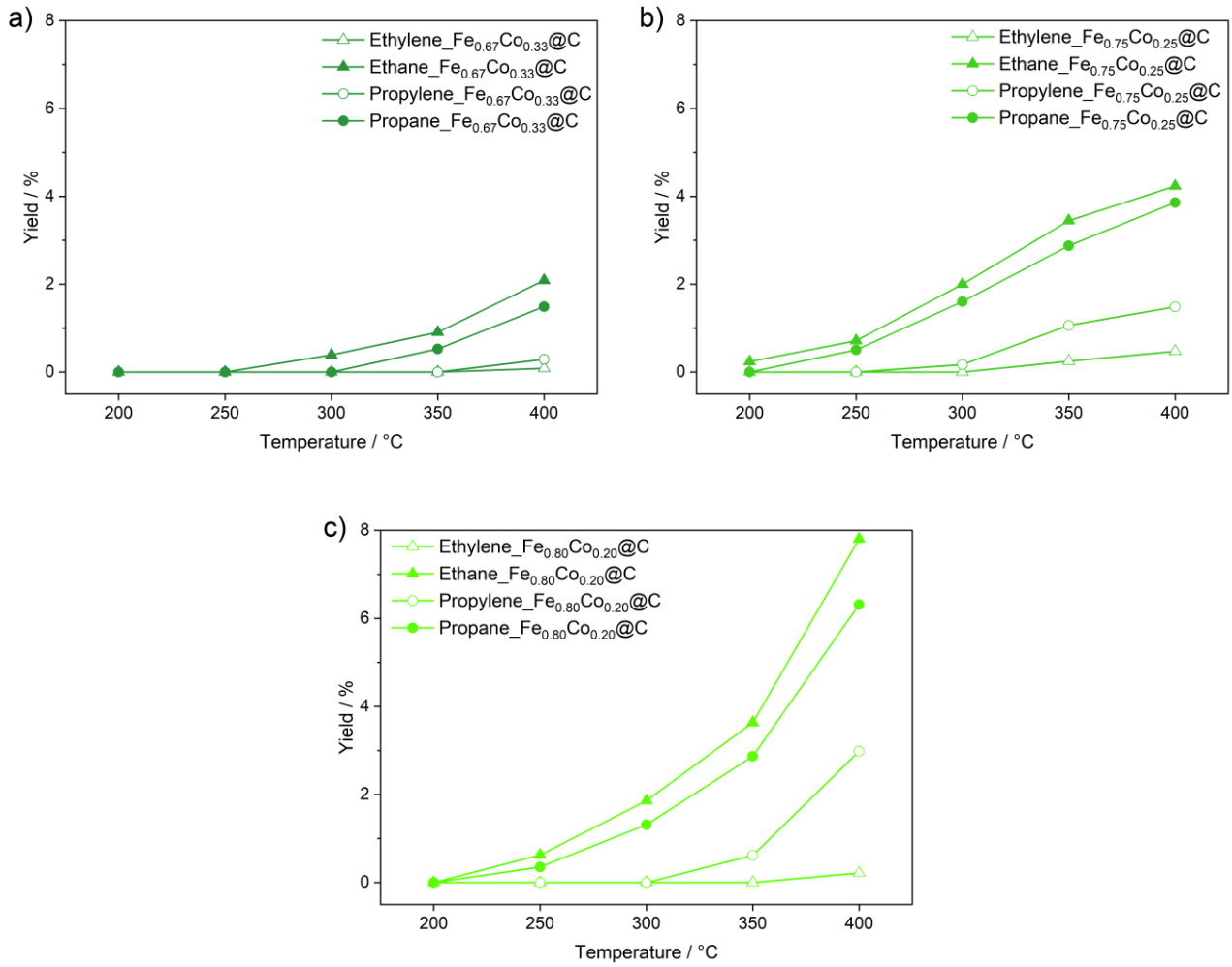

Figure 31: Temperature-dependent yields for alkanes (C_2 and C_3) and olefines (C_2 and C_3) for $Fe_{0.67}Co_{0.33}$@C (a), $Fe_{0.75}Co_{0.25}$@C (b) and $Fe_{0.80}Co_{0.20}$@C (c). Measured at 20 bar with a total flow of 25 mL/min (H_2/CO_2 = 3:1).

3.3 Multicomponent MOFMS CO_2-FTS catalysts

3.3.1 Synthesis and characterization of multicomponent MOF precursor

The previous results of the monometallic MOFMS catalysts showed, that high decomposition temperatures of 800 °C are beneficial for the generation of a protective carbon matrix and the enhancement of carbide phase formation. The bimetallic MOFMS catalyst series with additional cobalt displayed an increased stability under CO_2-FTS conditions. Hence, the beneficial properties of the carbon matrix were also observed for the spent catalysts after the time-on-stream experiment in the CO_2-FTS setup. However, high amounts of cobalt had a negative

impact on the performance during the CO_2-FTS testing, as the CO_2 conversion decreased and the product selectivity shifted heavily towards methane. The overall best performing catalysts from both tested catalyst series were monometallic Fe@C_800°C and the two bimetallic catalysts with the highest Fe content ($Fe_{0.75}Co_{0.25}$@C and $Fe_{0.80}Co_{0.20}$@C). Despite the comparatively high CO_2 conversion and high selectivity towards FTS product formation, all three catalysts feature relatively high methane yields and only minor selectivity towards olefines. To further enhance the positive properties of the three best catalysts and to simultaneously decrease the negative traits, different promoters have been added and are investigated in this chapter. The alkali metal potassium and the two transition metals copper and manganese were chosen as promoters. According to the literature, the addition of potassium to CO_2-FTS catalysts exhibited exceptional improvements in terms of the CO_2 adsorption, the generation and stabilization of χ-Fe_5C_2 and the increase in light olefine formation.[87,90] The addition of copper as CO_2-FTS promoter is known to enhance the reduction of iron oxide and to hinder sintering as well as causing a shift of the product selectivities towards longer hydrocarbon fractions.[97,98] The promoting effect of manganese is explained by an increased iron reduction as well as an inherent rWGS-catalyzing effect. Furthermore, Mn as CO_2-FTS promoter is known to shift the product selectivity from long hydrocarbon fractions towards light olefin fractions.[103,104] The synthesis approach to generate the promoted materials was similar to the previously discussed approaches. The MOF-based precursors were synthesized in a two-step approach. In a first step MIL-53(Fe) was generated *via* the solvothermal synthesis approach known from literature.[137] Afterwards, the respective promoter components were incorporated into the pore structure of the framework *via* incipient wetness impregnation. For the Fe/Co-containing MOF precursor, cobalt was added alongside the promoter to the incipient wetness impregnation process (cf. Chapter 3.2.1). The reaction scheme is illustrated in Scheme 7 for Fe@C-$Y_{0.20}$ and in Scheme 8 for $Fe_{0.75}Co_{0.25}$@C-$Y_{0.20}$ and $Fe_{0.80}Co_{0.20}$@C-$Y_{0.20}$.

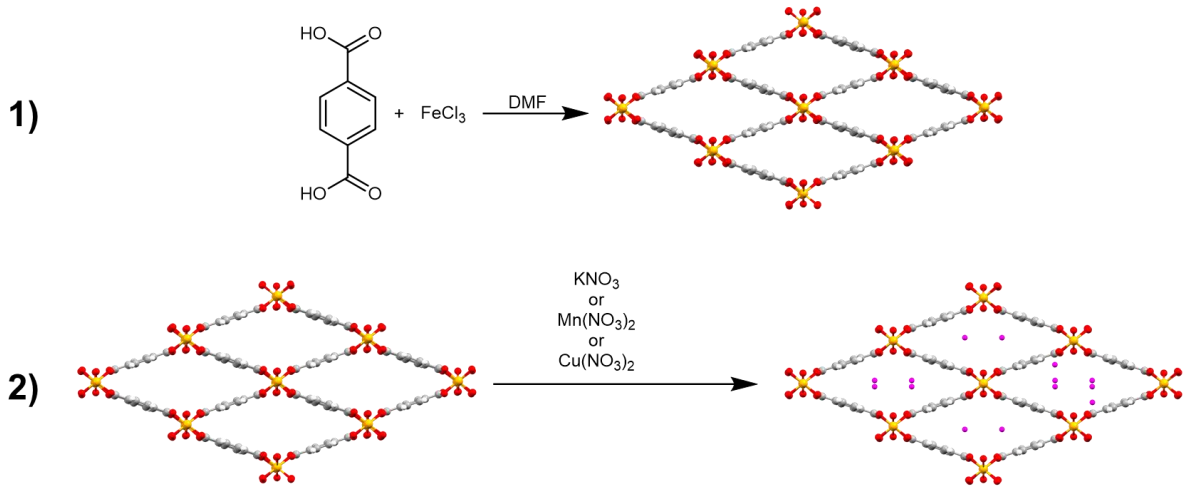

Scheme 7: Reaction scheme of the two-step synthesis approach used for the generation of MIL-53(Fe)-$Y_{0.20}$ precursor materials consisting of the synthesis of MIL-53(Fe) (1) followed by an incipient wetness impregnation of the promoter (2).

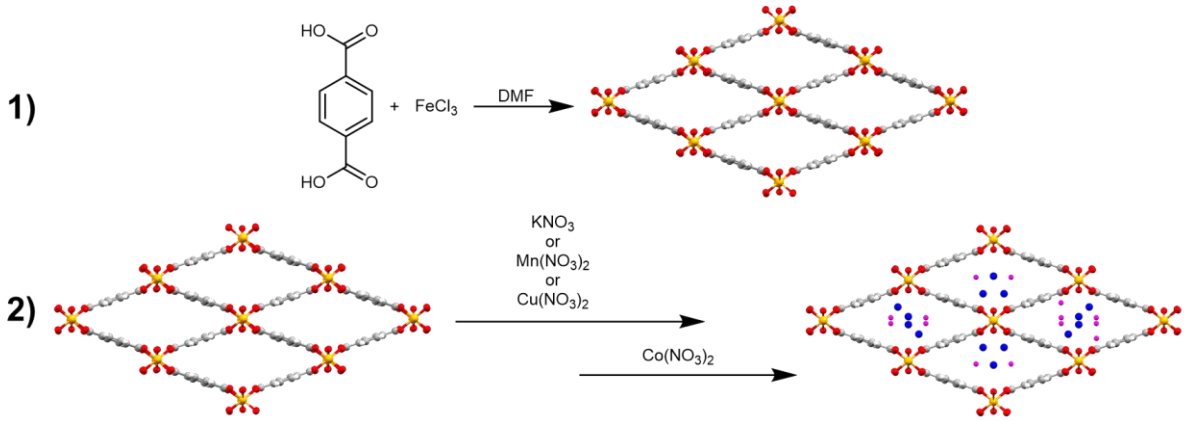

Scheme 8: Reaction scheme of the two-step synthesis approach used for the generation of MIL-53(Fe_xCo_{1-x})-$Y_{0.20}$ precursor materials consisting of the synthesis of MIL-53(Fe) (1) followed by an incipient wetness impregnation of the promoter and Co (2).

After the synthesis, each MOF precursor was analyzed using a combination of different characterization techniques. After the first synthesis step, PXRD patterns were measured to monitor structural changes to the flexible framework of MIL-53(Fe) before and after the impregnation process (Figure 32). The MOF structure shows a closed pore geometry with characteristic reflections at 2θ = 9.2 °, 12.7 °, 17.6 °, 18.5 ° and 25.5 °. These results match the observation of the MIL-53(Fe) precursor

for the monometallic MOFMS series (cf. Chapter 3.1.1). After the impregnation process, the MOF structure changes for all materials to a geometry similar to MIL-53(Co).[138] This structural variant contains pyridine-*N*-oxide within the pores to compensate the charge and therefore the pores are forced into an open geometry. Particularly the reflection at 2θ = 21.9 ° features an increased intensity for all loaded MOF precursors. This reflection corresponds to the (hkl) plane (220) running diagonal through the MOF pore. The enhanced intensity of the reflection is caused by the incorporated metal species, thus, the reflection is also more pronounced for the precursors loaded with Mn and Cu compared to the K loaded precursors. This effect was also observed for the bimetallic MOF precursors, which were synthesized *via* incipient wetness impregnation (cf. Chapter 3.2.1).

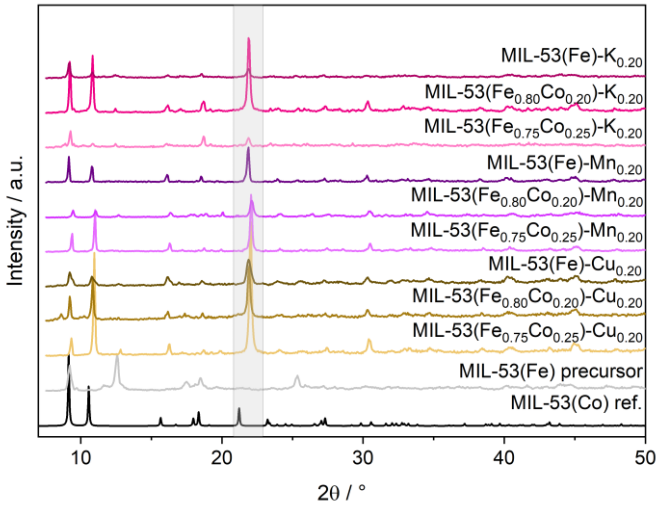

Figure 32: PXRD patterns of the MIL-53(Fe_xCo_{1-x})-$Y_{0.20}$ presursor series with MIL-53(Fe) in closed pore form and MIL-53(Co) in open pore form.

To investigate the purity of the precursor materials, ATR-IR spectroscopy was used (Figure 33). Possible impurities from the synthesis process are residual solvent (*N,N*-dimethylformamide) or free terephthalic acid linker molecules, which both show a characteristic IR-band at 1665 cm^{-1}. Only the characteristic band of *N,N*-dimethylformamide can be found in the spectra at very low intensity, therefore a successful synthesis of the MOF precursor materials in phase-pure form can be assumed. All MOF precursor materials show very similar IR spectra, with the exception of MIL-53($Fe_{0.75}Co_{0.25}$)-$Cu_{0.20}$, which shows a broad absorption band at 3260 cm^{-1}. This band and the overall broadness of the other bands indicate that the material is not fully dried. Since the linker molecules are mostly incorporated into the

framework structure, intense symmetric and asymmetric stretching vibrations of C-O at 1385 cm^{-1} and 1240 cm^{-1} are found in all measured spectra. Another characteristic band is the absorption band at 855 cm^{-1}, which is generated by the δ(OH) modes of the bridging hydroxyl group (Fe−O(H)−Fe) and the C-H bending vibration of the benzene ring of the terephthalic acid is displayed at 750 cm^{-1}.[157,160]

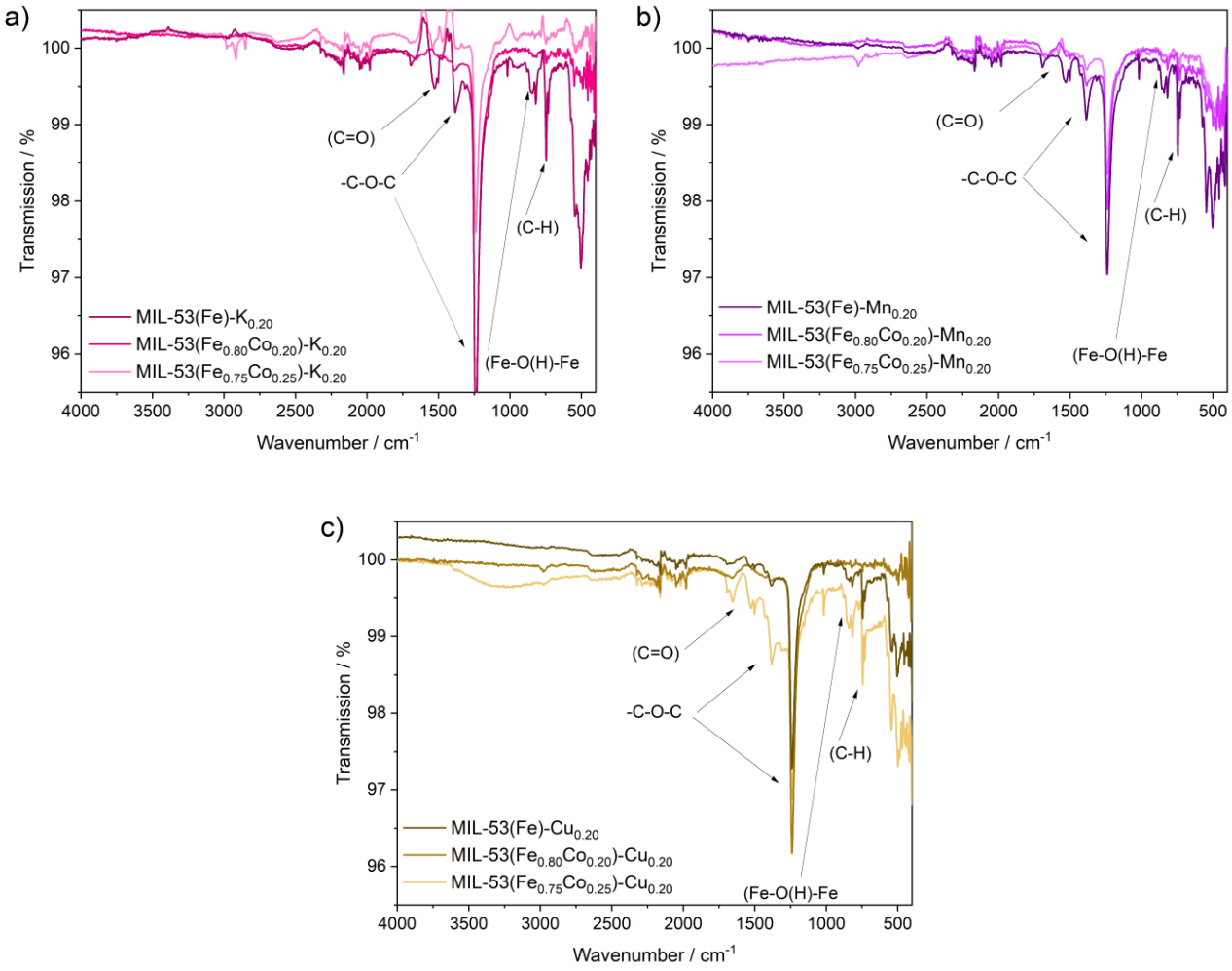

Figure 33: ATR-IR spectra of the MIL-53(Fe_xCo_{1-x})-$Y_{0.20}$ presursor materials containing K (a), Mn (b) and Cu (c) as promoters.

Furthermore, ICP-OES measurements were performed to confirm the metal ratios within the precursor materials. The measured metal ratio of Fe/Co matches the theoretical value with only small deviations for each precursor material respectively. Due to the synthesis *via* incipient wetness impregnation, these results were expected. The overall content of the three FTS active components incorporated in the framework is between 25.7 wt% for MIL-53($Fe_{0.75}Co_{0.25}$)-$Mn_{0.20}$ and 21.1 wt% for MIL-53($Fe_{0.80}Co_{0.20}$)-$K_{0.20}$ (Table 14).

Table 14: ICP-OES measurement results for the MIL-53(Fe_xCo_{1-x})-$Y_{0.20}$ presursor materials.

Sample	Ratio Fe/Co	Total metal loading / wt%
MIL-53(Fe)-$K_{0.20}$	-	24.4
MIL-53($Fe_{0.80}Co_{0.20}$)-$K_{0.20}$	78:22	22.5
MIL-53($Fe_{0.75}Co_{0.25}$)-$K_{0.20}$	71:29	21.1
MIL-53(Fe)-$Mn_{0.20}$	-	23.3
MIL-53($Fe_{0.80}Co_{0.20}$)-$Mn_{0.20}$	79:21	23.6
MIL-53($Fe_{0.75}Co_{0.25}$)-$Mn_{0.20}$	73:27	25.7
MIL-53(Fe)-$Cu_{0.20}$	-	23.5
MIL-53($Fe_{0.80}Co_{0.20}$)-$Cu_{0.20}$	77:23	20.2
MIL-53($Fe_{0.75}Co_{0.25}$)-$Cu_{0.20}$	74:26	23.2

To generate the MOFMS catalysts in the next chapter, the thermal stability of the MOF precursor materials was investigated under nitrogen atmosphere (Figure 34). The thermal decomposition for the K-containing materials shows a stepwise decomposition. The first step for all catalysts is the evaporation of physisorbed water at about 100 °C, followed by the decomposition of the incorporated nitrate, which is known to decompose in several steps mainly at around 200 °C.[164] The main weight loss occurs between 200 °C and 550 °C due to the decomposition of the organic parts in the K-containing MOF precursors. The $Fe_{0.75}Co_{0.25}$@C-$K_{0.20}$ catalyst displays the lowest thermal stability with a decomposition step at 225 °C and three close weight loss steps between 350 °C and 460 °C. A similar DTG curve is shown by $Fe_{0.80}Co_{0.20}$@C-$K_{0.20}$ with an identical weight loss at 225 °C and two weight loss steps shifted to slightly higher temperatures of 440 °C and 550 °C. The highest thermal stability is displayed by Fe@C-$K_{0.20}$ with various weight loss steps between 330 °C and 500 °C and an intense weight loss at 650 °C. The stepwise decomposition of the

precursor material is caused by the decomposition of the linker (terephthalic acid), which showed also a stepwise decomposition in the previously shown TGA results (cf. Figure 10 and Figure 22). The unpromoted catalysts displayed additional weight loss at about 650 °C, which was presumably linked to the formation of Fe_3C carbide phase. This step is shifted for the Fe/Co-containing K-promoted materials to lower temperatures of under 600 °C. A possible explanation would be the enhancing effect on the carbide phase formation, which is known for K-promoted materials under high temperature environments and with excess to a carbon source. However, more research is needed to assign the weight loss displayed by the K-containing catalysts completely. A similar stepwise weight loss caused by the thermal decomposition of the MOF precursors is displayed by the Mn- and Cu-containing materials. Unlike the K-containing precursor materials, both the Mn and Cu series show matching weight loss steps for all three catalysts, respectively. The Mn series exhibits weight loss between 370 °C and 540 °C, which can be assigned to the decomposition of the organic MOF parts. Furthermore, the steps at 690 °C match the formation of Fe_3C phase as discussed in the previous chapters (cf. Chapter 3.1.1 and 3.2.1). The Cu series exhibits weight loss between 310 °C and 530 °C and around 680 °C, which again matches the thermal decomposition behavior of the other MOF precursor materials. Hence, the K-containing series displays the lowest thermal stability under nitrogen atmosphere with a complete decomposition of all precursor materials over 650 °C. The other two MOF precursor series display complete decomposition at temperatures above 700 °C. Previous results showed that a high thermal decomposition temperature and a complete decomposition of the MOF precursor under nitrogen atmosphere is beneficial for the resulting catalyst system. Therefore, all MOFMS catalysts were synthesized at a temperature of 800 °C to ensure a complete decomposition process.

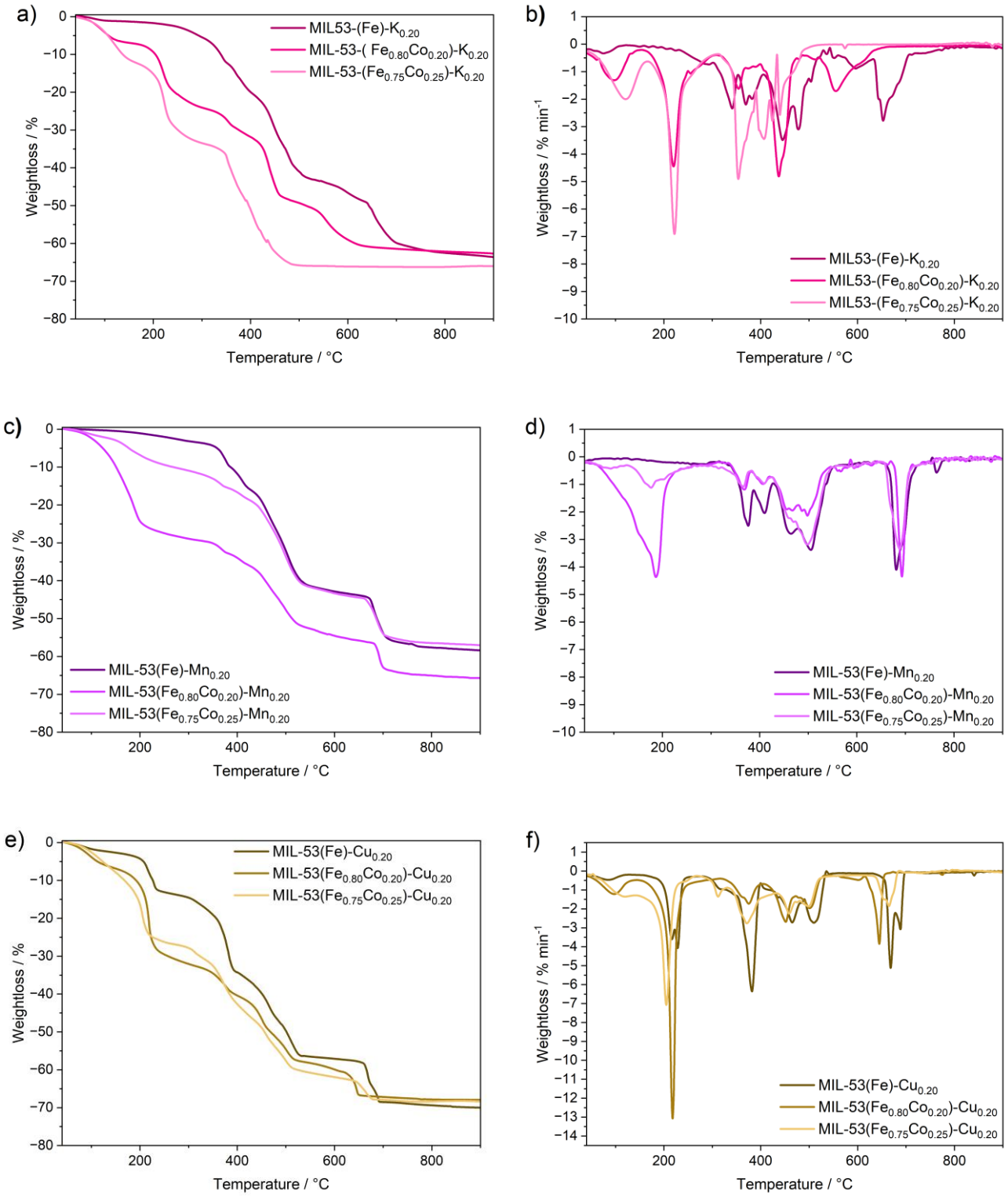

Figure 34: TGA (a, c and e) and DTG (b, d and f) measurements of the MIL-53(Fe_xCo_{1-x})-$Y_{0.20}$ presursor materials containing K (a and b), Mn (c and d) and Cu (e and f).

Additionally, the specific surface areas of the precursor materials were determined from the nitrogen physisorption isotherms *via* the BET method (Appendix Figure A 5). The specific surface areas of the materials are comparatively small, particularly for

MOFs. Due to the used incipient wetness impregnation synthesis method of the precursors, the pores are blocked by Co and the respective third component. The K-containing materials show especially low specific surface area values below 6 $m^2\ g^{-1}$, the other materials exhibit values of around 30-50 $m^2\ g^{-1}$ (Table 15).

Table 15: Specific surface areas of the MIL-53(Fe_xCo_{1-x})-$Y_{0.20}$ presursor materials derived from nitrogen physisorption isotherms using the BET method.

Sample	Specific surface area / $m^2\ g^{-1}$
MIL-53(Fe)-$K_{0.20}$	3
MIL-53($Fe_{0.80}Co_{0.20}$)-$K_{0.20}$	5
MIL-53($Fe_{0.75}Co_{0.25}$)-$K_{0.20}$	4
MIL-53(Fe)-$Mn_{0.20}$	13
MIL-53($Fe_{0.80}Co_{0.20}$)-$Mn_{0.20}$	79
MIL-53($Fe_{0.75}Co_{0.25}$)-$Mn_{0.20}$	54
MIL-53(Fe)-$Cu_{0.20}$	46
MIL-53($Fe_{0.80}Co_{0.20}$)-$Cu_{0.20}$	35
MIL-53($Fe_{0.75}Co_{0.25}$)-$Cu_{0.20}$	33

3.3.2 Synthesis and characterization of multicomponent MOFMS catalysts

The fully characterized MOF precursors were thermally decomposed at 800 °C for 2 h under an inert nitrogen atmosphere. These conditions were chosen, because of the TGA results of the MOF precursors and the fact that they also led to the most beneficial properties for the previously discussed unpromoted MOFMS catalysts. After the MOFMS procedure, the catalysts were fully characterized with a combination of different methods to analyze the properties of the new materials. To investigate possible structural changes during the catalytic testing under CO_2-FTS

conditions and to understand performance differences, the spent catalysts were analyzed again with several different techniques.

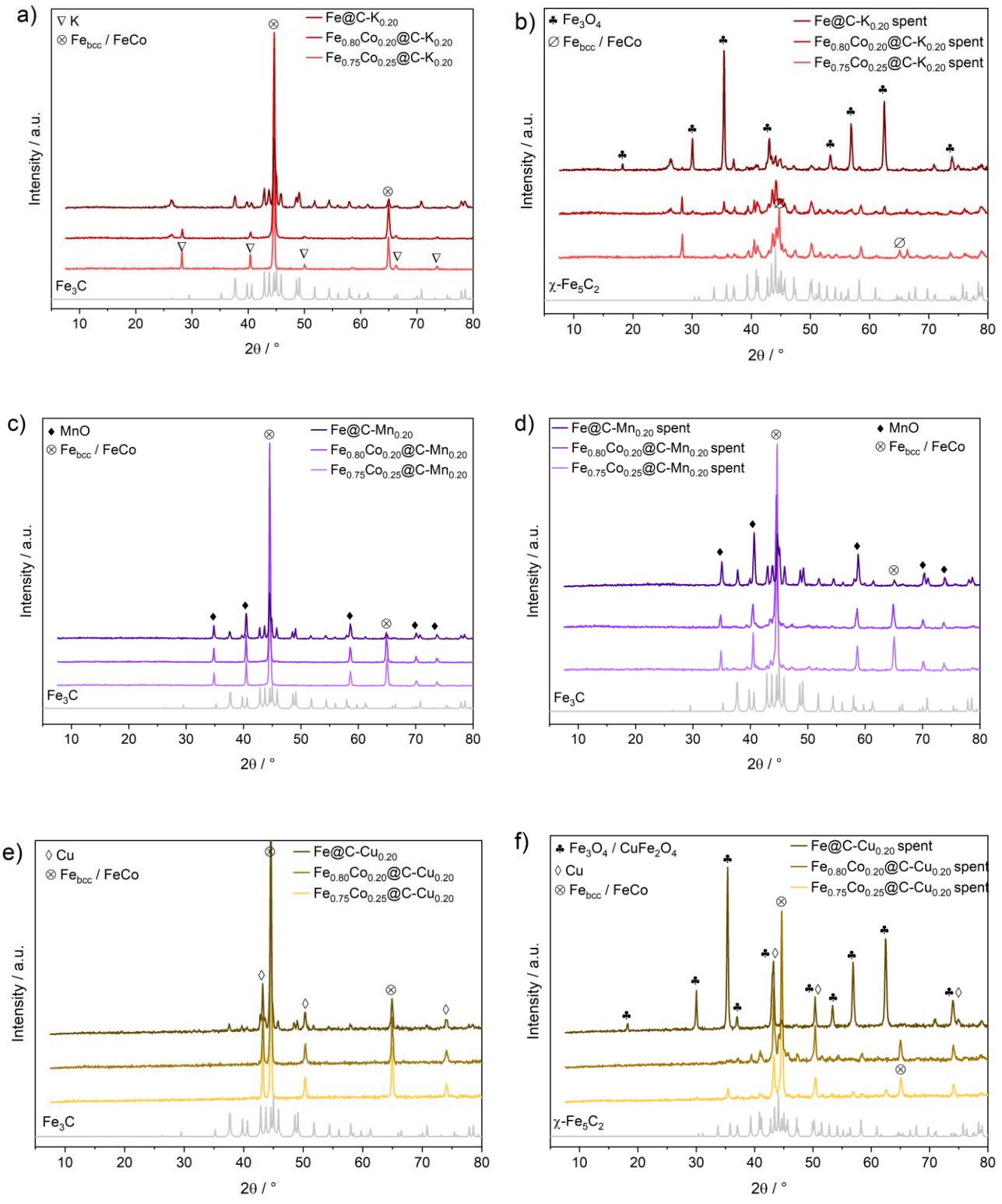

Figure 35: PXRD patterns of the Fe_xCo_{1-x}@C-$Y_{0.20}$ catalysts before and after the catalytic testing, with the promoters K (a and b), Mn (c and d) and Cu (e and f).

The structure of the catalysts was analyzed *via* PXRD measurements before and after the catalytic testing. Figure 35 a, c and e show the diffraction patterns of each material directly after the MOFMS process, Figure 35 b, d and f display the obtained diffraction patterns of the catalyst series after the catalytic testing to investigate occurring phase transitions during the FTS process. The MOFMS-generated catalysts series with K as promoter shows no residue of the structure of the precursor materials (cf. Figure 32). The obtained metal phases are all in a reduced or carbidic state, which was expected from the previous results of our studies and other research groups.[155,165] The bimetallic catalysts $Fe_{0.80}Co_{0.20}$@C-$K_{0.20}$ and $Fe_{0.75}Cu_{0.25}$@C-$K_{0.20}$ display only reduced Fe_{bcc} / FeCo phases, which both feature characteristic reflections at the 2θ = 44.6 ° and 64.9 ° positions. The monometallic Fe@C-$K_{0.20}$ catalyst exhibits a Fe_3C carbide phase additional to the main Fe_{bcc} phase (Figure 35 a). After the catalytic testing under FTS conditions all three materials show phases transitions. The main phase for the two catalysts containing Fe and Co is the highly FTS active χ-Fe_5C_2 phase, which is likely formed from the previously found and more stable Fe_3C phase.[97] This result matches the beneficial effect of K on the formation of χ-Fe_5C_2.[45,87] $Fe_{0.75}Co_{0.25}$@C-$K_{0.20}$ still displays a minor fraction of reduced $FeCo_{bcc,}$ while the diffraction pattern of $Fe_{0.80}Co_{0.20}$@C-$K_{0.20}$ shows only the newly acquired carbide phase. In contrast to the two Co-containing materials, Fe@C-$K_{0.20}$ features, additionally to the χ-Fe_5C_2 carbide phase, the characteristic reflections of the oxidized iron phase magnetite (Fe_3O_4). Due to the strong protection against oxidation of MOFMS materials, this leads to the assumption of a damaged carbon shell for this system after the CO_2-FTS. However, in contrast to the unpromoted Fe-catalyst (Fe@C_800°C), Fe@C-$K_{0.20}$ still displays the presence of a carbide phase, which is generally highly instable against oxidation. Thus, it can be assumed that the protective carbon shell was only partially damaged during the CO_2-FTS process.

The catalyst series with Mn as additional promoter component displays a similar trend. Therefore, no residues of the MOF structure are found in the diffraction patterns and the metal-containing phases show a fairly reduced state. The two Fe/Co-containing materials generate only reduced Fe and FeCo with a bcc structure. Fe@C-$Mn_{0.20}$ forms mainly Fe_{bcc} and the more stable Fe_3C carbide phase. Additionally, MnO is present in all three catalysts indicated by the characteristic reflections at 2θ = 34.8 °, 40.5 °, 58.7 °, 70.1 ° and 73.6 °. After the catalytic testing,

the catalysts show, in contradiction to the K-promoted series nearly no phase transitions. Fe@C-$Mn_{0.20}$ shows still the Fe_3C phase but no FTS active χ-Fe_5C_2 additional to Fe_{bcc}. The Fe/Co-containing catalysts display only reduced metal phases with MnO and low intensity reflections of carbide phase.

Following the trend, all three diffraction patterns of the catalysts with additional Cu promoter show mainly reduced Fe_{bcc} / FeCo phases and reduced Cu with the characteristic reflections at 2θ = 43.1 °, 50.3 ° and 74.1 °. Matching the previously discussed promoted catalysts, Fe@C-$Cu_{0.20}$ displays reflections of an additional Fe_3C phase with low intensity (Figure 35 e). After the catalytic testing, all three materials exhibit phase transitions during time-on-stream under FTS conditions. Fe@C-$Cu_{0.20}$ shows only Fe_3O_4 (magnetite) reflections in the diffraction pattern, hence, the protective carbon matrix was damaged during the catalytic testing similarly to Fe@C-$K_{0.20}$. Unlike in Fe@C-$K_{0.20}$, the iron within the spent Fe@C-$Cu_{0.20}$ catalyst is fully oxidized and no residual carbide phase is found in the pattern. Compared to the other Fe-based catalysts, it can be assumed that the addition of Co, Mn and K increases the stability of the MOFMS catalysts, while Cu displayed no beneficial influence on the stability against the harsh CO_2-FTS conditions. However, the carbon matrix of spent Fe@C-$K_{0.20}$ was at least partially damaged. $Fe_{0.80}Co_{0.20}$@C-$Cu_{0.20}$ displays still Fe_{bcc} / FeCo and Cu as main phases, although a small fraction of χ-Fe_5C_2 was formed under the FTS conditions similar to the K-promoted material. $Fe_{0.75}Co_{0.25}$@C-$Cu_{0.20}$ shows nearly no changes before and after the testing with only broad additional reflections (Figure 35 f). The Co-containing catalysts display higher resistance under the CO_2-FTS conditions as indicated by the presence of reduced metal phases after the catalytic testing. However, none of the Fe/Co-containing catalysts developed a carbide phase during the MOFMS process. The χ-Fe_5C_2 phase, which can be generated during the catalytic testing, was also a lot less intense for the Mn- and Cu-promoted catalysts compared to the Fe@C-$Mn_{0.20}$ and Fe@C-$Cu_{0.20}$ counterparts. Contrary to this, the spent $Fe_{0.80}Co_{0.20}$@C-$K_{0.20}$ and $Fe_{0.75}Co_{0.25}$@C-$K_{0.20}$ catalysts generated the highest amounts of carbide phase under the CO_2-FTS conditions.

Table 16: ICP-OES measurement results for Fe_xCo_{1-x}@C-$Y_{0.20}$ catalysts before and after the catalystic testing.

Sample	Ratio Fe/Co	Total metal loading fresh / wt%	Total metal loading spent / wt%
Fe@C-$K_{0.20}$	-	53.7	34.4
$Fe_{0.80}Co_{0.20}$@C-$K_{0.20}$	78:22	59.4	43.4
$Fe_{0.75}Co_{0.25}$@C-$K_{0.20}$	71:29	59.3	42.5
Fe@C-$Mn_{0.20}$	-	51.9	45.7
$Fe_{0.80}Co_{0.20}$@C-$Mn_{0.20}$	78:22	64.2	62.9
$Fe_{0.75}Co_{0.25}$@C-$Mn_{0.20}$	73:27	60.8	59.1
Fe@C-$Cu_{0.20}$	-	56.7	31.1
$Fe_{0.80}Co_{0.20}$@C-$Cu_{0.20}$	79:21	63.2	31.8
$Fe_{0.75}Co_{0.25}$@C-$Cu_{0.20}$	75:25	66.9	45.7

The properties of the newly gained protective carbon shell were further investigated by a combination of ICP-OES, nitrogen physisorption, TGA and TPR measurements. To analyze the carbon-to-metal ratio generated during the MOFMS process and the potential influence of the catalytic testing, ICP-OES measurements were performed before and after the catalytic testing (Table 16). The metal content of the two component catalysts before the catalytic testing is between 51.9 % for Fe@C-$Mn_{0.20}$ and 56.7 % for Fe@C-$Cu_{0.20}$. The metal contents for the three component systems are slightly higher with 59.3 % up to 66.9 %. These very high metal contents coupled with comparably small particles (cf. Figure 35) are a special feature of MOFMS catalysts, which is explained by the fact that the metal particles are embedded into the carbon matrix. This feature additionally prevents sintering even at high metal loadings. The previously shown unpromoted catalyst series displayed slightly lower metal contents of around 50 % (cf. Chapter 3.1.1 and 3.2.2). In contrast to the

catalysts directly after synthesis, the spent catalysts display decreased contents of the active metal components. The relative weight loss is the highest for the Cu-containing catalysts with 21.2 % to 31.4 %. It can be speculated that a lot of coking occurred during the catalytic testing due to the carbon containing syngas used for the CO_2-FTS process, which explains the lower relative metal mass. However, the relative decrease of the metal content is far less pronounced for the Mn-containing catalysts. This supports the assumption of heavy coking during the catalytic testing due to the overall low FTS activity displayed by the Mn-promoted catalysts (cf. Chapter 3.3.3). Additionally, the Fe@C-$Y_{0.20}$ catalysts displayed strong phase transitions (Figure 35), where the formerly reduced Fe got oxidized during the catalytic testing. The formation of Fe oxides compared to reduced Fe also decreases the relative metal content in the catalyst material. Therefore, Fe@C-$Y_{0.20}$ shows a significantly lower metal content after the catalytic testing than the Fe_xCo_{1-x}@C-$Y_{0.20}$ catalysts.

Table 17: Specific surface areas and average pore diameter of the Fe_xCo_{1-x}@C-$Y_{0.20}$ catalysts derived from nitrogen physisorption isotherms using the BET method and the BJH plot, respectively.

Sample	Specific surface area / $m^2\ g^{-1}$	Average pore diameter / nm	Pore volume / $cm^3\ g^{-1}$
Fe@C-$K_{0.20}$	52	28	0.301
$Fe_{0.80}Co_{0.20}$@C-$K_{0.20}$	54	20	0.255
$Fe_{0.75}Co_{0.25}$@C-$K_{0.20}$	125	11	0.219
Fe@C-$Mn_{0.20}$	244	13	0.439
$Fe_{0.80}Co_{0.20}$@C-$Mn_{0.20}$	229	13	0.502
$Fe_{0.75}Co_{0.25}$@C-$Mn_{0.20}$	209	13	0.461
Fe@C-$Cu_{0.20}$	207	16	0.624
$Fe_{0.80}Co_{0.20}$@C-$Cu_{0.20}$	189	17	0.514
$Fe_{0.75}Co_{0.25}$@C-$Cu_{0.20}$	150	17	0.359

The specific surface area of each catalyst was determined by nitrogen physisorption measurements according to the BET method (Table 17). The isotherms and respective plots are shown in the Appendix (Figure A 6). The specific surface area of the catalysts increases compared to the MOF precursor materials. Due to the synthesis method used for the MOF precursors, the resulting materials had shown an open pore geometry with pores that are filled by Co and the respective third component. Hence, the specific surface area was very small particularly for MOF materials (cf. Table 15). The MOFMS catalysts consist of active metal nanoparticles embedded into a carbon matrix and the measured specific surface areas between 52 m^2 g^{-1} and 244 m^2 g^{-1} match the expect values from literature.[151] The K-containing series displays particularly low specific surface areas between 52 m^2 g^{-1} and 125 m^2 g^{-1}. The average pore size of the materials was difficult to determine due to the complex mixture of meso- and micropores generated by the carbon matrix. However, the pore volume determined *via* the BJH plot revealed that the Fe@C-$Y_{0.20}$ seems to have the largest pore volume and the addition of K leads to a decreased pore volume, which could be linked to a pore blocking effect of excessive amounts of the K promoter, which is known from literature.[89]

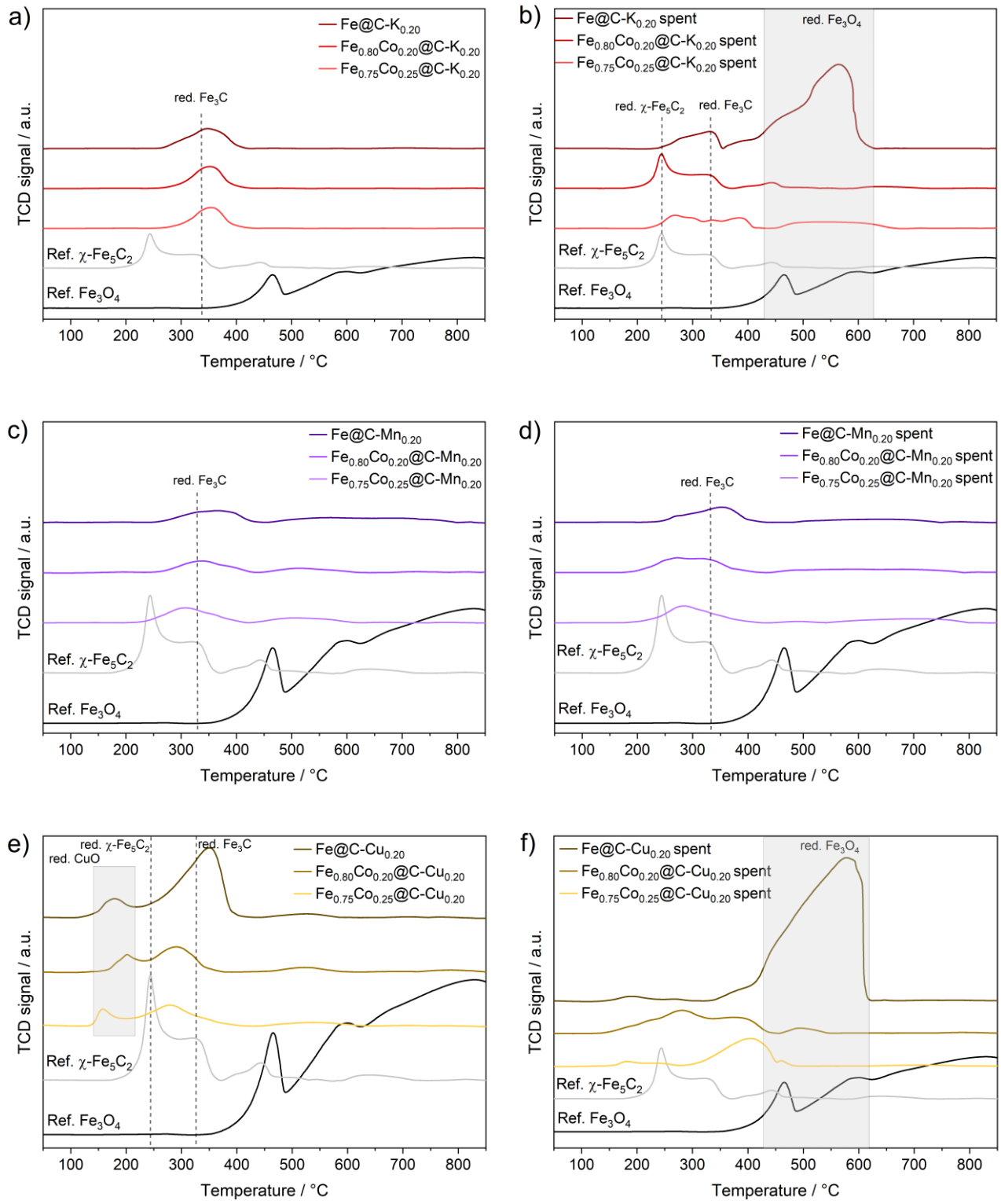

Figure 36: TPR measurements of the Fe_xCo_{1-x}@C-$Y_{0.20}$ catalysts before and after catalytic testing, with K (a +b), Mn (c + d) and Cu promoter (e + f).

MOFMS catalysts posses the unique property of oxidation prevention of the active metal, whereby the catalysts display only reduced metal phases in the diffraction patterns before the catalytic testing. This unique property was discussed in the

previous chapter for the unpromoted bimetallic MOFMS catalyst series (Chapter 3.2.2) and is further investigated by temperature-programmed reduction measurements of the promoted catalysts (Figure 36). Due to the major phase changes of the materials during the catalytic testing, the measurements were performed before and after the time-on-stream experiment in the CO_2-FTS model plant. As reference for the reduction behavior of χ-Fe_5C_2, the measured TPR profile of the spent $Fe_{0.80}Co_{0.20}$@C-$K_{0.20}$ catalyst was used due to the commercial unavailability of the material and the purity of the generated Hägg carbide phase, as indicated by the PXRD measurements (cf. Figure 35).

The fresh K-containing catalysts show only one H_2 consumption peak between 250 and 400 °C. In this temperature range no oxidic iron is reduced and the multistep reduction of oxidic iron starts only at around 400 °C and continues up to temperatures of 800 °C (referenced in black). It was assumed that the reduced metal nanoparticles are protected by a thin oxidation stable Fe_3C layer around the active metal. This assumption is supported by the identical peak position shown by all three catalysts, while only Fe@C-$K_{0.20}$ exhibits a reducible Fe_3C phase in the PXRD pattern. The spent K-containing catalysts display different reduction peaks with a two-step reduction for $Fe_{0.80}Co_{0.20}$@C-$K_{0.20}$ and $Fe_{0.75}Co_{0.25}$@C-$K_{0.20}$ between 200 °C and 400 °C and two separated peaks for Fe@C-$K_{0.20}$ at around 300 °C and between 400 °C and 650 °C. The K- and Co-containing catalysts show mainly χ-Fe_5C_2 in the PXRD patterns, which matches the assumed two-step reduction from χ-Fe_5C_2 to Fe_3C and further to reduced Fe. The second H_2 consumption peaks for the spent $Fe_{0.80}Co_{0.20}$@C-$K_{0.20}$ and $Fe_{0.75}Co_{0.25}$@C-$K_{0.20}$ catalysts match also the temperature range of the observed peak in the fresh catalyst materials, which further indicates a protective layer of Fe_3C around the metal nanoparticles in the MOFMS catalysts. The spent Fe@C-$K_{0.20}$ catalyst displays a highly intense peak between 400 °C and 650 °C, which can be assigned to Fe_3O_4. This peak also matches the observed iron oxide in the diffraction pattern (cf. Figure 35 b). The smaller and broader peak between 250 °C and 350 °C can be assigned to the reduction of Fe_3C, which was also observed in the PXRD pattern.

The fresh Mn-containing catalysts show a small H_2 consumption peak between 250 °C and 400 °C and a broader peak between 500 °C and 600 °C. The first peak can be assigned to the reduction of a protective Fe_3C layer, similarly to the K-

containing catalysts. The second peak is assigned to further reduction of manganese oxides to MnO, which suggests that oxidized manganese nanoparticles are present, which were not observed in the PXRD measurements (cf. Figure 35 c). The spent Mn-containing catalysts show similar TPR profiles and only minor phase transitions during the CO_2-FTS process. However, the H_2 consumption of the spent $Fe_{0.80}Co_{0.20}$@C-$Mn_{0.20}$ and $Fe_{0.75}Co_{0.25}$@C-$Mn_{0.20}$ catalysts start at slightly lower temperatures. The shift to lower temperatures matches the reduction pattern observed for χ-Fe_5C_2 (Figure 36 b). This indicates that the uncrystalline carbide phase found in the PXRD patterns is most likely an *in situ* generated Hägg carbide phase.

All fresh Cu-containing catalysts show two H_2 consumption peaks at 150 °C and a broader peak between 250 °C and 350 °C. The literature suggest that the first peak is assigned to the reduction of CuO nanoparticles.[166] However, the second peak can be either assigned to the reduction of CuO bulk-like particles or Fe_3C, as previously discussed. Due to the absence of CuO reflections in the diffraction patterns of the fresh catalysts, the assumption of a thin protective Fe_3C layer is further supported. This is further indicated by the higher intensity of the peak for Fe@C-$Cu_{0.20}$ due to an enhanced formation of the carbide phase for this material (Figure 35 e). The spent materials show different H_2 consumption peaks, most notable a highly intense peak of the spent Fe@C-$Cu_{0.20}$ catalyst between 400 °C and 600 °C. This peak matches the peak found in the TPR profile of the spent Fe@C-$K_{0.20}$ catalyst and is therefore assigned to the reduction of Fe_3O_4, which matches the PXRD measurements (cf. Figure 35 f). The spent $Fe_{0.80}Co_{0.20}$@C-$Cu_{0.20}$ and $Fe_{0.75}Co_{0.25}$@C-$Cu_{0.20}$ catalysts both lost the first characteristic peak assigned to the reduction of CuO nanoparticles at 150 °C during the time-on-stream, which indicates sintering of the metal oxide promoter during the catalytic testing.

The unique phase transitions during the CO_2-FTS process were further analyzed using XAS measurements. Due to limited beamline access, only the best performing catalysts (cf. Chapter 3.3.3) were investigated. XAS measurements were performed at the Fe K-edge (7112 eV) for Fe@C-$K_{0.20}$, $Fe_{0.80}Co_{0.20}$@C-$K_{0.20}$, Fe@C-$Cu_{0.20}$ and $Fe_{0.80}Co_{0.20}$@C-$Cu_{0.20}$ before and after the catalytic testing for CO_2-FTS. Additionally, the Co K-edge (7709 eV) was measured for $Fe_{0.80}Co_{0.20}$@C-$K_{0.20}$ and $Fe_{0.80}Co_{0.20}$@C-$Cu_{0.20}$ respectively. The E-space of the K-containing catalysts

displays a reduced state of Fe before the catalytic testing due to the presence of a small white line comparable to Fe foil (Figure 37 a). $Fe_{0.80}Co_{0.20}$@C-$K_{0.20}$ shows a similar spectrum compared to the Fe foil reference, which matches the PXRD results of only reduced Fe_{bcc} prior to the catalytic testing (cf. Figure 35 a). However, the spent catalysts show a very intense white line for Fe@C-$K_{0.20}$ and still a fairly reduced state of Fe for $Fe_{0.80}Co_{0.20}$@C-$K_{0.20}$. The high intensity of the white line indicates the oxidation of Fe, which matches also the PXRD result (cf. Figure 35 b).[167] The PXRD pattern of $Fe_{0.80}Co_{0.20}$@C-$K_{0.20}$ after the catalytic testing displayed Fe_{bcc} as the main phase and newly formed χ-Fe_5C_2. Hence, the small white line increase is explained by the carbide phase, which contains Fe in a higher oxidation state. The spectra measured at Co K-edge show a similar trend for $Fe_{0.80}Co_{0.20}$@C-$K_{0.20}$ as the Fe K-edge spectra. In E-space, highly reduced Co can be found before the catalytic testing and slightly less reduced Co afterwards (Figure 37 b). To further analyze the chemical environment of the catalyst materials, the R-space is also shown in Figure 37 b and c. The R-space measured at the Fe K-edge displays no difference between the first three peaks of R = 2.20 Å, 3.66 Å and 4.49 Å of Fe foil and the fresh catalyst materials. This confirms the bcc structure of the iron in the catalysts and particle sizes >5 nm. After the catalytic testing Fe@C-$K_{0.20}$ displays two intense peaks at R = 1.58 Å and 2.75 Å which are characteristic for metal oxides due to the reduced bond length of metal-oxygen compared to metal-metal.[168] $Fe_{0.80}Co_{0.20}$@C-$K_{0.20}$ still shows a peak at 2.17 Å originating from the Fe-Fe scattering in the χ-Fe_5C_2 carbide phase. However, the peak gained an additional shoulder at 1.53 Å, which indicates the formation of the χ-Fe_5C_2 carbide phase and therefore new “soft” neighboring atoms (in form of carbon) around the central iron. The R-space measured at the Co K-edge shows a deviation between the Co foil reference and $Fe_{0.80}Co_{0.20}$@C-$K_{0.20}$. The reason for this is the formation of FeCo in bcc structure (Figure 37 a) compared to the classical fcc structure of reduced Co. After the catalytic testing Hägg carbide (χ-Fe_5C_2) was the main phase found in the PXRD pattern (Figure 37 b). Hence, the neighboring atoms of Co consist of iron and carbon which explains the similar peak shape compared to the Fe K-edge with an additional shoulder at 1.53 Å.

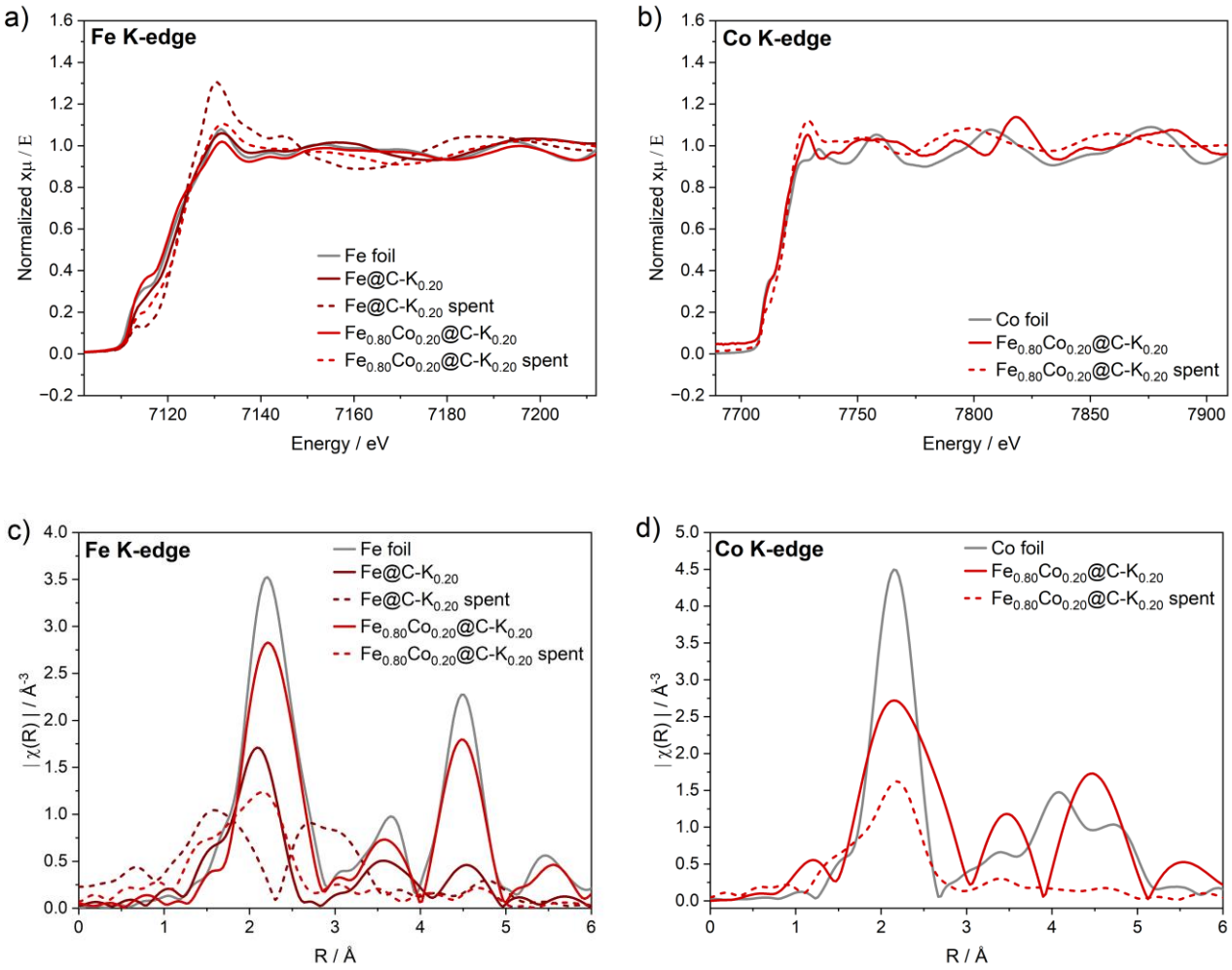

Figure 37: XAS measurements of Fe@C-$K_{0.20}$ and $Fe_{0.80}Co_{0.20}$@C-$K_{0.20}$ before and after the catalytic testing in E-space (a and b) and R-space (c and d). The samples were measured at the Fe K-edge (a and c) and the Co K-edge (b and d).

The XAS measurements for the Cu-containing catalysts in E-space (Figure 38 a) show a similar trend to the K-containing materials. Hence, the fresh catalysts both display reduced Fe very similar to the Fe foil reference. Fe@C-$Cu_{0.20}$ shows a more oxidized state of the iron due to the increased white line, which matches the previously shown PXRD pattern (cf. Figure 35 f). The E-space spectra, measured at the Co K-edge for $Fe_{0.80}Co_{0.20}$@C-$Cu_{0.20}$ before and after the catalytic testing, shows reduced cobalt but with significant differences compared to the Co foil reference. The R-space spectra measured at the Fe K-edge of Fe@C-$Cu_{0.20}$ and $Fe_{0.80}Co_{0.20}$@C-$Cu_{0.20}$ before the catalytic testing match the Fe foil reference and, therefore, it can be assumed that Fe is in a reduced bcc structure with a full coordination shell at radial distances <5 Å. This was expected due to the intense reflections of Fe_{bcc} found in the PXRD patterns of these catalysts (cf. Figure 35 e).

The Fe@C-$Cu_{0.20}$ catalyst, which was oxidized after the catalytic testing, shows similar to Fe@C-$K_{0.20}$ the characteristic peaks for metal oxides with R = 1.54 Å for the metal-oxide scattering path and R = 2.87 Å for the metal-metal scattering path. $Fe_{0.80}Co_{0.20}$@C-$Cu_{0.20}$ shows the same shoulder at the first peak as $Fe_{0.80}Co_{0.20}$@C-$K_{0.20}$, due to the Fe-C scattering of the newly formed carbide. However, contrary to $Fe_{0.80}Co_{0.20}$@C-$K_{0.20}$ the second and third peak in the R-space spectrum match the peaks of Fe_{bcc} at R = 3.55 Å and 4.50 Å. This is in line with the PXRD results, which show Fe_{bcc} still as the main phase even after the formation of χ-Fe_5C_2. The R-space spectra of $Fe_{0.80}Co_{0.20}$@C-$Cu_{0.20}$ measured at the Co K-edge displays the same trend as $Fe_{0.80}Co_{0.20}$@C-$K_{0.20}$ with cobalt being forced into the bcc structure of the FeCo mixed phase and, shifted peaks compared to the Co_{fcc} foil. Additionally, the spent $Fe_{0.80}Co_{0.20}$@C-$Cu_{0.20}$ exhibits a shoulder at the first peak (1.59 Å) due to the neighboring carbon from the carbide phase formed during the FTS process.

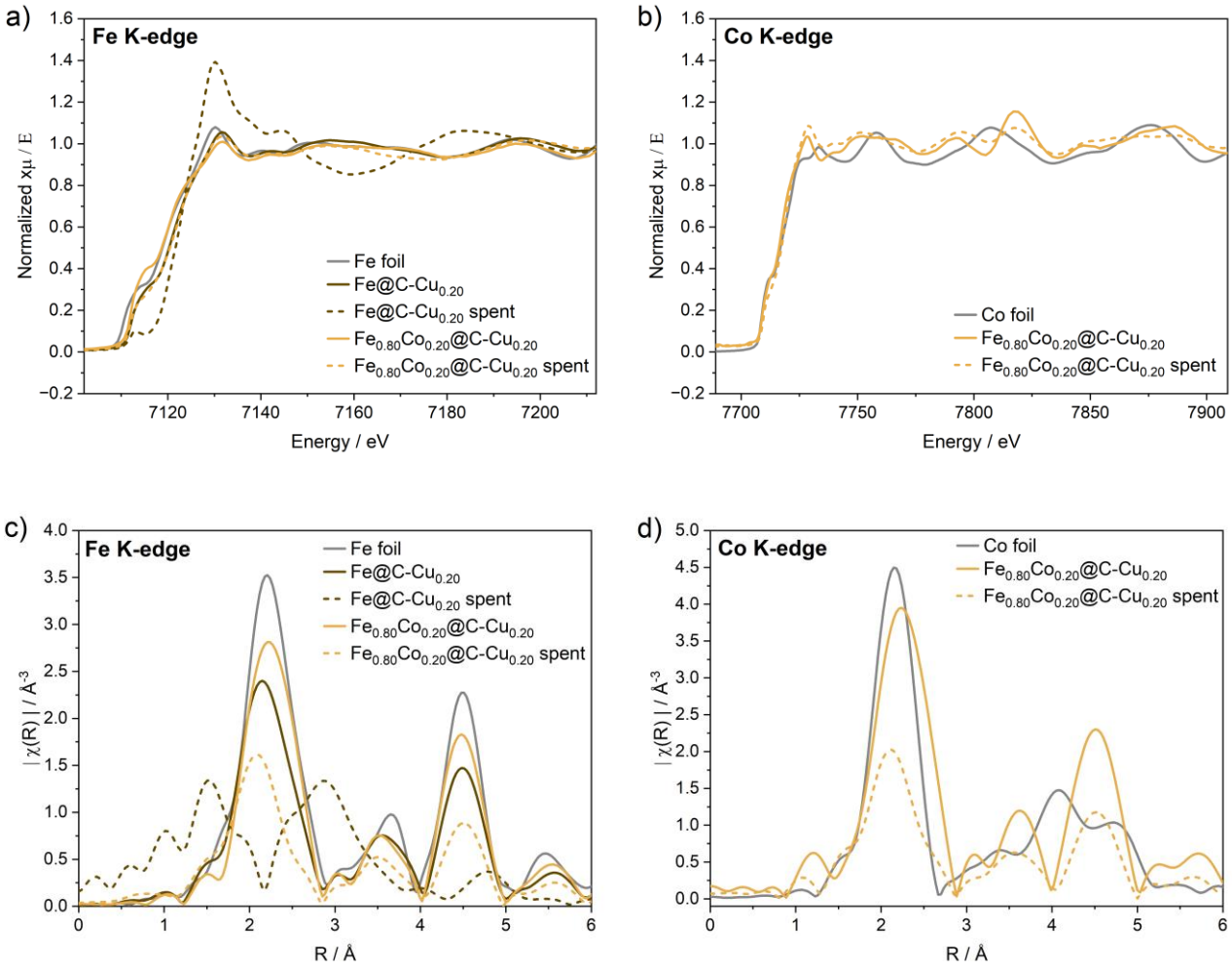

Figure 38: XAS measurements of Fe@C-$Cu_{0.20}$ and $Fe_{0.80}Co_{0.20}$@C-$Cu_{0.20}$ before and after the catalytic testing in E-space (a and b) and R-space (c and d). The samples were measured at the Fe K-edge (a and c) and the Co K-edge (b and d).

3.3.3 Catalytic testing of multicomponent MOFMS catalysts

All catalysts were tested in a time-on-stream experiment for 12 h with constant flow, pressure, and temperature. Afterwards, the FTS activity at different reaction temperatures were investigated. Figure 39 shows the CO_2 conversion for each catalyst during the 12 h time-on-stream. The K-containing catalyst series displays a relatively high overall CO_2 conversion of more than 23 % with stable conversion levels after 5 h. The highest conversion is shown by $Fe_{0.80}Co_{0.20}$@C-$K_{0.20}$ with a stable conversion of 33 %. The lowest overall CO_2 conversion is shown by Fe@C-$K_{0.20}$ with only 23 % in the steady-state region, which indicates an increase in CO_2 conversion with the addition of Co to the catalyst system. This result matches the CO_2 conversion trend observed for the unpromoted materials (Fe@C_800°C and

$Fe_{0.80}Co_{0.20}$@C). However, Fe@C-$K_{0.20}$ exhibits an activity loss in the first 3 h of testing with a CO_2 conversion drop from 56 % to the stable 23 % afterwards. A possible explanation is given by the previously shown PXRD results, where only the Fe-containing catalysts were oxidized after the catalytic testing, which indicates a damaged carbon shell due to the loss of the oxidation protection. This damage to the carbon shell might be occurring in the first 3 h of the reaction. The assumption of a damage carbon shell is supported by the poor resistance against oxidation of unsupported χ-Fe_5C_2.[44,47]

The Mn-containing catalyst series shows the overall lowest CO_2 conversions of all tested catalyst series. All three systems display conversion levels under 10 % with the same trend as the K-containing series, where the Fe/Co-containing catalysts show higher conversions than the catalyst Fe@C-$Mn_{0.20}$. The characterization results already hinted at a poor FTS activity of the catalyst series, because no significant formation of the highly FTS active Hägg carbide phase was observed during the catalytic testing. Furthermore, the Mn-containing catalysts displayed only minor amounts of coking during the testing compared to the K- and Cu-containing materials (cf. Table 16).

The Cu-containing catalyst series displays the highest overall CO_2 conversion with around 35 % for $Fe_{0.80}Co_{0.20}$@C-$Cu_{0.20}$ and 26 % for Fe@C-$Cu_{0.20}$ and the same trend of the last two series, where the CO_2 conversion was the lowest for the catalyst containing only Fe and the highest for the catalyst containing 20 % of Co. These results support the assumption of an enhancing effect from Co with regard to the CO_2 conversion. However, Fe@C-$Cu_{0.20}$ exhibits a similar activity loss during the first 2 h as shown previously for Fe@C-$K_{0.20.}$ The CO_2 conversion shown by Fe@C-$Cu_{0.20}$ decreases from 38 % during the first measurement to the stable 26 % afterwards. The PXRD measurements after the testing show again oxidized metal particles, which indicate an unstable carbon shell if no Co is present within the material.

The addition of K and Cu enhanced particularly the CO_2 conversion of the Fe/Co-containing catalysts. Thus, unpromoted $Fe_{0.80}Co_{0.20}$@C displayed only about 29 % CO_2-conversion, while $Fe_{0.80}Co_{0.20}$@C-$Cu_{0.20}$ and $Fe_{0.80}Co_{0.20}$@C-$K_{0.20}$ both exhibit constant CO_2 conversions of about 35 %.

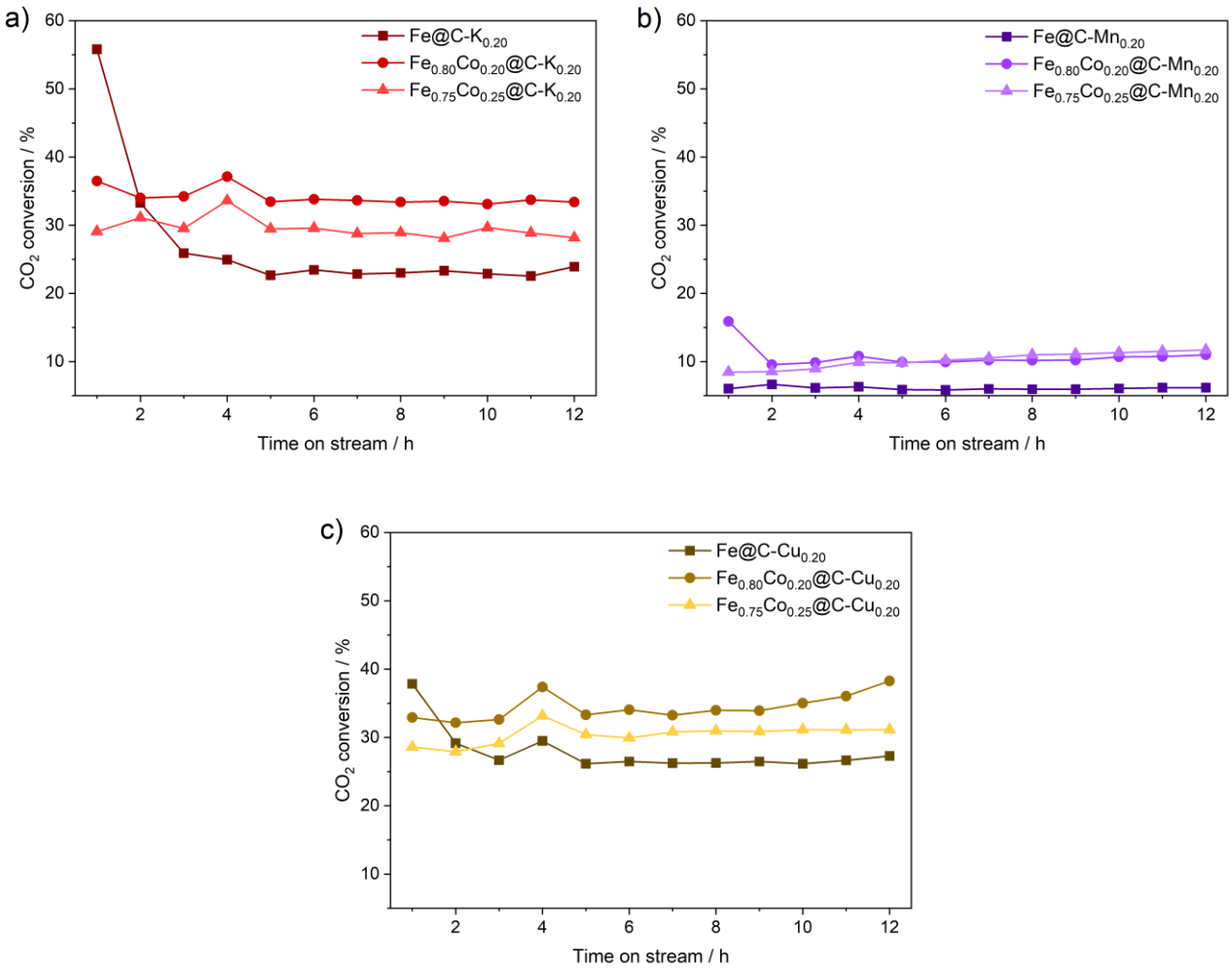

Figure 39: CO_2 conversions of the Fe_xCo_{1-x}@C-$Y_{0.20}$ catalysts containing K (a), Mn (b) and Cu (c) over a TOS period of 12 h at 350 °C, 20 bar with a total flow of 25 mL/min (H_2/CO_2 = 3:1).

The reaction temperature variation was measured between 200 °C and 400 °C in steps of 50 K to cover both conventional LTFT and HTFT conditions. The resulting temperature-dependent yields and CO_2 conversions of the different C-fractions are shown in Figure 40 for the K-promoted catalysts, in Figure 41 for the Mn-promoted catalysts and in Figure 42 for the Cu-promoted catalysts. The selectivities towards CO, CH_4, C_{2+} and C_{5+} product fractions were calculated from the measured product yield fractions (Table 18-20).

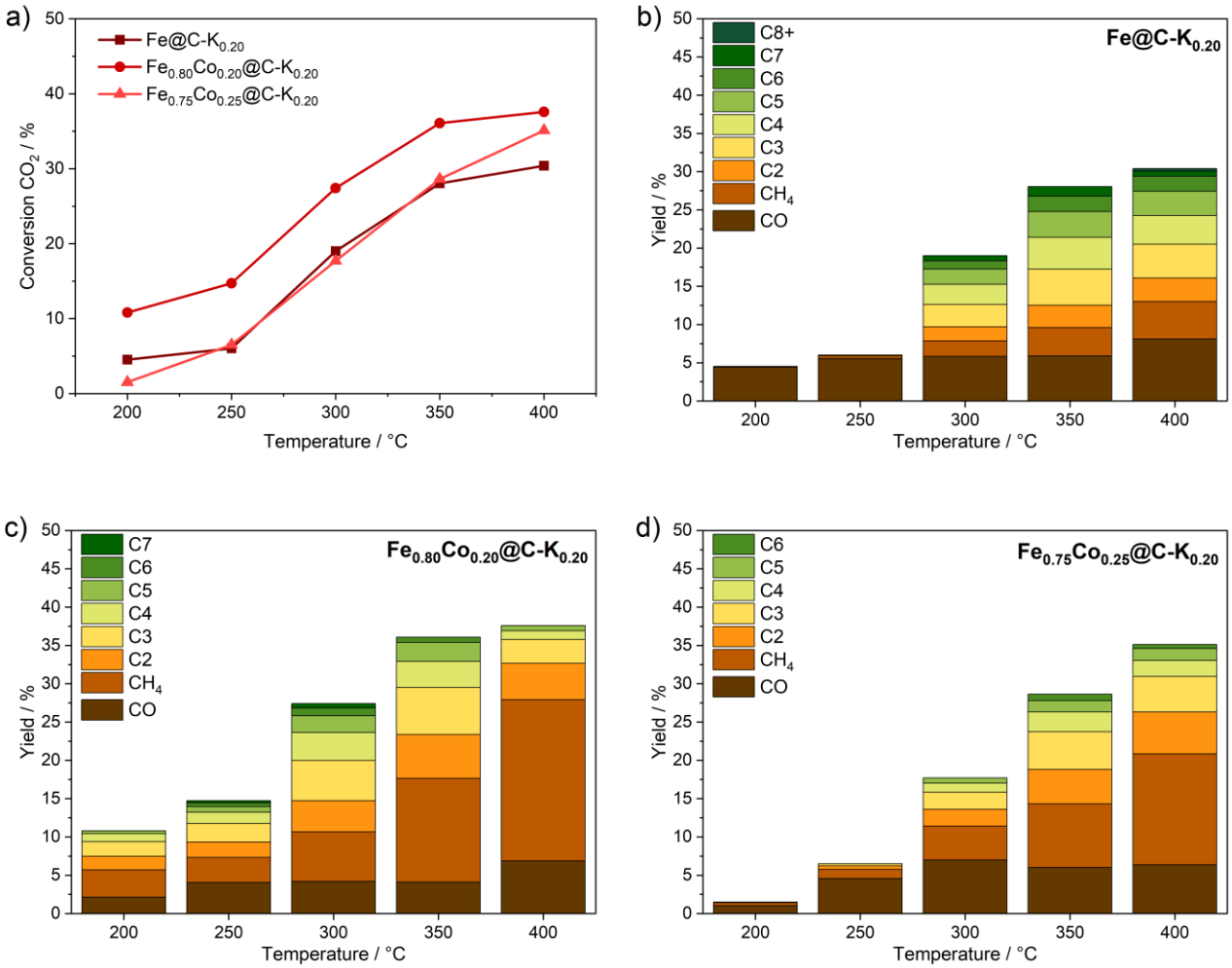

Figure 40: Temperature-dependent CO_2 conversions for the K-containing Fe_xCo_{1-x}@C-$K_{0.20}$ catalysts (a) and temperature-dependent yields for Fe@C-$K_{0.20}$ (b), $Fe_{0.80}Co_{0.20}$@-$K_{0.20}$ (c) and $Fe_{0.80}Co_{0.20}$@-$K_{0.20}$ (d) measured at 20 bar with a total flow of 25 mL/min (H_2/CO_2 = 3:1).

The overall CO_2 conversion of the K-containing catalysts follows the trend displayed in Figure 39 a) with Fe@C-$K_{0.20}$ displaying the lowest conversion above a reaction temperature of 200 °C and $Fe_{0.80}Co_{0.20}$@C-$K_{0.20}$ showing the highest conversion at every tested reaction temperature respectively. Fe@C-$K_{0.20}$ exhibits only minor FTS activity at the low reaction temperatures of 200 °C and 250 °C with CO as the main product. However, at the higher reaction temperatures product fraction of up to C_{8+} are generated with a very low selectivity towards methane. The selectivity towards C_{2+} and C_{5+} FTS products is the highest at 350 °C with 65.7 % and 23.7 % respectively. As expected, the CH_4 selectivity simultaneously decreases to only 13.3 % at 350 °C. Compared to the unpromoted variant of the catalyst (cf. Chapter 3.1.3), the C_{2+} increased from 53.9 % to 67.5 % and the C_{5+} selectivity is more than doubled, while the comparatively high methane selectivity of

Fe@C_800°C decreased from 35.2 % to only 13.3 % for the K-promoted system. Similar to Fe@C_800°C, the reaction temperature of 350 °C is still favored. This was expected since similar temperature ranges are used industrially for Fe-based catalysts during HTFT. Opposing to this, $Fe_{0.80}Co_{0.20}$@C-$K_{0.20}$ displays FTS activity for all tested reaction temperatures with minor yields of C_5 at 200 °C. Until a reaction temperature of 300 °C the methane yield is relatively small and longer hydrocarbon chains up to C_7 are found, despite the overall smaller yields of these fractions compared to Fe@C-$K_{0.20.}$ At the higher reaction temperatures of 350 °C and 400 °C, the selectivity shifts towards methane with 55.9 % at 400 °C. Hence, the optimal reaction temperature for $Fe_{0.80}Co_{0.20}$@C-$K_{0.20}$ is 300 °C with a C_{2+} selectivity of 61.2 % and a C_{5+} selectivity of 13.8 %. The selectivity towards methane is also decreased to 23.4 %. These results are contrary to unpromoted $Fe_{0.80}Co_{0.20}$@C, which displayed no increased methane selectivity at higher reaction temperatures. However, the catalytic testing results of the $Fe_{0.80}Co_{0.20}$@C-$K_{0.20}$ catalyst match the literature, where cobalt-containing catalysts display a strong shift towards methane formation under HTFT conditions.[38,54,92] $Fe_{0.75}Co_{0.25}$@C-$K_{0.20}$ shows a FTS activity above 250 °C which is similar to Fe@C-$K_{0.20,}$ but the overall selectivity towards methane is higher and the generated hydrocarbon fractions are shorter and lower in yield. Compared to $Fe_{0.80}Co_{0.20}$@C-$K_{0.20,}$ the methane selectivity at high reaction temperatures is lower, but the CO_2 conversion is also comparatively small.

Table 18: Temperature-dependent selectivity towards CO, CH_4, C_{2+} fractions and C_{5+} fractions for the Fe_xCo_{1-x}@C-$K_{0.20}$ catalysts measured at 20 bar and a with a 25 mL/min flow of H_2/CO_2 = 3:1.

Sample	Temperature	X_{CO_2}	S_{CO}	S_{CH_4}	$S_{C_{2+}}$	$S_{C_{5+}}$
Fe@C-$K_{0.20}$	200 °C	4.5	97.8	2.2	0.0	0.0
	250 °C	6.0	92.1	5.5	2.4	0.0
	300 °C	19.0	30.6	10.7	58.6	19.8
	350 °C	28.1	21.0	13.3	65.7	23.7
	400 °C	30.4	26.7	16.1	57.2	20.2
$Fe_{0.80}Co_{0.20}$@C-$K_{0.20}$	200 °C	10.8	19.8	32.9	47.2	3.5
	250 °C	14.7	27.5	22.3	50.2	10.3
	300 °C	27.4	15.3	23.6	61.1	13.8
	350 °C	36.1	11.4	37.6	51.1	8.8
	400 °C	37.6	18.3	55.9	25.7	1.8
$Fe_{0.75}Co_{0.25}$@C-$K_{0.20}$	200 °C	1.5	69.1	24.9	5.9	0.0
	250 °C	6.5	70.3	17.9	11.8	0.0
	300 °C	17.7	39.4	25.1	35.5	3.9
	350 °C	28.6	21.0	29.0	49.9	8.2
	400 °C	35.1	18.1	41.3	40.6	5.9

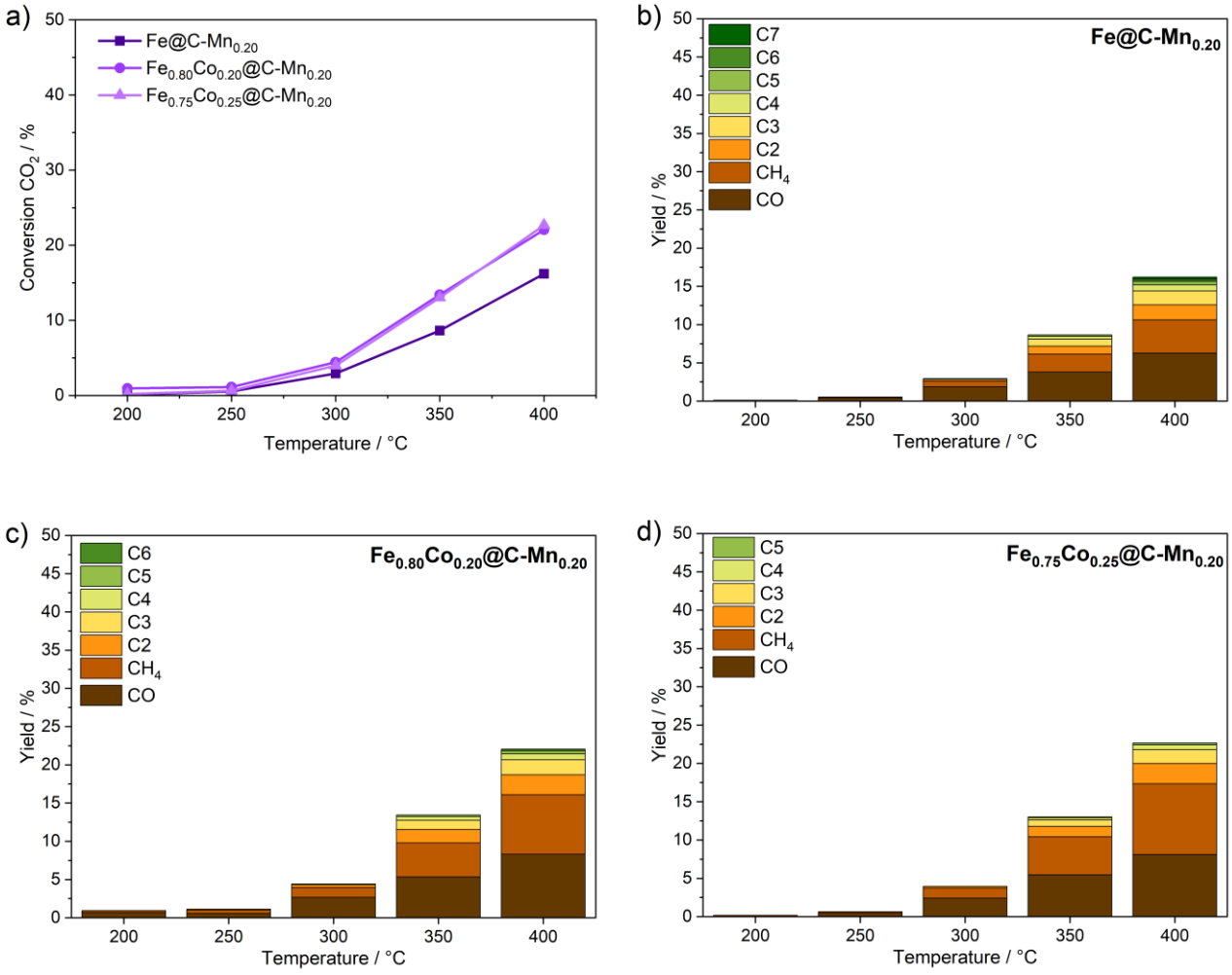

Figure 41: Temperature-dependent CO_2 conversions for the Mn-containing Fe_xCo_{1-x}@C-$Mn_{0.20}$ catalysts (a) and temperature-dependent yields for Fe@C-$K_{0.20}$ (b), $Fe_{0.80}Co_{0.20}$@-$Mn_{0.20}$ (c) and $Fe_{0.80}Co_{0.20}$@-$Mn_{0.20}$ (d) measured at 20 bar with a total flow of 25 mL/min (H_2/CO_2 = 3:1).

The Mn-containing catalyst series shows the same trend for the reaction temperature variation as in the time-on-stream experiment, with very low conversions for all tested reaction temperatures (Figure 41). Below a reaction temperature of 300 °C none of the tested catalysts displays any significant FTS activity with only minor yields of CO. The main product at the higher reaction temperatures is methane for all three catalysts with only minor fractions of longer hydrocarbons up to a very small yield of C_7 for Fe@C-$Mn_{0.20}$. Even at high reaction temperatures, all three catalysts display lower CO_2 conversions than their unpromoted counterparts. Despite the beneficial effect of Mn, which is catalyzing the rWGS reaction, this promoter is also known to reduce the generated chain length of the formed hydrocarbons.[84,103,104] This property of Mn seems to be more pronounced for the tested MOFMS catalysts, which results in an overall negative impact on the FTS activity.

Table 19: Temperature-dependent selectivity towards CO, CH_4, C_{2+} fractions and C_{5+} fractions for the Fe_xCo_{1-x}@C-$Mn_{0.20}$ catalysts measured at 20 bar and a with a 25 mL/min flow of H_2/CO_2 = 3:1.

Sample	Temperature	X_{CO_2}	S_{CO}	S_{CH_4}	$S_{C_{2+}}$	$S_{C_{5+}}$
Fe@C-$Mn_{0.20}$	200 °C	0.1	0.0	100	0.0	0.0
	250 °C	0.5	79.3	20.7	0.0	0.0
	300 °C	2.9	63.6	24.3	12.1	0.0
	350 °C	8.6	43.7	27.3	28.9	2.1
	400 °C	16.2	38.7	26.8	34.5	6.1
$Fe_{0.80}Co_{0.20}$@C-$Mn_{0.20}$	200 °C	0.9	73.6	26.4	0.0	0.0
	250 °C	1.1	49.7	38.5	11.8	0.0
	300 °C	4.4	59.9	29.4	10.8	0.0
	350 °C	13.4	39.7	33.1	27.1	1.5
	400 °C	22.1	37.7	35.3	27.1	2.8
$Fe_{0.75}Co_{0.25}$@C-$Mn_{0.20}$	200 °C	0.2	0.0	100	0.0	0.0
	250 °C	0.6	75.2	24.8	0.0	0.0
	300 °C	3.9	60.6	33.7	5.8	0.0
	350 °C	13.1	41.9	38.1	19.9	0.9
	400 °C	22.7	35.8	40.7	23.5	1.2

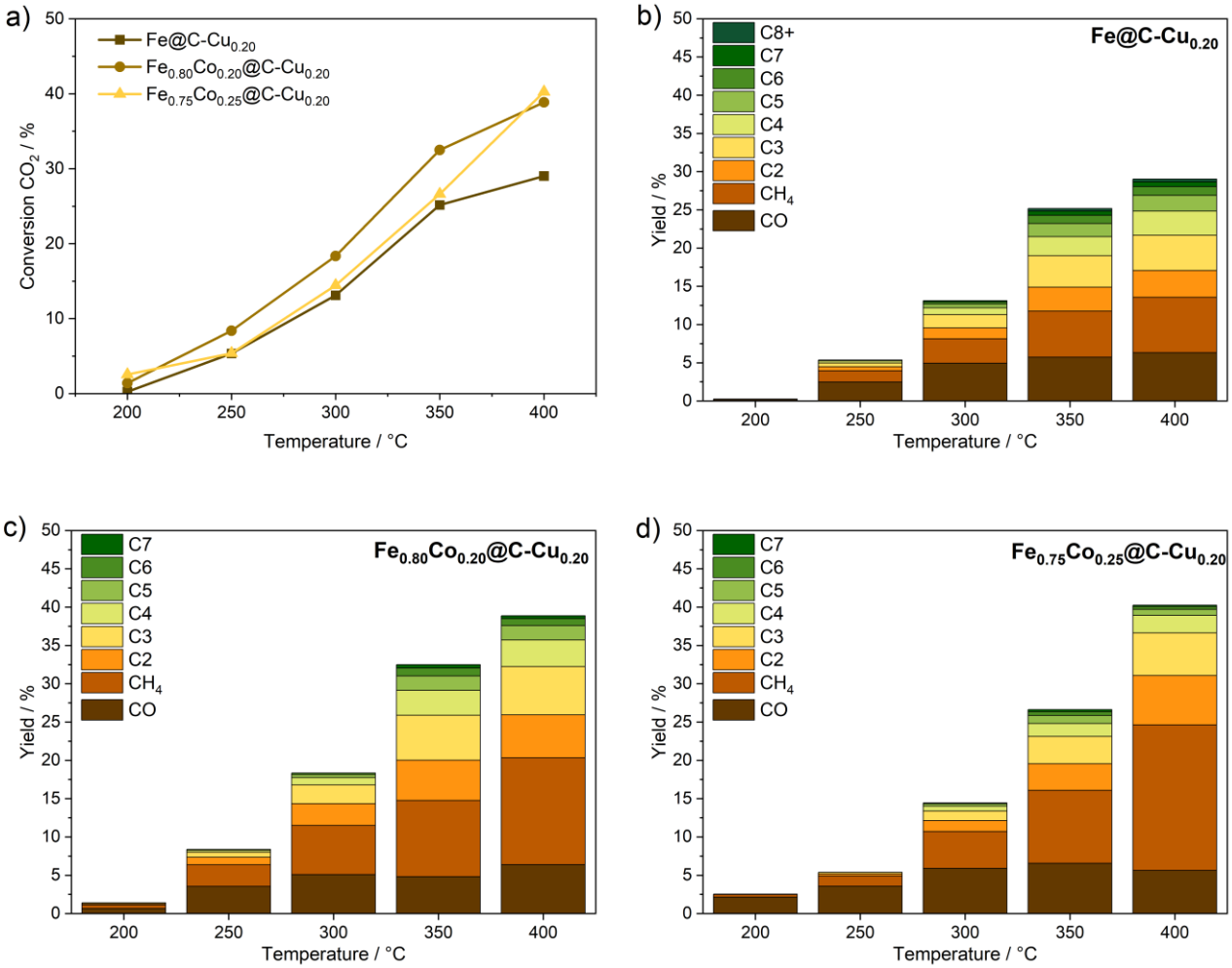

Figure 42: Temperature-dependent CO_2 conversions for the Cu containing Fe_xCo_{1-x}@C-$Cu_{0.20}$ catalysts (a) and temperature-dependent yields for Fe@C-$Cu_{0.20}$ (b), $Fe_{0.80}Co_{0.20}$@-$Cu_{0.20}$ (c) and $Fe_{0.80}Co_{0.20}$@-$Cu_{0.20}$ (d) measured at 20 bar with a total flow of 25 mL/min (H_2/CO_2 = 3:1).

Compared to the K-containing catalyst series, the reaction temperature variation shows higher overall CO_2 conversion if Cu was added to the catalyst systems (Figure 42). Therefore, the highest conversions of all tested catalysts are achieved with 38 % and 40 % with $Fe_{0.80}Co_{0.20}$@C-$Cu_{0.20}$ and $Fe_{0.75}Co_{0.20}$@C-$Cu_{0.25}$, respectively. However, the product selectivity for these two catalysts shifts heavily towards methane at high reaction temperatures with 35.8 % and 47.2 % at 400 °C. Opposing to the K-containing catalysts, FTS activity was only observed for all three catalysts at temperatures of 250 °C or higher with minor fractions of longer hydrocarbon yield. The selectivity toward longer CH chains is the highest for Fe@C-$Cu_{0.20}$, despite the methane yield being still relatively high compared to Fe@C-$K_{0.20}$. Compared to the unpromoted variations of the catalysts, Fe@C-$Cu_{0.20}$ displays a slight increase in C_{2+} and C_{5+} selectivity from 46.1 % and 9.8 % to 53.3 % and 14.5 %, respectively, at

400 °C and a decrease in methane selectivity from 35.7 % to 24.9 %. However, the other two catalysts exhibit no significant benefits regarding the FTS activity if Cu is added. Particularly the shift towards C_{5+} products, which has been reported in literature, was not observed during the catalytic testing of the Cu-containing MOFMS catalysts.[98,101]

Table 20: Temperature-dependent selectivity towards CO, CH_4, C_{2+} fractions and C_{5+} fractions for the Fe_xCo_{1-x}@C-$Cu_{0.20}$ catalysts measured at 20 bar and a with a 25 mL/min flow of H_2/CO_2 = 3:1.

Sample	Temperature	X_{CO_2}	S_{CO}	S_{CH_4}	$S_{C_{2+}}$	$S_{C_{5+}}$
Fe@C-$Cu_{0.20}$	200 °C	0.3	74.6	25.4	0.0	0.0
	250 °C	5.4	46.4	27.6	25.9	2.3
	300 °C	13.1	37.8	24.2	38.1	7.0
	350 °C	25.2	22.8	23.9	53.3	14.6
	400 °C	29.1	21.8	24.9	53.3	14.5
$Fe_{0.80}Co_{0.20}$@C-$Cu_{0.20}$	200 °C	1.4	47.4	32.2	20.4	0.0
	250 °C	8.4	42.3	33.8	23.9	1.3
	300 °C	18.4	27.7	34.9	37.3	3.4
	350 °C	32.5	14.8	30.6	54.6	10.3
	400 °C	38.9	16.5	35.9	47.7	8.1
$Fe_{0.75}Co_{0.25}$@C-$Cu_{0.20}$	200 °C	2.5	84.4	13.8	1.8	0.0
	250 °C	5.4	66.3	24.6	9.0	0.0
	300 °C	14.4	40.8	33.3	25.9	3.0
	350 °C	26.6	24.7	35.8	39.5	6.8
	400 °C	40.3	13.9	47.2	38.8	3.3

Additionally, the formation of alkanes and olefines was analyzed. Figure 43 shows the temperature-dependent yields of ethane/ethylene and propane/propylene for each catalyst of the tested series. The Fe@C-$Y_{0.20}$ catalysts display only minor amounts of light olefines for the Mn- and Cu-promoted systems. However, with the addition of K, the selectivity shifts heavily towards the generation of light olefine products. Above a reaction temperature of 300 °C, the alkane fractions ethane and propane show only minor yields below 1 %, while 4.2 % yield of propylene is formed at 350 °C. The generation of ethylene and propylene follows the same trend for all temperatures, with a maximum selectivity for both light olefines at 350 °C. The measured yield of propylene is higher than for ethylene at every tested reaction temperature for Fe@C-$K_{0.20}$. Despite the overall poor performance of the Mn-containing catalysts, these results match the literature. Hence, alkali metal promoters are used to increase the selectivity towards light olefines and Cu is used to enhance the C_{5+} formation during the CO_2-FTS process.[101] For the Fe/Co-containing catalysts $Fe_{0.80}Co_{0.20}$@C-$Y_{0.20}$ and $Fe_{0.75}Co_{0.25}$@C-$Y_{0.20}$ (Figure 43 b + c), a similar trend is observed. Thus, the Mn- and Cu-containing catalysts display nearly no light olefine yield. The only significant olefine yield (1.4 %) was detected for $Fe_{0.80}Co_{0.20}$@C-$Cu_{0.20}$ at 350 °C. With the addition of the potassium, the selectivity shifts heavily towards the light olefin fractions, which are generated as main fractions at every temperature step. Following the trend of Fe@C-$K_{0.20}$, the propylene generation is more pronounced than the ethylene generation up to a reaction temperature of 350 °C. At the highest tested reaction temperature of 400 °C, however, the yield of propylene decreases from 5.3 % to 2.4 % for $Fe_{0.80}Co_{0.20}$@C-$K_{0.20}$ and from 3.8 % to 2.6 % for $Fe_{0.75}Co_{0.25}$@C-$K_{0.20}$, while the yield of propane stays the same for $Fe_{0.80}Co_{0.20}$@C-$K_{0.20}$ and slightly increases for $Fe_{0.75}Co_{0.25}$@C-$K_{0.20}$. Hence, a selectivity shift occurs at the highest reaction temperature of 400 °C. Particularly for $Fe_{0.80}Co_{0.20}$@C-$K_{0.20}$ a strong increase of the methane yield was also observed during the temperature-dependent experiments (cf. Figure 40). Compared to the unpromoted catalysts (Fe@C_800°C, $Fe_{0.80}Co_{0.20}$@C and $Fe_{0.75}Co_{0.25}$@C), the selectivity towards light olefines could be remarkably enhanced by the addition of K as promoter for all three catalysts. Similar to the unpromoted catalysts, the yield of propylene is higher than the yield of ethylene at all temperatures for each catalyst. The highest propylene yield was measured for $Fe_{0.80}Co_{0.20}$@C-$K_{0.20}$ with 5.3 % at 350 °C, the unpromoted catalysts displayed only under 2 % yield of propylene at

every reaction temperature. However, unlike the unpromoted catalyst, $Fe_{0.80}Co_{0.20}$@C-$K_{0.20}$ and $Fe_{0.75}Co_{0.25}$@C-$K_{0.20}$ displayed a severe decrease of the light olefines at high reaction temperatures of 400 °C. This could be linked to an enhancing effect of the alkali metal promoter on cobalt, which is known to shift its selectivity towards methane at these high reaction temperatures.[10,15]

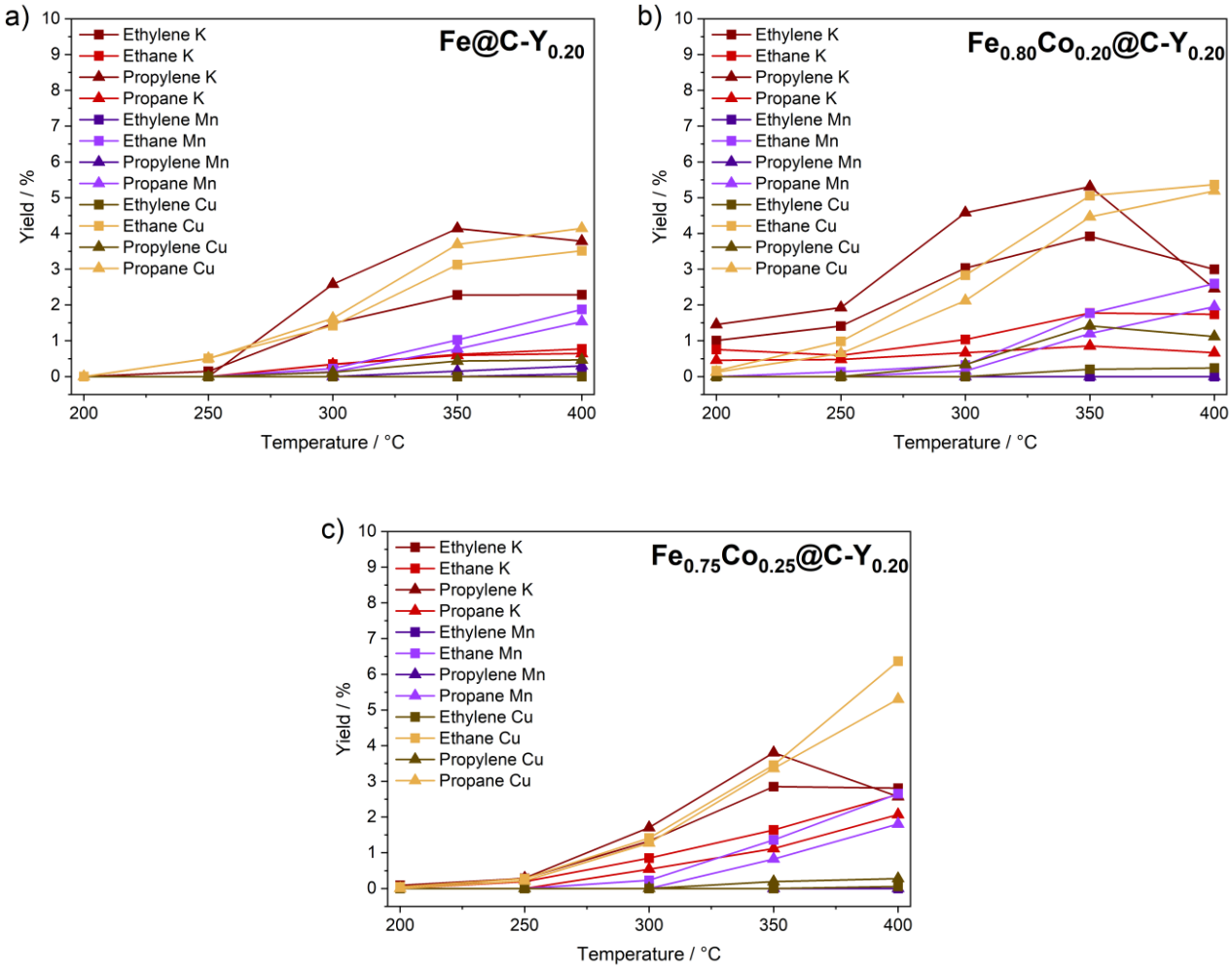

Figure 43: Temperature-dependent yield distribution towards alkanes (C_2 and C_3) and olefines (C_2 and C_3) for Fe@C-Y (a), $Fe_{0.75}Co_{0.25}$@C-Y (b) and $Fe_{0.80}Co_{0.20}$@C-Y (c) measured at 20 bar with a total flow of 25 mL/min (H_2/CO_2 = 3:1).

Hence, K seems to be the best of the three tested promoters to shift the selectivity from alkanes to olefines, with an optimal reaction temperature of 350 °C. Cu inhibits the olefine formation and is therefore preferred if only alkanes are desired. Mn as promoter displayed only negative effects on the FTS activity with a decreased CO_2 conversion as well as a lower selectivity towards higher hydrocarbon fractions.

Due to the limited time for the experimental studies during this work, the unpromoted MOFMS catalysts were only promoted with a relatively large amount of promoter material (20 mol%). Further testing with 1 mol% and 5 mol% promoter material were planned as mentioned in the motivation chapter (cf. Chapter 2). Despite the beneficial effects found for the high amounts of alkali promoter on the CO_2-FTS activity,[88] negative effects are also described within the literature. Excessive amounts of potassium might block pores and active sites of CO_2-FTS catalysts within peer-reviewed studies. This effect was particularly mentioned for Co-based catalysts.[90] This matches the observed poor CO_2-FTS performance of $Fe_{0.80}Co_{0.20}$@C-$K_{0.20}$ and $Fe_{0.75}Co_{0.25}$@C-$K_{0.20}$ at high reaction temperatures. Unfortunately, the effect of different amounts of Cu and Mn as promoters are poorly researched until now. However, Mn is known to enhance the rWGS reaction, but also to suppress C-C coupling reaction.[103,104] The excessive amount of Mn combined with the inhibition on C-C coupling could be a possible explanation for the overall poor CO_2-FTS performance of all three Mn-containing catalysts. The addition of smaller amounts of promoter material should be investigated in future works to compare not only the effects between the different promoter materials but also investigate the influence of their concentrations. Furthermore, the addition of varying amounts of promoter material would allow better insights regarding the beneficial and disadvantageous effects on novel MOFMS CO_2-FTS catalysts.

4 Summary

The goal of this work was the synthesis of Fe- and bimetallic Fe/Co-containing MOFMS catalysts for the CO_2-FTS process. All catalysts were fully characterized and tested regarding their CO_2-FTS activity under different reaction conditions. Furthermore, the most promising catalysts were further modified with different promoter materials.

In the first part of the work, monometallic Fe-containing MOFMS catalysts were synthesized with the focus on the optimization of reaction parameters during the MOFMS process. To accomplish this, the MOF precursor MIL-53(Fe) was synthesized and characterized in a first step. PXRD, ATR-IR spectroscopy, nitrogen physisorption and ICP-OES measurements were used to confirm the successful synthesis of MIL-53(Fe) with a closed pore geometry. To investigate the effect of different decomposition temperatures during the following MOFMS procedure, TGA measurements under inert N_2 atmosphere were performed. The MOF precursor displayed a three-stage decomposition with the evaporation of physisorbed water and solvent residues at about 100 °C, the decomposition of the organic components of the framework between 200 °C and 550 °C and another weight loss step between 650 °C and 750 °C, which could be linked to the formation of iron carbides. Based on these results, the decomposition temperatures for the MOFMS process were chosen to be 400 °C, 600 °C and 800 °C. The resulting catalysts after the thermal decomposition were investigated regarding their newly formed metal phases *via* PXRD, Mössbauer spectroscopy and XAS measurements. Furthermore, the protective carbon shell which was formed during the MOFMS process was analyzed using a combination of nitrogen physisorption, TGA and ICP-OES. Different metal phases were formed during the thermal decomposition depending on the chosen temperature. Fe@C_400°C displayed a large microporous carbon shell with only 26.9 wt% of Fe within the catalysts. The PXRD patterns showed only broad reflections. However, the Mössbauer measurements revealed the formation of highly oxidized Fe_3O_4. The diffraction pattern of Fe@C_600°C displayed reflections of α-Fe, FeO and Fe_3O_4, which was further confirmed by Mössbauer spectroscopy. The relative Fe content was increased to 42.3 wt% and the nitrogen physisorption measurements displayed a type IV isotherm with a mix of micro- and mesopores.

Due to the oxidation-preventing effect found for the MOFMS catalysts, it was assumed that the protective carbon shell was only partially formed at this decomposition temperature. At the highest decomposition temperature of 800 °C, the catalyst generated a mixture of reduced α-Fe and iron carbide (Fe_3C), which was confirmed by PXRD, Mössbauer and XAS measurements. To investigate the CO_2-FTS activity of the catalyst series, a time-on-stream measurement of 12 h and a temperature variation experiment, where the reaction temperature was increased from 200 °C up to 400 °C in 50 K steps, were conducted. Fe@C_400°C displayed only minor FTS activity with a low CO_2 conversion of only about 12 % during the TOS experiment and no measured selectivity towards C_{2+} products, independent on the reaction temperature. Despite the still low CO_2 conversion of Fe@C_600°C during the TOS experiment (about 12 %), the catalyst displayed a selectivity of 35.9 % towards C_{2+} products at a reaction temperature of 300 °C. This could be further enhanced up to a C_{2+} selectivity of 56.3 % and a C_{5+} selectivity of 13.6 % at 400 °C. However, the measured methane selectivity was still high with 30.5 %. The highest FTS activity was shown by the catalyst Fe@C_800°C with a stable CO_2 conversion of about 27 % during the TOS experiment. The selectivity towards longer hydrocarbon formation was also the highest with a C_{2+} selectivity of 53.9 % and a C_{5+} selectivity of 14.2 % at 350 °C. It was assumed that both the initially found carbide phase and the reduced nature of the other iron nanoparticles enhance the *in situ* formation of the highly FTS-active Hägg carbide phase during the testing of Fe@C_800°C. However, the Fe-containing MOFMS catalyst series was again characterized after the catalytic testing. PXRD measurements revealed that the catalyst systems were unstable against the CO_2-FTS conditions. Therefore, all three spent catalysts displayed only reflections of the highly oxidized Fe_3O_4 phase.

The second of the present work focused on the synthesis of bimetallic Fe/Co-containing MOFMS catalysts for the CO_2-FTS process. Similar to the monometallic catalyst series, the first step was the synthesis and characterization of the bimetallic MOF precursors. To analyze the effect of different metal ratios on the FTS activity of the catalysts, a series of MIL-53(Fe_xCo_{1-x}) materials with different Fe/Co ratios (4:1, 3:1, 2:1, 1:1, 1:2 and 1:3) were synthesized. For the MOFs with Co/Fe ratios >1 a direct synthesis approach was found. For the MOF precursors with higher Fe contents a two-step synthesis approach was utilized, where cobalt was added *via*

incipient wetness impregnation. The generated MOF precursor displayed an open pore geometry due to the presence of pyridine-*N*-oxide within the pores for the Co-rich MOFs and the Co species within the pores for the materials synthesized *via* the impregnation approach. The phase purity of the newly generated precursors was confirmed by ATR-IR measurements. Furthermore, the thermal stability was tested using TGA measurements. The bimetallic MOF series showed a similar behavior to MIL-53(Fe). Hence, the decomposition temperature for the MOF-mediated synthesis was chosen to be 800 °C due to the favorable properties for CO_2-FTS shown by the catalyst Fe@C_800°C. After the MOFMS procedure, the catalysts series was again fully characterized by a combination of different analysis methods. PXRD and XAS measurements revealed the presence of stable reduced metal nanoparticles with a bcc structure. Due to the structural similarity of Fe_{bcc} and $FeCo_{bcc}$, the exact ratio of the two phases could not be determined. The crystallite size increased with increasing Fe content from 15 nm to 38 nm with a relative metal content of 55 wt% to 60 wt% for all materials. The MOFMS catalysts displayed a specific surface area from 170 $m^2\ g^{-1}$ to 315 $m^2\ g^{-1}$ with a mixture of meso- and micropores similar to Fe@C_800°C. To understand the oxidation-preventing effect of the carbon shell generated during the MOFMS process, TPR measurements were performed. The TPR measurements revealed a small H_2 consumption peak in the same temperature range for all materials of the series. The peak could be assigned to the reduction of the more stable carbide phase Fe_3C. However, neither PXRD nor XAS revealed the occurrence of iron carbide within the catalysts. It was assumed that a thin iron carbide layer was formed around the metal nanoparticles during the MOFMS process, which protects the reduced materials against further oxidation. Afterwards the catalysts were tested under the same conditions as the monometallic Fe-based MOFMS catalysts. During the time-on-stream experiment over 12 h, $Fe_{0.25}Co_{0.75}$@C displayed the highest CO_2 conversion with about 28 %. However, unlike the other catalysts, $Fe_{0.80}Co_{0.20}$@C showed a strong CO_2 conversion increase after 5 h TOS from 12 % to about 26 %. During the temperature-dependent measurement, the Fe-rich catalysts $Fe_{0.75}Co_{0.25}$@C and $Fe_{0.80}Co_{0.20}$@C showed the highest CO_2 conversion at every tested temperature step. Further analysis revealed that only $Fe_{0.75}Co_{0.25}$@C and $Fe_{0.80}Co_{0.20}$@C show a significant FTS activity above a reaction temperature of 300 °C with the generation of up to C_7 products. The highest selectivity towards C_{2+} and C_{5+} product generation was shown by $Fe_{0.80}Co_{0.20}$@C at

400 °C, with 68.2 % and 11.6 % respectively. The selectivity towards methane was 21.8 % at 400 °C. Similar to the Fe-based catalysts, light olefines were only produced in minor amounts. The catalysts were again characterized after the time-on-stream experiment. Interestingly, unlike in the monometallic Fe-based MOFMS catalysts, reduced Fe or FeCo was still present in all catalysts, without any evidence of oxidized metal phases. For $Fe_{0.80}Co_{0.20}$@C, an additional χ-Fe_5C_2 carbide phase was generated under the CO_2-FTS conditions. This phase is known from literature for its high FTS activity and could explain the exceptionally good performance of $Fe_{0.80}Co_{0.20}$@C during the testing. Furthermore, the steep increase in CO_2 conversion displayed during the TOS experiment was assumed to be linked to the formation of the χ-Fe_5C_2 phase.

The third part of the thesis focused on the optimization of the best catalysts with different promoter materials. Based on recent literature, the alkali metal potassium as well as the transition metals copper and manganese were chosen. From the previously tested unpromoted catalysts Fe@C_800°C, $Fe_{0.75}Co_{0.25}$@C and $Fe_{0.80}Co_{0.20}$@C were chosen with the goal of decrease the methane formation, while increasing the selectivities of light olefines or C_{5+} *via* an enhanced χ-Fe_5C_2 generation. Therefore, the first step was again the synthesis of the MOF precursors. To ensure a close contact between the promoter and the catalytically active component, the previously described incipient wetness impregnation approach was used to incorporate the promoter and, if necessary, cobalt into the pores of MIL-53(Fe). The resulting MOF precursors were analyzed regarding their structure, phase purity and thermal stability with a combination of PXRD, ICP-OES, ATR-IR and TGA measurements. The MOF precursors displayed an open pore geometry like the previously discussed materials synthesized with the impregnation approach. The behavior under MOFMS conditions were also similar to the unpromoted MOF precursors, thus, a full decomposition was achieved at temperatures above 750 °C for all materials and therefore 800 °C were chosen for the MOFMS process. The fresh Fe/Co-containing MOFMS catalysts showed reflections of Fe_{bcc} and $FeCo_{bcc}$ with additional reduced Cu phases and MnO phases, respectively. The catalysts without cobalt displayed an additional Fe_3C carbide phase. The metal content was slightly increased compared to the unpromoted catalysts from 53.7 wt% to 66.9 wt%. Nitrogen physisorption measurements showed again a combination of micro- and

mesopores and specific surface areas between 52 $m^2\ g^{-1}$ and 244 $m^2\ g^{-1}$. To confirm the assumption of a protective Fe_3C carbide layer around the metal nanoparticles, TPR measurements were performed. All fresh catalysts displayed the same small H_2 consumption peak as the unpromoted Fe/Co-containing catalyst materials. Additionally, the Cu-containing catalysts showed an H_2 consumption peak that could be assigned to the reduction of CuO nanoparticles. Afterwards, the catalysts were also tested for 12 h in a time-on-stream experiment and a temperature variation experiment in the range between 200 °C and 400 °C. The TOS experiment displayed the same trend independent of the additional promoter and, thus, $Fe_{0.80}Co_{0.20}$@C-$Y_{0.20}$ showed the highest stable CO_2 conversion while Fe@C-$Y_{0.20}$ showed the lowest CO_2 conversion. All K- and Cu-promoted catalysts displayed CO_2 conversions between 25 % and 35 % during the TOS experiment, the catalysts with additional Mn showed very low CO_2 conversions below 15 %. During the reaction temperature variation experiment, the Mn-containing catalysts displayed also a poor performance regarding the CO_2 conversion as well as the generation of FTS products. For the K-containing catalysts, the highest CO_2 conversion was achieved by $Fe_{0.80}Co_{0.20}$@C-$K_{0.20}$ with 37.6 % at 400 °C and the highest selectivity towards C_{2+} and C_{5+} hydrocarbons was shown by Fe@C-$K_{0.20}$ with 65.7 % and 23.7 % at 350 °C, respectively. For the Cu-containing catalysts, the highest CO_2 conversion was achieved by $Fe_{0.75}Co_{.0.25}$@C-$Cu_{0.20}$ with 40.2 % at 400 °C and the highest selectivity towards C_{2+} and C_{5+} products was displayed by $Fe_{0.80}Co_{0.20}$@C-$Cu_{0.20}$ with 54.6 % and 10.3 % at 350 °C respectively. Additionally, the temperature-dependent selectivity towards the formation of light olefines was investigated. The addition of Mn and Cu had only minor effects on the generation of light olefines, while the addition of K heavily increased the product yields of unsaturated hydrocarbons. The maximum light olefine generation was achieved for all three tested K-promoted catalysts at 350 °C. Hence, Mn decreased the CO_2-FTS performance of all tested MOFMS catalysts, while Cu promotion led to the highest increase of the CO_2 conversion and K promotion showed the most pronounced selectivity shift towards the formation of FTS product fractions and light olefines. After the catalytic testing, the materials were characterized again to investigate possible structural changes under CO_2-FTS conditions. The K- and Cu-containing catalysts exhibited the generation of the highly active Hägg carbide phase during the time-on-stream. However, the catalysts without Co contained oxidized Fe_3O_4 after catalysis similar to the unpromoted variant

(Fe@C_800°C), which indicates further that the addition of Co stabilizes the MOFMS system against the harsh reaction conditions during the CO_2-FTS process. The Mn-containing catalysts showed only minor structural changes after the catalytic testing. The structural changes observed in the PXRD patterns of the spent catalysts were further confirmed by XAS and TPR measurements. Hence, the goal of an enhanced χ-Fe_5C_2 generation could be achieved, which should be closely linked to the favorable traits of the K- and Cu-containing catalysts during the catalytic testing, particularly the greatly improved selectivity towards the formation of light olefines.

In summary, the overall goal of the synthesis and characterization of novel monometallic Fe-containing and bimetallic Fe/Co-containing MOFMS catalysts has been achieved. Furthermore, the most promising MOFMS synthesis parameters for the thermal decomposition were 800 °C for 2 h in N_2 atmosphere for both the monometallic Fe-containing and bimetallic Fe/Co-containing MOFMS catalysts. A Fe/Co ratio of 4:1 resulted in the best systems for both the unpromoted and promoted bimetallic catalysts. Among the three promoters, potassium featured the most beneficial effects regarding an increased selectivity towards light olefines and a decreased selectivity towards methane.

5 Experimental

5.1 Materials

The chemicals used were purchased from Sigma Aldrich, Merck or Alfa Aesar and used without further purification. Demineralized water was used for washing.

5.2 Synthesis procedures

5.2.1 Synthesis of MIL-53(Fe) precursor

The precursor materials were synthesized *via* solvothermal synthesis similar to the presented synthesis of Fèrey *et al.* for MIL-53(Fe).[137] Therefore, 6892 mg (25 mmol), $FeCl_3 \cdot 6xH_2O$ and 4236 mg (25 mmol) H_2BDC (terephthalic acid) were diluted in 200 mL DMF with an ultrasonic bath. The solution was heated afterwards for 18 h to a temperature of 150 °C in a Schott flask without stirring. The generated solid was separated from the hot suspension by using a glass frit (porosity 5) and washed three times with 20 mL heated DMF and dried at room temperature in air. The resulting yellow powder was dried further for 72 h at 130 °C.

5.2.2 Synthesis of MIL-53(Fe_xCo_{1-x}) precursor

Synthesis of bimetallic MOF-precursor materials with Fe content of 50 % and less: The precursor materials were synthesized *via* a one pot solvothermal synthesis similar to the presented synthesis approach of Mung *et al.* for MIL-53(Co) materials.[138] 1412 mg (8.500 mmol) H_2BDC (terephthalic acid), 808 mg (8.500 mmol) pyridine-N-oxide and the respective amount $FeCl_3 \cdot 6xH_2O$ and $Co(NO_3)_2 \cdot 6xH_2O$ (Table 21) were diluted in 50 mL DMF within 30 min in an ultrasonic bath. The solution was heated afterwards for 18 h to a temperature of 150 °C for MIL-53($Fe_{0.25}Co_{0.75}$), 120 °C for MIL-53($Fe_{0.33}Co_{0.67}$) and 130 °C for MIL-53($Fe_{0.50}Co_{0.50}$) in a Schott flask without stirring. The generated solid was separated from the hot suspension by using a glass frit (porosity 5) and washed three times with 20 mL heated DMF and dried at room temperature in air. The resulting yellow powder was dried further for 72 h at 130 °C. Each synthesis was carried out repeatedly, and the products were combined for the following MOFMS synthesis step.

Table 21: Synthesis parameter for the direct synthesis of MIL-53(Fe_xCo_{1-x}).

Sample	Amount of $FeCl_3 \cdot 6xH_2O$/ mg and mmol	Amount of $Co(NO_3)_2 \cdot 6xH_2O$/ mg and mmol
MIL-53($Fe_{0.25}Co_{0.75}$)	574 mg (2.125 mmol)	1855 mg (6.380 mmol)
MIL-53($Fe_{0.33}Co_{0.67}$)	689 mg (2.550 mmol)	1731 mg (5.950 mmol)
MIL-53($Fe_{0.50}Co_{0.50}$)	919 mg (3.400 mmol)	1484 mg (5.100 mmol)

Synthesis of bimetallic MOF-precursor materials with Fe content above 50 %: The MIL-53 based precursors were synthesized in a two-step process. The first step consisted of the synthesis of the monometallic MIL-53(Fe) (cf. Chapter 5.2.1). For the second step Co was incorporated into the framework structure *via* incipient wetness impregnation. The solvothermal MOF synthesis was similar to the presented synthesis of Fèrey *et al.* for MIL-53(Fe).[137] Therefore, 6892 mg (25 mmol), $FeCl_3 \cdot 6xH_2O$ and 4236 mg (25 mmol) H_2BDC (terephthalic acid) were diluted in 200 mL DMF with an ultrasonic bath. The solution was heated afterwards for 18 h to a temperature of 150 °C in a Schott flask without stirring. The generated solid was separated from the hot suspension by using a glass frit (porosity 5) and washed three times with 20 mL heated DMF and dried at room temperature in air. The resulting yellow powder was dried further for 72 h at 130 °C. Afterwards, 1965 mg (6.752 mmol for MIL-53($Fe_{0.67}Co_{0.33}$)), 1310 mg (4.501 mmol for MIL-53($Fe_{0.75}Co_{0.25}$)) and 982 mg (3.376 mmol for MIL-53($Fe_{0.80}Co_{0.20}$)) of $Co(NO_3)_2 \cdot 6xH_2O$ were diluted in 0.397 mL H_2O and added dropwise to 3200 mg (13.50 mmol) of the dried MIL-53(Fe). The brown powder was thoroughly mixed and dried for 48 h at 130 °C.

5.2.3 Synthesis of MIL-53(Fe_xCo_{1-x})-$Y_{0.20}$ precursor

The MIL-53 based precursors were synthesized in a two-step process. The first step consisted of the synthesis of the monometallic MIL-53(Fe). For the second step Co was incorporated into the framework structure *via* incipient wetness impregnation. The solvothermal MOF synthesis was similar to the presented synthesis of Fèrey *et al*. for MIL-53(Fe).[137] Therefore, 6892 mg (25 mmol), $FeCl_3 \cdot 6xH_2O$ and

4236 mg (25 mmol) H_2BDC (terephthalic acid) were diluted in 200 mL DMF with an ultrasonic bath. The solution was heated afterwards for 18 h to a temperature of 150 °C in a Schott flask without stirring. The generated solid was separated from the hot suspension by using a glass frit (porosity 5) and washed three times with 20 mL heated DMF and dried at room temperature in air. The resulting brown/yellow powder was dried further for 72 h at 130 °C. For MIL-53(Fe)-$Y_{0.20}$, the respective additional metal salt (Table 22) was diluted in 0.422 mL H_2O and added dropwise to 3400 mg (14.35 mmol) of dried MIL-53(Fe). For MIL-53($Fe_{0.80}Co_{0.20}$)-$Y_{0.20}$ a mixture of 1043 mg (3.587 mmol) $Co(NO_3)_2 \cdot 6xH_2O$ and the respective metal salt (Table 22) were diluted in 0.422 mL H_2O and added dropwise to 3400 mg (14.35 mmol) of dried MIL-53(Fe). For MIL-53($Fe_{0.75}Co_{0.25}$)-$Y_{0.20}$ a mixture of 1310 mg (4.782 mmol) $Co(NO_3)_2 \cdot 6xH_2O$ and the respective metal salt (Table 22) were diluted in 0.422 mL H_2O and added dropwise to 3400 mg (14.35 mmol) of dried MIL-53(Fe). The brown powder was thoroughly mixed and dried for 48 h at 130 °C for all samples.

Table 22: Synthesis parameter for the incipient wetness synthesis of MIL-53(Fe_xCo_{1-x})-$Y_{0.20}$.

Sample	**Additional metal salts**	**Amount of metal salt / mg and mmol**
MIL-53(Fe)- $K_{0.20}$	KNO_3	290 mg (2.869 mmol)
MIL-53(Fe)- $Mn_{0.20}$	$Mn(NO_3)_2 \cdot 4xH_2O$	720 mg (2.869 mmol)
MIL-53(Fe)- $Cu_{0.20}$	$Cu(NO_3)_2 \cdot 2.5xH_2O$	667 mg (2.869 mmol)
MIL-53($Fe_{0.80}Co_{0.20}$)- $K_{0.20}$	KNO_3	362 mg (3.587 mmol)
MIL-53($Fe_{0.80}Co_{0.20}$)- $Mn_{0.20}$	$Mn(NO_3)_2 \cdot 4xH_2O$	900 mg (3.587 mmol)
MIL-53($Fe_{0.80}Co_{0.20}$)- $Cu_{0.20}$	$Cu(NO_3)_2 \cdot 2.5xH_2O$	834 mg (3.587 mmol)
MIL-53($Fe_{0.75}Co_{0.25}$)- $K_{0.20}$	KNO_3	386 mg (3.826 mmol)
MIL-53($Fe_{0.75}Co_{0.25}$)- $Mn_{0.20}$	$Mn(NO_3)_2 \cdot 4xH_2O$	960 mg (3.826 mmol)
MIL-53($Fe_{0.75}Co_{0.25}$)- $Cu_{0.20}$	$Cu(NO_3)_2 \cdot 2.5xH_2O$	889 mg (3.826 mmol)

5.2.4 MOF-mediated synthesis of the Fe@C catalysts

The Fe@C catalyst systems were prepared *via* the MOF-mediated synthesis (MOFMS) approach. 3500 mg (15 mmol) of the previously synthesized MOF precursors were thermally decomposed in a fixed-bed reactor. The atmosphere during the pyrolysis was a constant stream through the fixed-bed of 100 mL/min N_2. The decomposition temperatures were reached with a 5 K/min heating ramp and varied depending on the catalyst (400 °C, 600 °C and 800 °C). All finished catalyst materials were binderless granulated to a particles size of 250 – 355 µm, prior to the catalytic testing. The resulting materials were stored under air and showed no structural changes even after several months.

5.2.5 MOF-mediated synthesis of the Fe_xCo_{1-x}@C and Fe_xCo_{1-x}@C-$Y_{0.20}$ catalysts

The Fe_xCo_{1-x}@C and Fe_xCo_{1-x}@C-$Y_{0.20}$ catalyst systems were prepared *via* the MOF-mediated synthesis (MOFMS) approach. 3500 mg (15 mmol) of the previously synthesized MOF precursors were thermally decomposed in a fixed-bed reactor. The atmosphere during the pyrolysis was a constant stream through the fixed-bed of 100 mL/min N_2. The decomposition temperature of 800 °C was reached with a 5 K/min heating ramp. All finished catalyst materials were binderless granulated to a particles size of 250 – 355 µm, prior to the catalytic testing. The resulting materials were stored under air and showed no structural changes even after several months.

5.3 Methods

5.3.1 Inductively coupled plasma optical emission spectroscopy

Inductively coupled plasma optical emission spectroscopy (ICP-OES) was used for the determination of absolute and relative metal amounts in the materials using an iCAP 6000 from Thermo Scientific. A six-point standard calibration was used and the curve results were analyzed in iTEVA9.8 software. Prior to the measurements, 5 mg of the samples were decomposed at 650 °C for 6 h. The cooled residue was mixed

with 1 mL HCl, which was evaporated *via* a gas burner. This process with HCl was repeated for a second time. The residue was then dissolved in 1 mL HNO_3 and diluted to 50 mL with de-mineralized water.

5.3.2 Infrared spectroscopy

The ATR-IR measurements were performed with an FT-IR Spectrometer Spektrum 3 from Perkin Elmer on the matching universal ATR sampling accessory. The transmission was measured in a wavelength range between 4000 and 400 cm^{-1} with a resolution of 2 cm^{-1}. The measured spectrum was averaged over 5 scans.

5.3.3 Nitrogen physisorption

Nitrogen adsorption isotherms were recorded with a Mircotrac – Belsorp Mini X. The samples were activated prior to the measurement at vacuum for 20 h at 130 °C, to remove water and solvent impurities. The surface areas of the samples were obtained by the Brunauer-Emmett-Teller (BET) method. The pore size distribution was obtained by using the Barrett-Joyner-Halenda (BJH) plot. Both analyses were performed with the BELmaster 7.3.2.0 software.

5.3.4 Mössbauer spectroscopy

Mössbauer spectra were recorded with a BAD3 from Oxford Instruments in the constant acceleration mode with a conventional spectrometer and a multi-channel analyzer in the time-scale mode (WissEL GmbH). Mössbauer spectra were taken at room temperature. After data transfer from the multi-channel analyzer to a PC the public domain program Vinda running on an Excel 2003 platform was used for data analysis. The Mössbauer spectra were analyzed by least-squared fits using Lorentzian line shapes. Line widths (Γ) are full widths at half maximum. Isomer shifts δ are given relative to α-iron at room temperature.

5.3.5 Thermogravimetric analysis

Thermogravimetric analysis (TGA) was measured on a Setaram Setsys 16/18. The measurements for the MOF precursors were performed under inert N_2 atmosphere, between 20 °C and 900 °C with a heating rate of 10 K/min to investigate the decomposition temperature of the precursor material. The measurements of the

Fe_xCo_{1-x}@C catalysts were performed under synthetic air atmosphere, between 20 °C and 900 °C with a heating rate of 10 K/min to investigate the carbon content of the materials.

5.3.6 Temperature-programmed reduction

Temperature programmed reduction measurements were performed with a Thermo Scientific TPDRO 1100. The sample was dried in He gas flow at 200 °C prior to the experiment. The reduction was performed in a temperature range between 45-900 °C with a gas mixture containing H_2/Ar 5%/95%. The temperature ramp was set to 5 K/min and a TCD conductivity detector was used.

5.3.7 X-ray absorption spectroscopy

X-ray absorption experiments at the Fe K-edge (7112 eV) were carried out at PETRA III beamline P65 at DESY in Hamburg (Germany). The PETRA III storage ring at DESY operates at 6 GeV particle energy with a current of 100 mA in top-up mode keeping the flux stable. While using the 1^{st} harmonic, the measurements have been carried out in transmission mode using a Fe foil for calibration of the beam. Simultaneously, the foil has been measured during the sample measurements as a reference. For beamline P65, an 11 period mini-undulator is the photon source which is providing a moderate photon flux density and the incident energy is selected using a water-cooled Si(111), double crystal monochromator. All samples were measured as pellets diluted with cellulose. For every sample, XANES and EXAFS analysis were carried out.

5.3.8 X-ray powder diffraction

X-ray powder diffraction (XRD) patterns were measured on a Siemens AXS type D 5005 with Cu K_α-radiation (λ = 0,15405 nm) at 35 kV and 25 mA. The spectra were scanned within the 2θ range of 4 °- 80 ° with a step width of 0.06 ° and a speed of 10 s per step. The crystallite sizes were calculated with the Scherrer equation.

5.4 Catalytic testing

The catalytic testing reactions were performed in a high-pressure bench-type apparatus equipped with a fixed-bed flow-type reactor made from stainless steel. The process flow diagram of the used CO_2-FTS setup is shown in Figure 44. Prior to the catalytic experiments, the catalysts were reduced *in situ* for 30 min in a nitrogen flow containing 50 % hydrogen. In general, the catalytic activities and yields of the catalysts were tested at 200 °C to 400 °C in 50 °C steps and also screened over a time-on-stream period of about 12 hours at 350 °C. The pressure was kept constant a 20 bar with a syngas flow of 25 mL/min at a molar ratio H_2/CO_2 of 3:1.

The online GC analysis was performed using a HP Agilent 6890 gas chromatograph with a FID detector and a TCD detector. As carrier gas H_2 was used in a temperature range between 40 °C and 270 °C. The used GC column was a HP-PLOT/Q (19095P-QO4) with the dimensions 30 m · 0.530 mm.

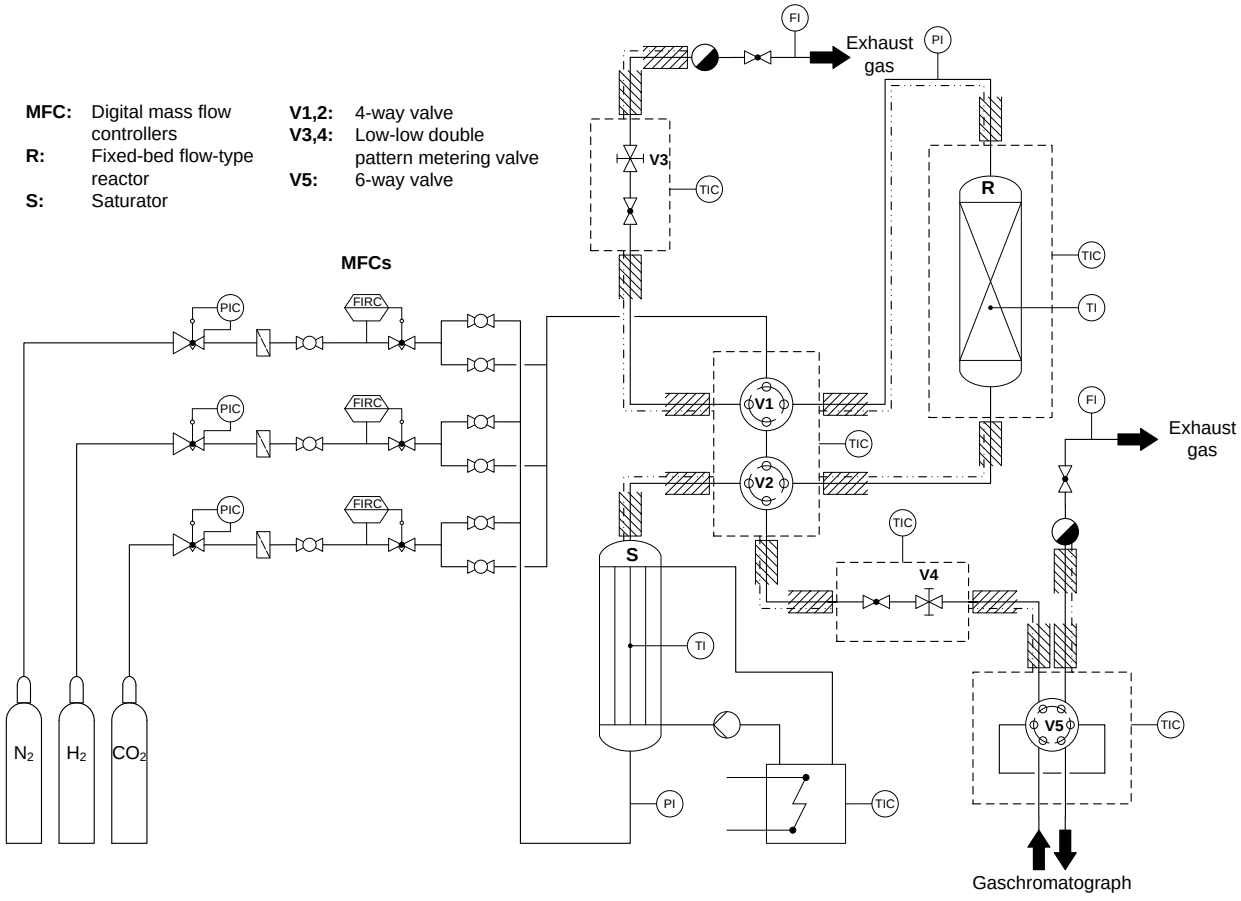

Figure 44: Process flow diagram for the CO_2-FTS setup.

5.4.1 Calculation of the composition of the product gas

For the analysis of the multicomponent samples, the method of surface normalization was used. The percentage ratios of the areas were assumed to correspond to the mass ratios within the samples (Eq. 6).

$$y_i = \frac{A_i}{\sum_j (A_j)} \qquad \text{Eq. 6}$$

However, heteroatom components within the samples lead to significant deviation for this first approximation. Hence, a device specific constant C and a substance-specific correction factor f_i were introduced as response factor. The mass m_i can now be calculated with the area A_i and the two factors (Eq. 7).

$$m_i = f_i \cdot A_i \cdot C \qquad \text{Eq. 7}$$

The device specific constant is the same for all measured components and can therefore be determined *via* a measurement of a mixture of a standard and different component (Eq. 8). The substance specific factor is calculated by equating the standard equation for C and the component specific equation for C (Eq. 9).

$$C = \frac{m_S}{f_S \cdot A_S} \; and \; C = \frac{m_i}{f_i \cdot A_i} \qquad \text{Eq. 8}$$

$$f_i = f_S \cdot \left(\frac{A_S}{A_i}\right) \cdot \left(\frac{m_i}{m_S}\right) \qquad \text{Eq. 9}$$

The substance specific factor could now be calculated for each component and the mass fraction y_i of each component within a mixture could be determined with Eq. 10.

$$y_i = \frac{f_i \cdot A_i}{\sum_j (f_j \cdot A_j)} \qquad \text{Eq. 10}$$

To equalize the signals of FID- and WLD-detector, methane was used as reference, due to the detectability by both detectors. Therefore, the mass ratios of each component were calculated in relation to Methane (Eq. 11).

$$\zeta_i = \frac{f_i \cdot A_i}{f_{CH_4} \cdot A_{CH_4}} \quad \text{Eq. 11}$$

The mass ratios of CO and CO_2 from the WLD-detector can now be normalized with the mass ratios of the hydrocarbons from the FID-detector, which leads to the mass fractions in the product gas flow (Eq. 12).

$$y_i = \frac{\zeta_i}{\sum_j (\zeta_j)} \quad \text{Eq. 12}$$

To calculate the conversion and yields, the molar flow of each component in the product gas flow was needed. Therefore, the mole fraction x_i was calculated first (Eq. 13).

$$x_i = \frac{\frac{y_i}{M_i}}{\sum_j (\frac{y_j}{M_j})} \quad \text{Eq. 13}$$

The starting molar flow of CO_2 can be calculated with the starting volume flow of CO_2 and the ideal gas law (Eq. 14).

$$\dot{n}_{CO_2,0} = \frac{P_{CO_2,0} \cdot \dot{V}_{CO_2,0}}{R \cdot T} \quad \text{Eq. 14}$$

Afterwards, the mole fractions of the hydrocarbons were multiplied by the starting molar flow of CO_2 to calculate the molar flow of each component (Eq. 15).

$$\dot{n}_i = \dot{n}_{CO_2,0} \cdot x_i \frac{|v_{CO_2}|}{v_i} \quad \text{Eq. 15}$$

With molar flow of each component, the conversion of CO_2 and the respective yields and selectivities could be calculated (Eq. 16 – 18).

$$X_{CO_2} = \frac{\dot{n}_{CO_2,0} - \dot{n}_{CO_2}}{\dot{n}_{CO_2,0}} \quad \text{Eq. 16}$$

$$Y_P = \frac{\dot{n}_P \cdot |v_{CO_2}|}{\dot{n}_{CO_2,0} \cdot v_P} \quad \text{Eq. 17}$$

$$S_P = \frac{\dot{n}_P \cdot \left|v_{CO_2}\right|}{\left(\dot{n}_{CO_2,0} - \dot{n}_{CO_2}\right) \cdot v_P} \qquad \text{Eq. 18}$$

6 Literature

[1] A. N. Stranges, *A History of the Fischer-Tropsch Synthesis in Germany 1926-45*. *Studies in surface science and catalysis*, **2007**.

[2] R. B. Anderson, *Catal. Energ. Sc.* **1984**, 457.

[3] H. Mahmoudi, M. Mahmoudi, O. Doustdar, H. Jahangiri, A. Tsolakis, S. Gu, M. Lech Wyszynski, *Biofuels Eng.* **2017**, *2*, 11.

[4] M. E. Dry, *Catal. Today* **2002**, *2002*, 227.

[5] D. Glasser, D. Hildebrandt, X. Liu, X. Lu, C. M. Masuku, *Curr. Opin. Chem. Eng.* **2012**, *1*, 296.

[6] M. Ojeda, R. Nabar, A. U. Nilekar, A. Ishikawa, M. Mavrikakis, E. Iglesia, *J. Catal.* **2010**, *272*, 287.

[7] B. H. Davis, *Fuel Process. Technol.* **2001**, *2001*, 157.

[8] H. Schulz, *Fuel Process. Technol.* **1988**, *18*, 293.

[9] Z. Gholami, F. Gholami, Z. Tišler, J. Hubáček, M. Tomas, M. Bačiak, M. Vakili, *Catalyst* **2022**, *12*, 174.

[10] A. de Klerk (Ed.) *Fischer-Tropsch Refining*, Wiley-VCH, **2013**.

[11] X. Wang, M. Economides, *Advanced Natural Gas Engineering*, Elsevier Science, **2013**.

[12] W. Keim, *Angew. Chem. Int. Edit.* **1985**, *97*, 891.

[13] N. Moazami, H. Mahmoudi, K. Rahbar, P. Panahifar, A. Tsolakis, M. L. Wyszynski, *Chem. Eng. Sci.* **2015**, *134*, 374.

[14] F. Jiao, J. Li, X. Pan, J. Xiao, H. Li, H. Ma, M. Wei, Y. Pan, Z. Zhou, M. Li, S. Miao, J. Li, Y. Zhu, D. Xiao, T. He, J. Yang, F. Qi, Q. Fu, X. Bao, *Science* **2016**, *351*, 1065.

[15] D. Selvatico, A. Lanzini, M. Santarelli, *Fuel* **2016**, *186*, 544.

[16] A. P. Steynberg, M. E. Dry, B. H. Davis, B. B. Breman in *Studies in Surface Science and Catalysis*, Elsevier, **2004**, pp. 64–195.

[17] J. van de Loosdrecht, F. G. Botes, I. M. Ciobica, A. Ferreira, P. Gibson, D. J. Moodley, A. M. Saib, J. L. Visagie, C. J. Weststrate, J. W. Niemantsverdriet in *Fischer-Tropsch Refining* (Ed.: A. de Klerk), Wiley-VCH, **2013**, pp. 525–557.

[18] G. P. van der Laan, A.A. C. M. Beenackers, *Rev. Catal.* **1999**, *41*, 255.

[19] T. Donnelly, *Appl. Catal.* **1989**, *52*, 93.

[20] D. B. Bukur, *Appl. Catal.* **1990**, *61*, 329.

[21] E. Iglesia, S. C. Reyes, R. J. Madon, S. L. Soled in *Advances in Catalysis*, Elsevier, **1993**, pp. 221–302.

[22] D. Gilfillan, G. Marland, *Earth Syst. Sci. Data* **2021**, *13*, 1667.

[23] Y. F. Zhu, B. Xie, R. Amal, E. C. Lovell, J. Scott, *Small Struct.* **2023**, *4*, 2200285.

[24] M. D. Garba, M. Usman, S. Khan, F. Shehzad, A. Galadima, M. F. Ehsan, A. S. Ghanem, M. Humayun, *J. Environ. Chem. Eng.* **2021**, *9*, 104756.

[25] P. Gao, L. Zhang, S. Li, Z. Zhou, Y. Sun, *ACS Cent. Sci.* **2020**, *6*, 1657.

[26] A. D. Kamkeng, M. Wang, J. Hu, W. Du, F. Qian, *J. Chem. Eng.* **2021**, *409*, 128138.

[27] E. A. Quadrelli, G. Centi, J.-L. Duplan, S. Perathoner, *ChemSusChem* **2011**, *4*, 1194.

[28] J. Albero, Y. Peng, H. García, *ACS Catal.* **2020**, *10*, 5734.

[29] I. Amghizar, J. N. Dedeyne, D. J. Brown, G. B. Marin, K. M. van Geem, *React. Chem. Eng.* **2020**, *5*, 239.

[30] W. Li, H. Wang, X. Jiang, J. Zhu, Z. Liu, X. Guo, C. Song, *RSC Adv.* **2018**, *8*, 7651.

[31] R.-P. Ye, J. Ding, W. Gong, M. D. Argyle, Q. Zhong, Y. Wang, C. K. Russell, Z. Xu, A. G. Russell, Q. Li, M. Fan, Y.-G. Yao, *Nat. Commun.* **2019**, *10*, 5698.

[32] L. Zhou, J. Gao, X. Hao, Y. Yang, Y. Li, *React.* **2021**, *2*, 161.

[33] B. Todic, L. Nowicki, N. Nikacevic, D. B. Bukur, *Catal. Today* **2016**, *261*, 28.

[34] T. Riedel, *Appl. Catal. A* **1999**, *186*, 201.

[35] D. Goud, R. Gupta, R. Maligal-Ganesh, S. C. Peter, *ACS Catal.* **2020**, *10*, 14258.

[36] R. A. Iloy, K. Jalama, *Catalysts* **2019**, *9*, 807.

[37] E. de Smit, B. M. Weckhuysen, *Chem. Soc. Rev* **2008**, *37*, 2758.

[38] H. Schulz, T. Riedel, G. Schaub, *Top. Catal.* **2005**, *32*, 117.

[39] X. Nie, L. Meng, H. Wang, Y. Chen, X. Guo, C. Song, *Phys. Chem. Chem. Phys.* **2018**, *20*, 14694.

[40] M. Zhang, J. Ren, Y. Yu, *ACS Catal.* **2020**, *10*, 689.

[41] J.-X. Liu, P. Wang, W. Xu, E. J. Hensen, *Eng. J.* **2017**, *3*, 467.

[42] Y. Zhang, D. Fu, X. Liu, Z. Zhang, C. Zhang, B. Shi, J. Xu, Y.-F. Han, *ChemCatChem* **2018**, *10*, 1272.

[43] A. Nakhaei Pour, M. R. Housaindokht, S. F. Tayyari, J. Zarkesh, M. R. Alaei, *J. Mol. Catal.* **2010**, *330*, 112.

[44] E. de Smit, F. Cinquini, A. M. Beale, O. V. Safonova, W. van Beek, P. Sautet, B. M. Weckhuysen, *J. Am. Chem. Soc.* **2010**, *132*, 14928.

[45] Q. Chang, C. Zhang, C. Liu, Y. Wei, A. V. Cheruvathur, A. I. Dugulan, J. W. Niemantsverdriet, X. Liu, Y. He, M. Qing, L. Zheng, Y. Yun, Y. Yang, Y. Li, *ACS Catal.* **2018**, *8*, 3304.

[46] S. Li, R. J. O Brien, G. D. Meitzner, H. Hamdeh, B. H. Davis, E. Iglesia, *Appl. Catal. A* **2001**, *2001*, 215.

[47] T. Herranz, S. Rojas, F. J. Pérez-Alonso, M. Ojeda, P. Terreros, J. Fierro, *Appl. Catal. A* **2006**, *311*, 66.

[48] X. Zhang, Q. Lin, B. Liu, J. Zheng, F. Jiang, Y. Xu, X. Liu, *Appl. Catal. A* **2019**, *572*, 197.

[49] M. Ding, Y. Yang, B. Wu, Y. Li, T. Wang, L. Ma, *Appl. Energ.* **2015**, *160*, 982.

[50] A. Y. Khodakov, W. Chu, P. Fongarland, *Chem. Rev.* **2007**, *107*, 1692.

[51] A. Y. Khodakov, *Catal. Today* **2009**, *144*, 251.

[52] D. D. Suppiah, W. M. A. W. Daud, M. R. Johan, *Energ. Fuel* **2021**, *35*, 17261.

[53] Y. Zhang, G. Jacobs, D. Sparks, M. E. Dry, B. H. Davis, *Catal. Today* **2002**, *71*, 411.

[54] C. G. Visconti, L. Lietti, E. Tronconi, P. Forzatti, R. Zennaro, E. Finocchio, *Appl. Catal. A* **2009**, *355*, 61.

[55] Z. Shi, H. Yang, P. Gao, X. Li, L. Zhong, H. Wang, H. Liu, W. Wei, Y. Sun, *Catal. Today* **2018**, *311*, 65.

[56] R. Lizárraga, F. Pan, L. Bergqvist, E. Holmström, Z. Gercsi, L. Vitos, *Sci. Rep.* **2017**, *7*, 3778.

[57] I. C. ten Have, B. M. Weckhuysen, *Chem Catal.* **2021**, *1*, 339.

[58] T. Lin, Y. An, F. Yu, K. Gong, H. Yu, C. Wang, Y. Sun, L. Zhong, *ACS Catal.* **2022**, *12*, 12092.

[59] M. Wang, G. Zhang, J. Zhu, W. Li, J. Wang, K. Bian, Y. Liu, F. Ding, C. Song, X. Guo, *J. Chem. Eng.* **2022**, *446*, 137217.

[60] C. Scarfiello, D. Pham Minh, K. Soulantica, P. Serp, *Adv. Mater. Interfaces* **2023**, *10*.

[61] R. E. Owen, P. Plucinski, D. Mattia, L. Torrente-Murciano, V. P. Ting, M. D. Jones, *J. CO2 Util.* **2016**, *16*, 97.

[62] X. Ma, Q. Sun, W. Ying, D. Fang, *J. Nat. Gas Chem.* **2009**, *18*, 232.

[63] A. A. Mirzaei, A. B. babaei, M. Galavy, A. Youssefi, *Fuel Process. Technol.* **2010**, *91*, 335.

[64] A. Tavasoli, M. Trépanier, R. M. Malek Abbaslou, A. K. Dalai, N. Abatzoglou, *Fuel Process. Technol.* **2009**, *90*, 1486.

[65] R. Satthawong, N. Koizumi, C. Song, P. Prasassarakich, *J. CO2 Util.* **2013**, *3-4*, 102.

[66] F. Jiang, B. Liu, S. Geng, Y. Xu, X. Liu, *Catal. Sci. Technol.* **2018**, *8*, 4097.

[67] Z. Li, J. Liu, Y. Zhao, G. I. N. Waterhouse, G. Chen, R. Shi, X. Zhang, X. Liu, Y. Wei, X.-D. Wen, L.-Z. Wu, C.-H. Tung, T. Zhang, *Adv. Mater.* **2018**, *30*, 1800527.

[68] T. Numpilai, N. Chanlek, Y. Poo-Arporn, S. Wannapaiboon, C. K. Cheng, N. Siri-Nguan, T. Sornchamni, P. Kongkachuichay, M. Chareonpanich, G. Rupprechter, J. Limtrakul, T. Witoon, *Appl. Surf. Sci.* **2019**, *483*, 581.

[69] U. Tumuluri, J. D. Howe, W. P. Mounfield, M. Li, M. Chi, Z. D. Hood, K. S. Walton, D. S. Sholl, S. Dai, Z. Wu, *ACS Sustain. Chem. Eng.* **2017**, *5*, 9295.

[70] N. Boreriboon, X. Jiang, C. Song, P. Prasassarakich, *J. CO2 Util.* **2018**, *25*, 330.

[71] H. Suo, S. Wang, C. Zhang, J. Xu, B. Wu, Y. Yang, H. Xiang, Y.-W. Li, *J. Catal.* **2012**, *286*, 111.

[72] L. Torrente-Murciano, R. S. L. Chapman, A. Narvaez-Dinamarca, D. Mattia, M. D. Jones, *Phys. Chem. Chem. Phys.* **2016**, *18*, 15496.

[73] K. Cheng, V. V. Ordomsky, M. Virginie, B. Legras, P. A. Chernavskii, V. O. Kazak, C. Cordier, S. Paul, Y. Wang, A. Y. Khodakov, *Appl. Catal. A* **2014**, *488*, 66.

[74] M. J. Valero-Romero, M. Á. Rodríguez-Cano, J. Palomo, J. Rodríguez-Mirasol, T. Cordero, *Front. Mater.* **2021**, *7*, 617432.

[75] Y. Yang, K. Chiang, N. Burke, *Catalysis Today* **2011**, *178*, 197.

[76] K. P. Reddy, S. Dama, N. B. Mhamane, M. K. Ghosalya, T. Raja, C. V. Satyanarayana, C. S. Gopinath, *Dalton Trans.* **2019**, *48*, 12199.

[77] L. Guo, P. Zhang, Y. Cui, G. Liu, J. Wu, G. Yang, Y. Yoneyama, N. Tsubaki, *ACS Sustainable Chem. Eng.* **2019**, *7*, 8331.

[78] M. Albrecht, U. Rodemerck, M. Schneider, M. Bröring, D. Baabe, E. V. Kondratenko, *Appl. Catal. B* **2017**, *204*, 119.

[79] Y. A. Pokusaeva, A. E. Koklin, V. V. Lunin, V. I. Bogdan, *Mendeleev Communications* **2019**, *29*, 382.

[80] L. Guo, Y. Cui, P. Zhang, X. Peng, Y. Yoneyama, G. Yang, N. Tsubaki, *ChemistrySelect* **2018**, *3*, 13705.

[81] M. V. Landau, R. Vidruk, M. Herskowitz, *ChemSusChem* **2014**, *7*, 785.

[82] W. Ning, B. Li, B. Wang, X. Yang, Y. Jin, *Catal. Lett.* **2019**, *149*, 431.

[83] Z. He, M. Cui, Q. Qian, J. Zhang, H. Liu, B. Han, *Proc. Natl. Acad. Sci. USA* **2019**, *116*, 12654.

[84] D. Wang, Z. Xie, M. D. Porosoff, J. G. Chen, *Chem* **2021**, *7*, 2277.

[85] J. Wei, J. Sun, Z. Wen, C. Fang, Q. Ge, H. Xu, *Catal. Sci. Technol.* **2016**, *6*, 4786.

[86] N. Boreriboon, X. Jiang, C. Song, P. Prasassarakich, *Top. Catal.* **2018**, *61*, 1551.

[87] M. Russo, V. La Parola, G. Pantaleo, M. L. Testa, A. Bordoloi, R. K. Gupta, R. Bal, A. M. Venezia, *Top. Catal.* **2020**, *63*, 1424.

[88] R. Satthawong, N. Koizumi, C. Song, P. Prasassarakich, *Catal. Today* **2015**, *251*, 34.

[89] A. J. Barrios, D. V. Peron, A. Chakkingal, A. I. Dugulan, S. Moldovan, K. Nakouri, J. Thuriot-Roukos, R. Wojcieszak, J. W. Thybaut, M. Virginie, A. Y. Khodakov, *ACS Catal.* **2022**, *12*, 3211.

[90] B. H. Davis, *Ind. Eng. Chem. Res.* **2007**, *46*, 8938.

[91] S.-M. Hwang, S. J. Han, H.-G. Park, H. Lee, K. An, K.-W. Jun, S. K. Kim, *ACS Catal.* **2021**, *11*, 2267.

[92] W. Wang, E. Toshcheva, A. Ramirez, G. Shterk, R. Ahmad, M. Caglayan, J. L. Cerrillo, A. Dokania, G. Clancy, T. B. Shoinkhorova, N. Hijazi, L. Cavallo, J. Gascon, *Catal. Sci. Technol.* **2023**, *13*, 1527.

[93] Q. Yang, V. A. Kondratenko, S. A. Petrov, D. E. Doronkin, E. Saraçi, H. Lund, A. Arinchtein, R. Kraehnert, A. S. Skrypnik, A. A. Matvienko, E. V. Kondratenko, *Angew. Chem. Int. Edit.* **2022**, *61*, 202116517.

[94] M. Zhu, P. Tian, M. E. Ford, J. Chen, J. Xu, Y.-F. Han, I. E. Wachs, *ACS Catal.* **2020**, *10*, 7857.

[95] T. Zhang, J. Liu, D. Wang, Z. Zhao, Y. Wei, K. Cheng, G. Jiang, A. Duan, *Appl. Catal. B* **2014**, *148-149*, 520.

[96] L. Luo, C. Dai, A. Zhang, J. Wang, M. Liu, C. Song, X. Guo, *Catal. Sci. Technol.* **2015**, *5*, 3159.

[97] D. Pena, L. Jensen, R. M. A. Cognigni, T. Neumayer, W. van Beek, M. Ronning, *ChemCatChem* **2017**, *10*, 1300.

[98] P. A. Chernavskii, V. O. Kazak, G. V. Pankina, Y. D. Perfiliev, T. Li, M. Virginie, A. Y. Khodakov, *Catal. Sci. Technol.* **2017**, *7*, 2325.

[99] Z. H. Chonco, A. Ferreira, L. Lodya, M. Claeys, E. van Steen, *J. Catal.* **2013**, *307*, 283.

[100] Z. H. Chonco, L. Lodya, M. Claeys, E. van Steen, *J. Catal.* **2013**, *308*, 363.

[101] J. Liu, A. Zhang, X. Jiang, M. Liu, Y. Sun, C. Song, X. Guo, *ACS Sustain. Chem. Eng.* **2018**, *6*, 10182.

[102] Y. H. Choi, Y. J. Jang, H. Park, W. Y. Kim, Y. H. Lee, S. H. Choi, J. S. Lee, *Appl. Catal. B* **2017**, *202*, 605.

[103] J. Jiang, C. Wen, Z. Tian, Y. Wang, Y. Zhai, L. Chen, Y. Li, Q. Liu, C. Wang, L. Ma, *Ind. Eng. Chem. Res.* **2020**, *59*, 2155.

[104] B. Liang, T. Sun, J. Ma, H. Duan, L. Li, X. Yang, Y. Zhang, X. Su, Y. Huang, T. Zhang, *Catal. Sci. Technol.* **2019**, *9*, 456.

[105] S. L. James, *Chem. Soc. Rev.* **2003**, *32*, 276.

[106] H.-C. J. Zhou, S. Kitagawa, *Chem. Soc. Rev.* **2014**, *43*, 5415.

[107] Q. Wang, D. Astruc, *Chem. Rev.* **2020**, *120*, 1438.

[108] M. Liu, J. Wu, H. Hou, *Chemistry* **2019**, *25*, 2935.

[109] S. He, L. Wu, X. Li, H. Sun, T. Xiong, J. Liu, C. Huang, H. Xu, H. Sun, W. Chen, R. Gref, J. Zhang, *Acta Pharm. Sin. B* **2021**, *11*, 2362.

[110] J.-R. Li, R. J. Kuppler, H.-C. Zhou, *Chem. Soc. Rev.* **2009**, *38*, 1477.

[111] N. L. Rosi, J. Eckert, M. Eddaoudi, D. T. Vodak, J. Kim, M. O'Keeffe, O. M. Yaghi, *Science* **2003**, *300*, 1127.

[112] T. Qiu, Z. Liang, W. Guo, H. Tabassum, S. Gao, R. Zou, *ACS Energy Lett.* **2020**, *5*, 520.

[113] A. Sultana, A. Kathuria, K. K. Gaikwad, *Environ. Chem. Lett.* **2022**, *20*, 1479.

[114] K. Xiao, B. Shu, K. Lv, P. Huang, Q. Chang, L. Wu, S. Wang, L. Cao, *Catalysts* **2023**, *13*, 734.

[115] H. V. Tran, H. T. M. Dang, L. T. Tran, C. van Tran, C. D. Huynh, *Adv. Polym. Technol.* **2020**, *2020*, 1.

[116] D.-W. Lim, H. Kitagawa, *Chem. Soc. Rev.* **2021**, *50*, 6349.

[117] Q. Wang, Q. Gao, A. M. Al-Enizi, A. Nafady, S. Ma, *Inorg. Chem. Front.* **2020**, *7*, 300.

[118] R. A. Fischer, I. Schwedler, *Angew. Chem.* **2014**, *126*, 7209.

[119] S. R. Batten, N. R. Champness, X.-M. Chen, J. Garcia-Martinez, S. Kitagawa, L. Öhrström, M. O'Keeffe, M. P. Suh, J. Reedijk, *CrystEngComm* **2012**, *14*, 3001.

[120] I. Senkovska, F. Hoffmann, M. Fröba, J. Getzschmann, W. Böhlmann, S. Kaskel, *Microporous Mesoporous Mater.* **2009**, *122*, 93.

[121] J. Bitzer, W. Kleist, *Chem. Eur. J.* **2019**, *25*, 1866.

[122] A. D. Burrows, *CrystEngComm* **2011**, *13*, 3623.

[123] W. Yu, M. D. Porosoff, J. G. Chen, *Rev. Catal.* **2012**, *112*, 5780.

[124] L. J. Wang, H. Deng, H. Furukawa, F. Gándara, K. E. Cordova, D. Peri, O. M. Yaghi, *Inorg. Chem.* **2014**, *53*, 5881.

[125] S. M. Cohen, Z. Zhang, J. A. Boissonnault, *Inorg. Chem.* **2016**, *55*, 7281.

[126] T.-F. Liu, N. A. Vermeulen, A. J. Howarth, P. Li, A. A. Sarjeant, J. T. Hupp, O. K. Farha, *Eur. J. Inorg. Chem.* **2016**, *2016*, 4349.

[127] M. Meilikhov, K. Yusenko, D. Esken, S. Turner, G. van Tendeloo, R. A. Fischer, *Eur. J. Inorg. Chem.* **2010**, *2010*, 3701.

[128] D. N. Bunck, W. R. Dichtel, *Chem. Eur. J.* **2013**, *19*, 818.

[129] Z. Yin, Y.-L. Zhou, M.-H. Zeng, M. Kurmoo, *J. Chem Soc.* **2015**, *44*, 5258.

[130] C. Yildiz, K. Kutonova, S. Oßwald, A. Titze-Alonso, J. Bitzer, S. Bräse, W. Kleist, *ChemCatChem* **2020**, *12*, 1134.

[131] Q. Liu, H. Cong, H. Deng, *J. Am. Chem. Soc.* **2016**, *138*, 13822.

[132] H. J. Lee, Y. J. Cho, W. Cho, M. Oh, *ACS nano* **2013**, *7*, 491.

[133] F. Hillman, J. M. Zimmerman, S.-M. Paek, M. R. A. Hamid, W. T. Lim, H.-K. Jeong, *J. Mater. Chem. A* **2017**, *5*, 6090.

[134] F. Millange, R. I. Walton, *Isr. J. Chem.* **2018**, *58*, 1019.

[135] C. Serre, F. Millange, C. Thouvenot, M. Noguès, G. Marsolier, D. Louër, G. Férey, *J. Am. Chem. Soc.* **2002**, *124*, 13519.

[136] J. Bitzer, M. Teubnerová, W. Kleist, *Chem. Eur. J.* **2021**, *27*, 1724.

[137] F. Millange, N. Guillou, R. I. Walton, J.-M. Grenèche, I. Margiolaki, G. Férey, *Chem. Commun.* **2008**, 4732.

[138] A. S. Munn, G. J. Clarkson, F. Millange, Y. Dumont, R. I. Walton, *CrystEngComm* **2013**, *15*, 9679.

[139] T. Rodenas, M. van Dalen, E. García-Pérez, P. Serra-Crespo, B. Zornoza, F. Kapteijn, J. Gascon, *Adv. Funct. Mater.* **2014**, *24*, 249.

[140] M. Mubashir, Y. F. Yeong, K. K. Lau, T. L. Chew, J. Norwahyu, *Sep. Purif Technol.* **2018**, *199*, 140.

[141] H. Nasser Abdelhamid, A. P. Mathew, *J. Chem. Eng.* **2021**, *426*, 131733.

[142] L. Oar-Arteta, T. Wezendonk, X. Sun, F. Kapteijn, J. Gascon, *Mater. Chem. Front.* **2017**, *1*, 1709.

[143] B. Liu, H. Shioyama, T. Akita, Q. Xu, *J. Am. Chem. Soc.* **2008**, *130*, 5390.

[144] M. Enterría, J. L. Figueiredo, *Carbon* **2016**, *108*, 79.

[145] S. Deng, M. Kurttepeli, D. J. Cott, S. Bals, C. Detavernier, *J. Mater. Chem. A* **2015**, *3*, 2642.

[146] T. A. Wezendonk, Q. S. E. Warringa, V. P. Santos, A. Chojecki, M. Ruitenbeek, G. Meima, M. Makkee, F. Kapteijn, J. Gascon, *Faraday Discuss.* **2017**, *197*, 225.

[147] T. A. Wezendonk, X. Sun, A. I. Dugulan, A. J. van Hoof, E. J. Hensen, F. Kapteijn, J. Gascon, *J. Catal.* **2018**, *362*, 106.

[148] R. Das, P. Pachfule, R. Banerjee, P. Poddar, *Nanoscale* **2012**, *4*, 591.

[149] L. Oar-Arteta, M. J. Valero-Romero, T. Wezendonk, F. Kapteijn, J. Gascon, *Catal. Sci. Technol.* **2018**, *8*, 210.

[150] S. Hu, M. Liu, F. Ding, C. Song, G. Zhang, X. Guo, *J. CO2 Util.* **2016**, *15*, 89.

[151] K. O. Otun, X. Liu, D. Hildebrandt, *J. Energy Chem.* **2020**, *51*, 230.

[152] Y. Pei, Z. Li, Y. Li, *AIChE J.* **2017**, *63*, 2935.

[153] Z. Wang, G. Laddha, S. Kanitkar, J. J. Spivey, *Catal. Today* **2017**, *298*, 209.

[154] Q.-X. Luo, L.-P. Guo, S.-Y. Yao, J. Bao, Z.-T. Liu, Z.-W. Liu, *J. Catal.* **2019**, *369*, 143.

[155] V. P. Santos, T. A. Wezendonk, J. J. D. Jaén, A. I. Dugulan, M. A. Nasalevich, H.-U. Islam, A. Chojecki, S. Sartipi, X. Sun, A. A. Hakeem, A. C. J. Koeken, M. Ruitenbeek, T. Davidian, G. R. Meima, G. Sankar, F. Kapteijn, M. Makkee, J. Gascon, *Nat. Commun.* **2015**, *6*, 6451.

[156] B. An, K. Cheng, C. Wang, Y. Wang, W. Lin, *ACS Catal.* **2016**, *6*, 3610.

[157] R. Nivetha, P. Kollu, K. Chandar, S. Pitchaimuthu, S. K. Jeong, A. N. Grace, *RSC Adv.* **2019**, *9*, 3215.

[158] C.E. Johnson, *Hyperfine Interact.* **1992**, *72*, 15.

[159] M. Zhang, F. Yan, J. Bai, X. Li, X. Zheng, J. Dou, X. Wang, W. Zhang, B. Zhou, *Microporous Mesoporous Mater.* **2021**, *312*, 110627.

[160] P. Veerakumar, S. Balakumar, M. Velayudham, K.-L. Lu, S. Rajagopal, *Catal. Sci. Technol.* **2012**, *2*, 1140.

[161] X. Li, Z. Zhai, C. Tang, L. Sun, Y. Zhang, W. Bai, *RSC Adv.* **2016**, *6*, 62252.

[162] T. H. Pham, Y. Qi, J. Yang, X. Duan, G. Qian, X. Zhou, de Chen, W. Yuan, *ACS Catal.* **2015**, *5*, 2203.

[163] T. Riedel, M. Claeys, H. Schulz, G. Schaub, S.S. Nam, K.W. Jun, M.J. Choi, G. Kishan, K.w. Lee, *Appl. Catal. A* **1999**, *186*, 201.

[164] W. Brockner, C. Ehrhardt, M. Gjikaj, *Thermochim. Acta* **2007**, *456*, 64.

[165] N. Prinz, L. Schwensow, S. Wendholt, A. Jentys, M. Bauer, W. Kleist, M. Zobel, *Nanoscale* **2020**, *12*, 15800.

[166] W.P. Dow, Y.P. Wang, T.J. Huang, *Appl. Catal. A* **2000**, 25.

[167] D. Joseph, D. Bhattacharya, S.N. Jha, K.J. Milton, M. V. Ramanna, *Asian J. of Adv. Basic Sci.* **2014**, *3*, 60.

[168] S. Lyu, C. Guo, J. Wang, Z. Li, B. Yang, L. Lei, L. Wang, J. Xiao, T. Zhang, Y. Hou, *Nat. Commun.* **2022**, *13*, 6171.

7 Appendix

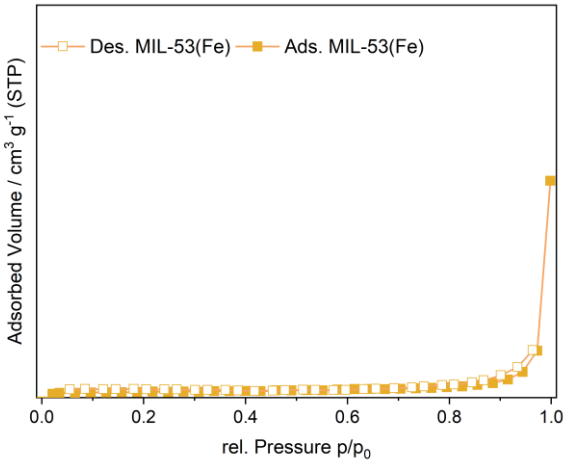

Figure A 1: Nitrogen physisorption isotherm of the MIL-53(Fe) MOF precursor.

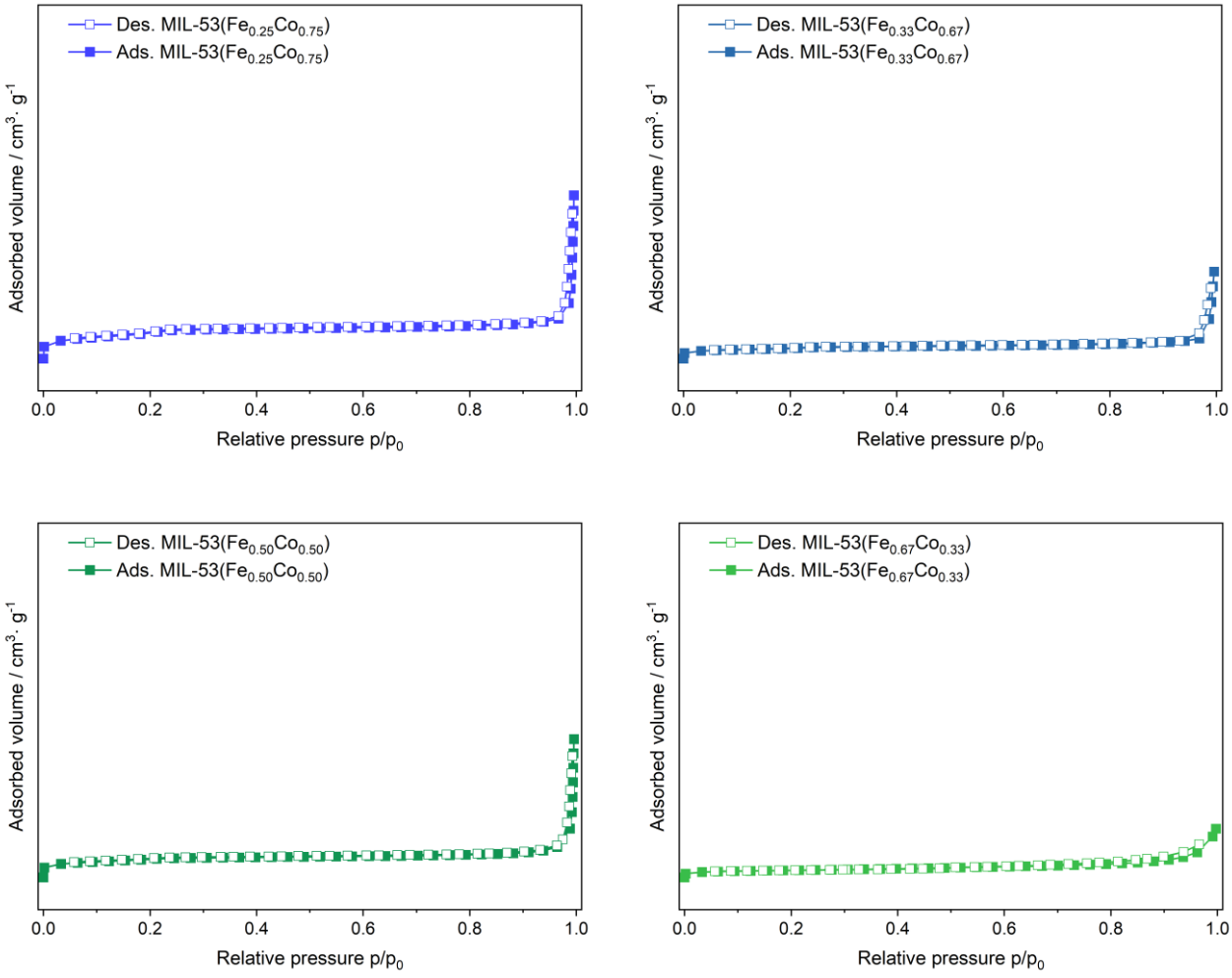

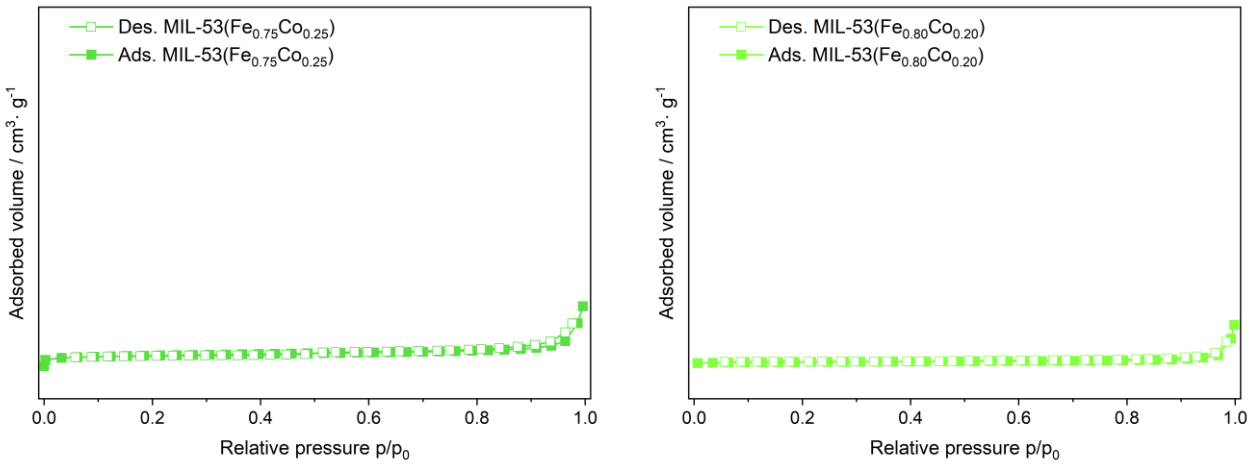

Figure A 2: Nitrogen physisorption isotherms of the MIL-53(Fe_xCo_{1-x}) MOF precursors.

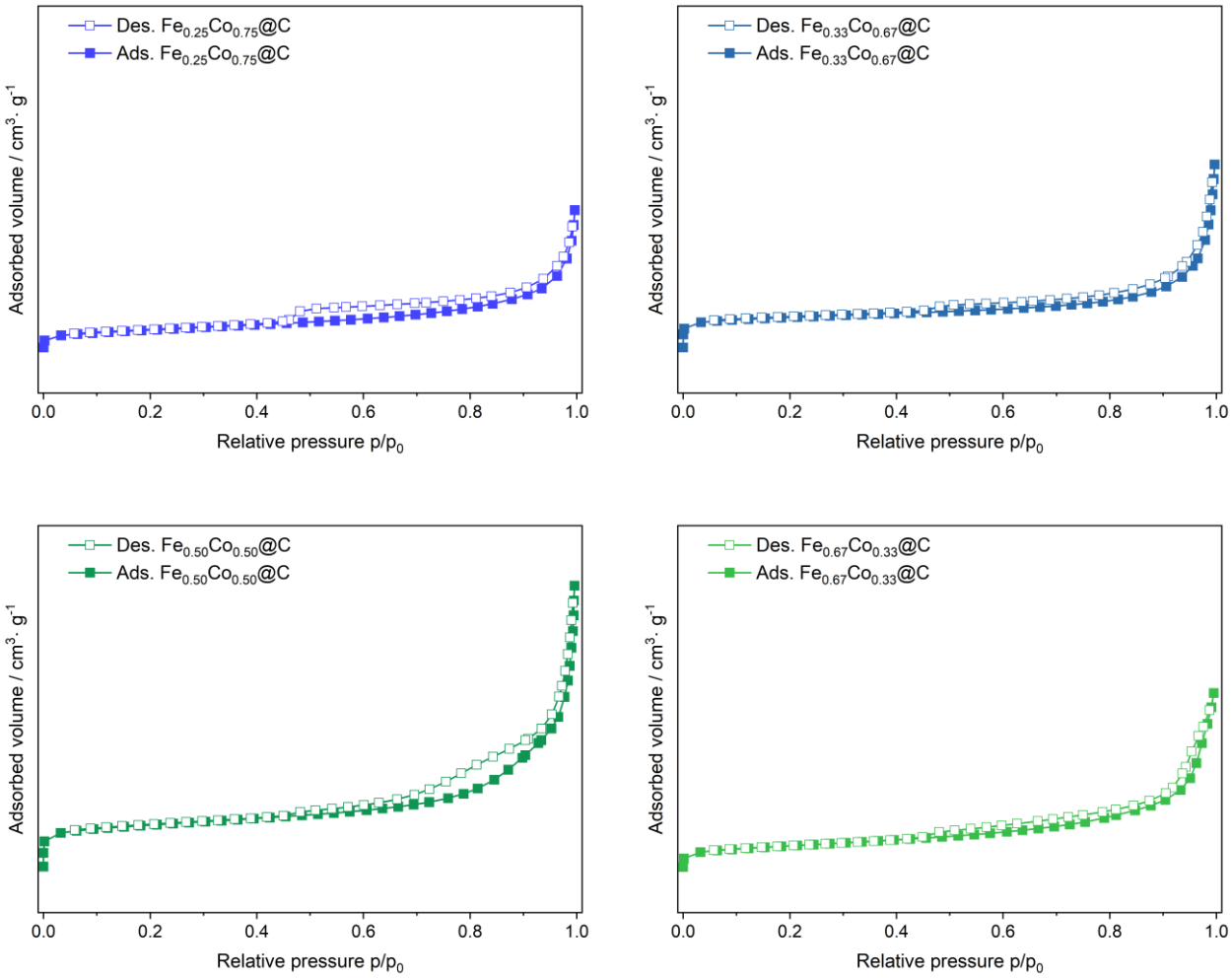

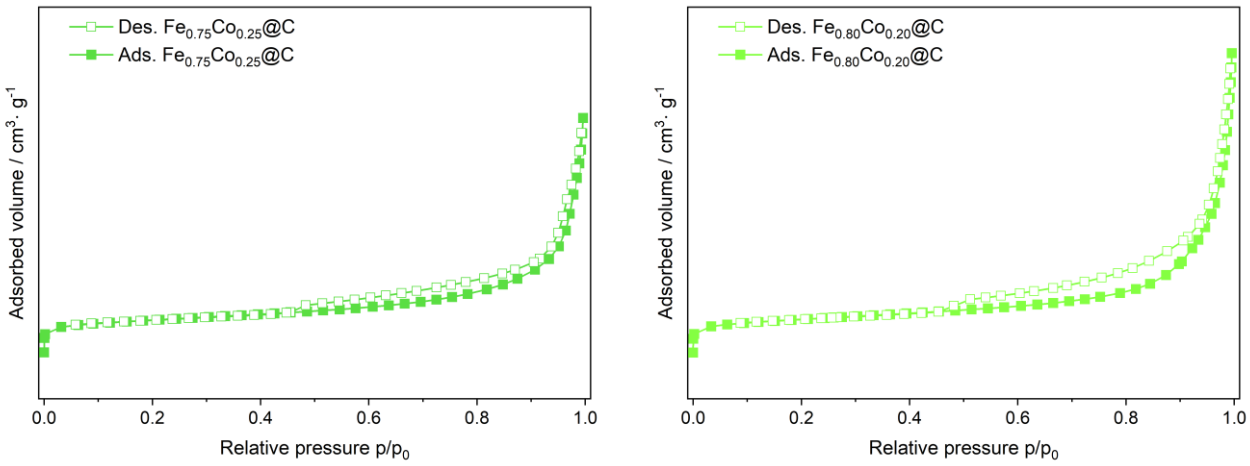

Figure A 3: Nitrogen physisorption isotherms of the Fe_xCo_{1-x}@C MOFMS catalysts.

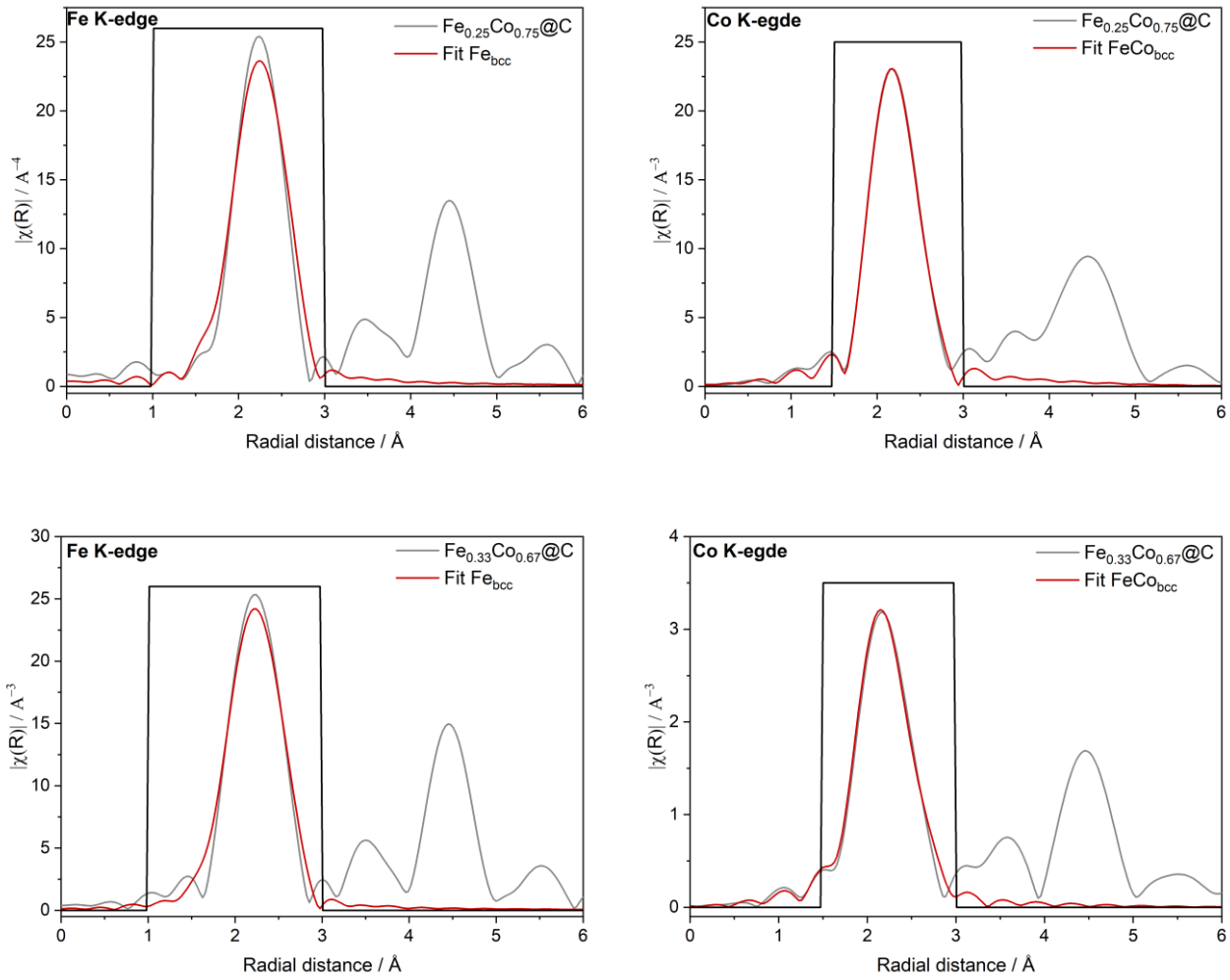

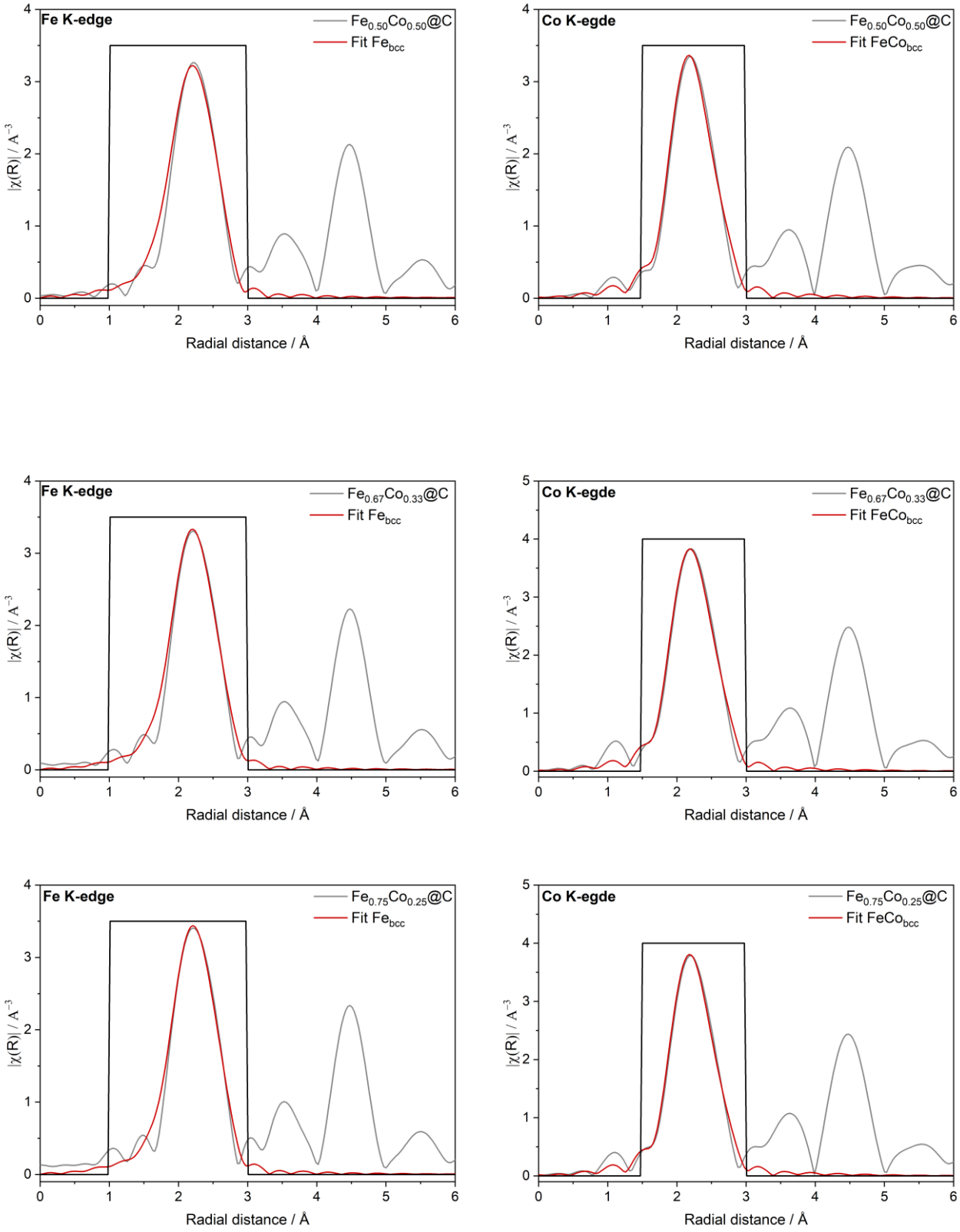

Figure A 4: R-space fits of the Fe_xCo_{1-x}@C MOFMS catalysts measured at the Fe K-edge and Co K-edge.

Table A 1: Fitting parameter of the R-space fits of the Fe_xCo_{1-x}@C MOFMS catalysts measured at the Fe K-edge and Co K-edge.

Sample	Scattering path	N	R_{eff}	ΔR	R	σ^2
$Fe_{0.25}Co_{0.75}$@C	Fe1- Fe_{bcc}	8	2.460	-0.0135±0.0203	2.446	0.0098±0.0014
Fe K edge	Fe2- Fe_{bcc}	6	2.840	-0.0351±0.0178	2.805	0.0053±0.0013
$Fe_{0.25}Co_{0.75}$@C	Fe - $FeCo_{bcc}$	8	2.458	0.0206±0.0097	2.479	0.0061±0.0005
Co K edge	Co - $FeCo_{bcc}$	6	2.839	0.0079±0.0134	2.847	0.0129±0.0026
$Fe_{0.33}Co_{0.67}$@C	Fe1- Fe_{bcc}	8	2.460	-0.0081±0.0080	2.439	0.0092±0.0013
Fe K edge	Fe2- Fe_{bcc}	6	2.840	-0.0081±0.0080	2.817	0.0059±0.0017
$Fe_{0.33}Co_{0.67}$@C	Fe - $FeCo_{bcc}$	8	2.458	0.0053±0.0169	2.464	0.0066±0.0009
Co K edge	Co - $FeCo_{bcc}$	6	2.839	0.0086±0.0025	2.833	0.0086±0.0025
$Fe_{0.50}Co_{0.50}$@C	Fe1- Fe_{bcc}	8	2.460	-0.0073±0.0082	2.442	0.0094±0.0014
Fe K edge	Fe2- Fe_{bcc}	6	2.840	-0.0073±0.0082	2.819	0.0055±0.0016
$Fe_{0.50}Co_{0.50}$@C	Fe - $FeCo_{bcc}$	8	2.458	0.0011±0.0240	2.459	0.00673±0.00136
Co K edge	Co - $FeCo_{bcc}$	6	2.839	-0.0033±0.0224	2.835	0.0067±0.0027
$Fe_{0.67}Co_{0.33}$@C	Fe1- Fe_{bcc}	8	2.460	-0.0014±0.0072	2.459	0.0087±0.0012

Fe K edge	Fe2- Fe_{bcc}	6	2.840	- 0.0014±0.0072	2.840	0.0062±0.0017
$Fe_{0.67}Co_{0.33}$@C	Fe - $FeCo_{bcc}$	8	2.458	- 0.0024±0.0204	2.459	0.0059±0.0011
Co K edge	Co - $FeCo_{bcc}$	6	2.839	0.0056±0.0203	2.839	0.0052±0.0020
$Fe_{0.50}Co_{0.50}$@C	Fe1- Fe_{bcc}	8	2.460	- 0.0026±0.0073	2.459	0.0085±0.0012
Fe K edge	Fe2- Fe_{bcc}	6	2.840	- 0.0026±0.0073	2.840	0.0056±0.0016
$Fe_{0.50}Co_{0.50}$@C	Fe - $FeCo_{bcc}$	8	2.458	0.0011±0.0192	2.459	0.0057±0.0010
Co K edge	Co - $FeCo_{bcc}$	6	2.839	0.0051±0.0194	2.844	0.0057±0.0021

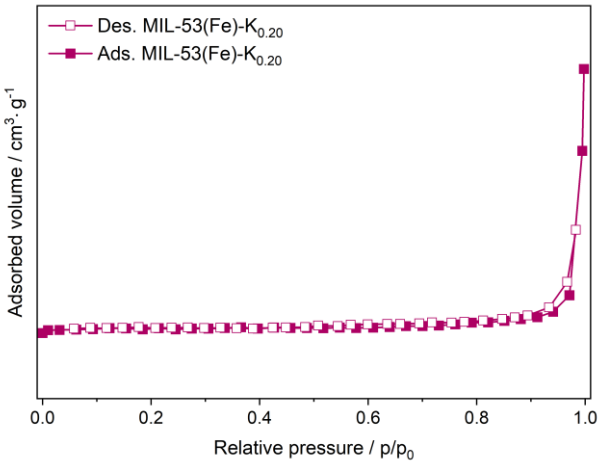

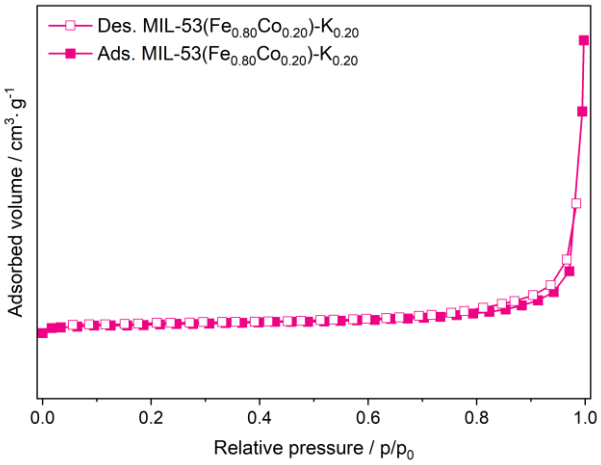

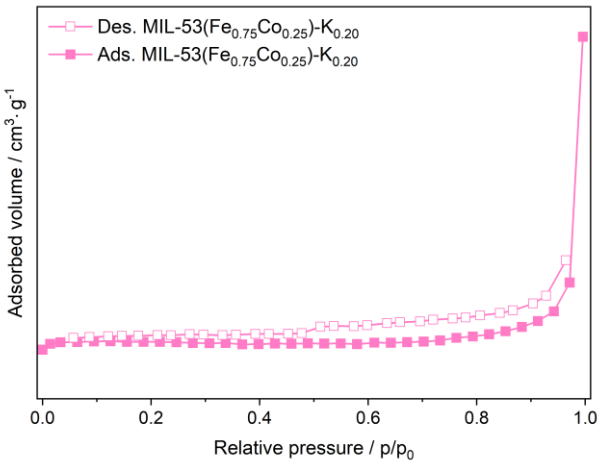
Des. MIL-53(Fe0.75Co0.25)-K0.20
Ads. MIL-53(Fe0.75Co0.25)-K0.20
Adsorbed volume / cm3.g-1
Relative pressure / p/p0
0.0
0.2
0.4
0.6
0.8
1.0

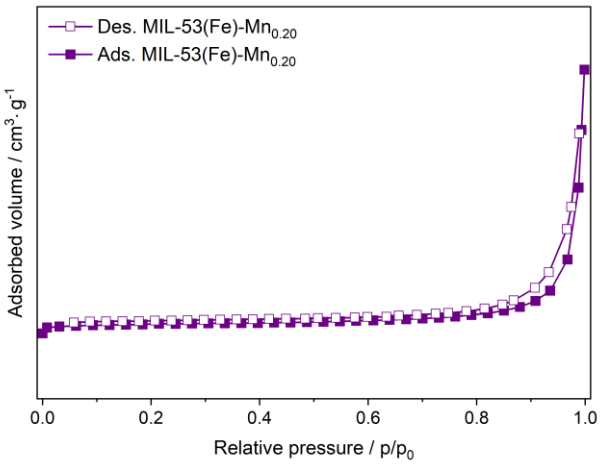
Des. MIL-53(Fe)-Mn0.20
Ads. MIL-53(Fe)-Mn0.20
Adsorbed volume / cm3.g-1
Relative pressure / p/p0
0.0
0.2
0.4
0.6
0.8
1.0

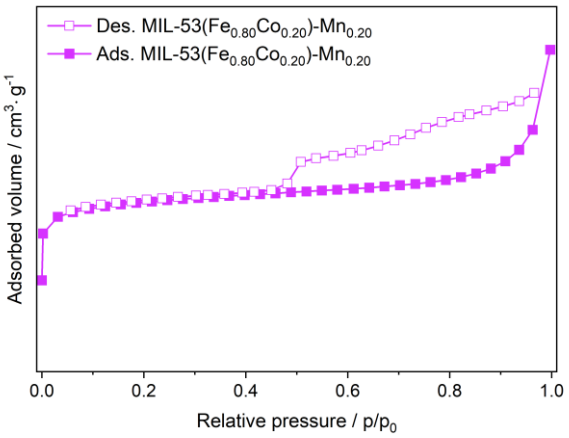
Des. MIL-53(Fe0.80Co0.20)-Mn0.20
Ads. MIL-53(Fe0.80Co0.20)-Mn0.20
Adsorbed volume / cm3.g-1
Relative pressure / p/p0
0.0
0.2
0.4
0.6
0.8
1.0

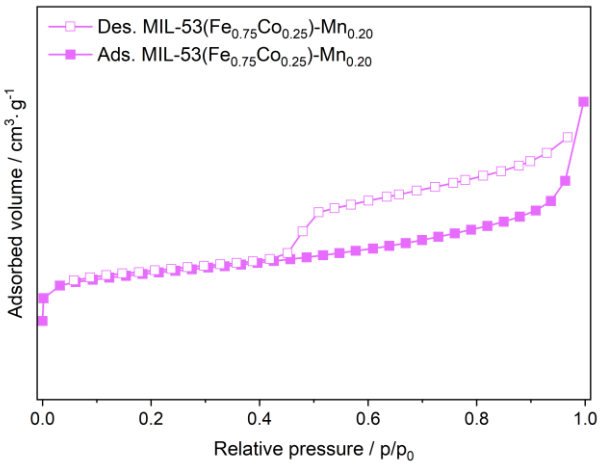
Des. MIL-53(Fe0.75Co0.25)-Mn0.20
Ads. MIL-53(Fe0.75Co0.25)-Mn0.20
Adsorbed volume / cm3.g-1
Relative pressure / p/p0
0.0
0.2
0.4
0.6
0.8
1.0

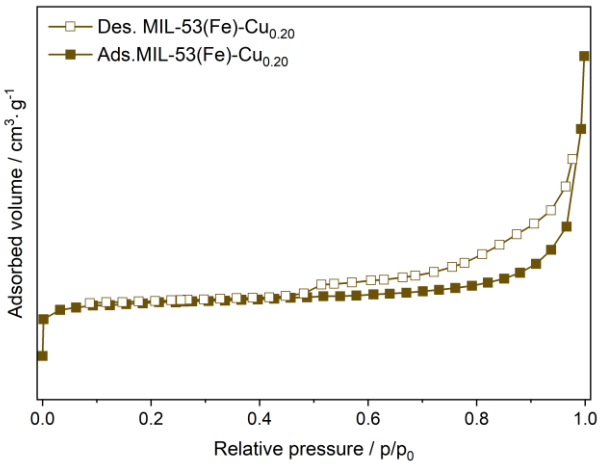
Des. MIL-53(Fe)-Cu0.20
Ads.MIL-53(Fe)-Cu0.20
Adsorbed volume / cm3.g-1
Relative pressure / p/p0
0.0
0.2
0.4
0.6
0.8
1.0

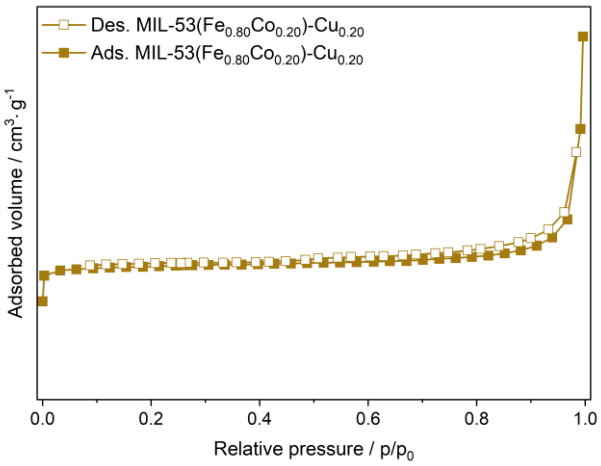
Des. MIL-53(Fe0.80Co0.20)-Cu0.20
Ads. MIL-53(Fe0.80Co0.20)-Cu0.20
Adsorbed volume / cm3.g-1
Relative pressure / p/p0
0.0
0.2
0.4
0.6
0.8
1.0

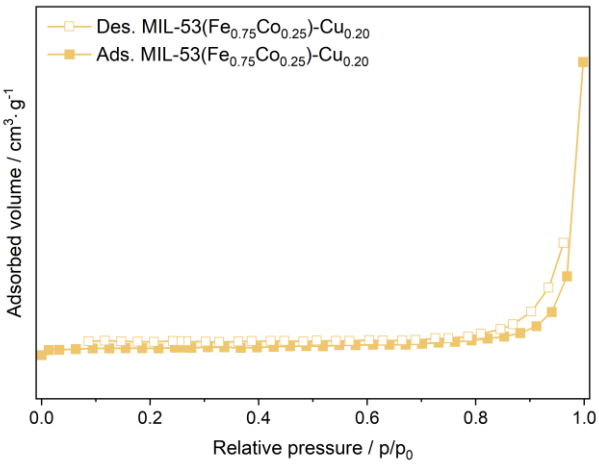

Figure A 5: Nitrogen physisorption isotherms of the MIL-53(Fe_xCo_{1-x})-$Y_{0.20}$ MOF precursors.

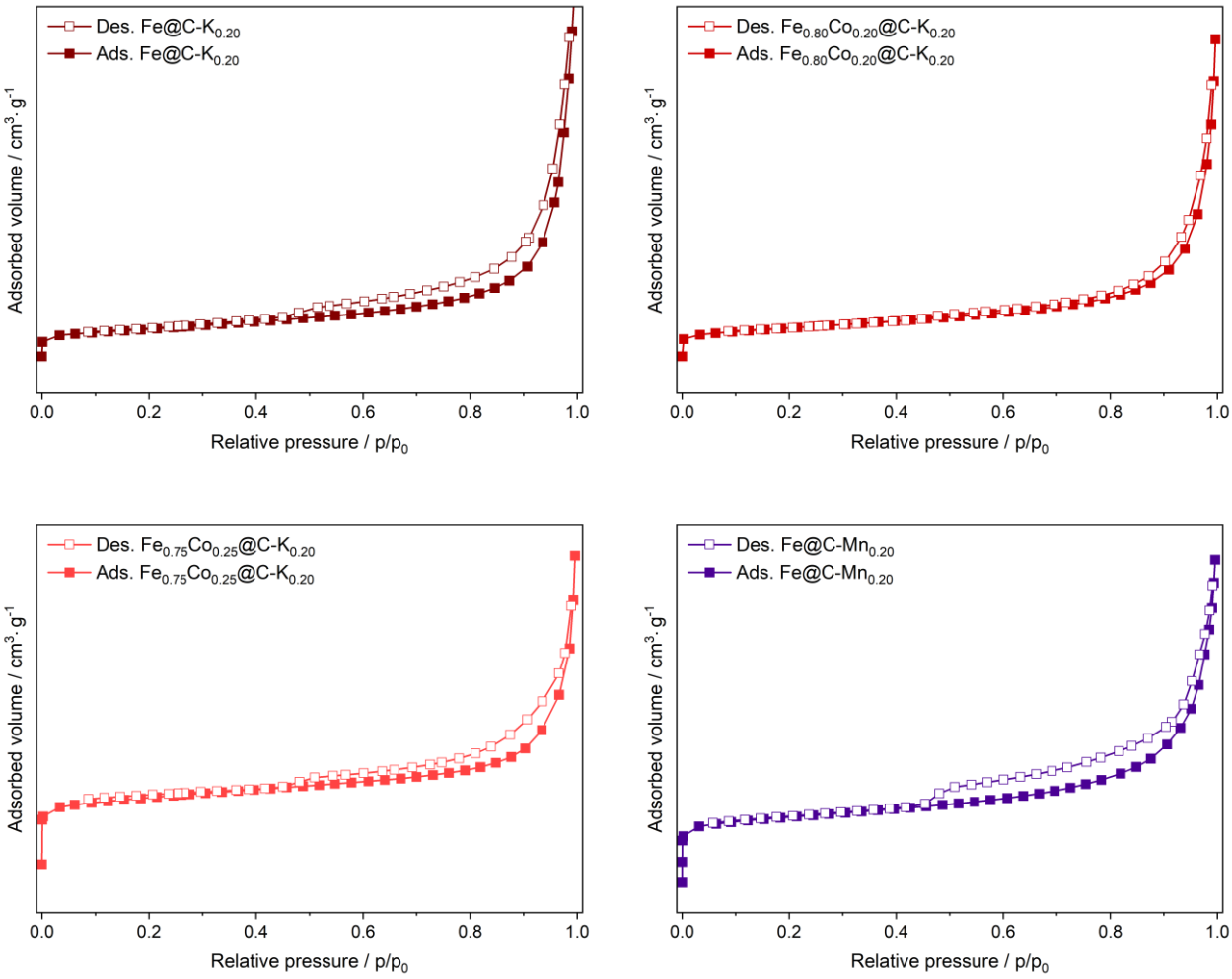

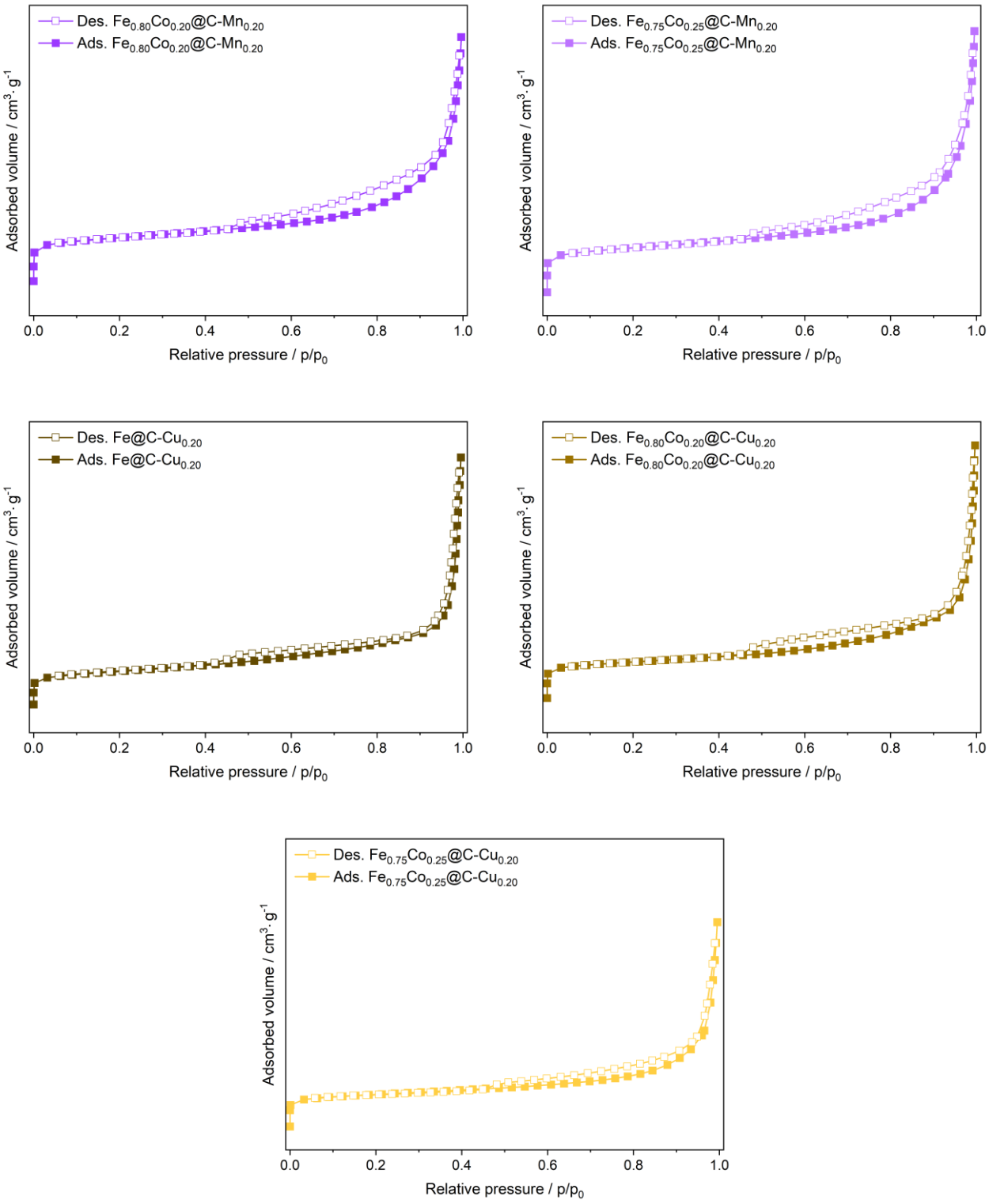

Figure A 6: Nitrogen physisorption isotherms of the Fe_xCo_{1-x}@C-$Y_{0.20}$ MOFMS catalysts.

8 Acknowledgement

First, I would like to thank Prof. Dr. Wolfgang Kleist for the opportunity to do my doctorate in his working group and for enabling me to research my topic. But also, for the many fruitful discussions during my PhD time and the overall pleasant working atmosphere both in Bochum and Kaiserslautern.

I would also like to thank my second examiner Prof. Dr. Martin Muhler. During my time in Bochum, I always felt very comfortable and warmly welcomed in the Technical Chemistry Department.

Additionally, I would like to thank my third examiner Prof. Dr. Werner Thiel, firstly as an examiner and secondly for the exciting EXAFS samples that I was allowed to measure and analyze at various beam-times.

Furthermore, I want to take the opportunity to thank Prof. Dr. Ute Krämer and Petra Düchting from the Ruhr University Bochum and Prof. Dr. Ekkehard Neuhaus, Dr. Isabel Keller and Dr. Benjamin Pommerrenig form RPTU Kaiserslautern-Landau for the chance to carry out ICP-OES measurements. I would also like to thank Dr. Edmund Welter for his support during various EXAFS measurements at the Deutsches Elektronen Synchrotron in Hamburg. My thanks go to Prof. Dr. Volker Schünemann and Marco Tummeley (RPTU Kaiserslautern-Landau) as well for carrying out and evaluating the Mössbauer samples.

From Prof. Kleist's working group, I first would like to thank Dr. Ceylan Yildiz, Dr. Johannes Bitzer and Dr. Milada Teubnerova for the warm welcome into the working group and the introduction to all the common working techniques of the working group when I joined the group during my Master's degree. From the colleagues in Kaiserslautern, I want to thank Dr. Christian Wilhelm for the introduction and support with any problems on the Fischer-Tropsch model plant. Furthermore, I would like to express my thanks to Rene Bachmann, Benjamin Heider, Janek Jost and Sven Schaefer. Our discussions in and outside the university have solved many of the problems that arose during my doctoral studies. In addition, the friendship we built up outside of work also contributed to the working atmosphere in a positive way. I would also like to thank all the other colleagues and students in the Kleist group.

From the working group of Prof. Muhler, I would like to thank Dr. Julia Büker and Dr. Jonas Schulwitz for the very scientific lunch breaks discussions during my time at the Ruhr University Bochum.

I would also like to thank my girlfriend Christin Marie Wozniak, my mother Elke Herrendorf and my cat Kitty for their mental support during my PhD studies.

9 Eidesstattliche Erklärung

Hiermit versichere ich, dass die vorliegende Arbeit selbstständig und nur unter Nutzung der angegebenen Quellen verfasst wurde. Außerdem versichere ich, dass diese Arbeit weder in dieser noch in ähnlicher Form einer anderen Prüfungskommission vorgelegt worden ist. Außer den mit dem Zulassungsgesuch urkundlich vorgelegten Graden habe ich keine weiteren akademischen Grade erworben oder versucht zu erwerben.

Kaiserlautern, den 04.10.2024

_____

Tim Herrendorf

10 Curriculum Vitae

Tim Herrendorf

Berufserfahrung

06/2024 – aktuell	**Wissenschaftlicher Mitarbeiter am MPI CEC** Max-Planck-Institut für chemische Energiekonversion (Mülheim, DE)
01/2021 – 07/2023	**Wissenschaftlicher Mitarbeiter an der RPTU** Rheinland-Pfälzische Uni. Kaiserslautern-Landau (Kaiserslautern, DE)
10/2019 – 12/2020	**Wissenschaftlicher Mitarbeiter an der RUB** Ruhr-Universität Bochum (Bochum, DE)

Bildungsweg

10/2019 – 07/2023 **Promotion im Bereich Technische Chemie**

Rheinland-Pfälzische Uni. Kaiserslautern-Landau (Kaiserslautern, DE)

Ruhr-Universität Bochum (Bochum, DE) bis 12/2020

- Generation of heterogeneous Fe- and Fe/Co-based catalysts from metal-organic framework precursors for the Fischer-Tropsch synthesis from carbon dioxide and hydrogen
- Fachbereich: Technische Chemie

10/2017 – 09/2019 **Master of Science im Bereich Chemie**

Ruhr-Universität Bochum (Bochum, DE)

- Synthesis of DUT-5-based metal-organic frameworks and their post-synthetic modification with biomedically relevant molecules
- Fachbereich: Technische Chemie

10/2013 – 09/2017 **Bachelor of Science im Bereich Chemie**
Ruhr-Universität Bochum (Bochum, DE)
- Synthese eines PNA-Replikators auf Basis der Click-Reaktion
- Fachbereich: Organische Chemie

09/2004 – 07/2013 **Abitur**
Albert-Einstein-Gymnasium (Duisburg, DE)

Veröffentlichungen

03/2024 X. Li, G. Lu, T. Wang, J.Y. Yang, T. Herrendorf, P. Schwiderowski, J. Schulwitz, P. Chen, W. Kleist, G. Zhao, M. Muhler, B. Peng, ChemSusChem, 2024, e202300871 (DOI: 10.1002/cssc.202300871)

01/2024 O. Pourshiani, Z. Romero, N. Ganji, T. Herrendorf, A. Seifert, A. Demchenko, M. H. Prosenc, W. Kleist, M. Kopnarski, B. Karimi, W. R. Thiel, ChemCatChem, 2024, e202301162 (DOI: 10.1002/cctc.202301162)

01/2024 C. Pflieger, T. Eckhard, J. Böttger, J. Schulwitz, T. Herrendorf, S. Schmidt, S. Salamon, J. Landers, H. Wende, W. Kleist, M. Muhler, F. Cerciello, Appl. Energy, 2024, 353, 122068 (DOI: 10.1016/j.apenergy.2023.122068)

11/2023 P. Telaar, P. Diehl, T. Herrendorf, S. Schaefer, W. Kleist, M. Muhler, Catal. Sci. Technol., 2023, 13, 6968-6980 (DOI: 10.1039/D3CY00957B)